Numerical analysis of open-ended coaxial line probes and its application to in-vivo dielectric measurements.

McArthur, Paul

Numerical Analysis of Open-ended Coaxial Line Probes and its Application to in-vivo Dielectric Measurements.

Paul McArthur

Kings College

A Thesis Submitted to the University of London

for the Degree of Doctor of Philosophy

1989

To my wife, Catherine

Abstract

A Time Domain Spectrometer was designed to measure the dielectric properties of human tissue *in-vivo* by incorporating open-ended coaxial line probes. Using this technique the permittivity of the sample may be found by studying the fringe field of the open-end and its perturbation by the unknown dielectric.

In order to relate the fringing field to the apparent measured permittivity the equivalent circuit for the open-end, consisting of two parallel capacitances and a conductance, must be found. Two numerical analysis techniques, the Method of Moments and the Finite Element Method, were used to study the equivalent circuit of open-ended coaxial line probes. In particular the Finite Element Method was extended to include high order polynomial approximating functions. Both techniques were used to simulate a variety of probe designs.

The Time Domain Spectrometer was designed around an HP 9216 microcomputer. Two independent time referencing procedures were included in the design to allow an experimental comparison of accuracy. The system was tested using two known liquid standards, formamide and ethanediol. After successful testing, measurements were made on the inner and outer jaw, the ear lobe, the tongue, the palm and the forearm in the frequency range 0.1 to 10 GHz.

Contents.

Chapter 1

General Introduction

1.1 The Background of Time Domain Spectroscopy

To study the dielectric properties of materials and biological substances, Time Domain Spectroscopy (TDS) was first introduced in 1969. The potential of the technique was reported by Fellner-Feldegg (1969) when he applied real time analysis on the reflection from a sample under investigation. This technique was limited in scope (Whittingham 1970) but initiated the theoretical and experimental advances in the TDS instrumentation. The real time analysis approach was expanded further by Fellner-Feldegg (1972) , van Gemert *et al* (1973) and Cole (1975).

The first application of Fourier transformation techniques was developed by Suggett *et al* (1970). This broadened the frequency band covered by Fellner-Feldegg and was closely followed by others who adopted a similar line of analysis (Loeb *et al* 1971, de Loor *et al* 1973, Clark *et al* 1974). The principles involved were similar to those in the real time domain analysis differing only in the fact that the reflection, or transmission, was Fourier transformed and the analysis undertaken in the frequency domain.

In the late 1970's to early 1980's there were several advances in the designs of TDS systems. Cole *et al* (1980) reported a new system that would perform precision dielectric measurements from 1 MHz to several GHz. Dawkins *et al* (1979) developed a system dedicated to total reflection measurements and was later adapted by Gabriel *et al* (1984) to encompass single reflection techniques. Gestblom *et al* (1980) then developed a computer controlled TDS system that allowed both reflections and transmissions to be used and reported an increase in the accuracy of the method over existing techniques.

Crucial to all techniques that use Fourier transformations is the finding of a common time origin, t_0. It has been shown (Gestblom *et al* 1980) that an error of δt, where $t_0 + \delta t$ is the new time origin, will give an error of $\omega\delta t$ in the phase of the scattering coefficient. The different TDS systems developed over the period approached this time referencing problem in different ways.

Cole *et al* (1980) used a two channel system which produced a small marker pulse on the reflection in constant relation to the signal from the sample. The marker was derived by coupling 10 dB of the input signal through the marker channel. The marker was fixed relative to the reflection and was unchanged by any change in sample. Accurate referencing was then possible by continually using the marker as the common time origin. Gestblom *et al* (1980) used a similar two pulse technique but derived the marker pulse by splitting the input signal into two identical pulses. The alignment then involved a complex numerical procedure where statistical analysis was used to determine the reference point. A completely different approach was adopted by Dawkins *et al* (1979) where the reference point was found on the reflection by an

extrapolation technique, first developed by Loeb *et al* (1971). This was relatively straightforward and required none of the additional hardware needed to derive the marker pulse.

The use of the extrapolation technique has come under severe criticism particularly from Gestblom (1981), where he says the fundamental drawback is the referencing to a point which changes with reflecting medium. By using a model of the reflected pulse he stated that the error in the extrapolation technique would be at least twice the size of the error in his own system. However Arcone *et al* (1986) pointed out that that the model of Gestblom (1981) was not sufficiently accurate and proved the maximum timing error in the extrapolation technique would actually be a fraction of Gestblom's prediction.

More recently open-ended coaxial line probes have been used in TDS measurements (Gabriel *et al* 1986). This is an extension of the work of Burdette *et al* (1980), Stuchly *et al* (1980) and Athey *et al* (1982) where similar probes were used extensively with network analysers. The method is based on the study of the fringe field of the aperture of the probe and its perturbation by an unknown dielectric in contact with it. By reducing the problem to a study of the end of the line impedances the reflection coefficient may be related to the sample permittivity.

1.2 The Equivalent Circuit Model

In order to use the coaxial line probes as an extension of the tools available to TDS the equivalent circuit of the aperture of the open-end has to be found. In the general case an open-ended coaxial line can be represented by an equivalent circuit consisting of a shunt lumped admittance, Y, terminating a transmission line of characteristic admittance, Y_0 (Fig 1.1(a)). Considering the case where the open end of the line is contacting a sample with dielectric parameter $\hat{\epsilon}$ the equivalent circuit consists of a parallel combination of a capacitance, $C(\hat{\epsilon})$, and a conductance, $G(\hat{\epsilon})$, Fig 1.1(b). The input admittance of the probe may then be written as

$$\begin{aligned} Y &= G(\hat{\epsilon}) + j\omega C(\hat{\epsilon}) \\ &= G(\hat{\epsilon}) + j\omega(C_f + \hat{\epsilon}C_o) \end{aligned} \tag{1.1}$$

where ω is the angular frequency and the total capacitance in the equivalent circuit has been split into two parallel capacitances, C_f and $\hat{\epsilon}C_o$, Fig 1.1(c).

The capacitance C_o, when multiplied by $\hat{\epsilon}$, represents the storage of energy in the dielectric contacting the aperture while the capacitance C_f represents the storage of energy in the fringing fields not affected by the dielectric.

If C_o and C_f vary with permittivity the capacitance, $C(\hat{\epsilon})$, does not have a linear relationship with $\hat{\epsilon}$. However a range of values of $\hat{\epsilon}$ may exist where C_f and C_o are relatively constant and the total capacitance can be approximated by to a linear function of the sample permittivity (Stuchly *et al* 1980, Gajda *et al* 1983).

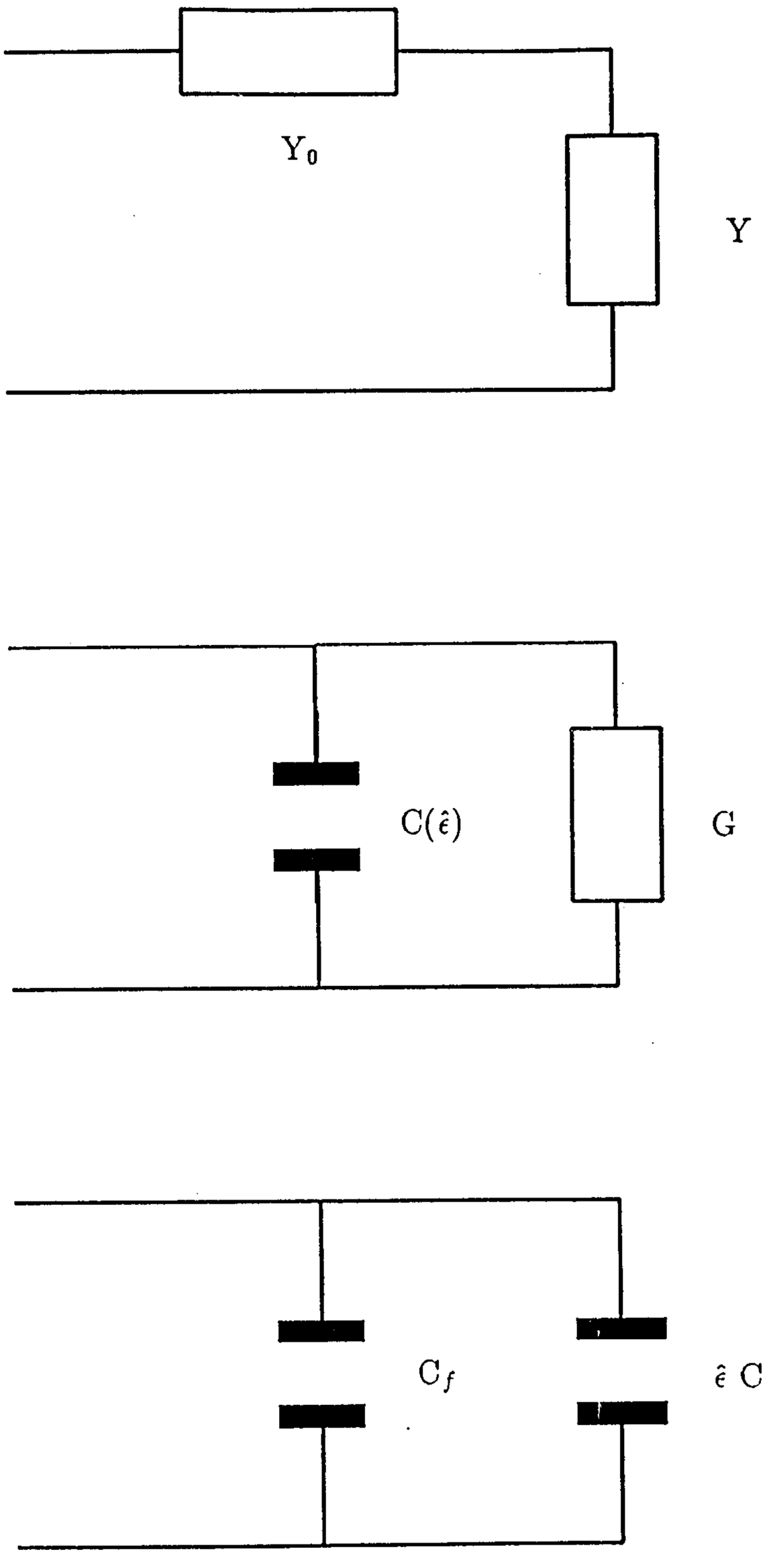

Fig 1.1 Equivalent Circuit of an open-ended coaxial line.

If a and b represent the inner and outer conductor radii respectively (Fig 1.2), it can be shown that when $a/\lambda < 0.04$ (Marcuwitz 1951, Gajda 1982, Stuchly *et al* 1980), the equivalent circuit may be simplified to that shown in Fig 1.1(c), where the admittance, Y, is the sum of the two fringe field capacitances, $\hat{\epsilon}C_o$ and C_f.

The permittivity may then be related to the reflection from the dielectric at the aperture by (Stuchly *et al* 1982, Gabriel *et al* 1986)

$$\hat{\epsilon} = \frac{1-\Gamma}{j\omega Z_o C_o(1+\Gamma)} - \frac{C_f}{C_o} \tag{1.3}$$

where Γ is the measured reflection coefficient and Z_o is the characteristic impedance of the line.

At higher frequencies the value of C_o increases with frequency (Marcuwitz 1951, Athey *et al* 1982, Kraszewksi *et al* 1983) due to the evanescent TM modes being excited at the interface. When these modes are taken into account the value of C_o can be corrected by using the equation (Kraszewski *et al* 1983)

$$C_o^{corr} = C_o + Af^2 \tag{1.4}$$

where A is a constant dependent on the line dimensions.

Above a certain value of permittivity placed at the interface the conductance term in the equivalent circuit may become significant. However it can be shown in (section 4.3.7) that in the new time domain spectrometer the contribution of the conductance term to the reflection coefficient measured can be minimised.

1.3 Criteria for Choice of Modelling Technique

The equivalent circuit of the open-ended probe can be used to find the permittivity of a sample contacting it provided the parameters C_o and C_f are known. Experimental techniques may be used to find the value of C_o but are limited in obtaining any accurate information as to the magnitude of C_f. Therefore it is necessary to calculate, theoretically, the capacitance values using some form of numerical analysis.

As the variation of the capacitances C_o and C_f with frequency is minimal within the frequency range of TDS (Kraszewski *et al* 1983) it is possible to state that they are static and any correction in the upper frequency band may be adequately dealt with using equation 1.4. Therefore the modelling technique chosen will have no frequency dependent term and, as a result, the permittivity of the sample can be thought of as lossless.

An equation for the total capacitance, C_T, of an open-ended coaxial line with an infinite groundplane and homogeneous air dielectric at the interface is given by (Marcuwitz 1951, Galejs 1969)

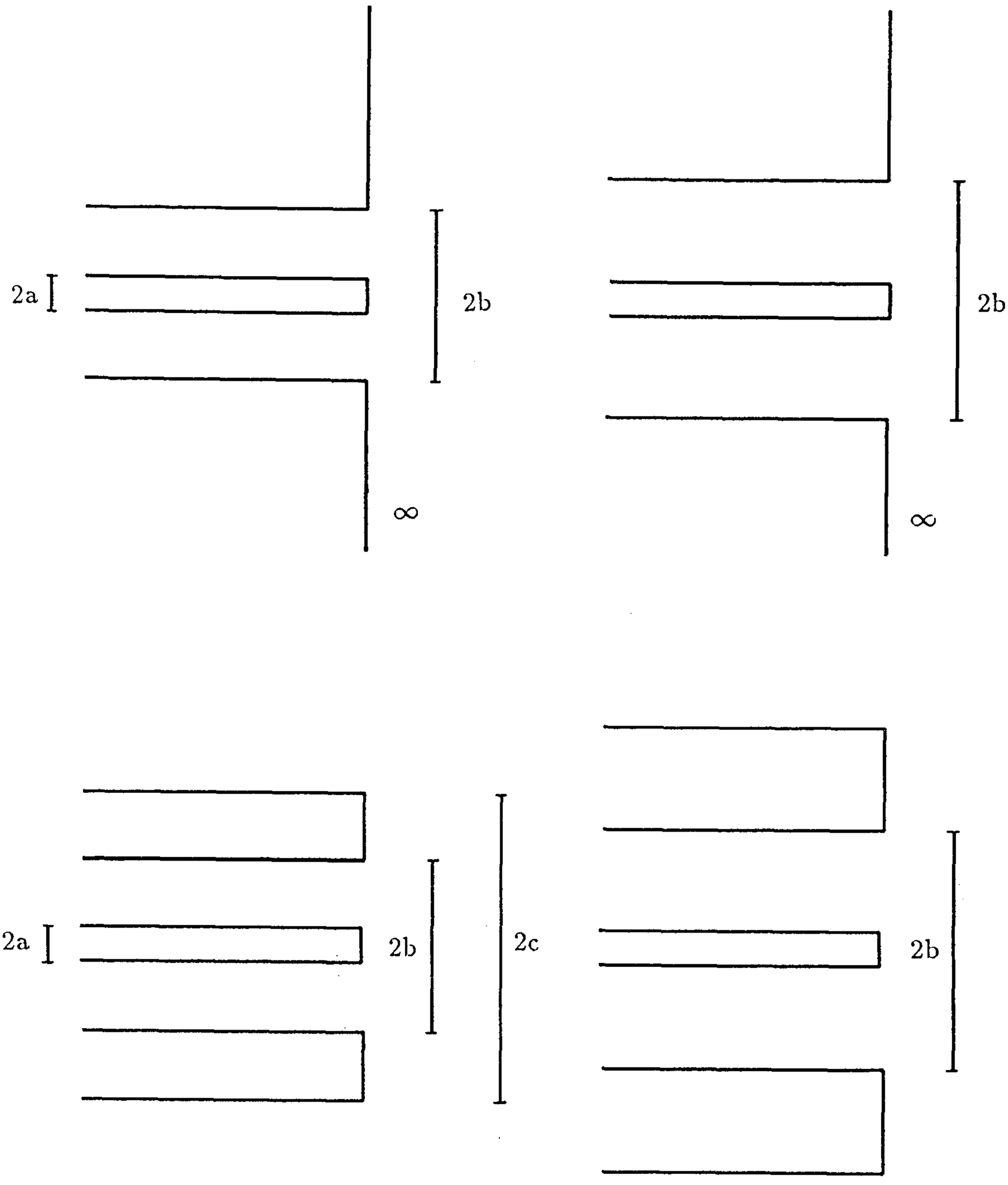

Fig 1.2 Some common probe dimensions

$$C_T = \frac{2\pi\epsilon_0}{\mathsf{K}\,[ln(b/a)]^2}\int_0^{\pi}[2Si(k\sqrt{a^2+b^2-2abcos\phi}) - Si(2kasin(\phi/2)) - Si(2kbsin(\phi/2)]d\phi \tag{1.5}$$

where $Si(x)$ is the sine integral function, $k = 2\pi/\lambda$, λ is the wavelength and ϵ_o is the permittivity of free space. Although this appears computationally complex, in the low frequency case the capacitance may be rewritten as

$$\lim_{\lambda \to \infty} C_T = \frac{8\epsilon_o(b+a)}{[ln(b/a)]^2}[E(\frac{2\sqrt{ab}}{b+a}) - 1] \tag{1.6}$$

where $E(x)$ is the complete elliptic integral of the second kind. This method of solution suffers from several disadvantages :

(a) The presence of an infinite groundplane in the plane of the aperture is assumed. This limits the calculations to probes with a similar configuration to that of Fig 1.2(a) only.

(b) There is no facility for changing the permittivity to a value of similar proportions to those encountered in actual experiments.

(c) As a result of (b) no information is obtained as to the magnitude of C_o and C_f.

Due to the valid assumption that the capacitances are static, Laplace's equation may be used to calculate the potentials in space and as a result the total capacitance for different permittivities. Several techniques exist to solve this equation, each suited to a particular application.

The use of Finite Differences in solving electromagnetic and electrostatic problems has proved accurate and simple to use (Wexler 1969, Lau *et al* 1986). The importance lies in the ease with which complicated mathematical functions and operators may be approximated to yield simple arithmetic computations. In the general case the region of solution is split into cells of a defined size and the unknown variables are solved on an iterative basis (Fig 1.3). Unless the cells are the same size throughout the model the storage needs will be large as additional information of the dimensions in each cell is needed (Fusco 1987). As a result a particular point in space may not be examined closely and information may be lost, particularly if the storage facilities are small. This will be the case in the present application where the aperture of the probes needs to be modelled by a very fine cell size and the memory of the computing facilites is relatively small.

Perhaps the most widely used techniques in the area of electrostatics are the Finite Element method and the Method of Moments (Harrington 1968, Silvester 1986). The construction of the system of equations is relatively straight forward and a particular portion of the region of solution may be closely examined without any increase in the model size. The Method of Moments is essentially the integral form

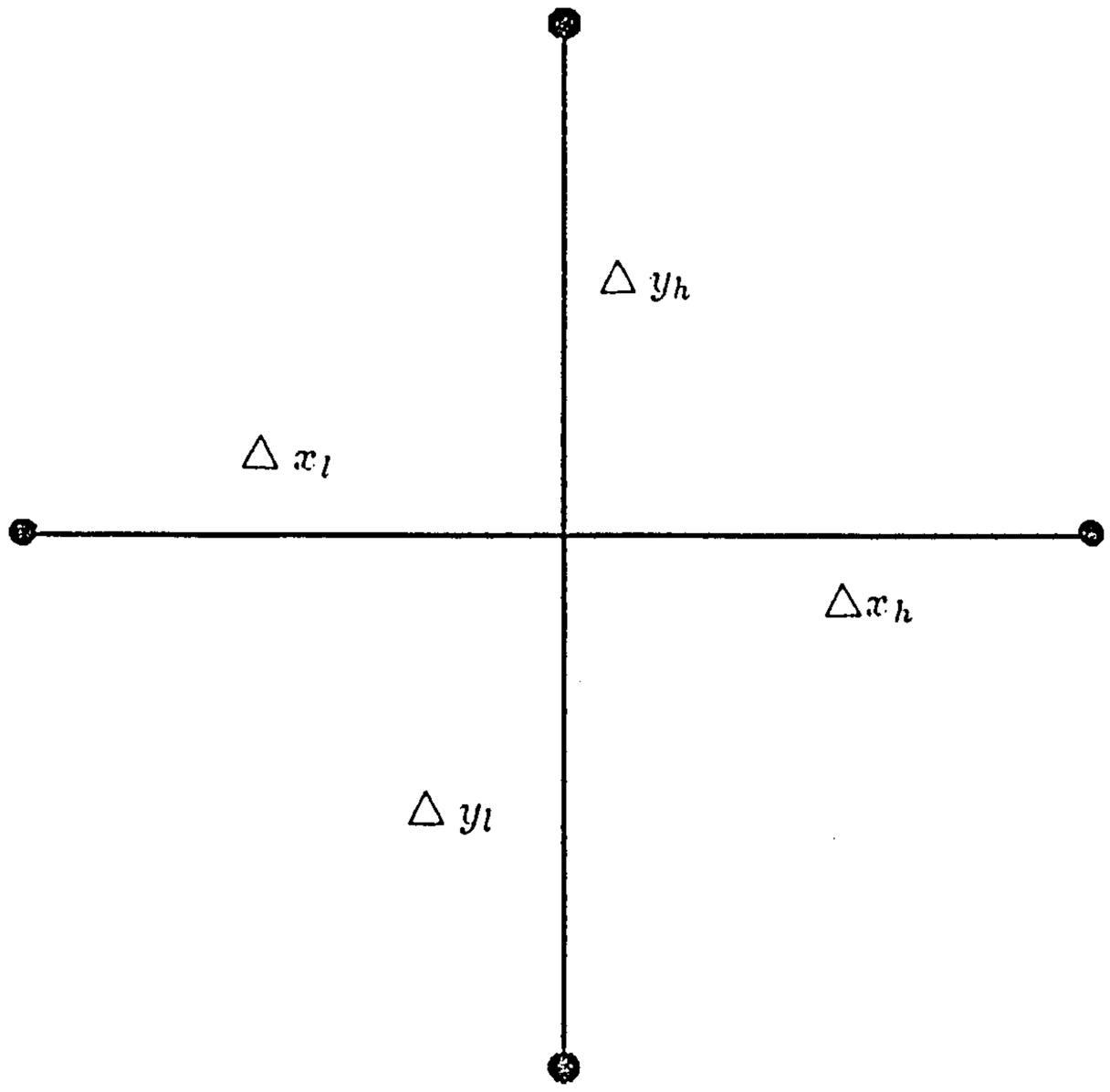

$$\frac{\phi_1 + \phi_3 - 2\phi_0}{\triangle y_l \triangle y_h(\triangle y_l + \triangle y_h)} + \frac{\phi_2 + \phi_4 - 2\phi_0}{\triangle x_l \triangle x_h(\triangle x_l + \triangle x_h)} = 0$$

$$if \triangle y_l = \triangle y_h = \triangle x_l = \triangle x_h \quad then$$

$$\frac{\phi_1 + \phi_2 + \phi_3 + \phi_4}{4} = \phi_0$$

Fig 1.3 Finite difference cell and iteration procedure.

of the Finite Element method (Fusco 1987) and both techniques utilize the principle that the region of solution can be subdivided into smaller regions and the defining equation solved in each subregion. Provided the problem can be adequately defined by the techniques, the use of both will yield the upper and lower limits on any capacitance values (Collin 1960).

With these points in mind it was decided to use the Method of Moments and the Finite Elements in order to calculate the upper and lower bounds of the capacitance.

1.4 The Main Research Aims

The use of open-ended coaxial line probes in the measurement of the dielectric parameters of materials and biological samples requires prior knowledge of the equivalent circuit to enable correct usage of equation 1.3. Although experimental values exist for the fringe field capacitance C_o (Gabriel *et al* 1986) the magnitude of C_f has not been accurately determined. As the capacitances are known to be static for much of the frequency range of interest in Time Domain Spectroscopy experiments a numerical solution to Laplace's equation will give theoretical limits to C_o and C_f.

As pointed out in section 1.3 the two techniques best suited to the application are the Method of Moments and the Finite Elements. From a previous study by Gajda *et al* (1983) the use of Finite Elements was the subject of criticism when it was pointed out that the values obtained for the capacitances were not sufficiently accurate and, as a result, studies from that time have concentrated on the Method of Moments (Anderson *et al* 1986, Stuchly *et al* 1986). Upon close examination of the facts there appears to be a discrepancy in the comparison. The main difference is that the model run in the Finite Element is of minimal proportions whereas that run in the Method of Moments is very large. Thus a true comparison cannot be drawn from such a series of tests (Trowbridge 1987).

The purpose of the theoretical work in this research is to use the two algorithms, one for the Method of Moments and one for the Finite Element, to model a variety of coaxial probes over differing situations (ie. the size of the model in each case and the defining approximating functions) and draw some valid conclusions as to the relative performance of each technique. It is hoped that the study of the two techniques will lead to a set of parameters that will enable novel probe designs to be studied and their equivalent circuits to be found.

The theoretical study of the probes is, in itself, a major undertaking. However once the unknown quantities are known, the probes may be used not only for the measurements of the dielectric properties of liquids but also for *in vivo* experiments. The need then arises for the design of a new Time Domain Spectrometer to apply the theoretical knowledge gained to a real experiment. This leads to several interesting questions as to the best design to use from the various instruments in existence and the experimental techniques to be incorporated.

In all the designs of TDS instruments the main differences are the interfacing of the dedicated microcomputer used as the controller for the experiment and the

procedure adopted for the time referencing. The interface problem is determined by the computer chosen and will therefore change as computer facilities change.

All of the studies concerning the choice of the best time referencing procedure have been of a theoretical nature (Gestblom 1981, Arcone *et al* 1986) and the outcome of each has provided conflicting results. Of the three techniques mentioned previously two incorporate a dual channel approach where the second channel is used to reference the response of the first. The most accurate results from the dual approach has to be that of Cole *et al* (1980) where dielectric parameters were measured with ϵ'' equal to 0.02. As a result it was decided to incorporate Cole's technique as well as the extrapolation procedure developed by Loeb *et al* (1971) and further advanced by Dawkins *et al* (1979). Both would be tested in a real experimental sense which would hopefully solve the controversy.

The testing of the TDS, using the probes modelled, was conducted on two liquids with known dielectric parameters, formamide and ethanediol. They are thought to be a good test of the scope and accuracy of the instrument. After passing the testing stage *in vivo* measurements on various parts of the human body would be taken.

1.5 An Outline of the Thesis

The use of open-ended coaxial line probes in TDS measurements requires prior knowledge of the magnitude of the capacitances in the equivalent circuit. Chapter 2 gives the theoretical basis of the Finite Element and the Method of Moments for rotationally symmetric problems. In particular, following a brief introduction of first order Finite Elements, the principles involved in creating and using high order polynomial expressions in the analysis are presented. In each case the models used in the analysis are discussed to indicate the boundary conditions encountered.

Chapter 3 deals with the results of the analysis of the coaxial line probes using the techniques outlined in chapter 2. The programs are briefly discussed before the results of probes with known equivalent circuits are presented. An optimum set of modelling parameters for both the Finite Element and the Method of Moments are derived and are used to calculate the fringe capacitances of several novel probe designs, to be used in the testing of a new Time Domain Spectrometer.

In chapter 4 the design of a new Time Domain Spectrometer is given. The basic theory of Time Domain Spectroscopy is briefly introduced, problems encountered in interfacing the experiment to a remote microcomputer are documented and the experimental procedures incorporated in the design are given.

Chapter 5 describes the results obtained in the testing of the new TDS with emphasis on the two time-referencing procedures. These results are shown for formamide and ethanediol at different temperatures and conclusions as to the best referencing technique are drawn. Finally the results of *in vivo* measurements on human skin are presented. In each case the probes used are those analysed in chapter 3.

Chapter 2

Numerical Analysis Techniques

2.1 Introduction

In order to find the fringe field capacitances of open-ended coaxial line probes, numerical techniques were applied to solve the relevant electrostatic problems (Wexler 1969, Gajda 1982). This chapter briefly describes the basis of two such techniques, namely the Finite Element Method and the Method of Moments (Harrington 1968, Zienkiewicz 1977, Konrad 1977). In the present studies, the coaxial line probes possess axial symmetry and the two techniques have been adapted to take advantage of such a property. In particular, the Finite Element Method has been extended from the basic first order element formulation to the higher order polynomial elements (Silvester 1969, Zienkiewicz 1977, Silvester *et al* 1986) to provide a higher degree of accuracy. A short discourse on variational calculus (Wexler 1969, Jones 1979)is included in this chapter.

2.2 Linear Operator Equations

2.2.1 Fundamentals

Most of the equations that arise in electrostatic field theory are of the form

$$Lu = f \tag{2.1}$$

where L is a linear operator with a prescribed set of boundary conditions, f is a known forcing function and u is the unknown desired solution function. In electrostatics, L may be either differential or integral. For example

$$L = -\nabla^2 \tag{2.2(a)}$$

or

$$L = \int_{\Omega} d\Omega \tag{2.2(b)}$$

Associated with equation 2.1 is an inner product, defined as the integral of the product of u and f over the region of solution,

$$< u, f > = \int_{\Omega} u \cdot f d\Omega \tag{2.3}$$

Each linear operator also has an adjoint operator L^a which satisfies

$$< Lu, f > = < u, L^a f > \tag{2.4}$$

If $L = L^a$ the operator is said to be self-adjoint.When L is differential, self-adjointness is determined by the associated boundary conditions of L (Wexler 1969), while for integral operators the kernel of the integral must be symmetric (McDonald *et al* 1974).

A second important property that exists is termed positive definiteness. If

$$< Lu, u > \; > \; 0 \quad u \neq 0 \tag{2.5(a)}$$

$$< Lu, u > \; = \; 0 \quad u = 0 \tag{2.5(b)}$$

the linear operator L is said to be positive definite and the solution to equation 2.1 is said to be unique (Wexler 1969).

In order to find the capacitances C_o and C_f of the coaxial line sensor two different linear operators may be used. The first is the case where L is differential and results in Laplace's equation

$$\nabla \cdot (\epsilon \nabla \phi) = 0 \tag{2.6}$$

where ∇ is the Laplacian operator and ϵ is the real part of the complex permittivity of the medium bounded by the problem. The function f is seen to be zero, while the function u is represented by the scalar potential ϕ. The capacitance values may be calculated once the unknown ϕ's are found.

The second formulation results in an equation where L is integral, (Daffe *et al* 1979)

$$\phi(x) = \int_{R} \sigma(x_0) G(x/x_0) dx_0 \tag{2.7}$$

where u is represented by the charge density σ, f by the potential ϕ and L by the integral of $G(x)$. It is worth mentioning that $G(x/x_0)$ is the Green's function representing the potential at x due to a point charge at x_0 and the integration is over the entire charge distribution R. Again the capacitance values may be found from the calculated values of σ.

2.2.2 Boundary Conditions

The most frequently occurring boundary conditions in linear operator equations applied to electrostatics are of two general forms. The first, termed the Dirichlet boundary, exists whenever the unknown function u is specified. The second, termed the Neumann boundary, exists whenever the normal gradient of u is specified. In the case to be solved the Dirichlet conditions represent conductors held at specified potentials while the Neumann conditions correspond to lines of the electric field since the normal derivative of the potential across the electric field line is zero.

These conditions may now be applied to the coaxial sensor problem. With reference to fig 2.1, the Dirichlet boundaries are provided by the conductor surfaces, which are held at specified potentials; and theoretically at infinity where the potential tends to zero. A Neumann boundary is provided by the symmetry of the problem, about $r = 0$. As the line is assumed to be infinitely long a vertical Neumann boundary is placed at $z = 0$ to represent the electric field line resulting from the TEM fields in an infinitely long line (Gajda *et al* 1983).

2.2.3 Variational Methods of Solution

To give an explanation of variational techniques it is required to answer three questions,

(i) **What are variational techniques ?**

Essentially variational techniques are methods which use known functions, termed functionals, to find an approximate solution to equation 2.1. The functional, usually defined in terms of inner products in L, u and f, will possess a stationary and minimal value at the point of solution (i.e. the first derivative will be zero and the second derivative positive at the solution point). Provided the linear operator is both self-adjoint and positive definite the function u which minimises the functional will also be a solution to equation 2.1.

(ii) **What are the functionals involved ?**

The functional for electrostatic problems is generally of the form (Wexler 1969)

$$F = < Lu, u > -2 < u, f > \tag{2.8}$$

where the variables L,u and f are of a known form.The formulation for equations 2.6 and 2.7 is relatively straight forward. For equation 2.6,

$$L = -\nabla^2 \quad u = \phi \quad and \quad f = 0 \tag{2.9(a),(b),(c)}$$

F may be written as (Wexler 1969, Costache *et al* 1975)

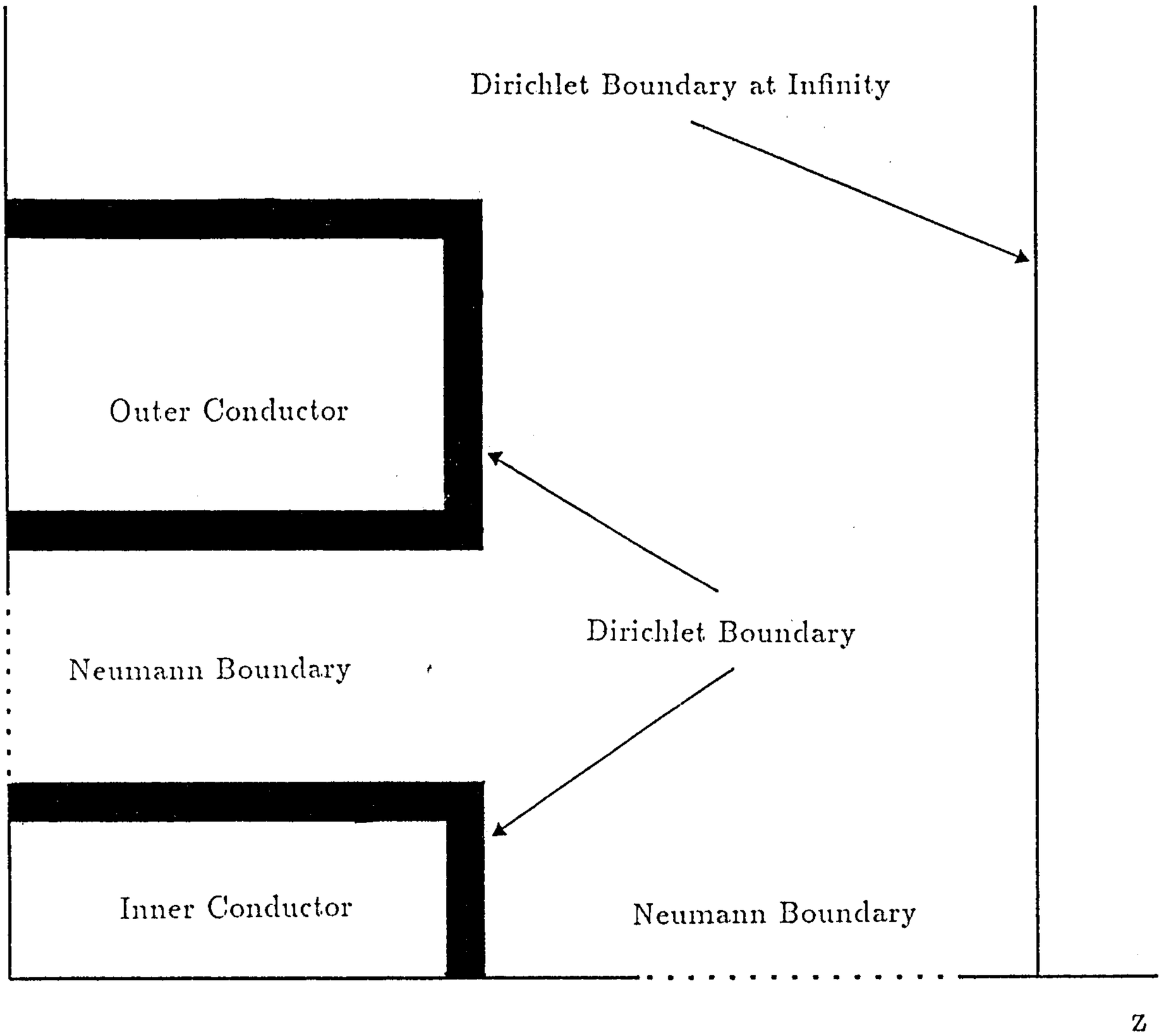

Fig 2.1 The general model used for the coaxial line probe

$$F = \int_{\Omega} \epsilon(\nabla^2 \phi) d\Omega \tag{2.10}$$

Since the problem to be solved is rotationally symmetric about the z axis, (i.e. there is no dependance on the angular variable θ in the (r, z, θ) co-ordinate system), equation 2.10 may be rewritten as

$$F = 2\pi \int_{r,z} \epsilon(\nabla^2 \phi) r dr dz \tag{2.11}$$

For equation 2.7

$$L = \int_R G(x/x_0) dx_0 \quad u = \sigma(x_0) \quad and \quad f = \phi(x) \tag{2.12(a),(b),(c)}$$

By substituting equations 2.9(a),(b),(c) into equation 2.8 F may be expressed as

$$F = \int \int \sigma(s) G(s/s') \sigma(s') ds ds' - 2 \int \sigma(s) \phi(s) ds \tag{2.13}$$

However for the problem to be solved there will be a contribution to the charge map $\sigma(s)$ from the dielectric interface, fig 2.2. This requires some manipulation of the functional (McDonald *et al* 1974, Daffe *et al* 1979, Gajda 1982) and results in the pair of coupled integral equations

$$\int_{S_C + S_I} \sigma(s') G(s/s') ds' = \phi(s) \quad s \; on \; S_C \tag{2.14(a)}$$

$$\frac{\epsilon_1 + \epsilon_2}{2} \sigma(s) + (\epsilon_1 - \epsilon_2) \int_{S_C + S_I} \sigma(s') \frac{\partial G}{\partial n}(s/s') ds' = 0 \quad s \; on \; S_I \tag{2.14(b)}$$

where the conductor surfaces are denoted by S_C, the interface surfaces between the two differing permittivities, ϵ_1 and ϵ_2, are denoted by S_I and equation 2.14(b) represents the distribution of the polarisation charge on the surface of the interface (McDonald *et al* 1974).

(iii) **How are the functionals used ?**

The true solution to equation 2.1 must satisfy the conditions outlined in (i) above. If we state that u may be represented by

$$u = \sum_{i}^{n} a_i u_i = \underline{\mathbf{a}}^T \underline{\mathbf{u}} = \underline{\mathbf{a}} \underline{\mathbf{u}}^T \tag{2.15}$$

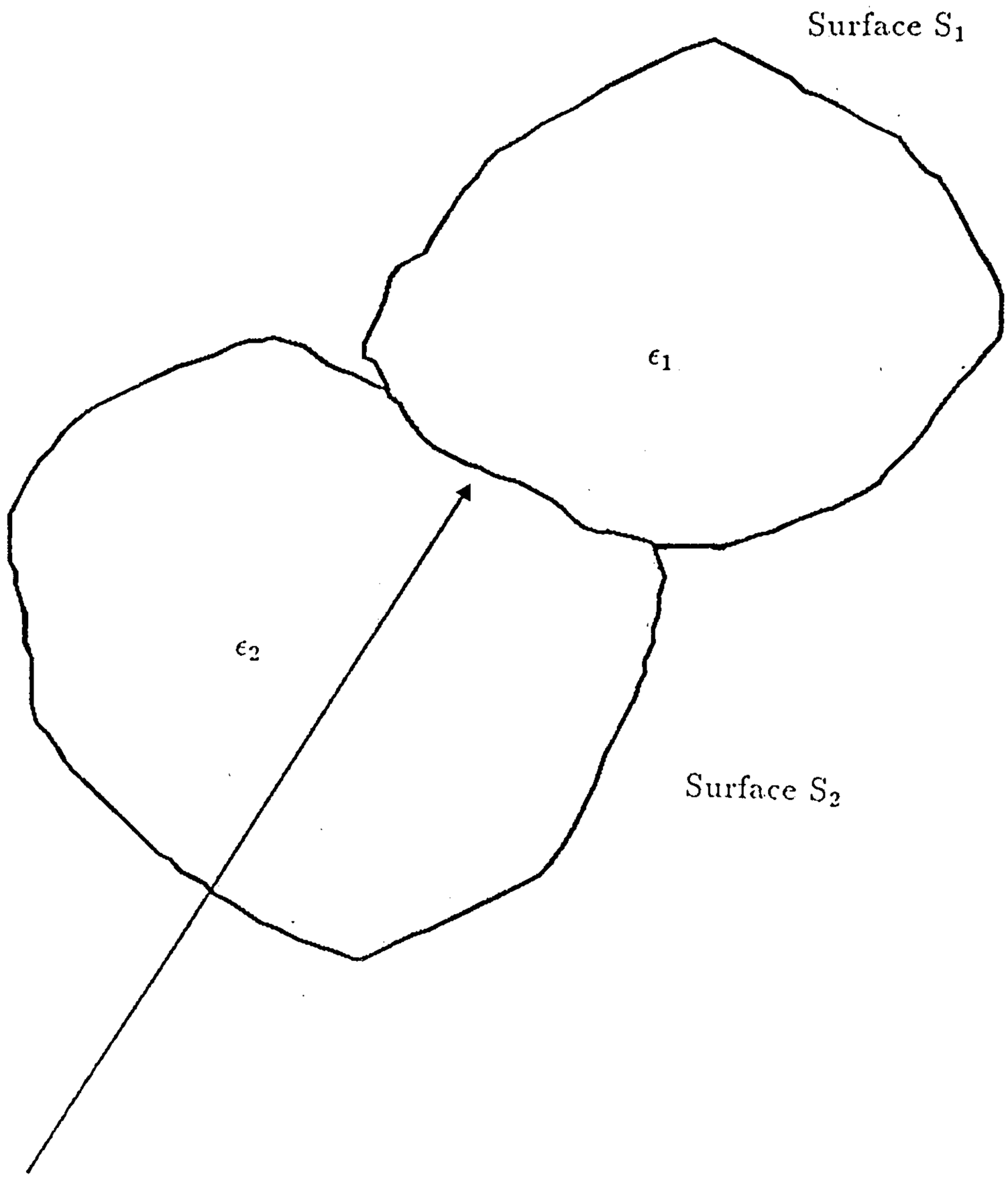

Fig 2.2 System used to solve the integral equations.
S_1 and S_2 represent the conductor surfaces.

where each u_i satisfies the boundary conditions and the a_i are unknowns, the functional in equation 2.8 will become

$$F = \underline{\mathbf{a}}^T < L\underline{\mathbf{u}}, \underline{\mathbf{u}}^T > \underline{\mathbf{a}} - 2\underline{\mathbf{a}}^T < \underline{\mathbf{u}}, f > \tag{2.16}$$

To satisfy the conditions in 2.2.3(i) the partial derivative must equal zero,

$$\frac{\partial F}{\partial a_i} = 0 \tag{2.17}$$

which, when applied to equation 2.8, results in

$$< L\underline{\mathbf{u}}, \underline{\mathbf{u}}^T > \underline{\mathbf{a}} = < \underline{\mathbf{u}}, f > \tag{2.18}$$

This may now be readily solved for the vector $\underline{\mathbf{u}}$. It is worth noting that F is equal to the amount of stored energy in the system when u is a true solution to equation 2.1.

2.3 Finite Element Solution of Laplace's Equation

2.3.1 Basic Rationale

The solution of equation 2.6

$$\nabla \cdot (\epsilon \nabla \phi) = 0$$

is often difficult to find analytically when the region of solution is of a complex and irregular shape. This would involve integrating the functional, equation 2.11, over the region of solution, which, in some cases, may become particularly difficult to perform. However, if itisassumed that the region of solution can be subdivided into smaller subregions, or elements, Fig 2.3, it can be stated that the functional can be enforced in each of these elements without loss of generality, provided care is taken to ensure continuity over adjoining elements, and subsequently continuity in adjoining element functionals (Richards *et al* 1972). The functional for the entire region of solution will then be

$$F = \sum_{e=1}^{n} F_e \tag{2.19}$$

where n is the number of elements in the region of solution and F_e is the element functional. The techniques outlined in equations 2.15 to 2.18 may then be used to find the unknown function ϕ.

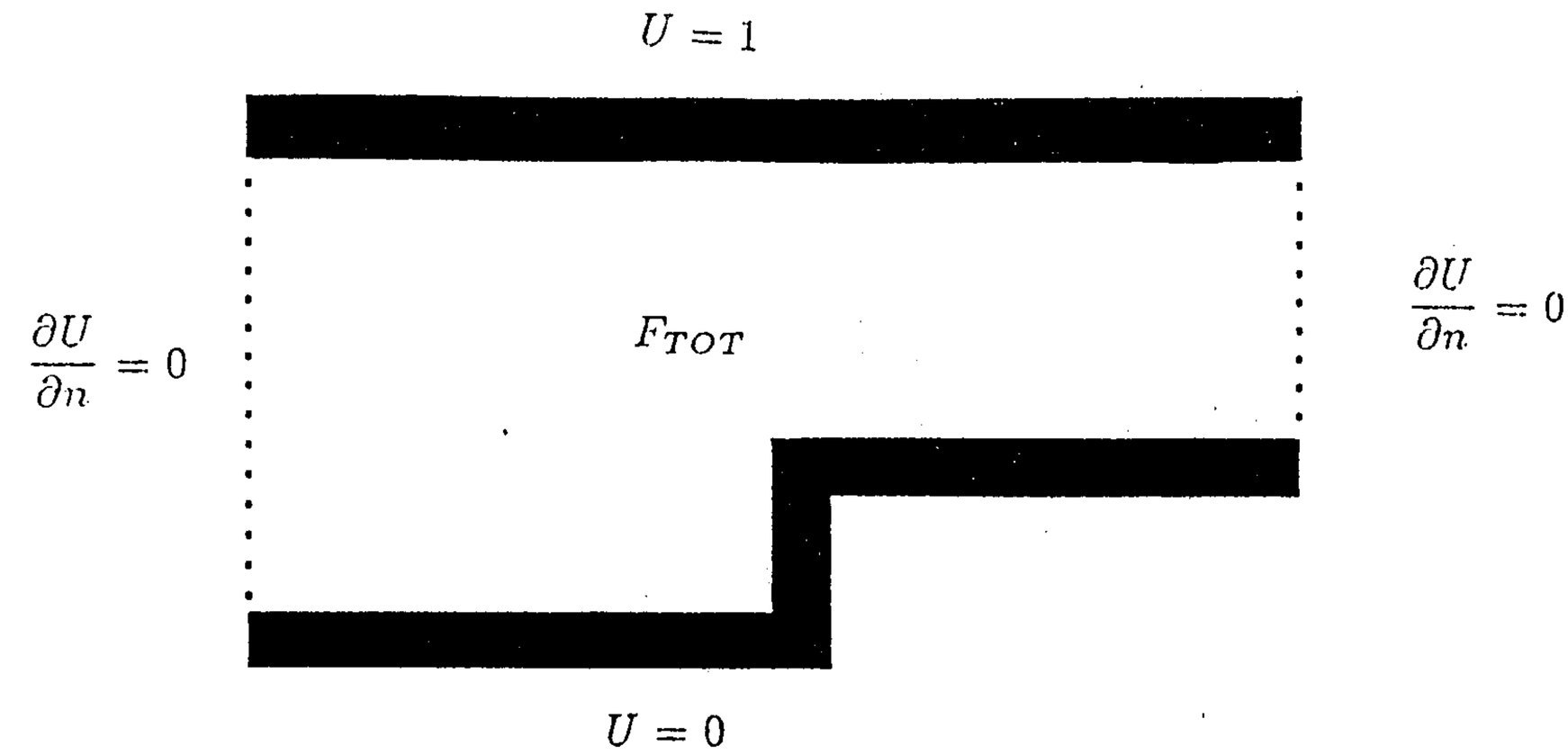

Fig 2.3(a) Region of solution before subsectioning.

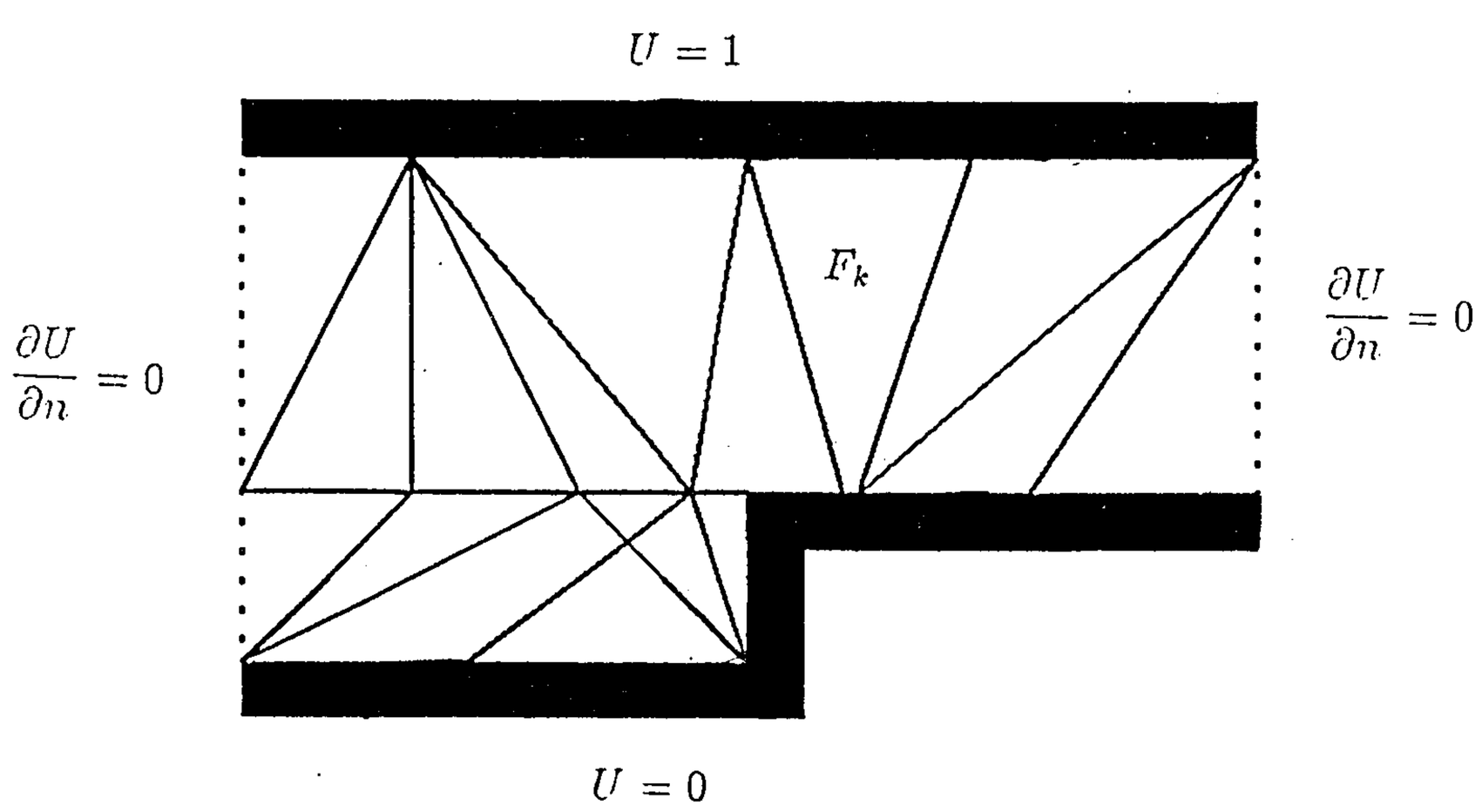

Fig 2.3(b) Region of solution after subsectioning.

2.3.2 First Order Finite Elements

Let the region of solution be subdivided into n elements. Substituting equation 2.11 into equation 2.19 we may write

$$F = \sum_{e=1}^{n} 2\pi \int_{\Omega_e} \epsilon_e (\nabla \phi)^2 r dr dz \tag{2.20}$$

where the integration is over the element Ω_e, Fig 2.3.

If it is now assumed the potential ϕ can be adequately approximated by a piecewise planar function, or first order polynomial, such that

$$\phi = a + bz + cr \tag{2.21}$$

where r and z are the co-ordinates of the point with potential ϕ, it is now possible to define ϕ in each element. Let one element be defined by the three vertices, or nodes, v_1, v_2 and v_3, with associated potentials ϕ_1, ϕ_2 and ϕ_3, Fig 2.4. Using equation 2.21 we can express each ϕ at the vertices as

$$\begin{aligned} \phi_1 &= a + bz_1 + cr_1 \\ \phi_2 &= a + bz_2 + cr_2 \\ \phi_3 &= a + bz_3 + cr_3 \end{aligned}$$

or

$$\begin{bmatrix} \phi_1 \\ \phi_2 \\ \phi_3 \end{bmatrix} = \begin{bmatrix} 1 & z_1 & r_1 \\ 1 & z_2 & r_2 \\ 1 & z_3 & r_3 \end{bmatrix} \begin{bmatrix} a \\ b \\ c \end{bmatrix} \tag{2.22}$$

By eliminating a, b and c, using equations 2.21 and 2.22, we obtain

$$\begin{aligned} \phi &= \begin{bmatrix} 1 & z & r \end{bmatrix} \begin{bmatrix} 1 & z_1 & r_1 \\ 1 & z_2 & r_2 \\ 1 & z_3 & r_3 \end{bmatrix}^{-1} \begin{bmatrix} \phi_1 \\ \phi_2 \\ \phi_3 \end{bmatrix} \\ &= \sum_{i=1}^{3} \alpha_i \phi_i \end{aligned} \tag{2.23}$$

where α_i is the a_i defined in equation 2.15, and in general is given by

$$\alpha_i = \frac{1}{2A}\{(z_{i+1}r_{i+2} - z_{i+2}r_{i+1}) + (r_{i+1} - r_{i+2})z + (z_{i+2} - z_{i+1})r\} \tag{2.24}$$

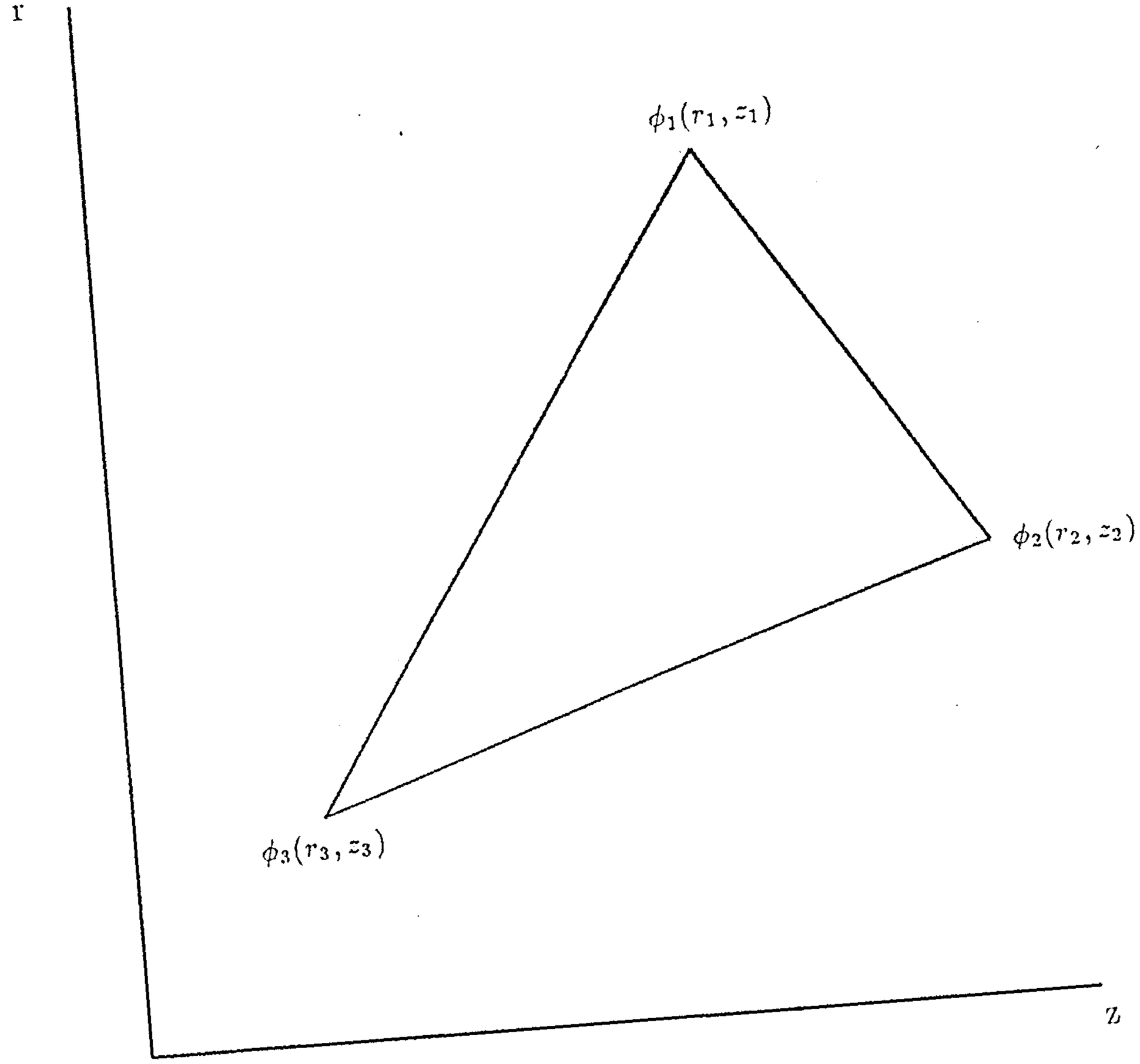

Fig 2.4 General triangle with node potentials ϕ_1, ϕ_2 and ϕ_3.

A represents the element area and the subscripts vary modulo 3 (i.e the variation is cyclic around 1, 2, 3, 1, ...). It can be seen that the α_i's satisfy the relationship

$$\begin{aligned} \alpha_i(z_j, r_j) &= 0 \qquad i \neq j \\ &= 1 \qquad i = j \end{aligned} \tag{2.25}$$

That is, α_1 will be 1 at node 1 and zero at all other nodes, and the potential along any element edge joining two nodes, will be the linear interpolation of the node potentials.

Upon substitution of equation 2.23 into equation 2.20 the functional for the element now becomes

$$F_e = 2\pi\epsilon_e \sum_{i=1}^{3}\sum_{j=1}^{3} \phi_i \int_{r,z} \nabla\alpha_i \cdot \nabla\alpha_j r dr dz \phi_j \tag{2.26}$$

which may be written in terms of matrices as

$$F_e = \phi^T \mathbf{S}_e \phi \tag{2.27}$$

where

$$\mathbf{S}_e = 2\pi\epsilon_e \sum_{i=1}^{3}\sum_{j=1}^{3} \int_{r,z} \nabla\alpha_i \cdot \nabla\alpha_j r dr dz \tag{2.28}$$

and $\mathbf{S}_e$ is termed the S matrix of the element. It is easily shown that $\mathbf{S}_{ij}$ of any element is given as

$$\mathbf{S}_{ij} = \frac{\pi\epsilon(r_1 + r_2 + r_3)}{6A}\{(r_{i+1} - r_{i+2})(r_{j+1} - r_{j+1}) + (z_{i+2} - z_{i+2})(z_{j+2} - z_{j+1})\}$$

where r_1, r_2 and r_3 are the radial co-ordinates of the three vertices. The functional for the complete solution then becomes

$$F = \sum_{e=1}^{n} \phi^T S_e \phi \tag{2.29}$$

when equation 2.27 has been substituted into equation 2.19. The minimal solution may now be found by differentiating equation 2.26 with respect to ϕ_i. This is simplified by noting that certain node potentials are fixed by the boundaries and subsequently will not contribute to the differential (Zienkiewicz 1977, Fernandez 1987). As a result the unknown ϕ's may be found from

$$\mathbf{S}_{ff}\phi_f = \mathbf{S}_{fb}\phi_b \tag{2.30}$$

where ϕ_f and ϕ_b denote free varying and boundary nodes respectively, $\mathbf{S}_{ff}$ represents the contribution of the element **S** matrices with one or more free potentials, and $\mathbf{S}_{fb}$ the contribution of the element **S** matrices with one or two boundary potentials. Upon rearrangement

$$\phi = \begin{bmatrix} -\mathbf{S}_{ff}^{-1}\mathbf{S}_{fb}\phi_b \\ \phi_b \end{bmatrix} \tag{2.31}$$

2.3.4 Boundary Conditions on the Region of Solution

The general boundary conditions for the coaxial model were outlined in section 2.2.2. The functional given in equation 2.11 must therefore satisfy all the Dirichlet and Neumann boundaries for a correct solution of ϕ to be obtained. The general ouline of the region of solution is shown in Fig 2.5.

The Dirichlet boundaries are provided by the conductors which are held at specified potentials and will be enforced by the presence of equation 2.29. The Neumann boundaries are natural boundary conditions of the Laplacian operator and will be satisfied automatically when the functional is minimised (Wexler 1969). It becomes apparent that the Dirichlet boundary at infinity will require the number of elements, in equation 2.19, to be infinitely large. This problem may be removed if a sufficient amount of the region is modelled enclosed by an artificial Neumann boundary (McDonald *et al* 1972, Trowbridge 1987, Richter 1987).

2.3.5 High Order Finite Elements

Equation 2.21 gives a piecewise planar, or first order polynomial, approximation to the potential ϕ. However if ϕ's variation within any element is of a more complex nature, errors in the solution of equation 2.6 will result. This may be improved if a piecewise polynomial is used in the approximation of ϕ. However this improvement will suffer one drawback. This takes the form of a more complex calculation of the α_i's in equation 2.23 and subsequently the calculation of element **S** matrix (Silvester1969, Silvester 1978).

With the introduction of some additional definitions it can be shown that the **S** matrix construction becomes easy to perform and will depend only on the angles subtended between the element edges (Silvester 1969, Konrad 1977). The technique will now be described.

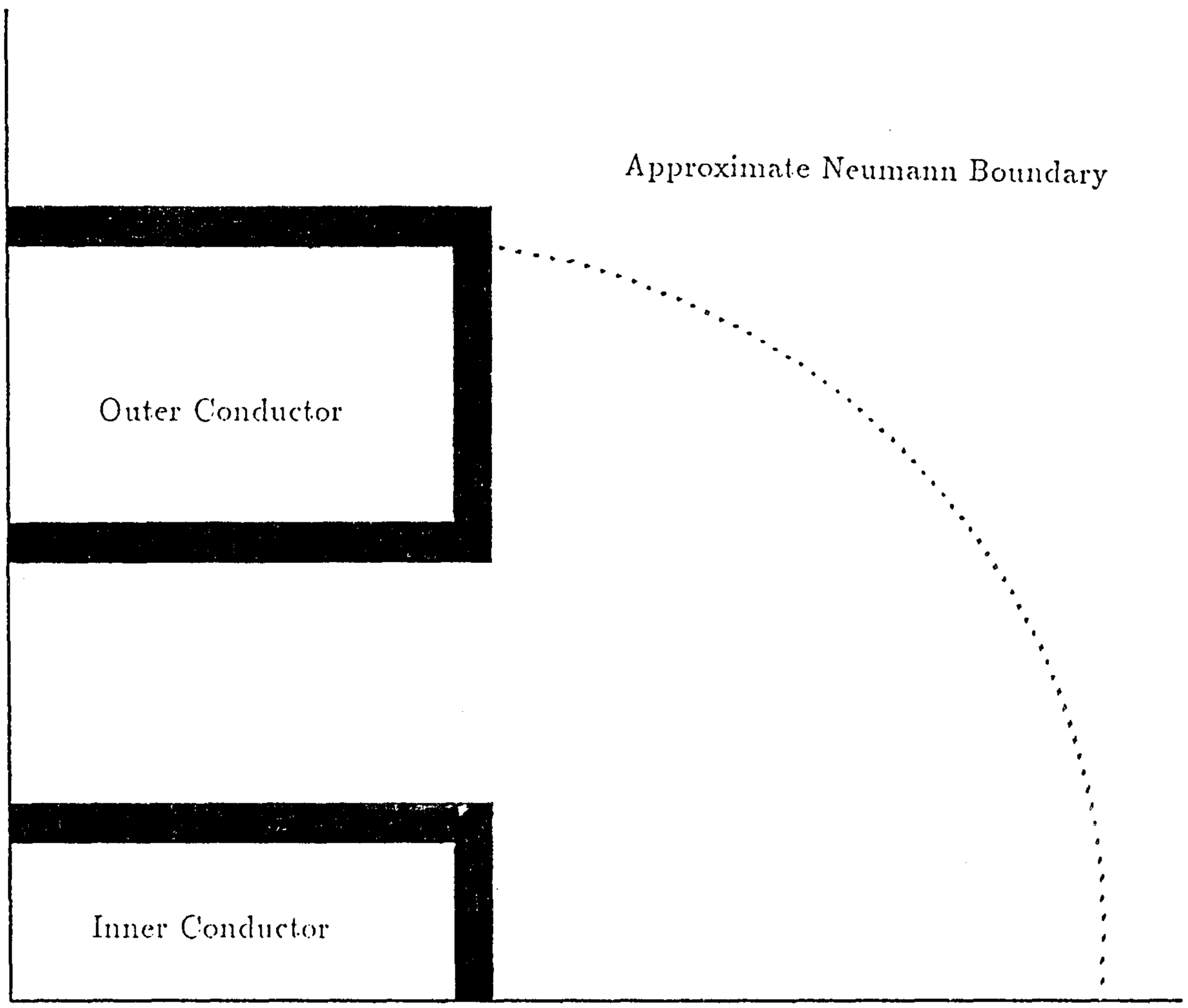

Fig 2.5 General model used in the Finite Element Analysis.

2.3.6 Local Co-ordinates

In general any triangular element E can be completely defined by 3 nodes. If E is then subdivided by a point P into 3 sub-elements, Fig 2.6(a), the area of the element E, $A(E)$ may be expressed as

$$A(E) = \sum_{t=1}^{3} A(E_t) \tag{2.32}$$

where $A(E_t)$ is the area of subelement E_t. If ξ_1 is now defined as

$$\xi_1 = \frac{area\ of\ triangle\ (\ node\ 2 \rightarrow node\ 3 \rightarrow P\ )}{area\ of\ triangle\ (\ node\ 1 \rightarrow node\ 2 \rightarrow node\ 3\ )}$$

it becomes apparent that ξ_1 will be proportional to the perpendicular distance to P from the edge joining node 2 to node 3 (Fig 2.6(b)). By defining two other ratios similarly

$$\xi_i = \frac{area\ of\ triangle\ (\ node(i+1) \rightarrow node(i+2) \rightarrow P\ )}{A(E)} \tag{2.33}$$

which will allow P to be defined uniquely within E in terms of ξ_1, ξ_2 and ξ_3. Furthermore it can be seen

$$\xi_1 + \xi_2 + \xi_3 = 1 \tag{2.34}$$

These values ξ_i are termed the local co-ordinates of the element E and will be in the range of 1 to 0.

2.3.7 Polynomial Approximations of ϕ

To find a polynomial approximation to the variable ϕ, the polynomial chosen must satisfy the criteria outlined in equation 2.25. If we have a polynomial of order N then it will contain n terms where

$$n = \frac{1}{2}(N+1)(N+2) \tag{2.35}$$

As a result, each element must have n independently specified parameters. For the element functional to be evaluated, ϕ must be continuous everywhere within the element. This stipulates that ϕ along any triangle edge is given by a polynomial of order N (Silvester *et al* 1986). Therefore it is necessary to specify ϕ at the vertices

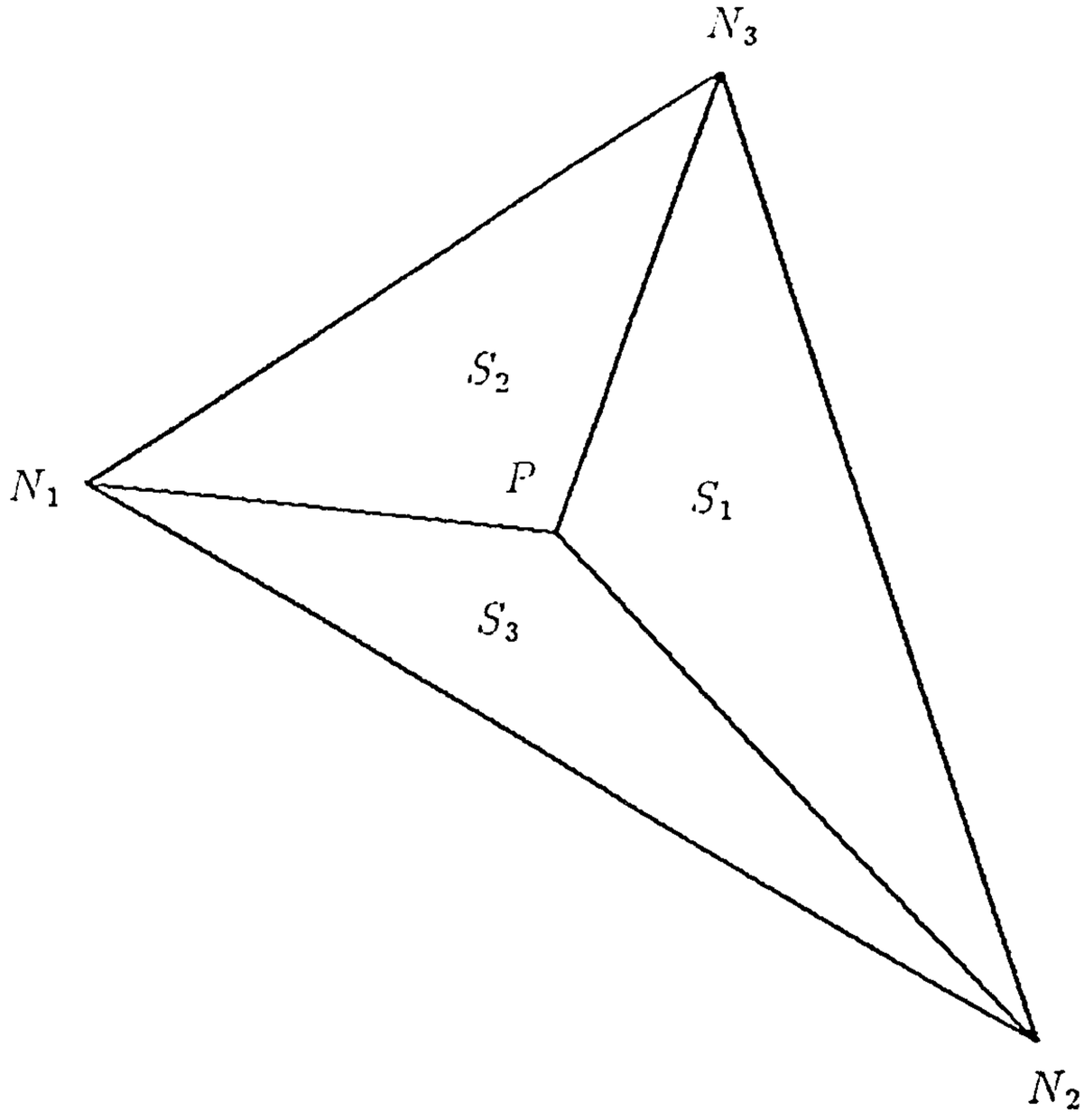

Fig 2.6(a) Subdivision of element due to interior point P.

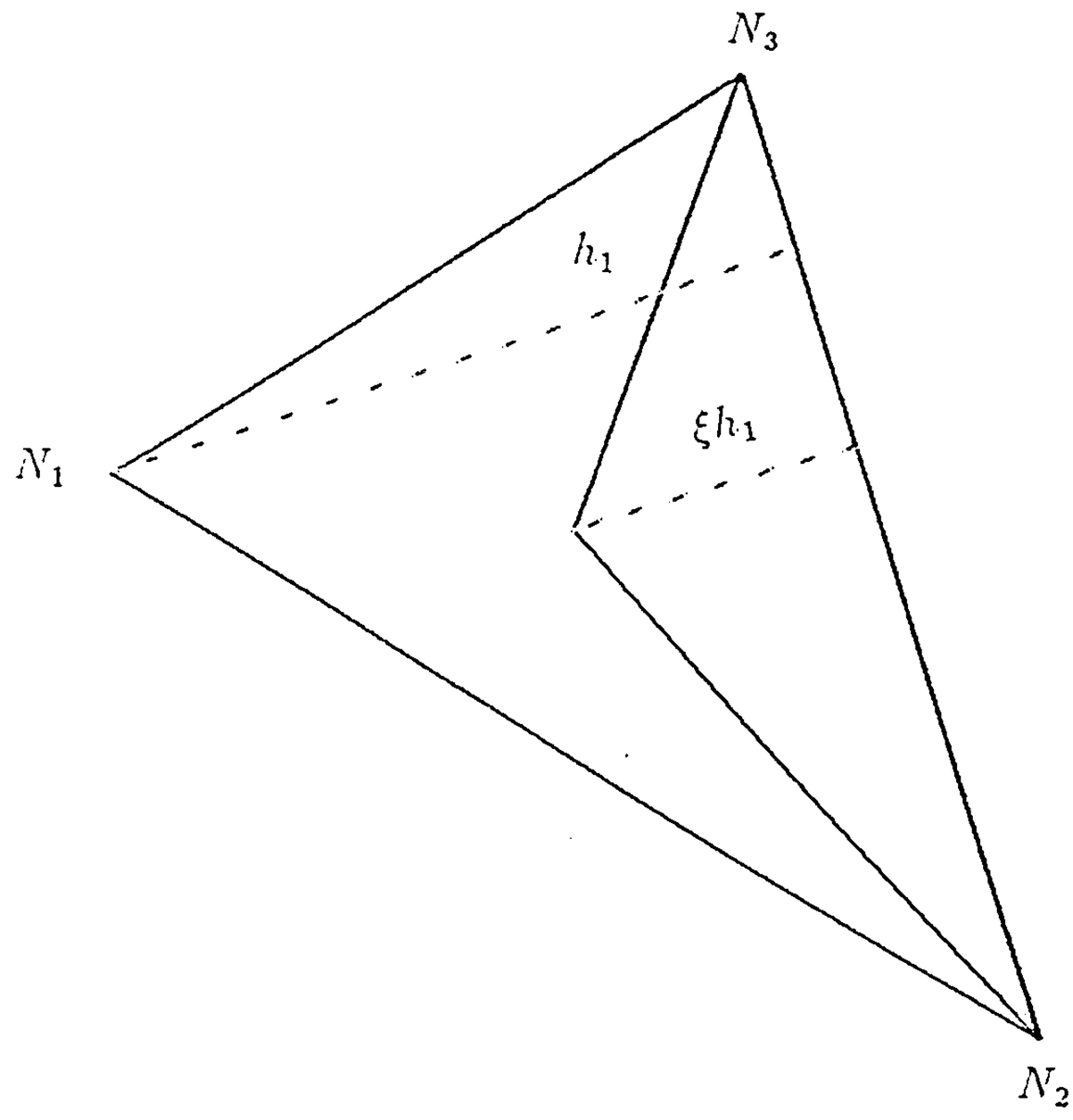

Fig 2.6(b) Relative distance of P along perpendicular h_1
with reference to local coordinate ξ_1.

and at $N-1$ intermediate points along each edge. When dealing with first order elements, $N=1$, it is trivial to formulate the planar function in terms of the space co-ordinates r, z. However for $N > 1$ it is of great benefit to define the polynomials in terms of the local co-ordinates (Silvester *et al* 1986, Fernandez 1987).

To define the polynomials let P_{ijk} be a set of regularly spaced points within the element E, which are completely defined by the local co-ordinates ξ_1, ξ_2, ξ_3 and the subscripts i, j and k satisfy

$$i+j+k=N \tag{2.36}$$

The graphical representation for $N=3$ is shown in Fig 2.7. It is clearly seen that the number of points defined in the element is equal to the number of coefficients in the polynomial. If we state that the potential at each point P_{ijk} is ϕ_{ijk}, as in equation 2.21, it is possible to rewrite equation 2.23 as

$$\phi(\xi_1,\xi_2,\xi_3)=\sum_{i=0}^{N}\sum_{j=0}^{N-i}\alpha_{ijk}(\xi_1,\xi_2,\xi_3)\phi_{ijk} \tag{2.37}$$

where the α_i's are now defined in terms of the local co-ordinates.

By defining a set of polynomials $P_m(\beta)$ as

$$\begin{aligned} P_m(\beta) &= \prod_{i=1}^{m}\left(\frac{N\beta-i+1}{i}\right) \qquad m\geq 1 \\ &= 1 \qquad\qquad\qquad\qquad m=0 \end{aligned} \tag{2.38}$$

where N is the order of the element, α can be written in terms of local co-ordinates only, i.e

$$\alpha_{ijk}=P_i(\xi_1)P_j(\xi_2)P_k(\xi_3) \tag{2.39}$$

where equation 2.35 holds. This polynomial expression of α_{ijk} satisfies the criterion outlined in equation 2.25, that is the value of α will be unity at node ijk and zero at all other nodes. By referring to Fig 2.7 it is seen that

Fig 2.7 Third order element with local coordinate polynomial expressions.

$$\alpha_{300} = P_3(\xi_1)P_0(\xi_2)P_0(\xi_3)$$

$$= \frac{3\xi_1(3\xi_1 - 1)(3\xi_1 - 2)}{6}$$

$$\alpha_{111} = P_1(\xi_1)P_1(\xi_2)P_1(\xi_3)$$

$$= 3\xi_1 3\xi_2 3\xi_3$$

This allows us to show that at point P_{300} the polynomial expression given for α_i is 1 at that particular point and zero at all others.Thus the α's and subsequently the ϕ's within the element are completely defined in terms of the local co-ordinates.

2.3.7 Construction of the Element S Matrix

The **S** matrix for any element may now be calculated using the definitions given in sections 2.3.4 and 2.3.5. At this point it should again be noted that all quantities vary modulo 3. The element functional, given in equation 2.20, may be written as

$$F_e = 2\pi\epsilon_e \sum_{p=1}^{n}\sum_{q=1}^{n} \phi_p \int_{r,z} \nabla\alpha_p \cdot \nabla\alpha_q r dr dz \ \phi_q$$

where n is the number of nodes in the system. By noting that the radius r is a linear function of the co-ordinate system, it can be shown that r may be expressed in terms of the local co-ordinates of the element and the radial value of the three vertices,

$$r = \sum_{h=1}^{3} r_h \xi_h \tag{2.40}$$

By substituting equation 2.40 into equation 2.20 we obtain

$$F_e = 2\pi\epsilon_e \sum_{h=1}^{3} r_h \sum_{p=1}^{n}\sum_{q=1}^{n} \phi_p \int_{r,z} \xi_h \nabla\alpha_p \cdot \nabla\alpha_q dr dz \ \phi_q \tag{2.41}$$

If $\nabla \cdot \nabla$ is expanded, equation 2.41 results in

$$F_e = 2\pi\epsilon_e \sum_{h=1}^{3} r_h \sum_{p=1}^{n}\sum_{q=1}^{n} \phi_p \int_{r,z} \xi_h \left(\frac{\partial\alpha_p}{\partial z}\frac{\partial\alpha_q}{\partial z} + \frac{\partial\alpha_p}{\partial r}\frac{\partial\alpha_q}{\partial r} \right) dr dz \ \phi_q \tag{2.42}$$

Noting that using the chain rule yields

$$\frac{\partial \alpha_p}{\partial z} = \sum_{i=1}^{3} \frac{\partial \alpha_p}{\partial \xi_i} \frac{\partial \xi_i}{\partial z} \tag{2.43}$$

and stating that (Silvester 1969)

$$\frac{\partial \xi_i}{\partial z} = \frac{(r_{i+1} - r_{i-1})}{2A} \tag{2.44}$$

where A is the element area, the element functional may be written as

$$F_e = 2\pi \epsilon_e \sum_{h=1}^{3} r_h \sum_{p=1}^{n} \sum_{q=1}^{n} \phi_p S_{pq} \phi_q \tag{2.45}$$

where

$$S_{pq} = \frac{1}{4A^2} \sum_{p=1}^{n} \sum_{q=1}^{n} (b_i b_j + c_i c_j) \int_{r,z} \xi_h \frac{\partial \alpha_p}{\partial \xi_i} \frac{\partial \alpha_q}{\partial \xi_j} dr dz \tag{2.46}$$

$$b_i = r_{i+1} - r_{i-1} \tag{2.47}$$

$$c_i = z_{i-1} - r_{i+1} \tag{2.48}$$

with modulo 3 progression in i, j and k. By examining Fig 2.8 it is clear that

$$\begin{aligned} cot\theta_1 &= cot(\frac{\pi}{2} - \beta - \gamma) \\ &= \frac{tan\gamma + tan\beta}{1 - tan\gamma tan\beta} \\ &= -\frac{(b_3 b_2 + c_2 c_3)}{2A} \end{aligned} \tag{2.49}$$

Similar equations can be found for $cot\theta_2$ and $cot\theta_3$. Using the identities for the cotangents it can be shown

$$b_i b_j + c_i c_j = -2A cot\theta_k \qquad i \neq j \tag{2.50}$$

$$b_i^2 + c_i^2 = 2A(cot^2\theta_j + cot^2\theta_k) \quad i = j \tag{2.51}$$

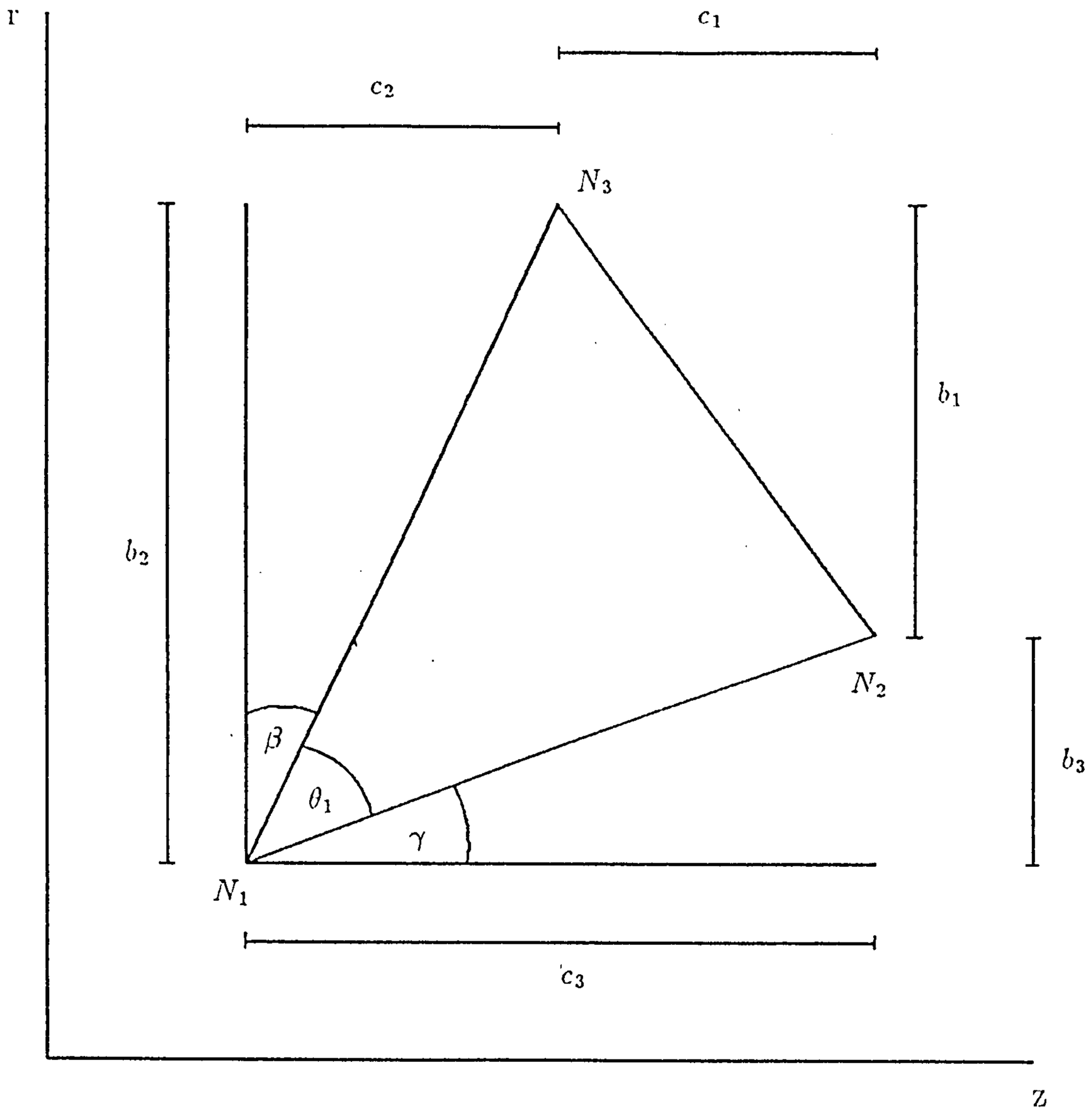

Fig 2.8 Geometry of triangle for use in proof of cotangent identity.

Substituting equations 2.50 and 2.51 into equation 2.46 and expanding and collecting terms yields

$$S_{pq} = \sum_{k=1}^{3} cot\theta_l Q_{pq}^{hk} \tag{2.52}$$

where

$$Q_{pq}^{hk} = \int_{r,z} \xi_h \left(\frac{\partial \alpha_p}{\partial \xi_{k+1}} \frac{\partial \alpha_p}{\partial \xi_{k-1}} \right) \left(\frac{\partial \alpha_q}{\partial \xi_{k+1}} \frac{\partial \alpha_q}{\partial \xi_{k-1}} \right) dr dz \tag{2.53}$$

The integral Q_{pq}^{hk} is dimensionless and only involves terms in the local co-ordinates. This allows it to be evaluated only once for each order of element. As the local co-ordinates satisfy equation 2.35 only three of the nine **Q** matrices for each element have to be known as the others will be simple permutations of the rows and columns of the three stored. Table 2.1 gives the matrices stored for $N = 1$ and $N = 2$. The construction of the **S** for each element then simplifies to the calculation of the three cotangents of the angles at the vertices summed with the predetermined **Q** matrices. After the **S** matrices have been calculated it is a simple matter of using equation 2.30 to solve for the unknown ϕ's.

2.3.8 Calculation of C_o and C_f

By solving equation 2.6 for ϕ it is possible to find the fringe field capacitance values for the coaxial probe. The capacitance C of the system may be expressed as

$$C = \frac{2W}{V^2} \tag{2.54}$$

where W represents the stored energy in the region of solution and V is the potential difference between the inner and outer conductors. By recalling equation 2.11 and noting that

$$\begin{aligned} W &= \frac{1}{2} \int_{\Omega} \epsilon_0 \epsilon (\nabla \phi)^2 d\Omega \\ &= 2\epsilon_0 F_{sol} \end{aligned}$$

where F_{sol} is the value of the functional at the solution point, it is possible to write (Gajda 1982)

$$C = \frac{\epsilon_0 F_{sol}}{V^2} \tag{2.55}$$

$$Q_{mk}^{11} = Q_{mk}^{21} = Q_{mk}^{31} = \frac{1}{6}\begin{bmatrix} 0 & 0 & 0 \\ 0 & 1 & -1 \\ 0 & -1 & 1 \end{bmatrix}$$

Q matrices for first order elements

$$Q_{mk}^{11} = \frac{1}{30}\begin{bmatrix} 0 & 0 & 0 & 0 & 0 & 0 \\ 0 & 24 & -24 & -2 & 0 & 2 \\ 0 & -24 & 24 & 2 & 0 & -2 \\ 0 & -2 & 2 & 3 & -4 & 1 \\ 0 & 0 & 0 & -4 & 8 & -4 \\ 0 & 2 & -2 & 1 & -4 & 3 \end{bmatrix}$$

$$Q_{mk}^{21} = \frac{1}{30}\begin{bmatrix} 0 & 0 & 0 & 0 & 0 & 0 \\ 0 & 8 & -8 & 3 & -4 & 1 \\ 0 & -8 & 8 & -3 & 4 & -1 \\ 0 & 3 & -3 & 9 & -11 & 2 \\ 0 & -4 & 4 & -11 & 16 & -5 \\ 0 & 1 & -1 & 2 & -5 & 3 \end{bmatrix}$$

$$Q_{mk}^{31} = \frac{1}{30}\begin{bmatrix} 0 & 0 & 0 & 0 & 0 & 0 \\ 0 & 8 & -8 & -1 & 4 & -3 \\ 0 & -8 & 8 & 1 & -4 & 3 \\ 0 & -1 & 1 & 3 & -5 & 2 \\ 0 & 4 & -4 & -5 & 16 & -11 \\ 0 & -3 & 3 & 2 & -11 & 9 \end{bmatrix}$$

Q matrices for second order elements

Table 2.1 : Q matrices necessary for high order elements

As a certain portion of this capacitance is due to TEM waves inside the line, the net fringe-field capacitance may be expressed as

$$\begin{aligned} C_{net} &= C - C_{TEM} \\ &= C - \frac{2\pi\epsilon_l\epsilon_0 l}{ln(b/a)} \end{aligned} \tag{2.56}$$

where ϵ_l is the relative permittivity inside the coaxial line, ϵ_0 is the free space permittivity, l is the length of the line and b and a are the inner and outer radii respectively. From the linear model of chapter 1

$$C_{net}(\epsilon) = C_f + \epsilon C_o \tag{2.57}$$

where $C_{net}(\epsilon)$ is the fringing field capacitance due to a permittivity of ϵ outside the line. By calculating C_{net} for $\epsilon = 1$, that is air outside the line, it can be shown that

$$C_o = \frac{C_{net} - C_{net}(air)}{\epsilon - 1} \tag{2.58(a)}$$

and

$$C_f = C_{net}(air) - C_o \tag{2.58(b)}$$

2.4 Method of Moment Solution of the Integral Equations

2.4.1 Basic Principles

From equation 2.1, a linear operator equation is of the form

$$Lu = f$$

By using the techniques outlined in equation 2.15, u may expressed as

$$u = \sum_n \alpha_n u_n \tag{2.59}$$

where α_n are the unknown constants. Using equation 2.59, equation 2.1 may be rewritten as

$$\sum_n \alpha_n L u_n = f \tag{2.60}$$

If ω_m is now defined as a set of weighting functions (Harrington 1968), also in the domain of L, the inner product of each ω_m with equation 2.60 results in

$$\sum_n \alpha_n < \omega_m, L u_n > = < \omega_m, f > \tag{2.61}$$

which may be recast as

$$[l_{mn}]\,[\alpha_n] = [f_m] \tag{2.62}$$

where

$$[l_{mn}] = \begin{bmatrix} < \omega_1, Lu_1 > & < \omega_1, Lu_2 > & . & . & . \\ < \omega_2, Lu_1 > & < \omega_2, Lu_2 > & . & . & . \\ < \omega_3, Lu_1 > & < \omega_3, Lu_2 > & . & . & . \\ . & . & . & . & . \end{bmatrix} \tag{2.63(a)}$$

$$[f_m] = \begin{bmatrix} < \omega_1, f_1 > \\ < \omega_2, f_2 > \\ < \omega_3, f_3 > \\ . \end{bmatrix} \tag{2.63(b)}$$

and

$$[\alpha_n] = \begin{bmatrix} \alpha_1 \\ \alpha_2 \\ \alpha_3 \\ . \end{bmatrix} \tag{2.63(c)}$$

The unknown function u may then be found from equations 2.59 and 2.62 as (Harrington 1968)

$$u = [u_1, u_2, ..., u_n]\,[l_{mn}]^{-1}\,[f_m] \tag{2.64}$$

By examining equations 2.14 (a) and (b),it can be seen that this technique of using weighting functions may be used to solve for $\sigma(s)$.

2.4.2 The Weighted System of Equations

To find the capacitances C_f and C_o, equation 2.7

$$\phi(x) = \int_R \sigma(x_0)G(x/x_0)dx_0$$

has to be solved. From section 2.2.3 the linear operator equation for the charge σ is transformed using variational techniques to the coupled integral equations (Daffe *et al* 1979)

$$\int_{S_C+S_I} \sigma(s')G(s/s')ds' = \phi(s) \quad s \ on \ S_C \tag{2.14(a)}$$

$$\frac{\epsilon_1+\epsilon_2}{2}\sigma(s) + (\epsilon_1-\epsilon_2)\int_{S_C+S_I} \sigma(s')\frac{\partial G}{\partial n}(s/s')ds' = 0 \quad s \ on \ S_I \tag{2.14(b)}$$

The solution of equations 2.14(a) and (b) can again become particularly difficult if the surface integrations to be performed are over a region which is complex in nature. Where the surfaces are complicated it is more convenient to define the integrals over a subsection of the entire problem domain (Daffe *et al* 1979). The conductor surfaces S_C and the dielectric interface S_I then become

$$S_C = \triangle S_1 + \triangle S_2 + \ \ldots \ + \triangle S_n \tag{2.65(a)}$$

$$S_I = \triangle S_{n+1} + \triangle S_{n+2} + \ \ldots \ + \triangle S_{n+m} \tag{2.65(b)}$$

where n denotes the number of conductor subsections, $n+m$ the total number of subsections in the problem and the general subsection is denoted by $\triangle S_i$.

Let the charge distribution $\sigma(s)$ be represented by

$$\sigma(s) = \sum_{j=1}^{n+m} \sigma_j f_j(s - \triangle s_j) \tag{2.66}$$

where the a_i constants of equation 2.15 have been replaced by the function $f_j(s-\triangle s_j)$, defined only over the subsection $\triangle s_j$ and σ_j is the unknown amplitude of the charge on the subsection. Substituting equation 2.66 for $\sigma(s')$ in equations 2.14(a) and 2.14(b) results in

$$\sum_{j=1}^{n+m} \sigma_j \int_{\triangle s_j} f_j(s - \triangle s_j)G(s/s')ds' = \phi(s) \tag{2.67(a)}$$

$$\frac{\epsilon_1+\epsilon_2}{2}\sigma(s)+(\epsilon_1-\epsilon_2)\sum_{j=1}^{n+m}\sigma_j\int_{\triangle s_j}f_j(s-\triangle s_j)\frac{\partial G}{\partial n}(s/s')ds'=0 \qquad (2.67(b))$$

If the charge on the subsection s is replaced by equation 2.5 enforced at subsection $\triangle s_i$, the weighting functions ω_m, from equation 2.61, are now defined to exist over each subsection in turn,

$$\omega=\omega_i(s-\triangle s_i)\quad i=1,2,...,n+m \qquad (2.68)$$

and the inner products of equation 2.61 are taken, the coupled integral eqations become

$$\sum_{j=1}^{n+m}\sigma_j\int_{\triangle s_j}\int_{\triangle s_i}\omega_i(s-\triangle s_i)f_j(s-\triangle s_j)G(s/s')ds'=$$

$$\int_{\triangle s_i}\omega_i(s-\triangle s_i)\phi(s)ds \qquad i=1,..,n \qquad (2.69(a))$$

$$(\epsilon_1-\epsilon_2)\sum_{j=1}^{n+m}\sigma_j\int_{\triangle s_i}\int_{\triangle s_j}\omega_i(s-\triangle s_i)f_j(s-\triangle s_j)\frac{\partial G}{\partial n}(s/s')ds'+$$

$$\frac{\epsilon_1+\epsilon_2}{2}\sum_{j=1}^{n+m}\sigma_j\int_{\triangle s_i}\omega_i(s-\triangle s_i)f_j(s-\triangle s_j)ds=0$$

$$i=n+1,...,n+m \qquad (2.69(b))$$

If $f_j(s-s_j)$ and $\omega_i(s-s_i)$ are defined such that

$$\begin{aligned} f_j(s-s_j)&=1 \quad ,s\ on\ \triangle s_j \\ &=0 \quad ,elsewhere \end{aligned} \qquad (2.70(a))$$

and

$$\omega_i(s-s_i)=\partial(s-s_i) \qquad (2.70(b))$$

equations 2.69(a) and 2.69(b) may be rewritten

$$\sum_{j=1}^{n+m}\sigma_j\int_{\triangle s_j}G(s_i/s')ds'=\phi(s_i)\qquad i=1,...,n \qquad (2.71(a))$$

$$\frac{\epsilon_1+\epsilon_2}{2}\sigma_i+(\epsilon_1-\epsilon_2)\sum_{j=1}^{n+m}\sigma_j\int_{\triangle s_j}\frac{\partial G}{\partial n}(s_i/s')ds'=0$$

$$i=n,...,n+m \qquad (2.71(b))$$

where $\triangle s_i$ denotes the i^{th} subsection. The integrals equations represent the contribution made by a charge on subsection $\triangle s_j$ to the potential on subsection $\triangle s_i$. This will then result in an $(n+m)$ by $(n+m)$ set of simultaneous equations for the unknown charge density function σ.

2.4.3 Rotationally Symmetric Green's Function

Solving equations 2.71(a) and 2.71(b) will give a good approximation to the charge σ. However it is apparent that solution will only be obtained if the Green's function, $G(s/s')$, is known. The Green's function representing the potential at point Ψ due to a point charge at Ψ_o is well known and given by (Daffe *et al* 1979, Gajda 1982)

$$G(\Psi/\Psi_o)=\frac{1}{4\pi\epsilon\epsilon_0 R}$$

$$=\frac{1}{4\pi\epsilon\epsilon_0\mid\Psi-\Psi_o\mid} \qquad (2.72)$$

where $\mid\Psi-\Psi_o\mid$ represents the length of the vector from the source to the observation point and ϵ is the permittivity of the medium. If the charge is now thought to lie on the circumference of an infinitesimally thin circular ring of radius r' and Ψ lies in the x,z plane, Fig 2.9, the magnitude of the vector $\underline{R}$ may be written

$$\mid\underline{R}\mid=\sqrt{(x-x')^2+(y-y')^2+(z-z')^2}$$

$$=\sqrt{(r+r')^2+(z-z')^2-4rr'cos^2\frac{\theta}{2}} \qquad (2.73)$$

which results in an increment in potential at Ψ due to an increment in charge at Ψ_o, being expressed as

$$d\phi(\Psi)=\frac{d\theta}{4\pi\epsilon\epsilon_0\sqrt{(r+r')^2+(z-z')^2-4rr'cos^2\frac{\theta}{2}}} \qquad (2.74)$$

To obtain the potential at Ψ equation 2.74 has to be integrated over the circle. Thus the Green's function for rotationally symmetric systems will be

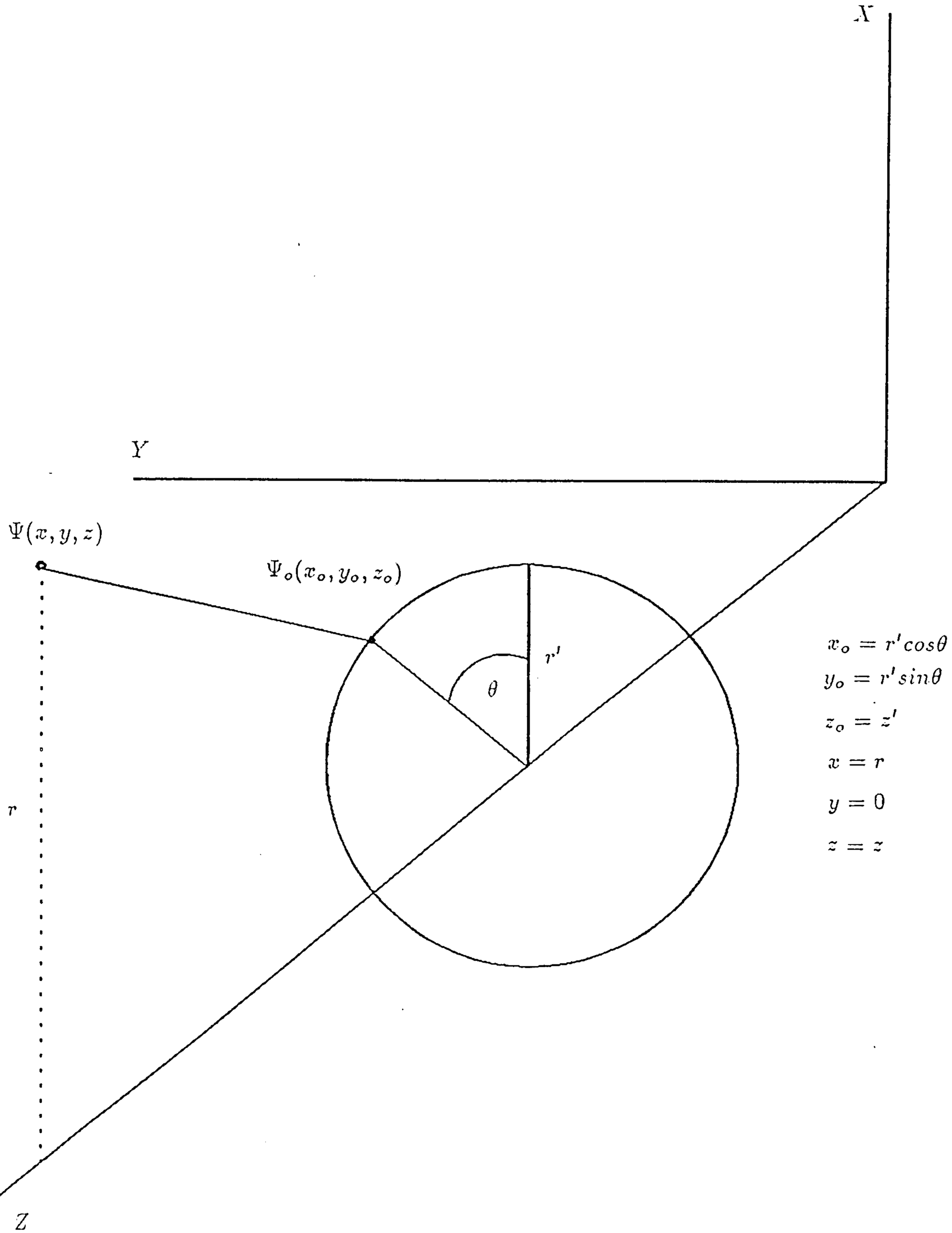

Fig 2.9 Circle of charge used to prove Green's identity.

$$G(r,z/r'z') = \int_0^{\pi/2} \frac{d\theta}{4\pi\epsilon\epsilon_0\sqrt{(r+r')^2+(z-z')^2-4rr'cos^2\frac{\theta}{2}}} \tag{2.75}$$

$$= \frac{F(m)}{\pi\epsilon\epsilon_0\sqrt{(r+r')^2+(z-z')^2}}$$

where

$$F(m) = \int_0^{\pi/2} \frac{d\theta}{\sqrt{1-msin^2\theta}} \tag{2.76(a)}$$

is the complete elliptic integral of the first kind and

$$m = \frac{4rr'}{(r+r')^2+(z-z')^2} \tag{2.76(b)}$$

From equation 2.71(b) the derivative of the Green's function is required. By noting that (Gajda 1982)

$$\frac{\partial G}{\partial n} = \nabla G \cdot \vec{n} \tag{2.77}$$

where $\vec{n}$ is the unit normal directed from region 1 to region 2, Fig 2.10, it can be shown (Daffe *et al* 1979, Gajda 1982)

$$\frac{\partial G}{\partial n} = \pm \frac{(z_i^+ - z_i^-)\partial G/\partial r - (r_i^+ - r_i^-)\partial G/\partial z}{\sqrt{(z_i^+ - z_i^-)^2+(r_i^+ - r_i^-)^2}} \tag{2.78}$$

where (r_i^+, z_i^+) and (r_i^-, z_i^-) represent the endpoints of the i^{th} subsection.

It should be noted that when the observation point is also the source point, $\Psi = \Psi_o$ the Green's function and it's derivative with respect to r becomes singular and great care must be taken when performing the integration (Gajda 1982, Anderson *et al* 1986).*

---

* Appendix to chapter2 outlines the method of integration

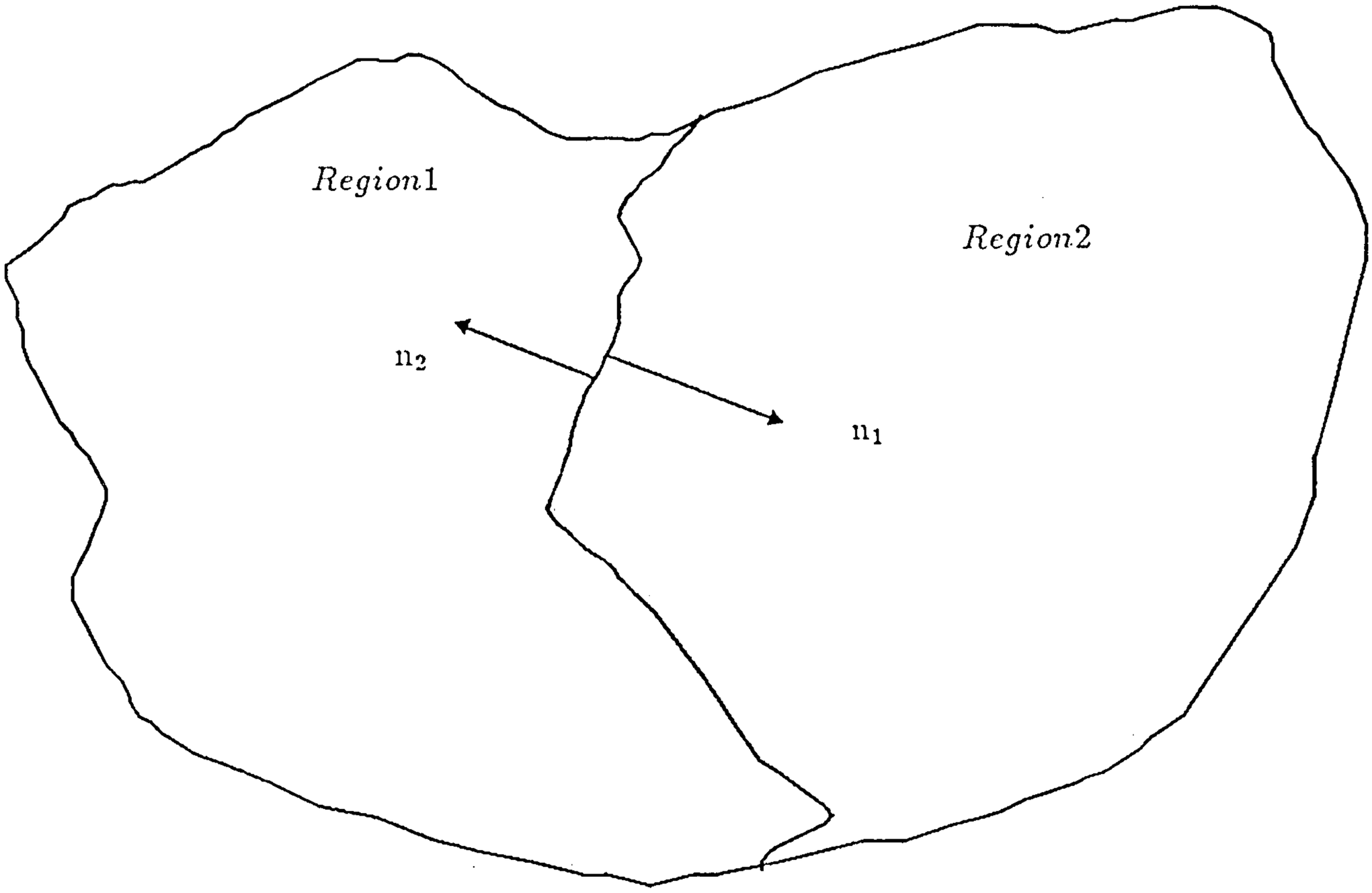

Fig 2.10 Position of normals directed from the interface.

2.4.4 Boundary Conditions on the Region of Solution

As stated previously the method of solution has to satisfy the boundary conditions imposed on the linear operator equation. By using the coupled integral equations the charge density map on the surface of the conductors is calculated. Subsequently due to the nature of the Green's function that has to be used the Dirichlet boundary conditions at infinity are satisfied (Anderson 1984, Trowbridge 1987). However the assumption of an infinitely long line implies that the charge distribution is uniform far from the open end of the line and as a result there will be a charge singularity at $z = 0$ in the solution of the equations. In order to counteract this singularity and correctly simulate the Neumann boundary the method of images is used (McDonald *et al* 1974, Gajda *et al* 1983).

With reference to Fig 2.11, the problem to be solved consists of the actual problem and it's reflection about the $z = 0$ plane. To implement the model, the real and image problems are subdivided into subsections numbered from $i = 1, ..n$ for conductors and $i = n + 1, ...n + m$ for the dielectric interface. Since the problem is symmetric about $z = 0$,

$$\triangle s_{image} = \triangle s_{real}$$

only one half of the problem needs to be subsectioned. This results in the new set of integral equations

$$\sum_{j=1}^{n+m} \sigma_j (K_{ij}^{real} + K_{ij}^{image}) = \phi_i \qquad i = 1, ..., n \qquad (2.79(a))$$

$$\frac{\epsilon_1 + \epsilon_2}{2} \sigma_i + (\epsilon_1 - \epsilon_2) \sum_{j=1}^{n+m} \sigma_j (L_{ij}^{real} + L_{ij}^{image}) = 0 \qquad i = n, ..., n + m \qquad (2.79(b))$$

where

$$K_{ij} = \int_{\triangle s_j} G(s_i / s') ds' \qquad (2.80(a))$$

$$L_{ij} = \int_{\triangle s_j} \frac{\partial G}{\partial n} (s_i / s') ds' \qquad (2.80(b))$$

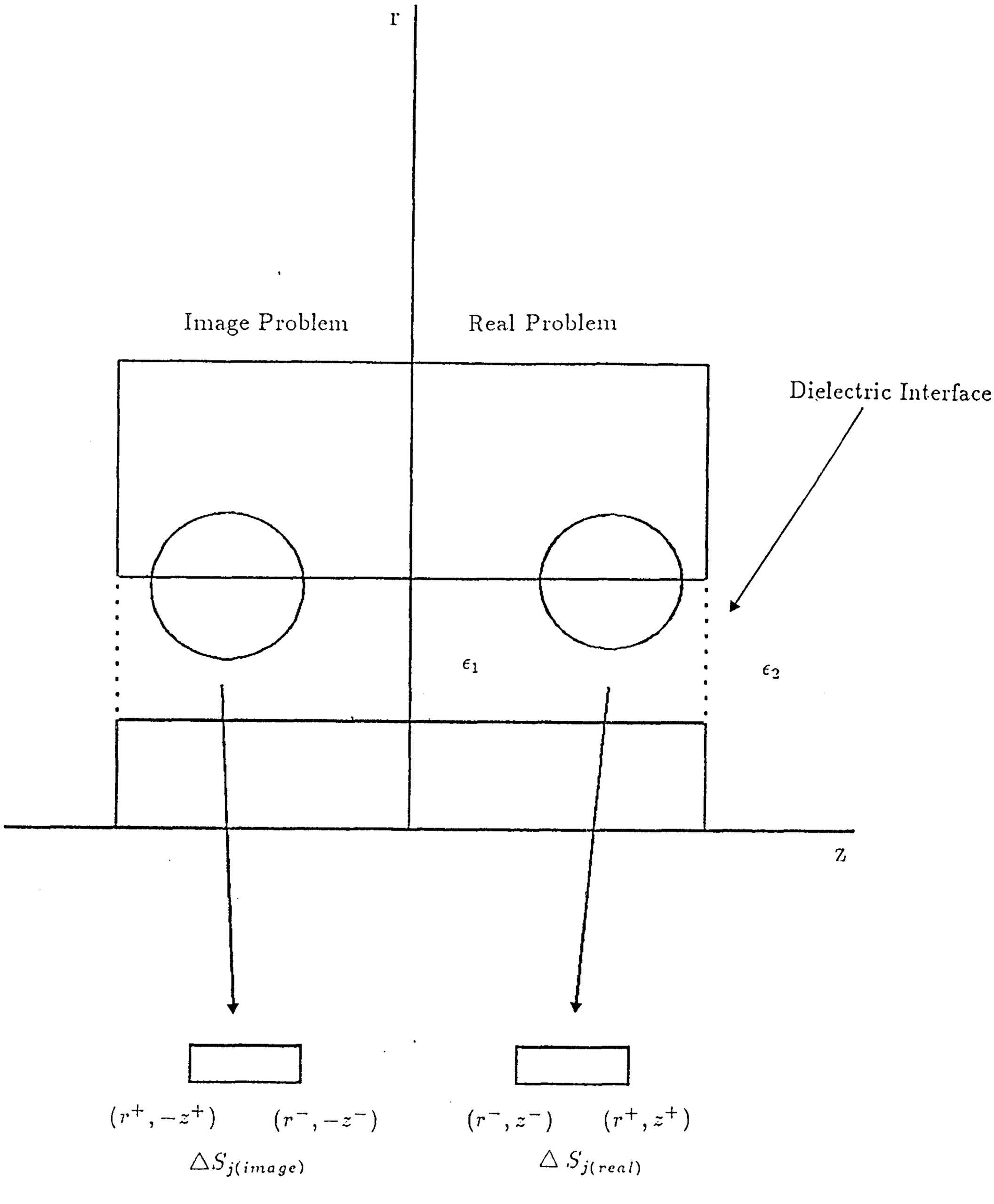

Fig 2.11 Model used in the Method of Moments.

2.4.5 Calculation of C_o and C_f

The capacitance values may be found from the calculated charge density map by (Anderson 1984)

$$C = \frac{1}{V} \int_{S_C} \epsilon_0 \epsilon(s) \frac{\partial \phi(s)}{\partial n} ds \tag{2.81}$$

where V is the potential difference on the conductor surfaces S_C, $\epsilon(s)$ is the permittivity contacting the conductor and $\partial\phi(s)/\partial n$ is the potential gradient terminating on the conductor. By noting that (Boast 1964)

$$\sigma(s) = \frac{\partial \phi(s)}{\partial n} \tag{2.82}$$

and using equations 2.66 and 2.70(a), equation 2.80 may be rewritten

$$C = \frac{1}{V} \sum_{i=1}^{k} \sigma_i \epsilon_0 \epsilon_i \int_{\triangle S_i} ds \tag{2.83}$$

where k is the total number of positively charged conductors. The calculation of C_o and C_f is then a straight forward application of equations 2.58(a) and 2.58(b).

Appendix to Chapter 2 Numerical Intergation Techniques.

The application of eqns 2.71(a) and 2.71(b) require the computation of surface integrals. Since the problem is rotationally symmetric the surface integral may be reduced to a line integral. The elementary surface may then be written as

$$ds = r\,dl \tag{A.1}$$

and the integral as

$$I = \int_{\triangle s_i} K(r,z)\,r\,dl \tag{A.2}$$

where K is a function of the surface coordinates r and z. Provided the r coordinate can be expressed by a function in z, $F(z)$, the elementary line length becomes

$$dl = \sqrt{1 + F'(z)^2}\,dz \tag{A.3}$$

If it is now stated that the endpoints of the surface $\triangle s_i$ are (r_i^+, z_i^+) and (r_i^-, z_i^-), and the r in the integral is lumped with the function $K(r,z)$ eqn A.2 may by rewritten as

$$I = \int_{z_i^-}^{z_i^+} H(F(z),z)\sqrt{1 + F'(z)^2}\,dz \tag{A.4}$$

By stating that

$$F(z) = \left\{\frac{(r_i^+ - r_i^-)}{(z_i^+ - z_i^-)}\right\}(z_i^+ - z_i^-) + r_i^+ \tag{A.5}$$

the line integral can be rewritten as an integral over z

$$I = \sqrt{1 + \left\{\frac{(r_i^+ - r_i^-)}{(z_i^+ - z_i^-)}\right\}} \int_{z_i^-}^{z_i^+} H(F(z),z)dz \tag{A.6}$$

By using a high order numerical quadrature such that

$$\begin{aligned} z &= \frac{(z_i^+ + z_i^-)}{2} + u\frac{(z_i^+ - z_i^-)}{2} \\ &= z_i + u\frac{(z_i^+ - z_i^-)}{2} \end{aligned} \tag{A.7}$$

where z_i is the midpoint of the i^{th} subsection, A.6 results in

$$I = \frac{\triangle l}{2}\int_{-1}^{+1} H\left(r_i + u\frac{\triangle r_i}{2},\, z_i + u\frac{\triangle z_i}{2}\right) du \tag{A.8}$$

where

$$\triangle l = \sqrt{\triangle r_i^2 + \triangle z_i^2}$$

$$\triangle r_i = (r_i^+ - r_i^-)$$

$$\triangle z_i = (z_i^+ - z_i^-)$$

A.8 is in a convenient form for integration. However it is worth analysing the case when the source point is also the observation point. $F(m)$ in eqn 2.76(a) may be rewritten (Abrahamowitz 1964)

$$F(m) = (a_0 + a_1(1-m) + a_2(1-m)^2) + (b_0 + b_1(1-m) + b_2(1-m)^2)\, ln\left(\frac{1}{1-m}\right) \tag{A.9}$$

where a_i and b_i are constant. If Ψ and Ψ_o are replaced by their r and z coordinates, (r, z) and (r', z'), the approximation given in eqn A.9 will become singular as $m \rightarrow 1$, or in terms of the coordinates as $r \rightarrow r'$ and $z \rightarrow z'$. The values of the function over these subsections needs special consideration.

From eqns 2.75 and 2.80(a)

$$K_{ii} = \int_{\triangle s_i}\int_0^{2\pi} \frac{d\theta ds'}{4\pi\epsilon\sqrt{(r_i + r')^2 + (z_i + z')^2 - 4r_i r' cos^2\frac{\theta}{2}}} \tag{A.10}$$

By stating that $r_i = r'$ and $z_i = z'$ and using eqn A.7 we may write

$$r' = r_i + u\frac{\triangle r_i}{2} \tag{A.11(a)}$$

and

$$z' = z_i + u\frac{\triangle z_i}{2} \tag{A.11(b)}$$

If eqns A.11(a) and A.11(b) are substituted into eqn A.10, we obtain

$$K_{ii} = \int_{\triangle s_i} \int_0^{2\pi} \frac{d\theta ds'}{4\pi\epsilon\sqrt{4r_i^2 + 2ur_i \triangle r_i + u^2 \triangle l^2 - 4r_i(r_i + u \triangle r_i/2cos^2\frac{\theta}{2})}} \quad (A.12)$$

As the function H is the function K lumped with the r in eqn A.1 and a change of variables is undertaken A.12 may be rewritten as

$$K_{ii} = \frac{\triangle l}{4\pi} \int_{-1}^{+1} \int_0^{\pi} \frac{(r_i + u \triangle r_i/2)d\theta\, du}{\sqrt{4r_i(r_i + u \triangle r_i/2)sin^2\theta + u^2 \triangle l^2/4}} \quad (A.13)$$

Let the integral be split such that

$$K_{ii} = \frac{\triangle l}{4\pi} \int_{-1}^{+1} \int_0^{\pi} \frac{r_i d\theta\, du}{\sqrt{4r_i\ (\ r_i + u \triangle r_i/2\ )\ sin^2\theta + u^2 \triangle l^2/4}}$$

$$+ \int_{-1}^{+1} \int_0^{\pi} \frac{u \triangle r_i/2 d\theta\, du}{\sqrt{4r_i\ (\ r_i + u \triangle r_i/2\ )\ sin^2\theta + u^2 \triangle l^2/4}} \quad (A.14)$$

This is of the form

$$K_{ii} = M\left(\int_{-1}^{1} \frac{u}{\sqrt{R}} du + \int_{-1}^{1} \frac{1}{\sqrt{R}} du\right)$$

where

$$R = a + bu + cu^2$$

and

$$M = \frac{\triangle l}{4\pi} \int_0^{\pi} d\theta$$

From general integral theory (Gradshteyn 1965)

$$\int_i^j \frac{u du}{\sqrt{R}} = [\frac{\sqrt{R}}{c}]_i^j - \frac{b}{2c} \int_i^j \frac{du}{\sqrt{R}}$$

and

$$\int_i^j \frac{du}{\sqrt{R}} = \frac{1}{\sqrt{c}} ln\left(2\sqrt{Rc} + 2cu + b\right)$$

where

$$a = 4r_i^2 sin^2\theta$$

$$b = 2r_i \triangle r_i sin^2\theta$$

$$c = \triangle l^2/4$$

Upon rearrangement of the result of the integration in u A.14 will result in

$$K_{ii} = \frac{1}{\pi}\int_0^{\pi/2} \frac{\triangle r_i}{\triangle l}\left[a(r_i^+,\theta) - a(r_i^-,\theta)\right] d\theta \qquad A.15$$

$$+ \frac{1}{\pi}\int_0^{\pi/2} r_i\left(1 - 2\frac{\triangle r_i}{\triangle l}sin^2\theta\right) ln\left\{\frac{a(r_i^+,\theta) + \frac{\triangle l}{2} + 2r_i\frac{\triangle r_i}{\triangle l}sin^2\theta}{a(r_i^-,\theta) - \frac{\triangle l}{2} + 2r_i\frac{\triangle r_i}{\triangle l}sin^2\theta}\right\} d\theta$$

where

$$a(x,\theta) = \sqrt{\triangle l^2/4 + 4r_i x sin^2\theta} \qquad (A.16)$$

This integration in θ may now may carried out using a low order numerical integration technique, such as Simpson's Rule, over a large number of points.

Chapter 3

Numerical Analysis of Coaxial Line Probes

3.1 Introduction

By solving Laplace's equation the fringe field capacitances of coaxial line probes can be calculated. Two techniques have been presented that may be applied to cases where the defined problem possesses rotational symmetry and a brief discourse of the theory behind these analysis tools has been given. In order to test the reliability of these two techniques, simple structures with defined capacitance values have been modelled over a variety of conditions and the computed results are compared to the expected values.

Upon agreement of the computed results in this study and previously published values (Marcuvitz 1951, Gajda *et al* 1983), more complex novel probe designs, to be used in a new time domain system, were modelled. The novel probe capacitances, as well as the test simulations as functions of the number of nodes and order of the system in the Finite Element and of the number of subsections in the Method of Moments, are presented. Brief descriptions of the software packages written to carry out the simulations are also given.

3.2 The Numerical Models

3.2.1 The Computer System

The Finite Element (FEM) and the Method of Moments (MOM) software packages have been developed and implemented on the Digital Equipment Coorporation MicroVax II located within the King's College Physics Department. This is a 32 bit multi-user system configured with 9 Mbytes of main memory, two disc units capable of 71 Mbytes and 160 Mbytes storage respectively, as well as two floppy disc units each with 500 kbytes storage.

3.2.2 Software Support

Both of the modelling packages were written using FORTRAN 77 and required the usual software support utilites. These consist of the VMS FORTRAN compiler and Debugger, the latter allowing the software to be followed step by step as it is executed. Also available and used extensively in the MOM implementation was the NAG FORTRAN LIBRARY, mark 12, a general numerical algorithm library.

3.2.3 Finite Element Simulation Program

The structure of the FEM set of programs is shown in Fig 3.1. The main parts of the package are the mesh generator and the construction and minimisation of the functional.

The mesh generator, MESHIN, works on the principle that the problem space can be subdivided into quadrilaterals of varying size and that each quadrilateral can in turn be subdivided into triangular units. The problem space is defined by the user and the position in space of each quadrilateral is input as well as the order of the system. Thereafter the generator works out the numbering and coordinates of each node and the geometry of each element for the given order.

The main numerical analysis is achieved by AXIS. After reading in the data generated by MESHIN, the local element **S** matrix is constructed for each element in turn and embedded into the global **S** matrix. On completion of this process for all elements the system of equations is solved for ϕ and the capacitance is calculated for the values found. All numerical computations are carried out using the double precision data format of FORTRAN 77.

The actual execution of the simulation program AXIS is controlled by ELEMENT.COM. This enables the calculation to proceed either in real time or in the batch mode.

3.2.4 Method of Moments Simulation Program

The MOM programs have the same structure as the FEM software (Fig 3.2). The main section of code is within two subprograms, SURFACE and MODEL.

SURFACE carries out the same tasks as MESHIN, with the exception that only conductor and interface surfaces need to be defined. The program will automatically subdivide the problem space on receipt of the total number of subsections in the region of solution and the position of each of the main surfaces to be subdivided. The coordinates and the orientation of each subsection are then stored on disc.

The execution program, MODEL, consists of two parts. Firstly the main system of equations is constructed and secondly the capacitance is calculated for the charge densities found.

Off diagonal elements used in the construction of the matrix were computed using a 32 point Legrande Gauss quadrature (Abrahamowitz 1964), outlined in the Appendix to chapter2, and the calculation of the Green's function kernel in equation 2.75 was computed using the NAG S21BBF subroutine. Derivatives of the Green's function were calculated using central difference approximations.

The elements in the matrix where the Green's function becomes singular were evaluated using a combination of analytic and numerical integration (as shown in the Appendix, equation A.15). The Green's function is integrated analytically over

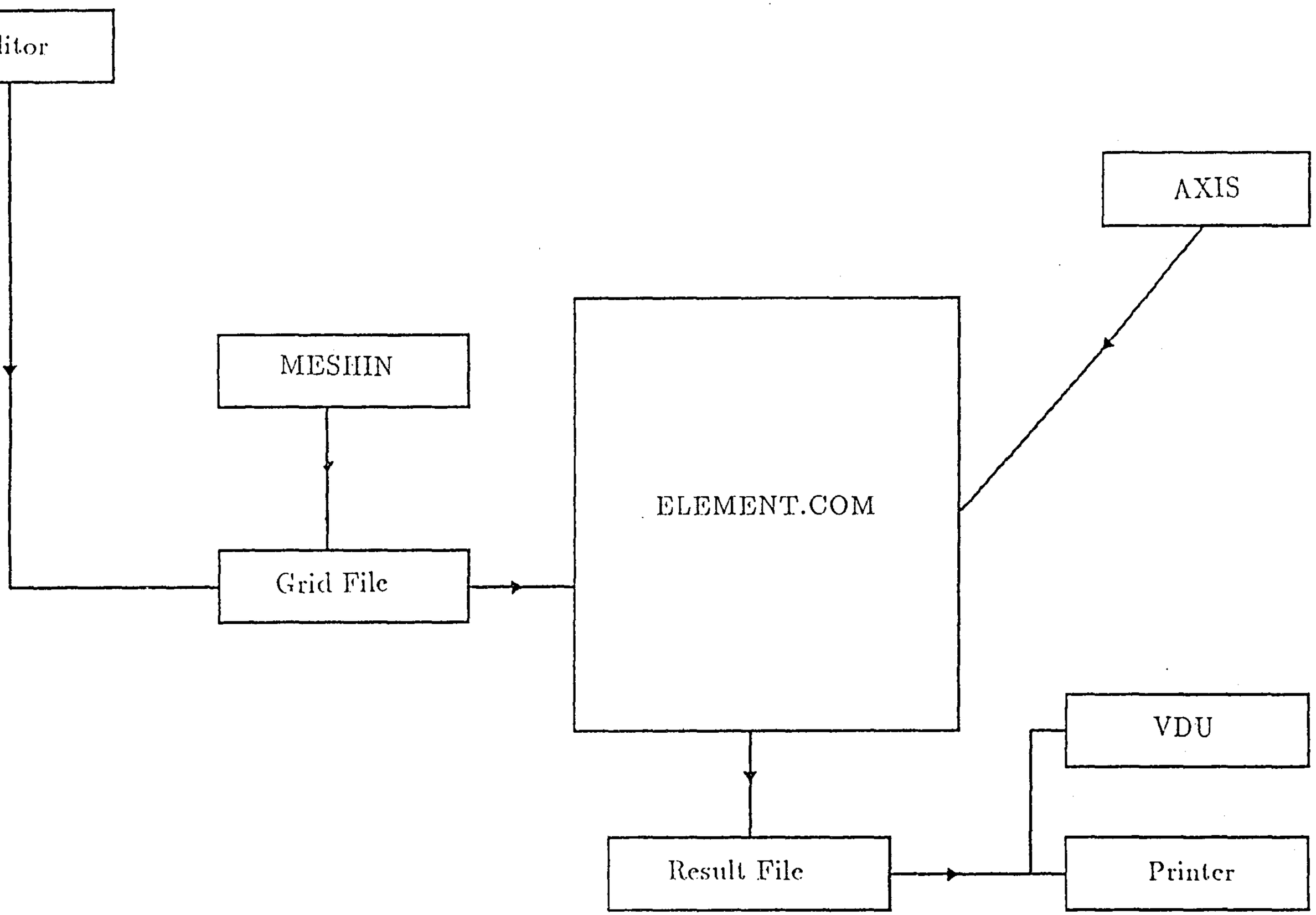

Fig 3.1 Structure of the software for the Finite Element progam.

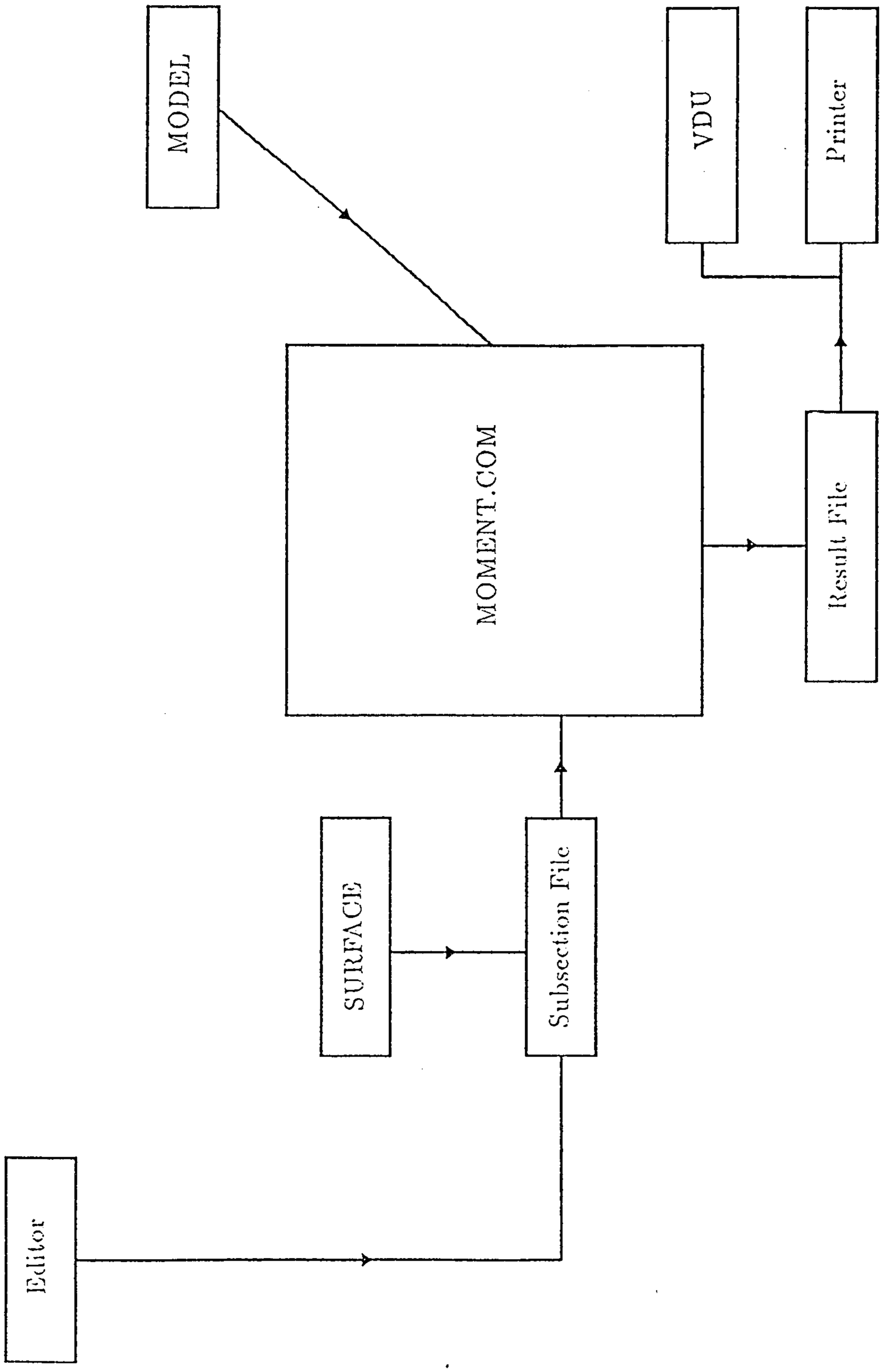

Fig 3.2 Structure of the software for the Method of Moments progam.

the subsection and then integrated numerically over the angular coordinate, θ, using the rectangle integration rule over 3000 points.

As with the FEM analysis programs MOMENT.COM controls the execution of MODEL. However the calculation of the system of integral equations takes up to 9 times longer than the FEM analysis and as a result is always run in batch mode.

3.3 The Analysis of Probes with known Capacitances

3.3.1 The Conditions for the Evaluation of the Two Models

In order to test the simulation packages various probe shapes with known equivalent circuits were analysed. Each probe was modelled over a variety of conditions, itemised below, while the sample permitivitty, ϵ_m, was varied from 1 to 100 in each case to simulate the range of dielectric parameters that could be encountered by the Time Domain Spectrometer. The conditions can be listed as :

(a) The number of subsections in the MOM model were stepped from 35 to 170. This would allow a check for convergence and accuracy in the model.

(b) The number of nodes in the FEM was varied from 250 to 1500, (the maximum number of nodes allowed due to the limitations of the computer hardware), allowing the convergence rate to be examined.

(c) For a fixed number of nodes the order of the polynomial expression in the FEM was varied from 1 to 4, again as a check of convergence and increase in accuracy.

(d) The positioning of the approximate Neumann boundary was moved along the z-axis until no apparent change in the capacitance was seen.

The total capacitance was found in each case and from this value C_o and C_f, the external and internal fringe field capacitances respectively, were calculated.

The experimental results quoted are from a previous paper by Gajda (1982), the results obtained previously for the MOM and FEM by Gajda *et al* (1983) are given, while the theoretical results are from Marcuvitz (1951).

3.3.2 50Ω Airline with a Groundplane

The basic configuration for the model is shown in Fig 3.3(a). The ratio of outer to inner conductor radii, b/a, was set at 2.303 with the inner radius, a, equal to 1.0 mm. The groundplane was taken to be 7 times the outer conductor radius. The MOM model was run under the conditions set out in item (a) in the previous section and the results are shown in Table 3.1 and Fig 3.4. Table 3.1 shows

All dimensions are normalised to the inner conductor radius

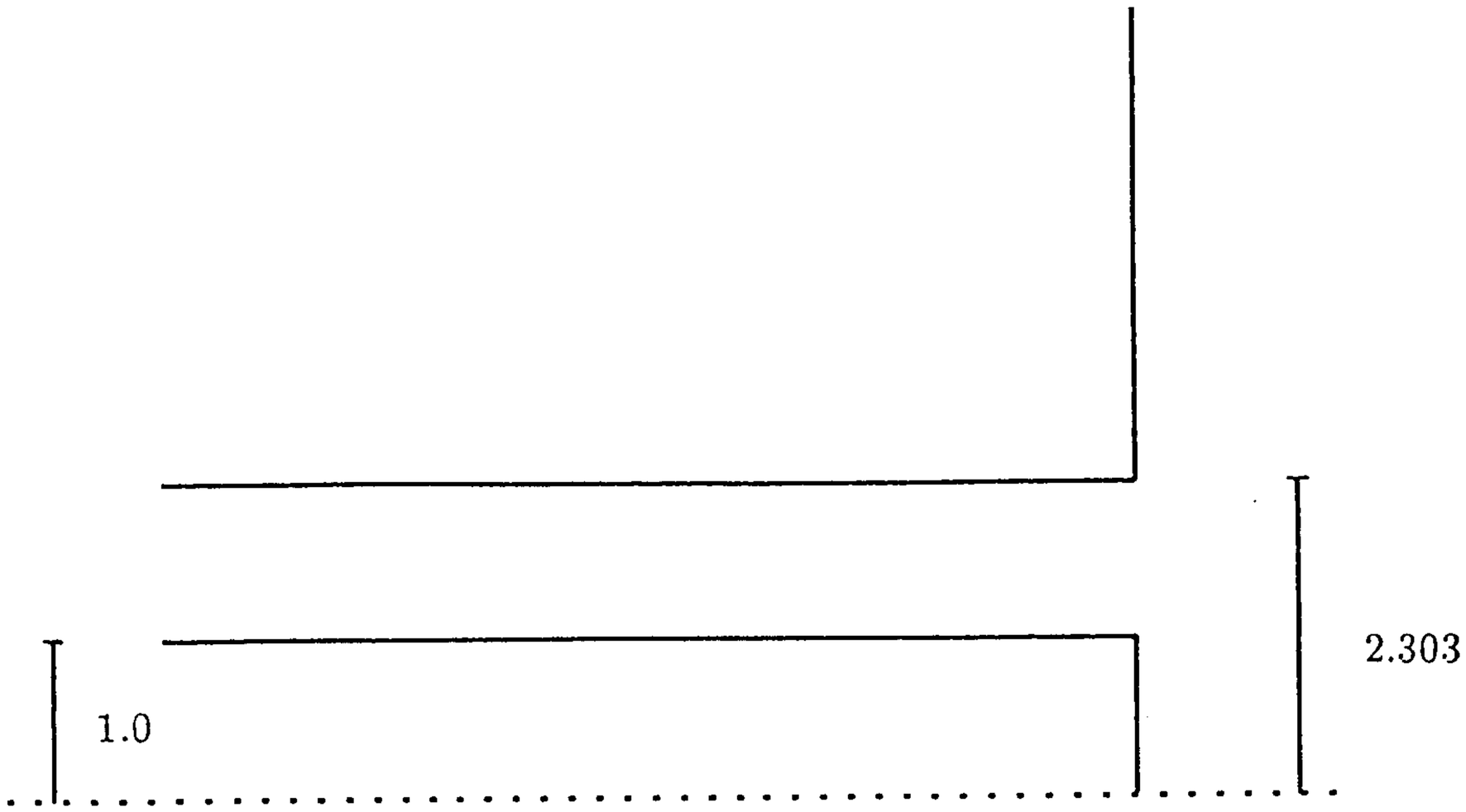

Fig 3.3(a) Airline with a groundplane.

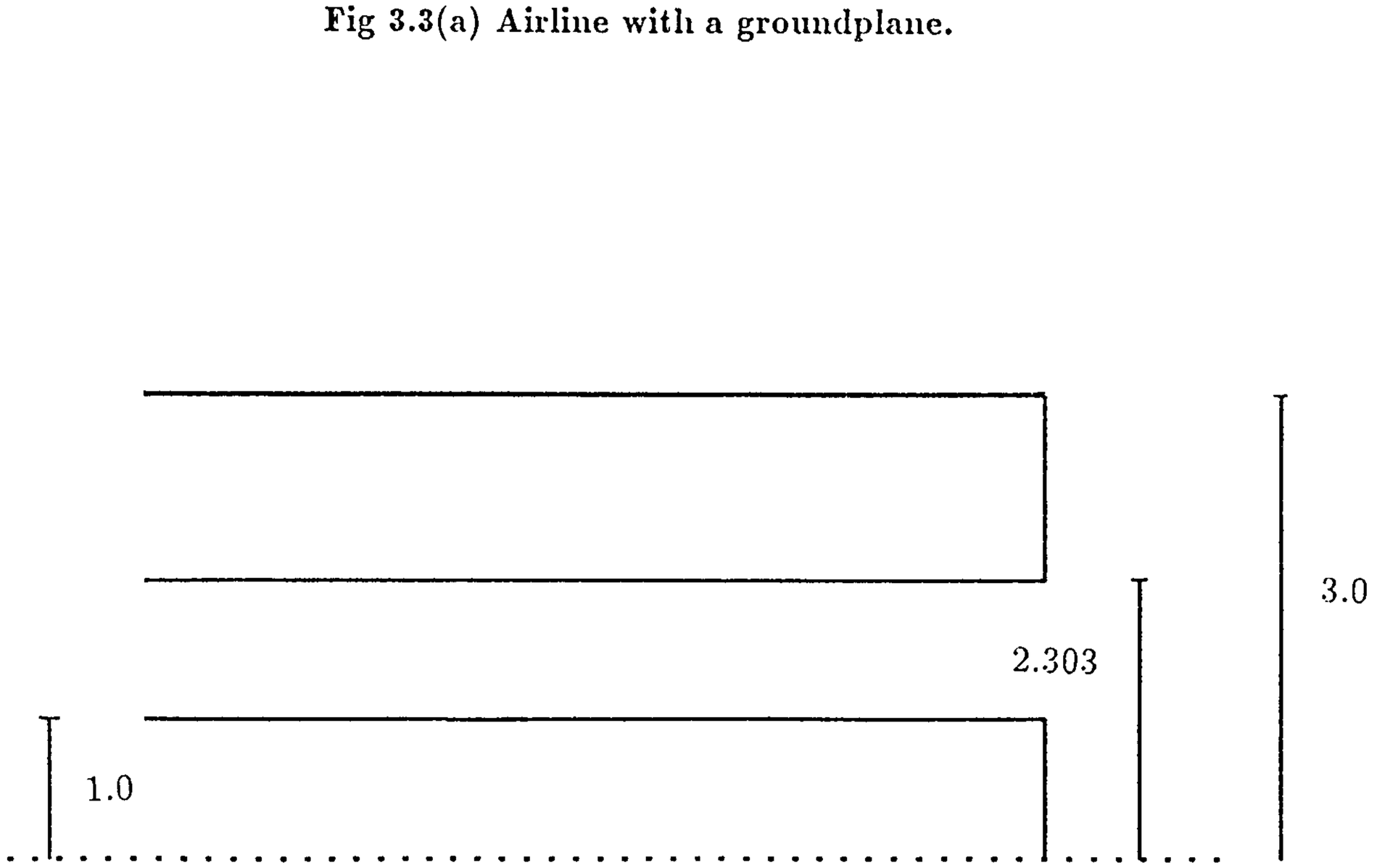

Fig 3.3(b) Airline without a groundplane.

the variation in the ratio of C_f/C_o for different values of permittivity and the number of subsections in the problem. Fig 3.4 is an illustration of the effect the number of subsections in the problem has on the total capacitance for ϵ_m equal to 1 and 100.

	Number of Subsections in MOM Model					
ϵ_m	35	60	80	100	130	170
5	0.0334	0.0991	0.1134	0.1136	0.1136	0.1137
10	0.0339	0.0999	0.1153	0.1154	0.1156	0.1157
30	0.0348	0.1081	0.1252	0.1254	0.1254	0.1253
50	0.0350	0.1098	0.1274	0.1275	0.1275	0.1276
70	0.0351	0.1107	0.1284	0.1285	0.1286	0.1286
90	0.0352	0.1111	0.1289	0.1289	0.1290	0.1291
100	0.0352	0.1112	0.1291	0.1292	0.1292	0.1293

Table 3.1 : C_f/C_o as a function of the sample permittivity and the number of subsections in the problem for a 50Ω airline with a groundplane.

The results of the FEM analysis are shown in Tables 3.2 and 3.3 and in Fig 3.5. Table 3.2 shows the values obtained for the ratio, C_f/C_o by increasing the number of nodes in the problem with the polynomial set at first order. The results obtained by increasing the order of the polynomial expression, N, with the number of nodes set at 1500 are shown in Table 3.3. Fig 3.5 is a graphical representation of the effects the number of nodes and the order of the system have on the capacitance C_T when ϵ_m is set at 100.

	Number of Nodes in FEM Model					
ϵ_m	200	500	750	1000	1250	1500
5	0.0501	0.0511	0.0532	0.0536	0.0563	0.0582
10	0.0543	0.0563	0.0571	0.0588	0.0607	0.0622
30	0.0571	0.0587	0.0604	0.0626	0.0651	0.0678
50	0.0596	0.0607	0.0619	0.0636	0.0664	0.0686
70	0.0609	0.0626	0.0631	0.0654	0.0673	0.0699
90	0.0612	0.0628	0.0641	0.0665	0.0683	0.0707
100	0.0613	0.0631	0.0651	0.0678	0.0692	0.0712

Table 3.2 : C_f/C_o as a function of the sample permittivity and the number of nodes in the problem for a 50Ω airline with a groundplane.

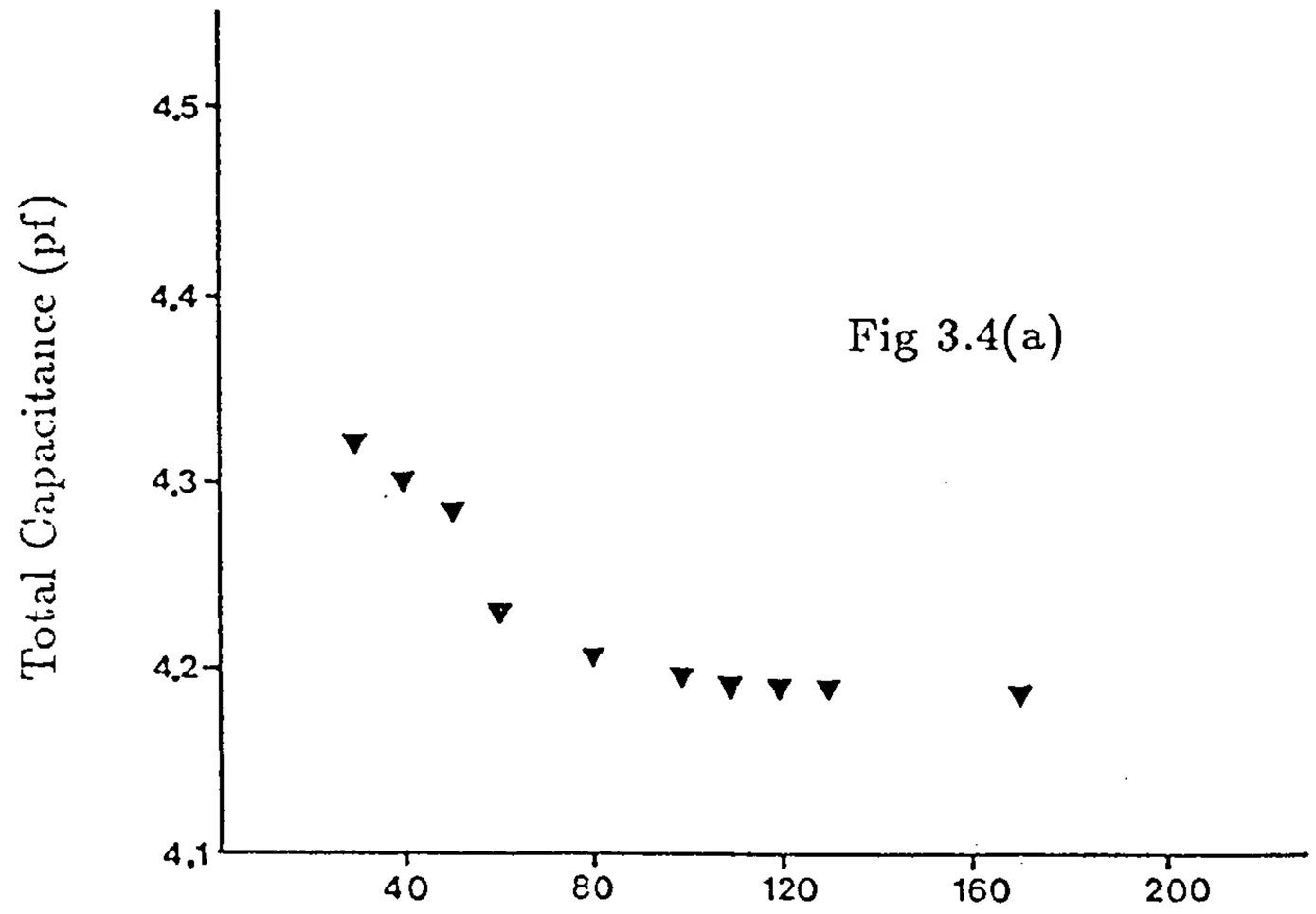

Fig 3.4(a)

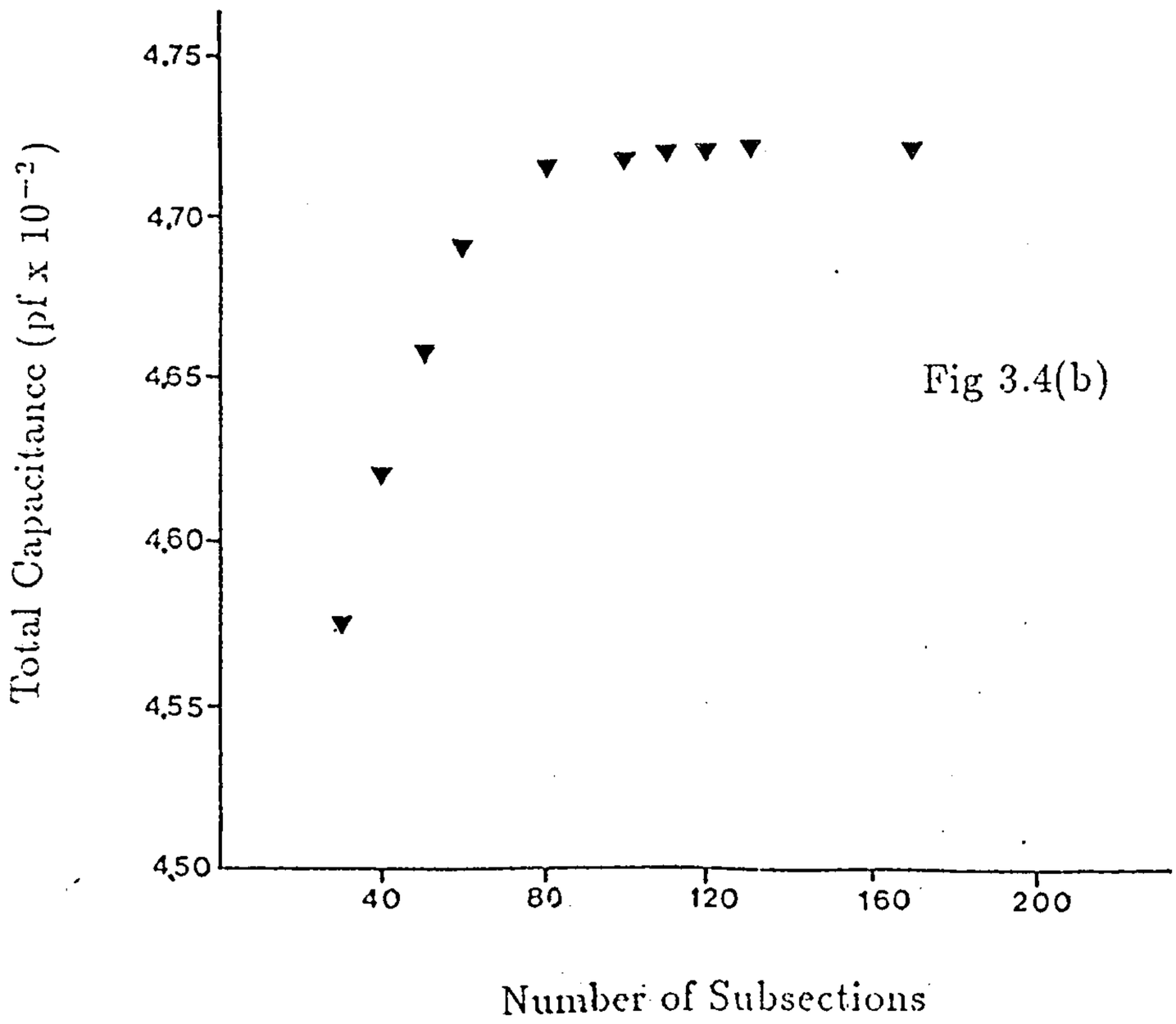

Fig 3.4(b)

Fig 3.4 The effects on the total capacitance for the 50Ω airline with a groundplane by varying the number of subsections in the problem.
(a) Permittivity equal to 100.
(b) Permittivity equal to 1.

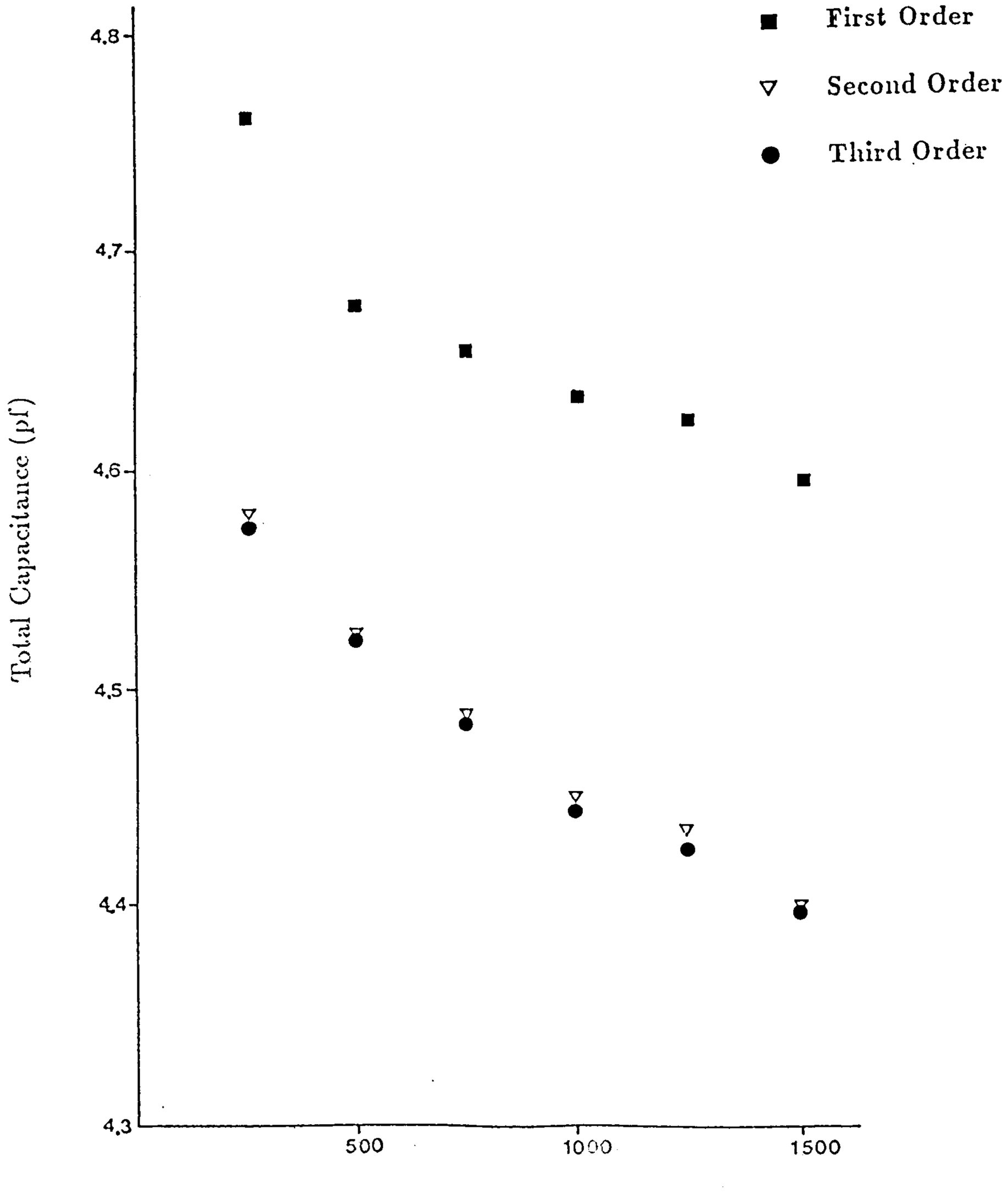

Fig 3.5 Variation of the total capacitance, for the 50Ω airline with a groundplane, by increasing the number of nodes in the problem for first, second and third order polynomial functions.

	Order of FEM Polynomial			
ϵ_m	1	2	3	4
5	0.0582	0.0591	0.0591	0.0591
10	0.0622	0.0642	0.0643	0.0643
30	0.0678	0.0689	0.0690	0.0689
50	0.0686	0.0694	0.0697	0.0697
70	0.0699	0.0711	0.0713	0.0711
90	0.0707	0.0718	0.0718	0.0719
100	0.0712	0.0728	0.0728	0.0728

Table 3.3 : C_f/C_o as a function of the sample permittivity and the order of the system polynomial for a 50Ω airline with a groundplane.

Fig 3.6 shows the variation of C_T with increasing permittivity for both the MOM, 100 subsections, and the FEM, 1500 nodes and N=2, while Fig 3.7 shows the variation of C_o and C_f with increasing permittivity.

3.3.3 50Ω Airline without a Groundplane

Using the same configuration and conditions in the previous section the groundplane was removed and the outer conductor's outer radius was set at 3.0 times a, Fig 3.3(b). Fig 3.8 shows the total capacitance, C_T, plotted against varying permittivity for each simulation. The number of nodes in the FEM was set at 1500, with $N = 2$, and the number of subsections in the MOM was set to 100.

The variation of C_o and C_f as a function of permittivity is presented in Fig 3.9, the simulation being run under the same conditions of $N = 2$, the number of nodes set at 1500 and the number of subsections held at 100.

3.3.4 50Ω Teflon Filled Line with a Groundplane.

Solutions for the teflon filled line, Fig 3.10(a), (permittivity inside the line is 2.05) are presented in Table 3.4 and Fig 3.11 for the MOM and in Tables 3.5 and 3.6 and Fig 3.12 for the FEM analysis. The ratio, b/a, for the line was set at 3.27 while the groundplane was set at 7 times the outer conductor radius.

Table 3.4 shows the variation of the ratio C_f/C_o with sample permittivity while Fig 3.11 is a graphical representation of the effect the number of subsections has on C_T for ϵ_m equal to 100.

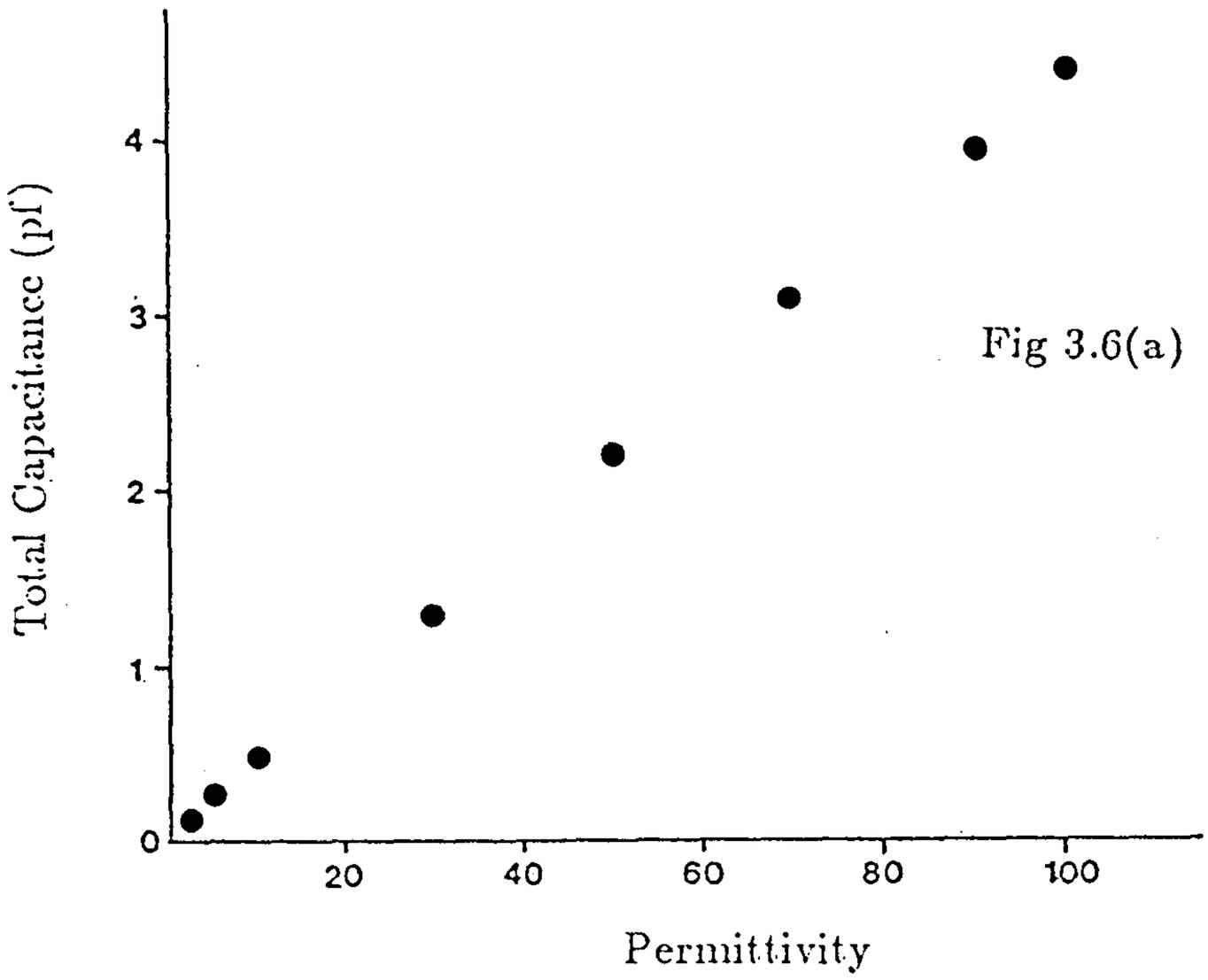

Fig 3.6(a)

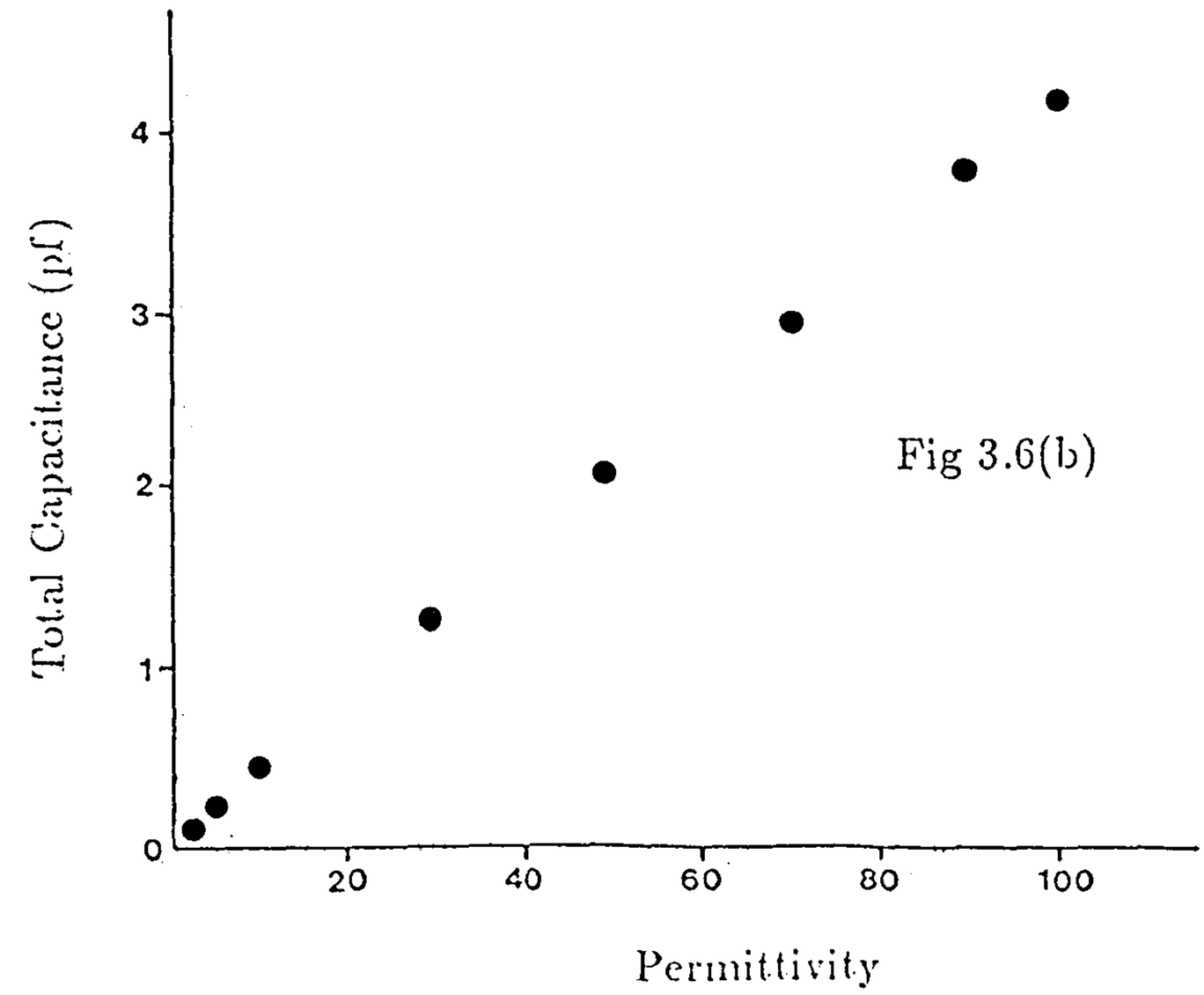

Fig 3.6(b)

Fig 3.6 Total capacitance plotted against permittivity for a 50Ω airline with a groundplane.
(a) Finite Element with N=2 and 1500 nodes.
(b) Method of Moments with 100 subsections.

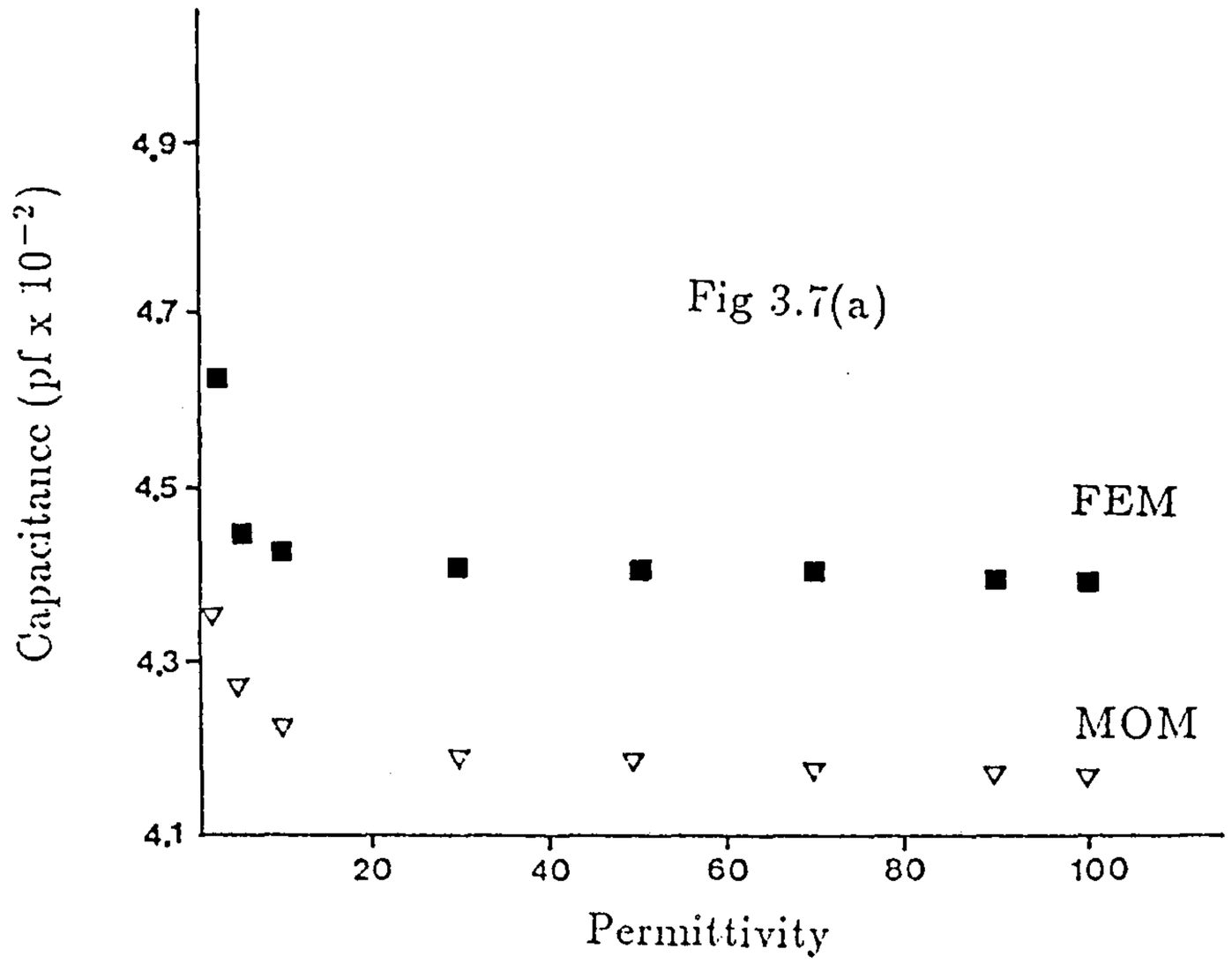

Fig 3.7(a)

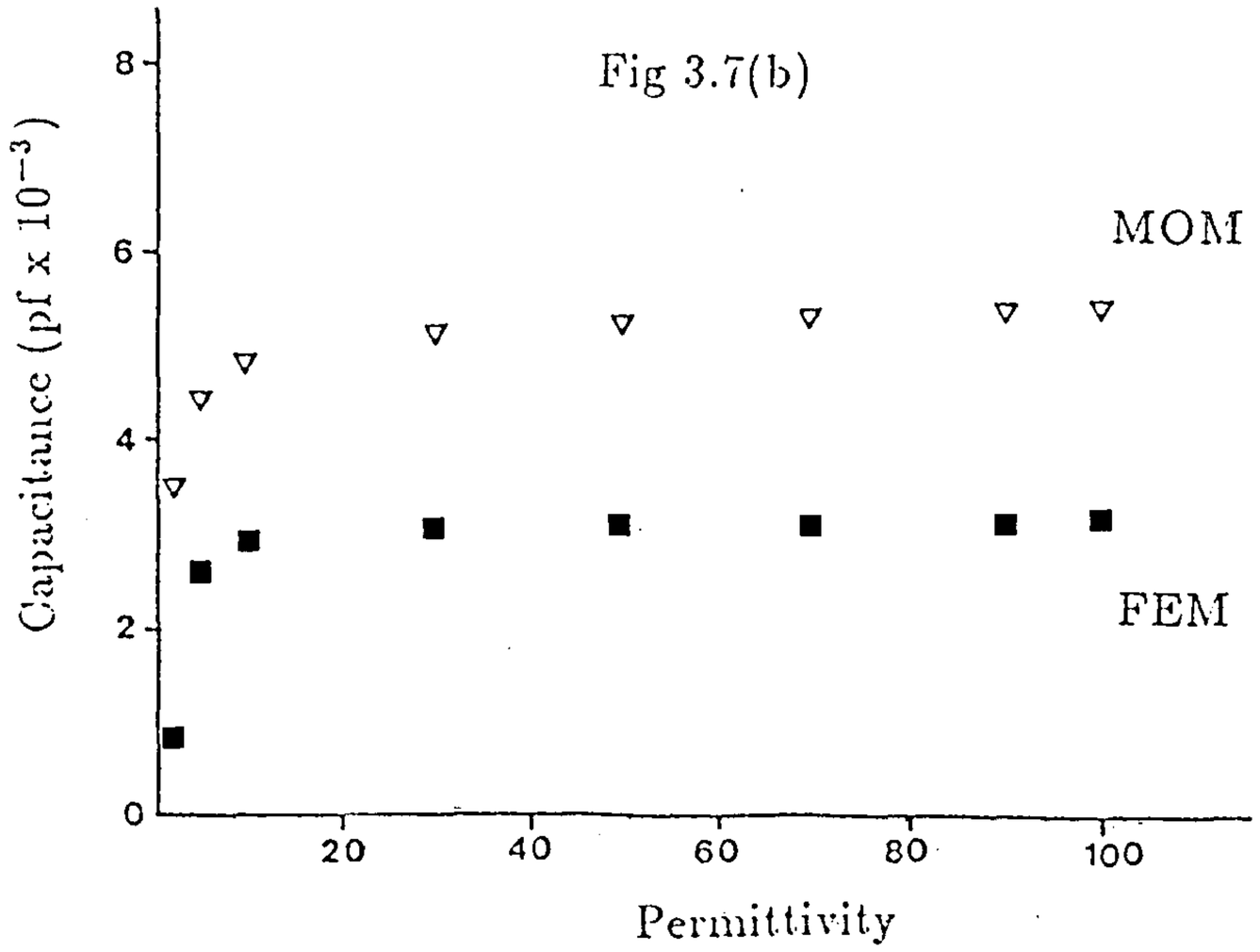

Fig 3.7(b)

Fig 3.7 C_o and C_f plotted against permittivity for a 50Ω airline with a groundplane.
(a) C_o
(b) C_f

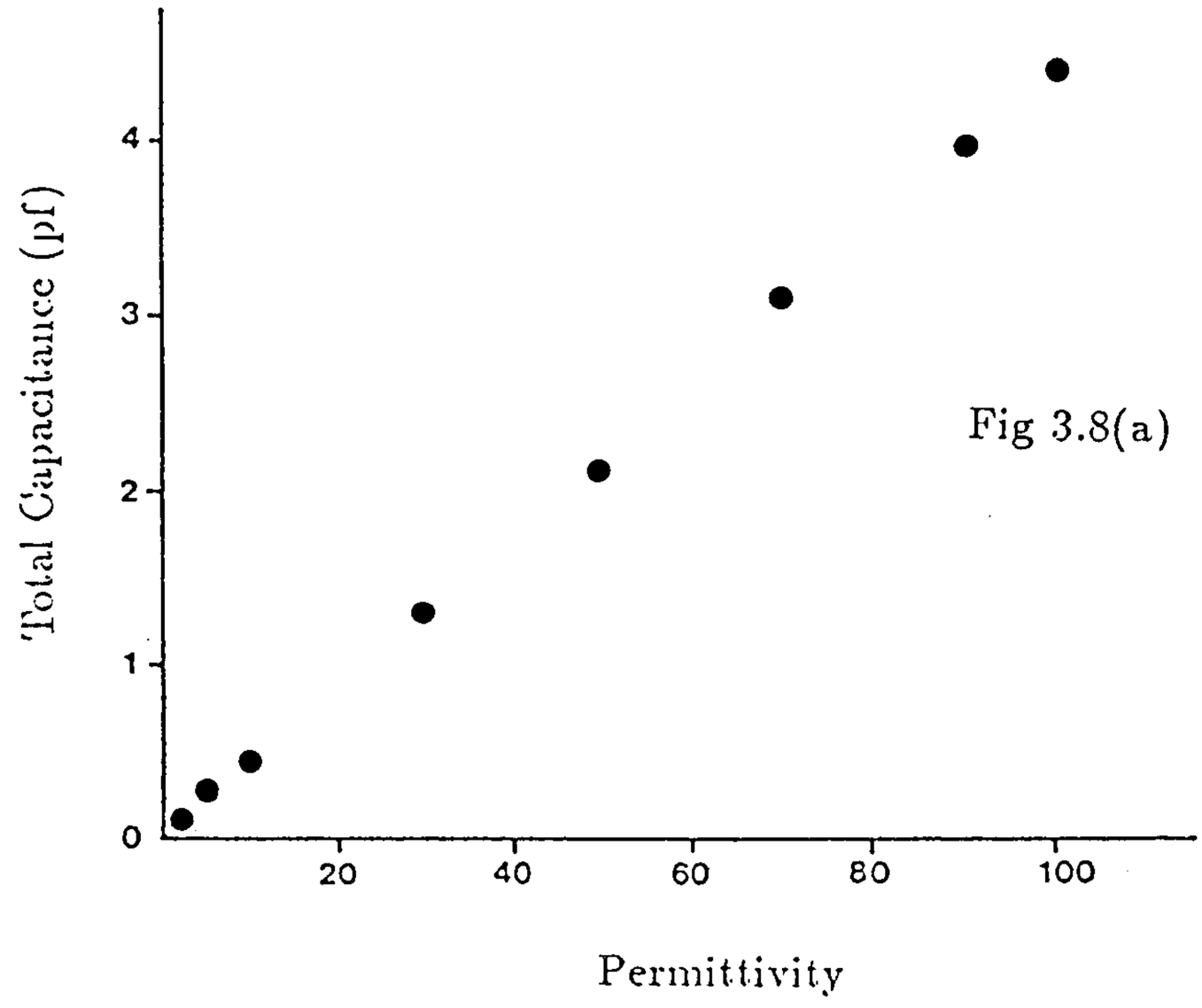

Fig 3.8(a)

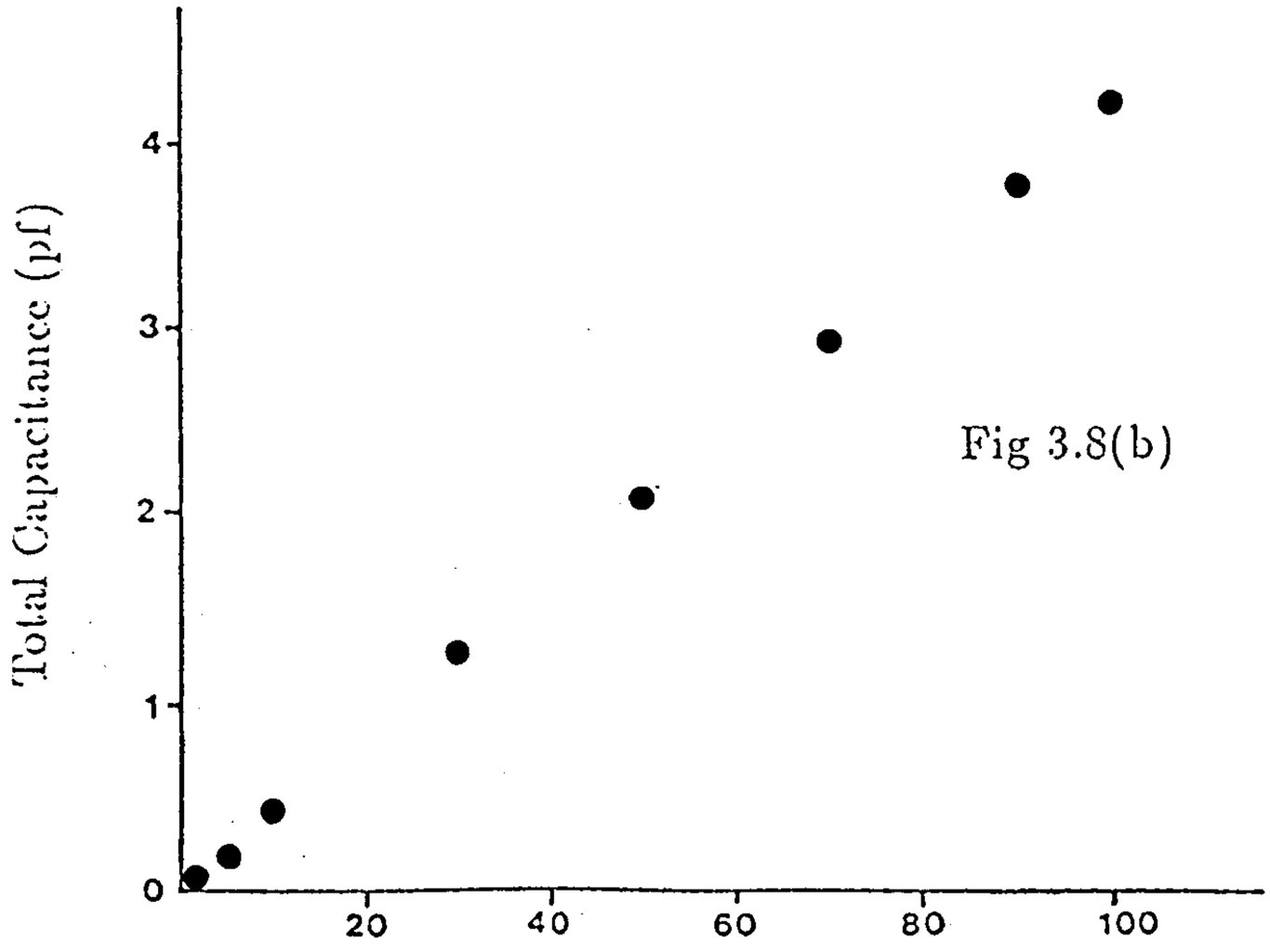

Fig 3.8(b)

Fig 3.8 Total capacitance plotted against permittivity for a 50Ω airline without a groundplane.
(a) Finite Element with N=2 and 1500 nodes.
(b) Method of Moments with 100 subsections.

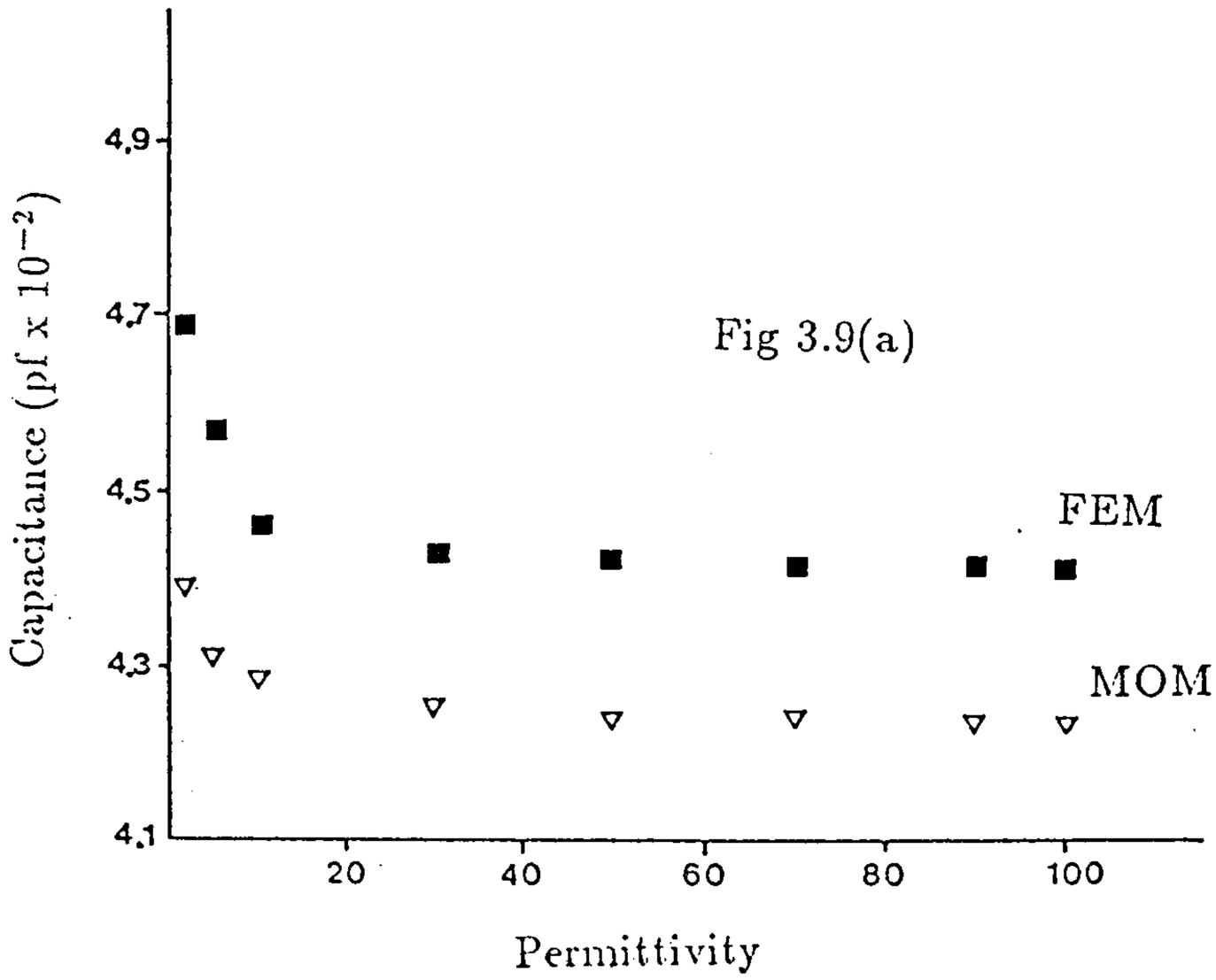

Fig 3.9(a)

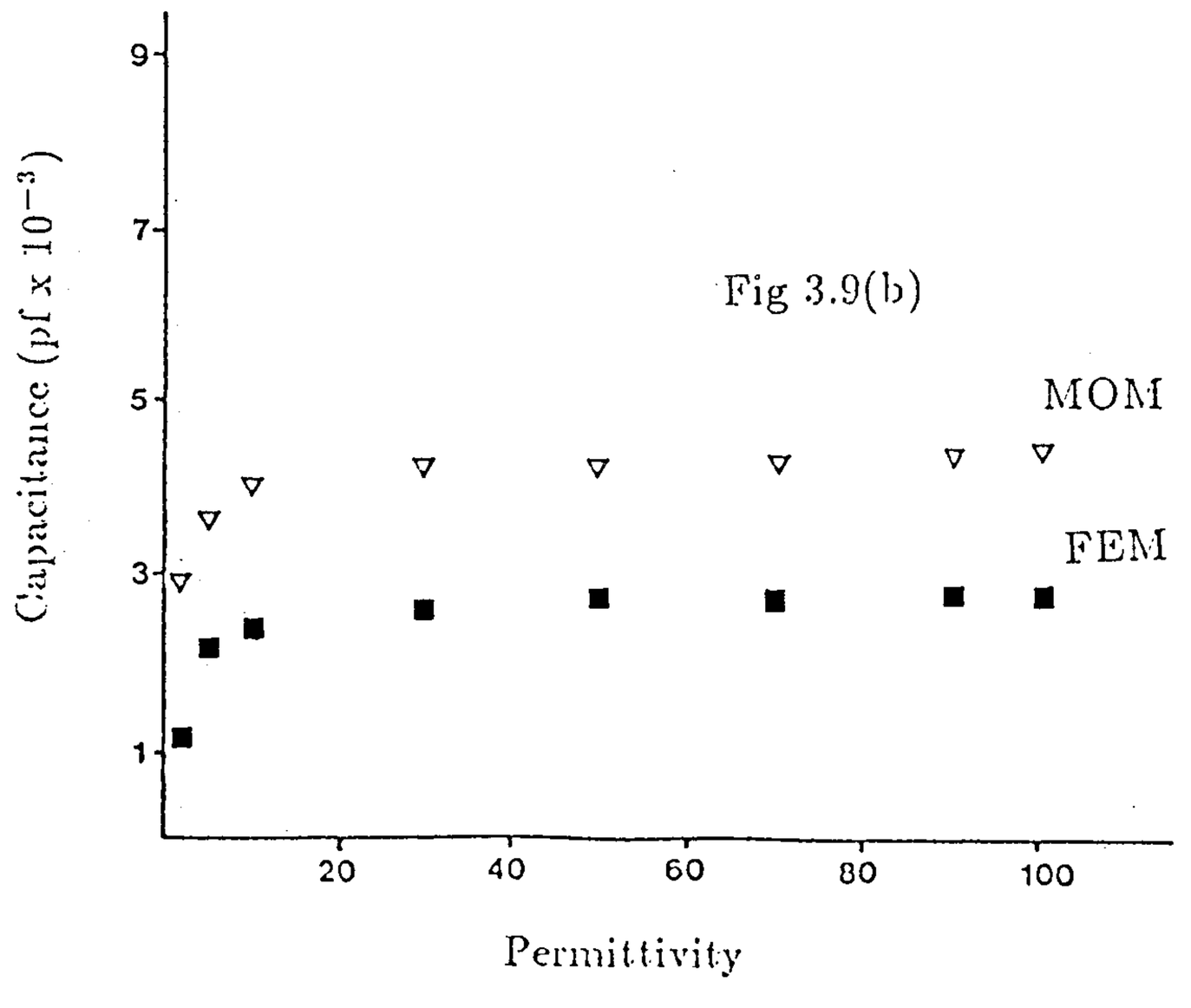

Fig 3.9(b)

Fig 3.9 C_o and C_f plotted against permittivity for a 50Ω airline without a groundplane.
(a) C_o
(b) C_f

All dimensions are normalised to the inner conductor radius

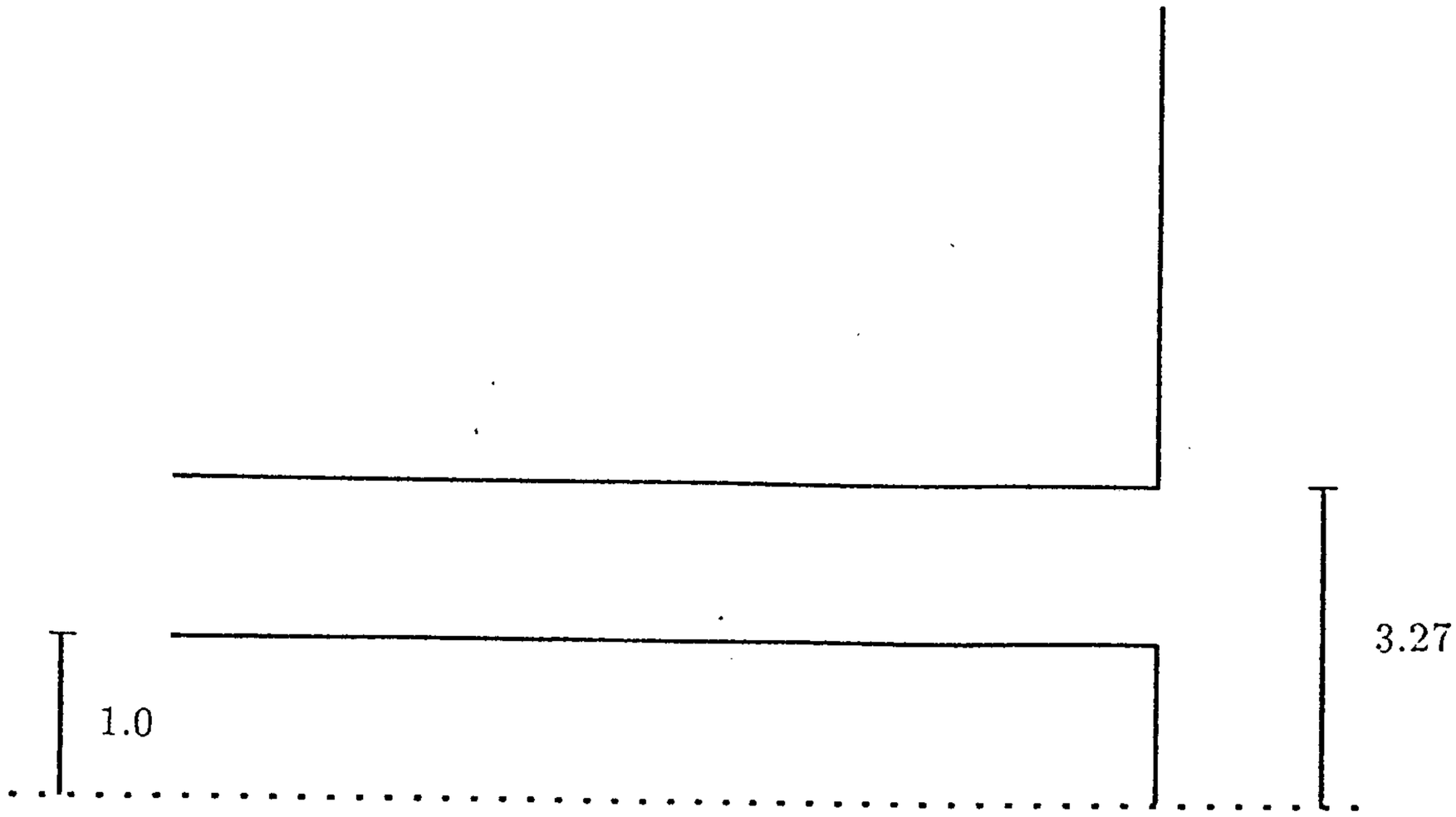

Fig 3.10(a) Teflon filled line with a groundplane.

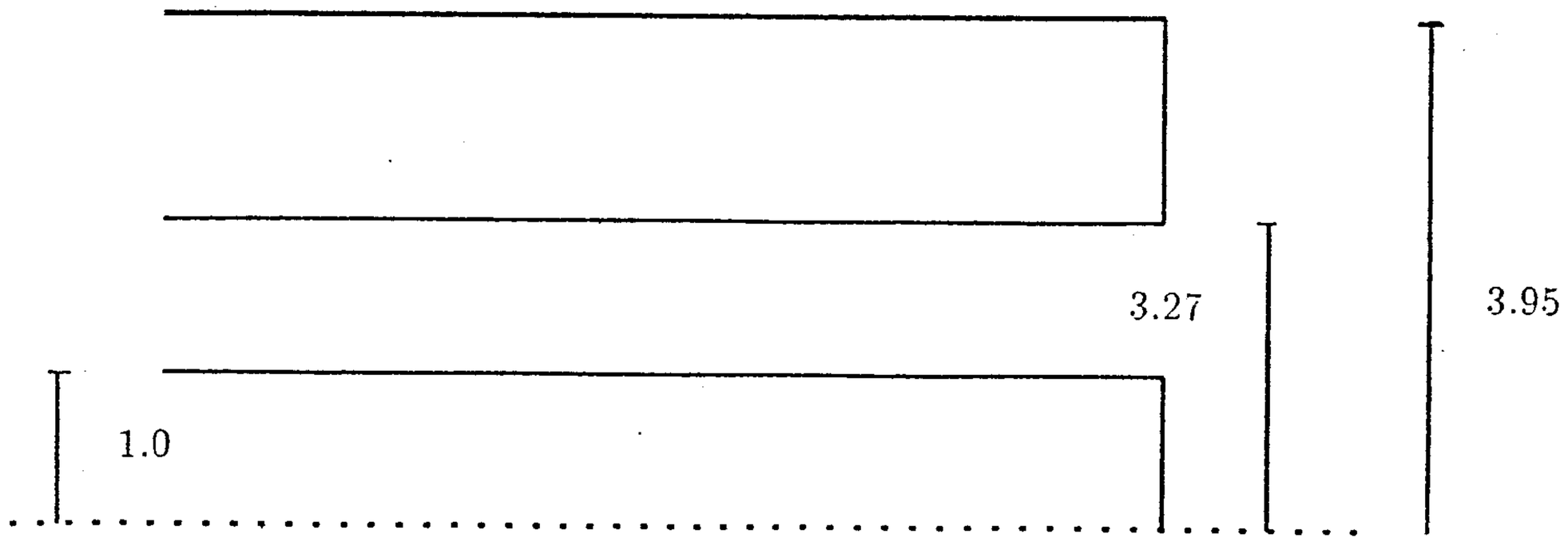

Fig 3.10(b) Teflon filled line without a groundplane.

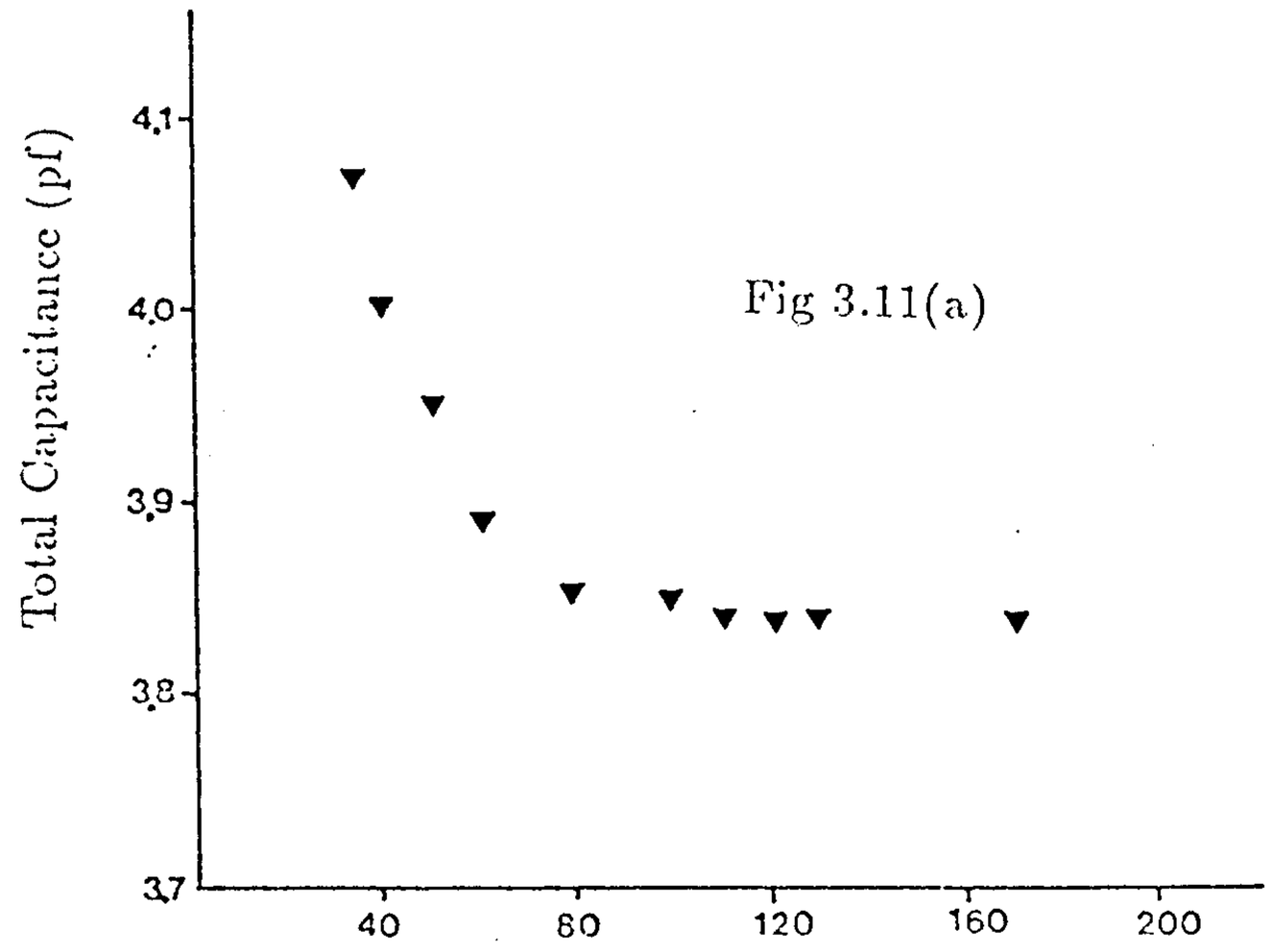

Fig 3.11(a)

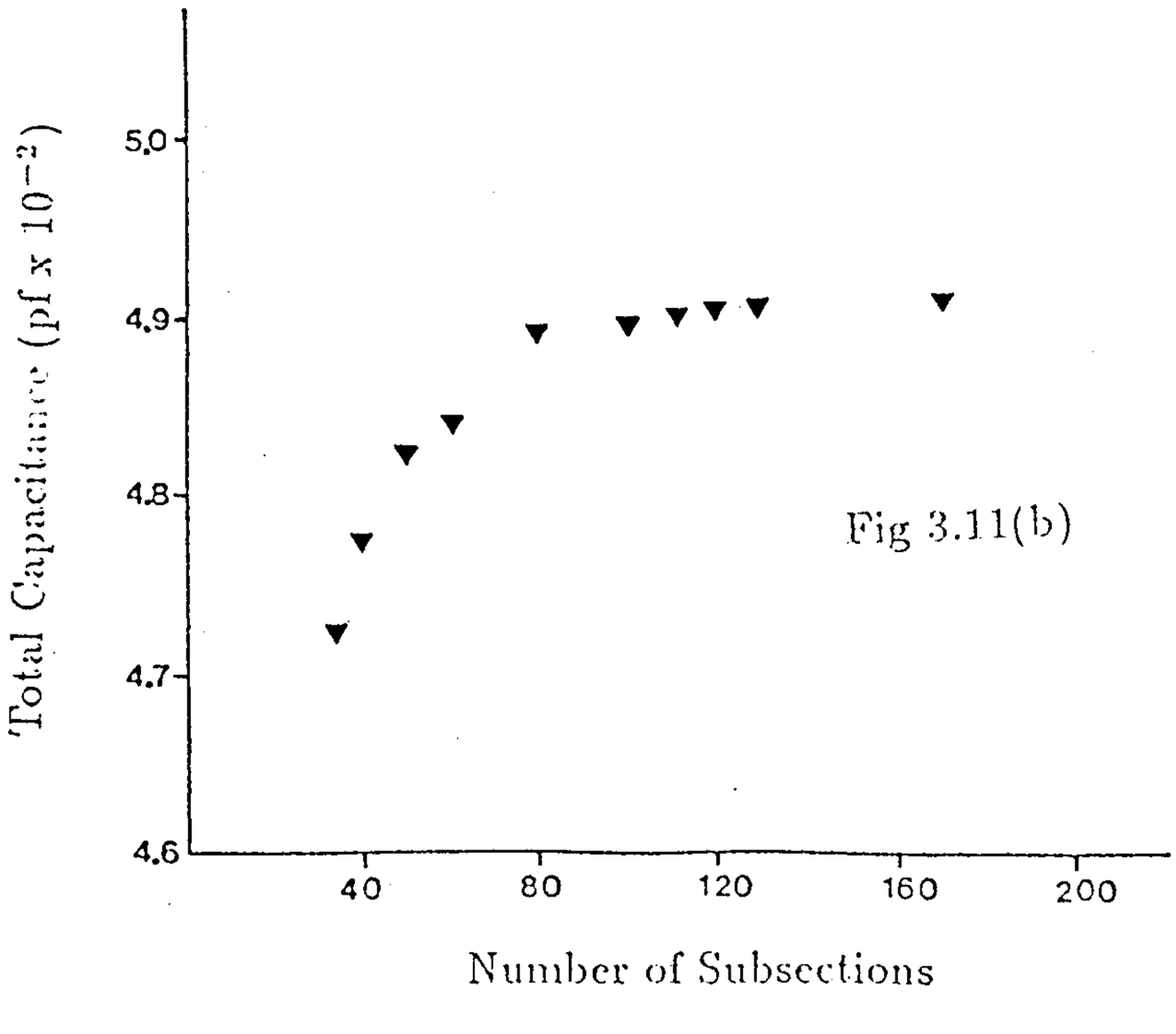

Fig 3.11(b)

Fig 3.11 The effects on the total capacitance, for the 50Ω teflon filled line with a groundplane by varying the number of subsections in the problem.
(a) Permittivity equal to 100.
(b) Permittivity equal to 1.

	Number of Subsections in MOM Model					
ϵ_m	35	60	80	100	130	170
5	0.1312	0.1903	0.2195	0.2197	0.2197	0.2199
10	0.1385	0.1995	0.2232	0.2235	0.2236	0.2236
30	0.1560	0.2305	0.2517	0.2518	0.2518	0.2519
50	0.1603	0.2394	0.2616	0.2618	0.2618	0.2620
70	0.1622	0.2434	0.2662	0.2663	0.2664	0.2665
90	0.1634	0.2457	0.2687	0.2689	0.2690	0.2690
100	0.1639	0.2465	0.2697	0.2699	0.2699	0.2701

Table 3.4 : C_f/C_o as a function of the sample permittivity and the number of subsections in the problem for a 50Ω teflon filled line with a groundplane.

Tables 3.5 and 3.6 show the variation of the capacitive ratio for differing number of nodes and order of polynomial expression in the FEM simulations and Fig 3.12 shows the effect of the varying conditions on C_T while ϵ_m was held constant.

	Number of Nodes in FEM Model					
ϵ_m	200	500	750	1000	1250	1500
5	0.0975	0.1008	0.1033	0.1130	0.1141	0.1156
10	0.1003	0.1022	0.1061	0.1145	0.1181	0.1254
30	0.1055	0.1088	0.1119	0.1194	0.1232	0.1309
50	0.1141	0.1193	0.1229	0.1278	0.1305	0.1439
70	0.1162	0.1229	0.1266	0.1320	0.1383	0.1465
90	0.1171	0.1231	0.1288	0.1340	0.1397	0.1486
100	0.1228	0.1281	0.1349	0.1427	0.1466	0.1532

Table 3.5 : C_f/C_o as a function of the sample permittivity and the number of nodes in the problem for a 50Ω teflon filled line with a groundplane.

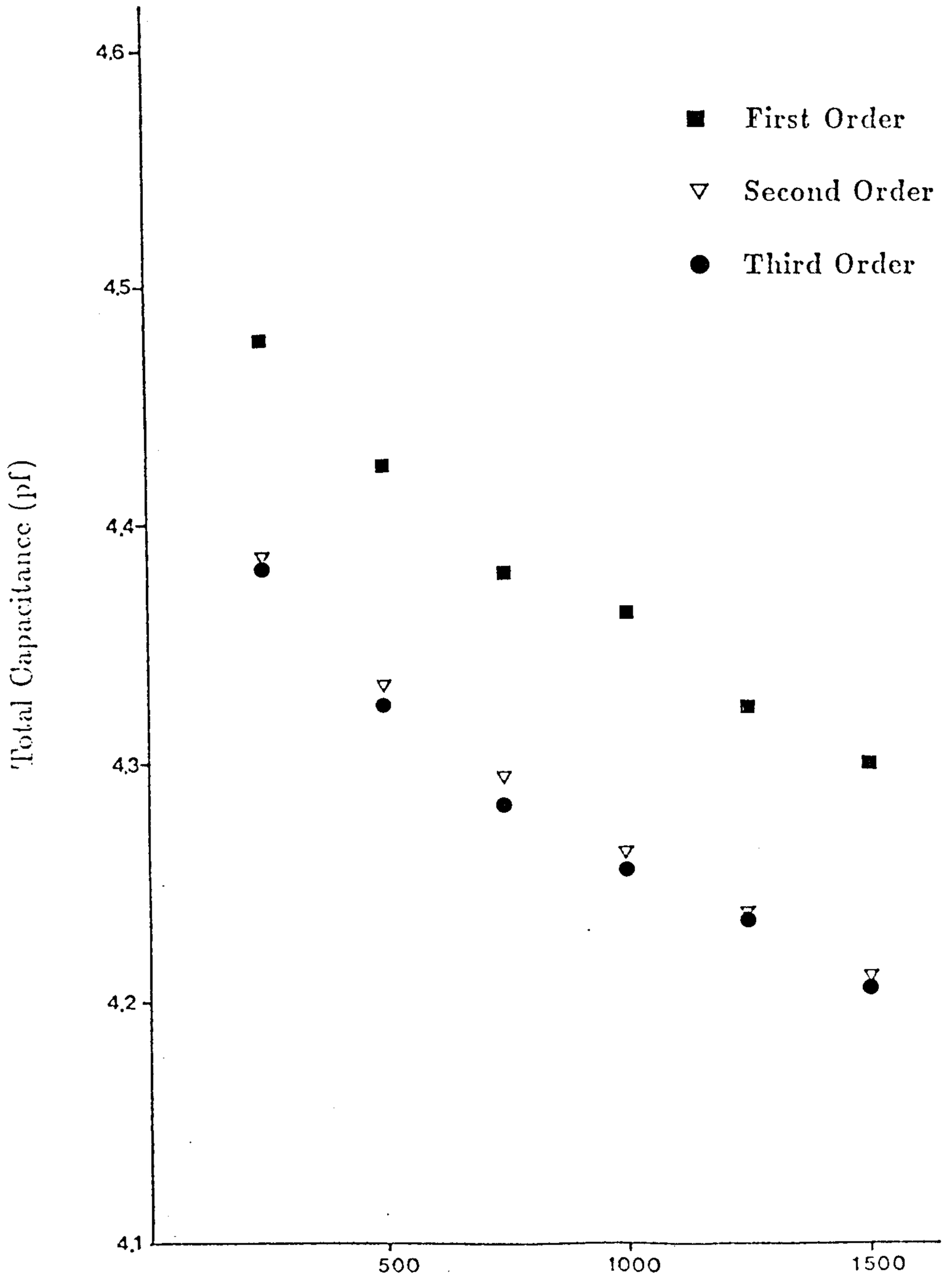

Fig 3.12 Variation of the total capacitance, for the 50Ω teflon filled line with a groundplane by increasing the number of nodes in the problem for first, second and third order polynomial functions.

	Order of FEM Polynomial			
ϵ_m	1	2	3	4
5	0.1156	0.1210	0.1211	0.1211
10	0.1254	0.1410	0.1410	0.1410
30	0.1309	0.1528	0.1530	0.1531
50	0.1439	0.1618	0.1619	0.1620
70	0.1465	0.1656	0.1655	0.1656
90	0.1486	0.1705	0.1705	0.1706
100	0.1532	0.1735	0.1735	0.1740

Table 3.6 : C_f/C_o as a function of the sample permittivity and the order of the system polynomial for a 50Ω teflon filled line with a groundplane.

Fig 3.13 shows the total capacitance plotted against permittivity, ϵ_m, in the range 1 to 100, while the variation of C_o and C_f are plotted in Fig 3.14.

3.3.5 50Ω Teflon Filled Line without a Groundplane

The groundplane in section 3.3.4 was removed and the outer conductor outer radius was set at 3.95 times a, Fig 3.10(b). By varying the permittivity of the sample Figs 3.15 and 3.16 were obtained. Fig 3.15 shows the total capacitance plotted against ϵ_m while Fig 3.16 shows the fringe field capacitances as a function of ϵ_m. In each case the modelling parameters were held constant at 1500 nodes, $N = 2$ and 100 subsections.

3.3.6 Discussion of the Results

The main objective of the simulations carried out was to find an optimum set of conditions for each technique which could be used in the analysis of several probes with unknown capacitance values. As a result no error analysis has been undertaken as this study would, in itself, be a major project (Trowbridge 1987, Richter 1987, Silvester 1987). The errors are dependent on a number of conditions. The number of elements or subsections in the problem, the concentration of elements or subsections in a particular subregion of the solution and computational round off errors are but three.

The analysis of the results can be broken down into four sections :

(a) A general conclusion for the equivalent circuit.

(b) An examination of the Method of Moments.

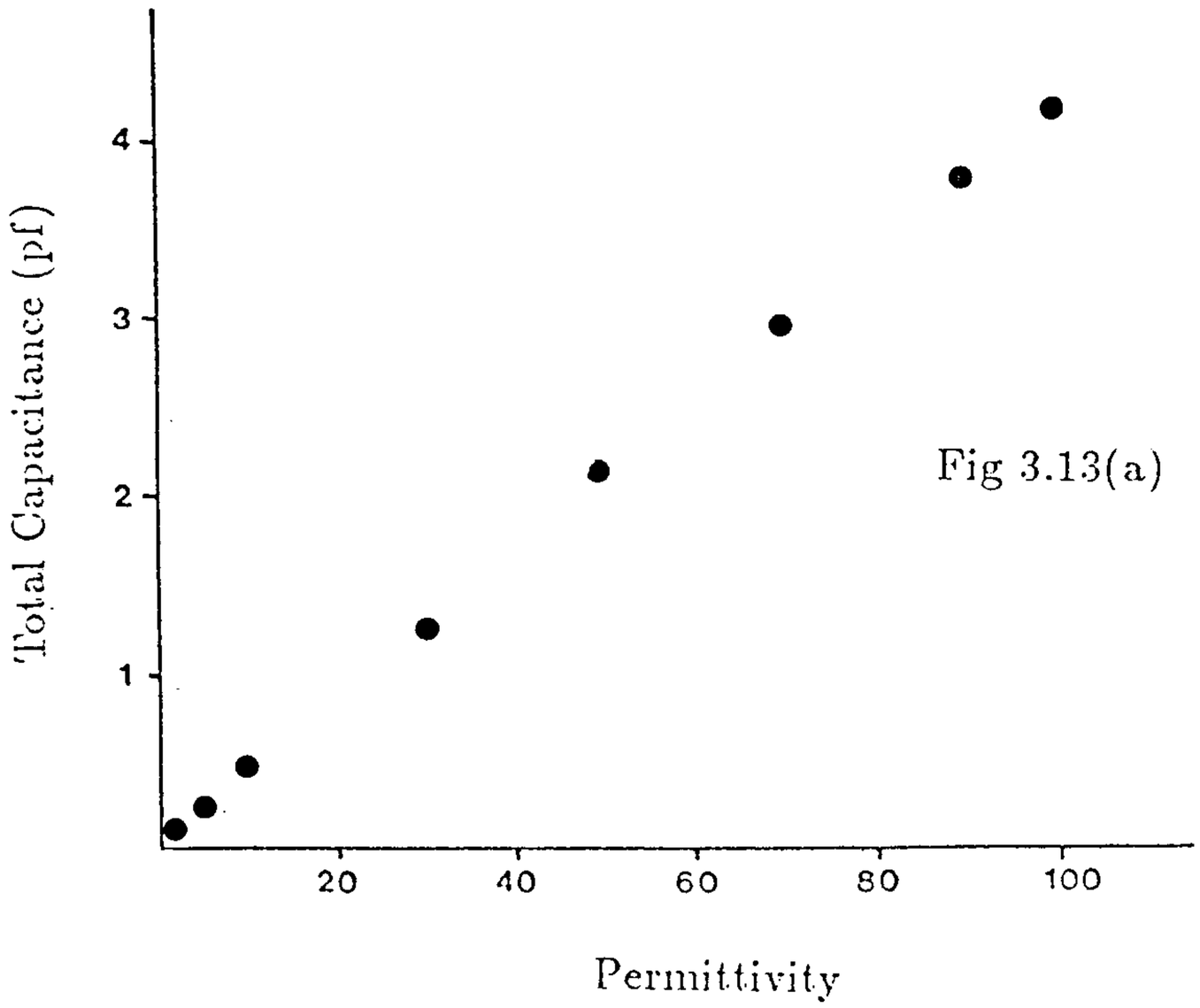

Fig 3.13(a)

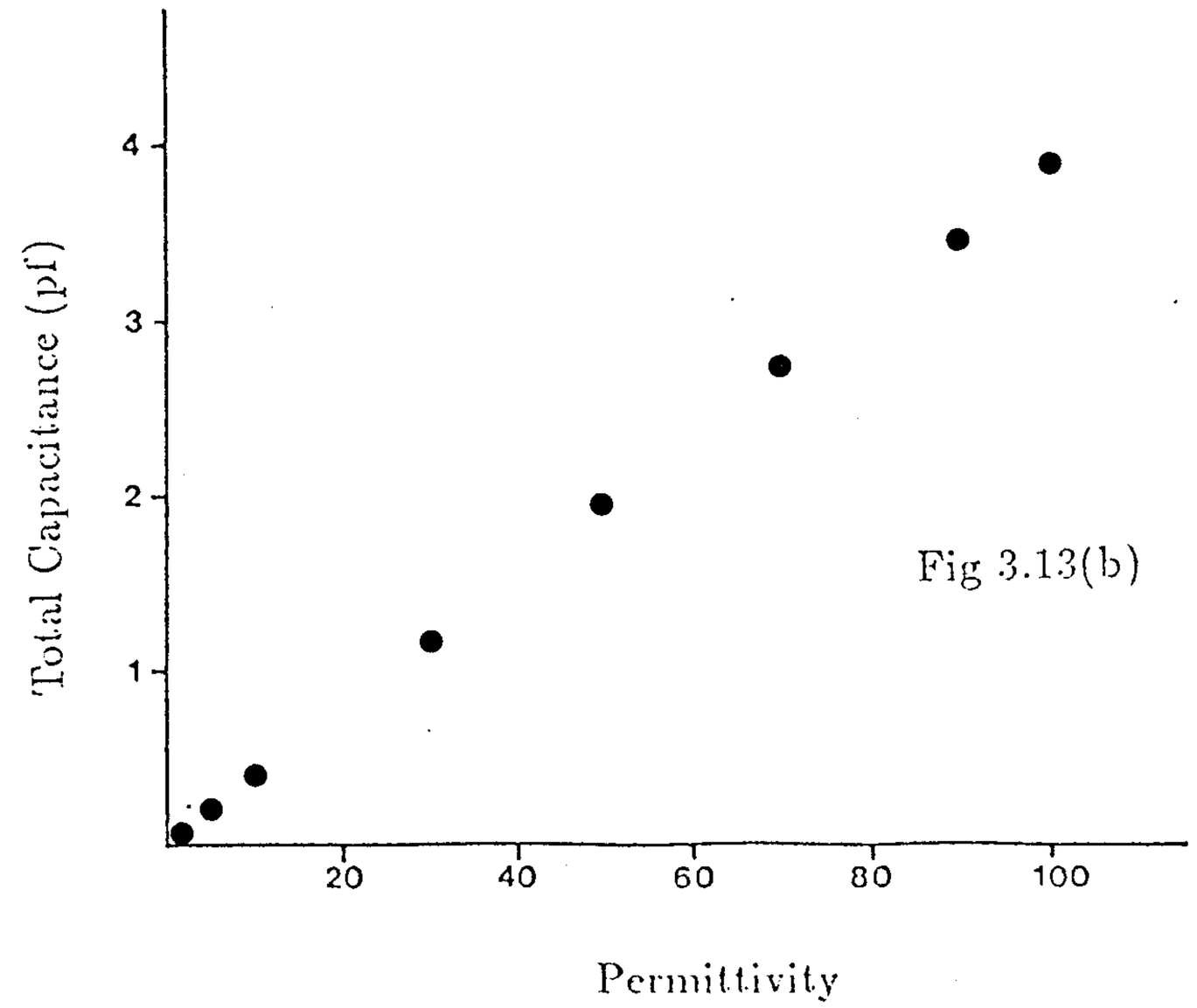

Fig 3.13(b)

Fig 3.13 Total capacitance plotted against permittivity for a teflon filled line without a groundplane.
(a) Finite Element with N=2 and 1500 nodes.
(b) Method of Moments with 100 subsections.

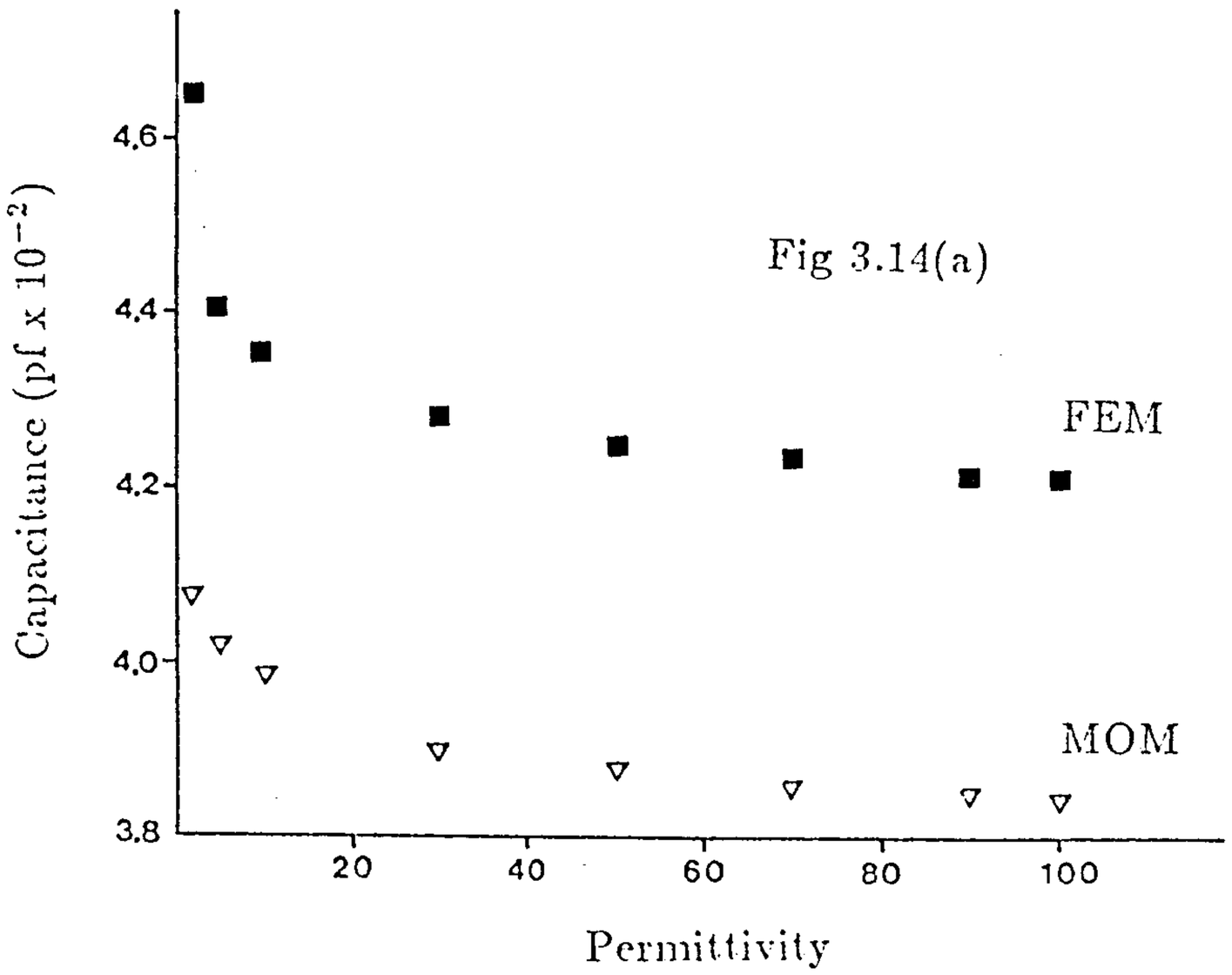

Fig 3.14(a)

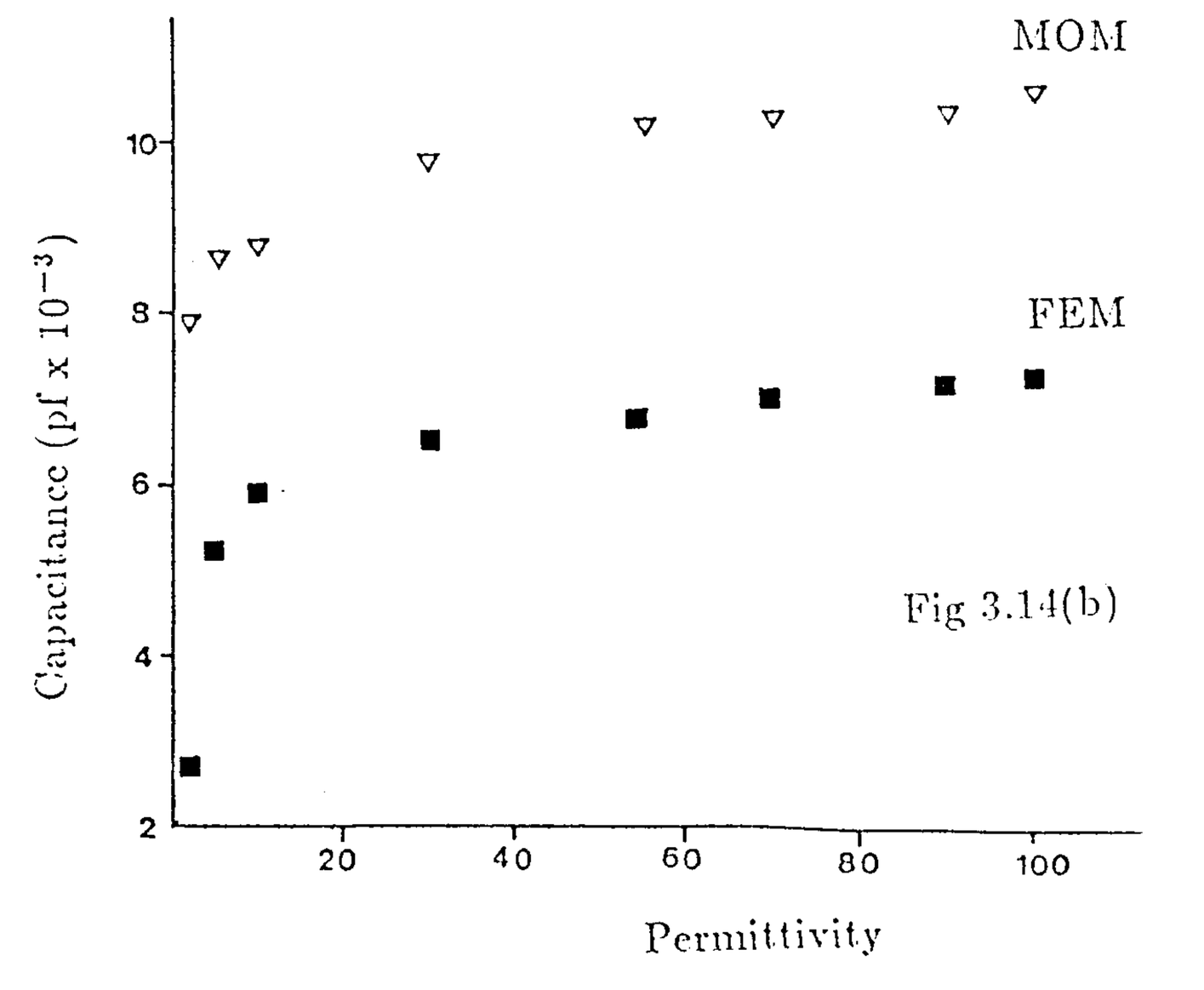

Fig 3.14(b)

Fig 3.14 C_o and C_f plotted against permittivity for a teflon filled line without a groundplane.
(a) C_o
(b) C_f

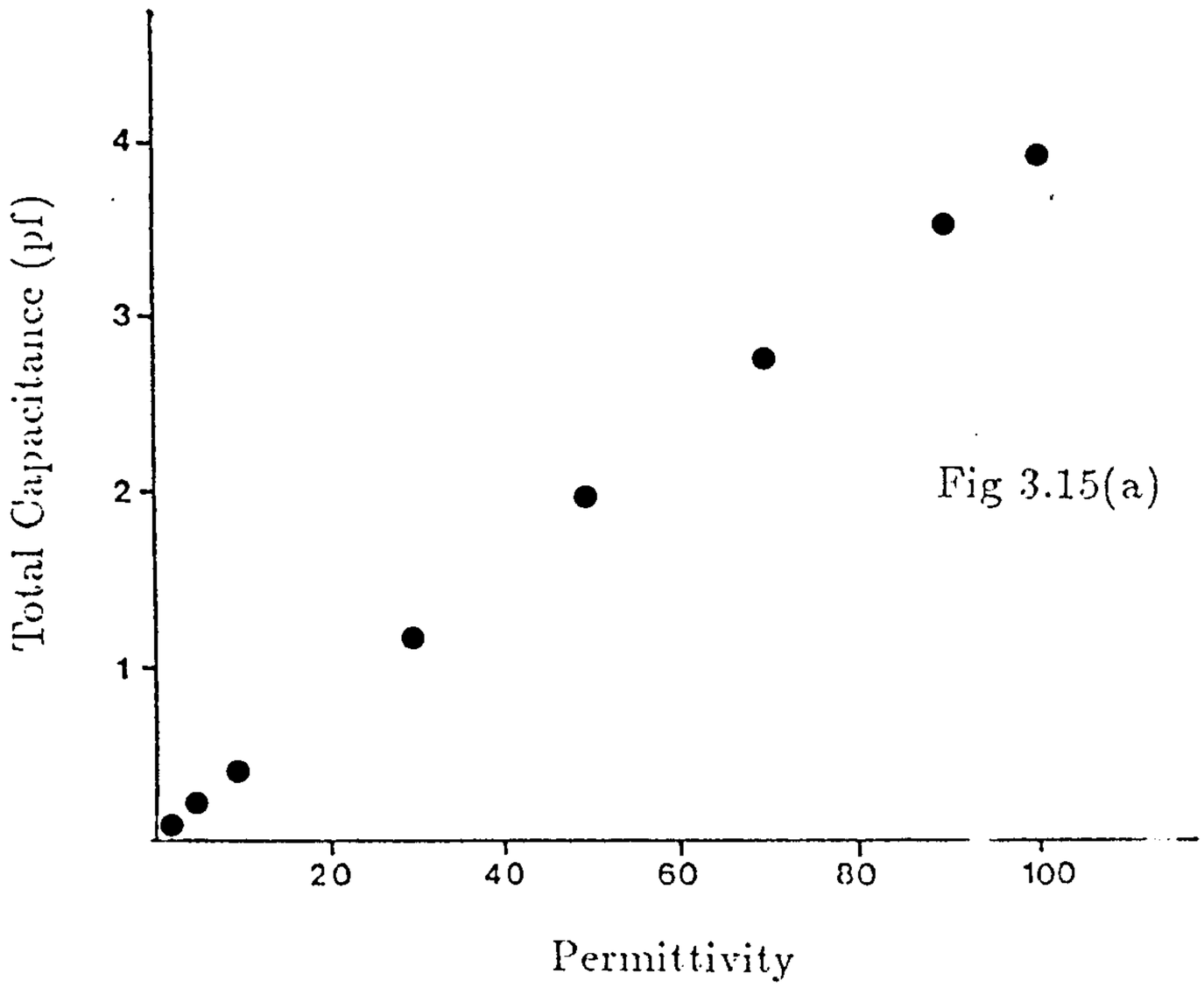

Fig 3.15(a)

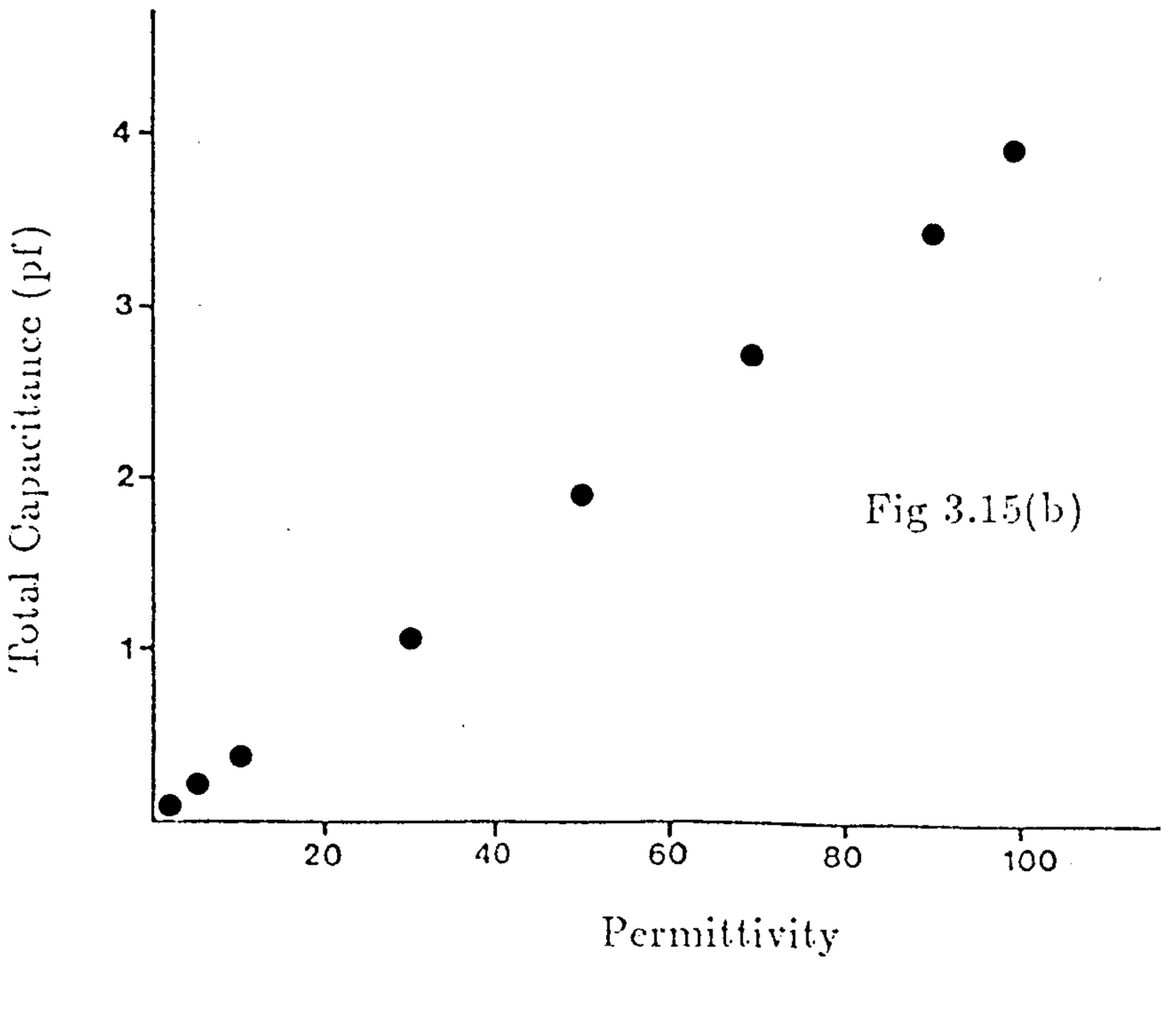

Fig 3.15(b)

Fig 3.15 Total capacitance plotted against permittivity for a teflon filled line without a groundplane.
(a) Finite Element with N=2 and 1500 nodes.
(b) Method of Moments with 100 subsections.

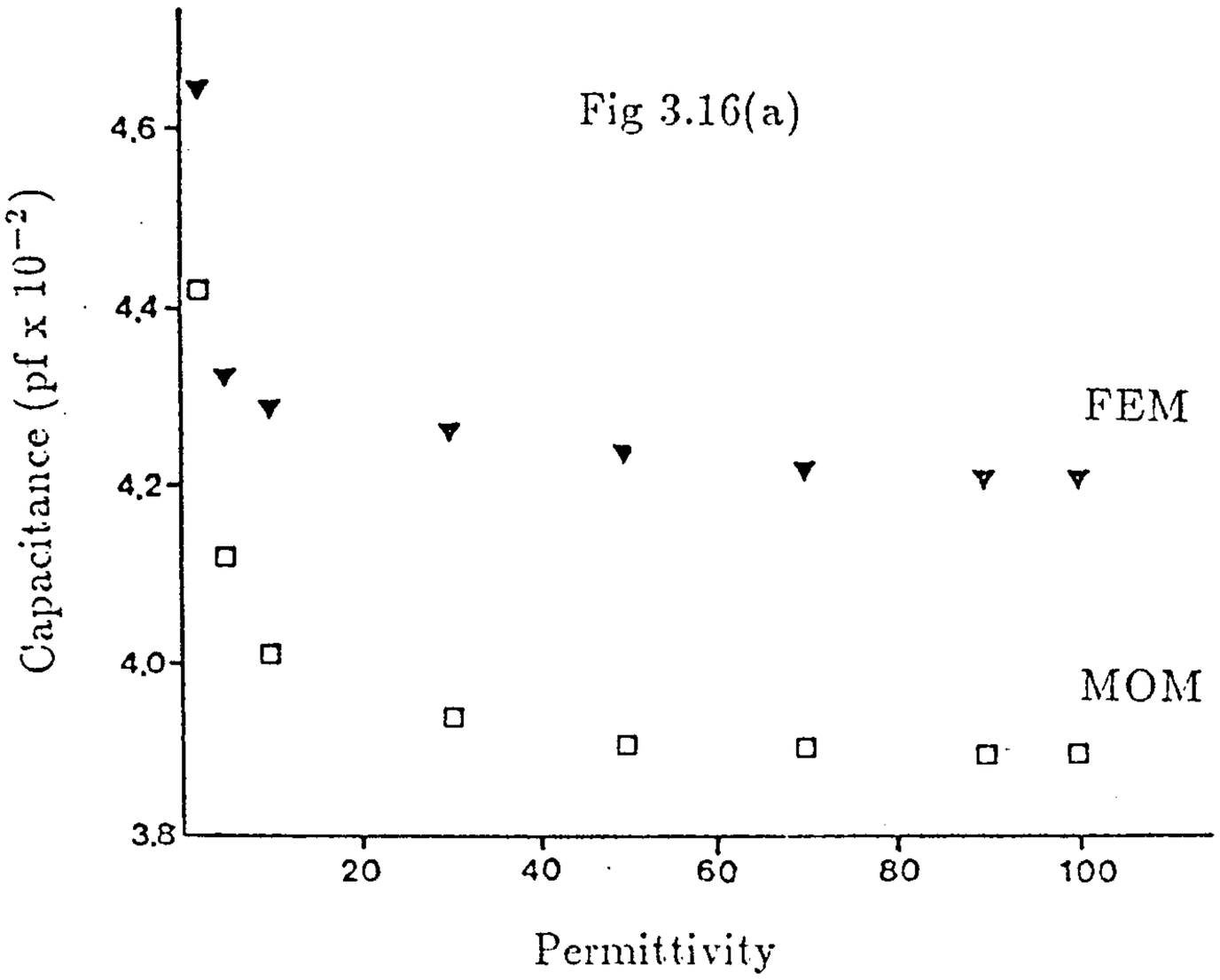

Fig 3.16(a)

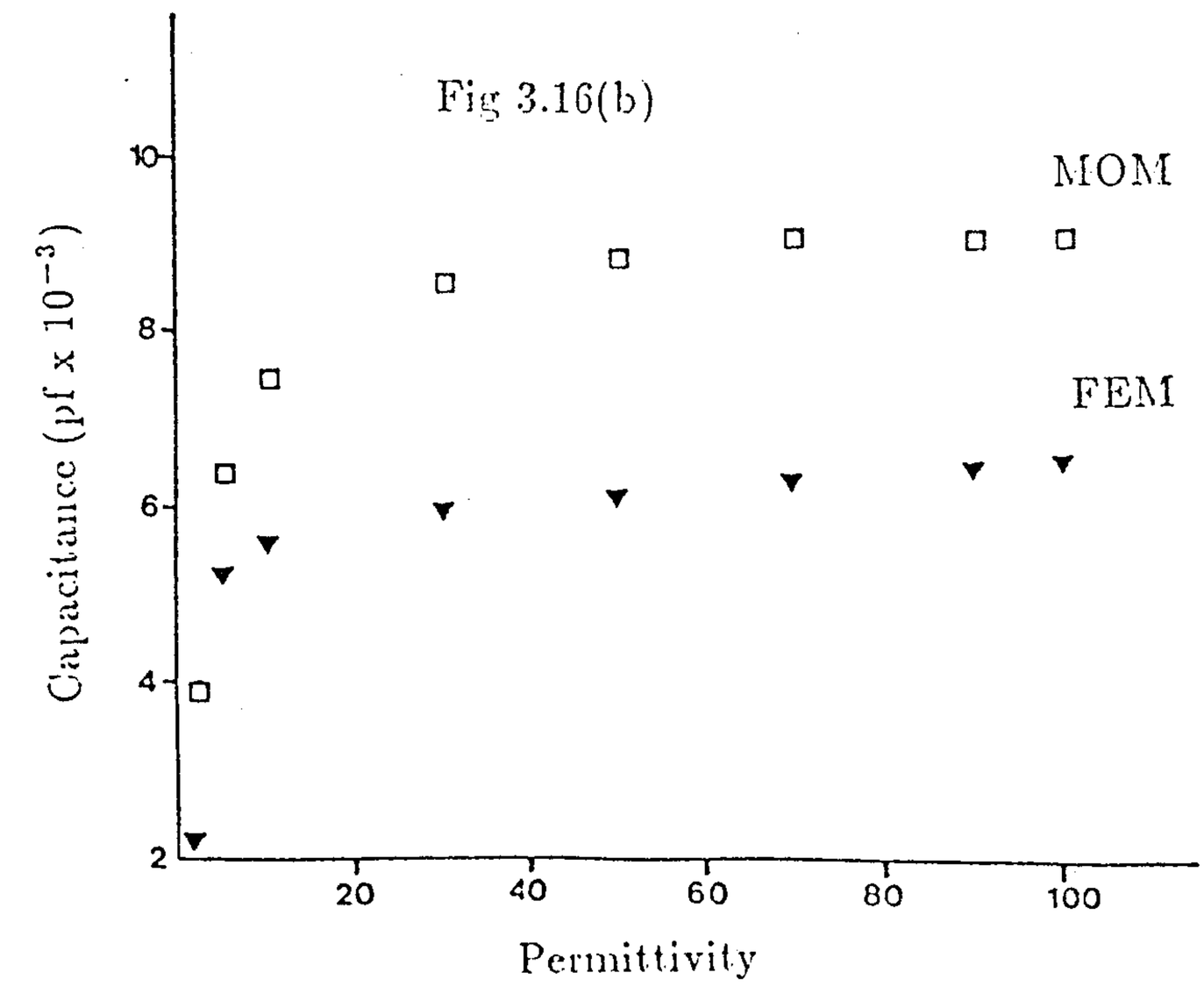

Fig 3.16(b)

Fig 3.16 C_o and C_f plotted against permittivity for a teflon filled line without a groundplane.
(a) C_o
(b) C_f

(c) An examination of the Finite Element.

(d) A comparison of the two techniques.

From the results of both techniques the values obtained for the total capacitance with varying permittivity validates the theory for the simplified linear static approximation outlined in Chapter 1. Above a certain value for the sample permittivity, ϵ_m, the values of both C_o and C_f do not change significantly and as such the total capacitance is directly proportional to ϵ_m (Figs 3.6, 3.8, 3.13 and 3.15). However the point at which the fringe field capacitances are no longer dependent on a change in ϵ_m will also be dependent on the geometry of the probe. In order to set a value for the linear circuit model, examination of the results suggests ϵ_m should be greater than 10.

In all of the cases modelled the MOM converges rapidly when the number of subsections in the problem is increased. Above the value of 100 there is no apparent increase in the total capacitance. This would suggest that any increase in the number of subsections will only increase the computing time required with no gain in the accuracy of the calculated capacitance. In each case the values obtained for C_T and for the ratio of C_f/C_o agree with data previously published (Gajda *et al* 1983).

The results from the FEM analysis show that there is a very slow rate of convergence as the model size is increased. When the model was set at the maximum number of nodes in the problem, determined by the limitations of the computer hardware, the values for C_T and C_f/C_o are still slightly different from the MOM results although they are converging slowly towards them. This convergence is far greater when the order of the system, N, is stepped from one to two but no apparent gain is achieved when increasing N any higher. Therefore, for the computer system in present use, the number of nodes should be set at the maximum available, 1500, and the order of the system set at two.

The movement of the approximate Neumann boundary along the z axis had little effect on the capacitance after a value of 3 times the outer conductor inner radius, b, Table 3.7. This suggests that the approximation of the Dirichlet boundary by the Neumann boundary is valid provided a sufficient space is enclosed. Another solution to the problem of the boundary at infinity is that of using infinite elements. However after several discussions (Trowbridge 1987, Molinari 1987) it was decided that for the application, the technique of approximating the Dirichlet boundary was sufficiently accurate.

	$r = 1.0b$	$r = 2.0b$	$r = 3.0b$	$r = 4.0b$	$r = 5.0b$	$r = 6.0b$	$r = 7.0b$
C_T	4.2879	4.4022	4.4241	4.4242	4.4242	4.4242	4.4243

Table 3.7 : Variation of the total capacitance, C_T, by increasing the artificial Neumann boundary radius with the permittivity equal to 100. All capacitance values are in $10^{-12}F$.

The placement of the elements in the region of solution is an important issue. During the modelling of the probes the results obtained changed markedly for the

worse when the element mesh was generated with an even distribution of elements throughout the entire problem space. The ideal situation should then be a concentration of elements of small area about the aperture of the probe with the element size increasing with distance from the aperture (Fig 3.17).

To compare the two techniques the values for the airline with a groundplane and the sample permittivity set at 1 are tabulated, Table 3.8. The values obtained experimentally by Gajda (1982) (G.Exp) numerically by Gajda *et al* (1983) for the Finite Element and Method of Moments (G.FEM and G.MOM) and the theoretical value of the capacitance from Marcuvitz (1951) (Marc) are also presented.

	Marc.	G.FEM	G.MOM	G.Exp	FEM	MOM
C_T	4.9550	4.9734	4.7021	4.5221	4.7180	4.7071

Table 3.8 : Comparison of the results obtained from this study with that of a previous study (Gajda *et al* 1983). All capacitance values are in $10^{-14}F$.

The results obtained using 1500 nodes and an order of 2 correspond closely to the values generated for the MOM and to the experimental values obtained by Gajda (1982). However the theoretical value and the result of the FEM analysis of Gajda *et al* (1983) where the number of nodes was 95 and the order of the system was 1 are 6% higher. From the studies presented the reasons for this discrepancy in the latter case are evident. The number of nodes in the problem is far too small for any conclusions to be drawn in a comparison with the MOM. The value obtained from Marcuvitz (1951) is a very coarse approximation formula only to be used as a guideline as to the expected magnitude of the capacitance values.

An examination of the effects of the sample permittivity on both C_f and C_o for a 50Ω airline without a groundplane (c=3.0a) are given in Table 3.9. The values obtained for C_o using the FEM analysis are greater than those obtained from the MOM while the opposite can be said for C_f. However, theoretically any differential variational technique will yield an upper bound on the capacitance obtained and the integral technique will yield the lower bound (Collin 1960). This explains the higher values for C_o but does not contribute to an understanding of the values obtained for C_f. It has been said (Gajda 1982) that the higher values for C_o, obtained from the FEM, cannot be used as the upper limit for the capacitance due to the approximating boundary. The values obtained by the FEM technique in this study can be seen to decrease as the order and the number of nodes are increased, with no effect if the boundary is increased in radius. It can therefore be concluded that by progressively stepping up the number of elements in the problem, while encompassing a large area of the region of solution, the true value of the upper limit of the external capacitance will become increasingly likely.

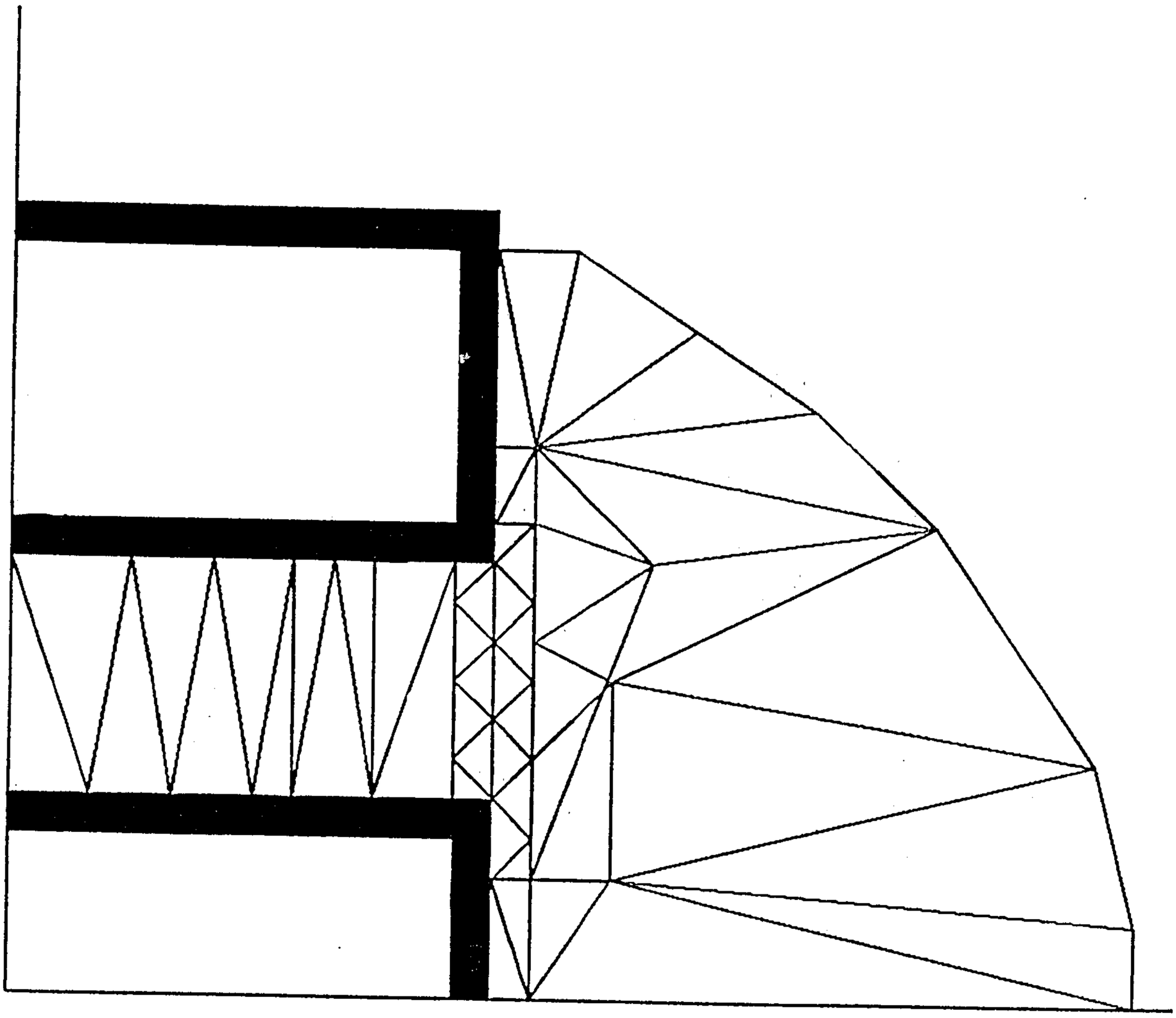

Fig 3.17 Distribution of elements in the ideal situation.

	FEM		MOM	
ϵ_m	C_o	C_f	C_o	C_f
5	4.5780	0.2145	4.3182	0.3652
10	4.4690	0.2362	4.2819	0.4023
30	4.4470	0.2580	4.2522	0.4312
50	4.4393	0.2666	4.2456	0.4378
70	4.4357	0.2702	4.2427	0.4407
90	4.4288	0.2771	4.2411	0.4423
100	4.4241	0.2818	4.2405	0.4429

Table 3.9 : Variation of the fringe field capacitances, C_o and C_f, with increasing permittivity for a 50Ω airline without a groundplane. All capacitance values are in $10^{-14}F$.

The higher values for C_f in the MOM was thought to be due to a combination of two reasons. The use of images in the MOM may increase the error in the calculated value of the charge densities (Gadja 1982). This is not the case as the charge densities found on the conductor subsections are those found theoretically for an infinite line (King 1955, Stuchly 1979). The second reason is that in using the FEM model the number of nodes placed inside the line is not sufficient for a true value to be obtained. In order to verify the latter theory the probe of section 3.3.2 was modelled with the number of nodes inside the line increased from 50 to 300 while ϵ_m was set at 80 and 100. As can be seen from Table 3.10 the results are increasing but are still less than those obtained by the MOM. This indicates that the number of nodes inside the line should be increased to a maximum possible value for the true limit on the internal capacitance to be found.

	Number of Nodes					
ϵ_m	50	100	150	200	250	300
70	0.2901	0.2980	0.3130	0.3424	0.3522	0.3800
100	0.2908	0.3108	0.3201	0.3365	0.3612	0.3875

Table 3.10 : Variation of the C_f due to an increase in the number of nodes inside the line. All capacitance values are in $10^{-14}F$.

One point of interest that has not been discussed is the ease with which each technique can be used and the relative time taken to run each simulation. The generation of both the models takes approximately 5 to 10 minutes due to the two programs, MESHIN and SURFACE. However the MOM set of programs takes much longer to run than the FEM, this time being about 9 times greater for a 100 subsection model in the MOM than for a 1500 $N = 2$ FEM simulation. As a result there is a slight trade off between the time taken for the solution to converge to its true value and the computer time to perform the task.

To conclude, the results obtained from the two techniques are in agreement with the linear model. However with an increase in computer resources the FEM

may be stepped to a size where the results obtained will yield the true upper bound for the capacitances C_o and C_f. It is believed that the values obtained from the MOM are a true indication of the lower bound for the capacitance as any increase in the size of model has little effect on the computed values of the charge densities and the associated capacitance values. With these points in mind the models to be run in future will be 1500 nodes in size with N=2 for the FEM and the number of subsections in the model set at 90 to 100 for the MOM, the latter depending on the geometry of the probe.

3.4 The Determination of Novel Probe Capacitances

3.4.1 A 0.5 mm Inner Radius Teflon Probe

In order to make measurements at high frequencies the probe dimensions must be small compared with the wavelength of propagation. The configuration for such a probe is shown in Fig 3.18. The inner to outer conductor radius ratio was set at 3.27 with a equal to 0.5 mm while the outer conductor outer radius was equal to $3.95a$ (Gabriel et al 1989).

The MOM solution was modelled using 90 subsections over a range of sample permittivity values while the FEM model was configured with 1500 nodes and N equal to 2. All experimental results are from Gabriel (1987).

From the results printed in Table 3.11 the value of C_o ranges from an average value of 0.01794 pf for the MOM to 0.0195 pf for the FEM. It is apparent that above a permittivity of 10 there is no significant variation in the values of C_o and C_f.

	FEM		MOM	
ϵ_m	C_o	C_f	C_o	C_f
5	2.0533	0.1909	1.8732	0.4043
10	1.9861	0.2362	1.8085	0.4777
30	1.9666	0.2559	1.7965	0.4909
50	1.9531	0.2693	1.7934	0.4944
70	1.9472	0.2753	1.7918	0.4962
90	1.9432	0.2793	1.7881	0.5004
100	1.9401	0.2833	1.7853	0.5036

Table 3.11 : Variation of the fringe field capacitances, C_o and C_f, with increasing permittivity for a teflon filled line with inner conductor radius equal to 0.5mm. All capacitance values are in $10^{-14}F$.

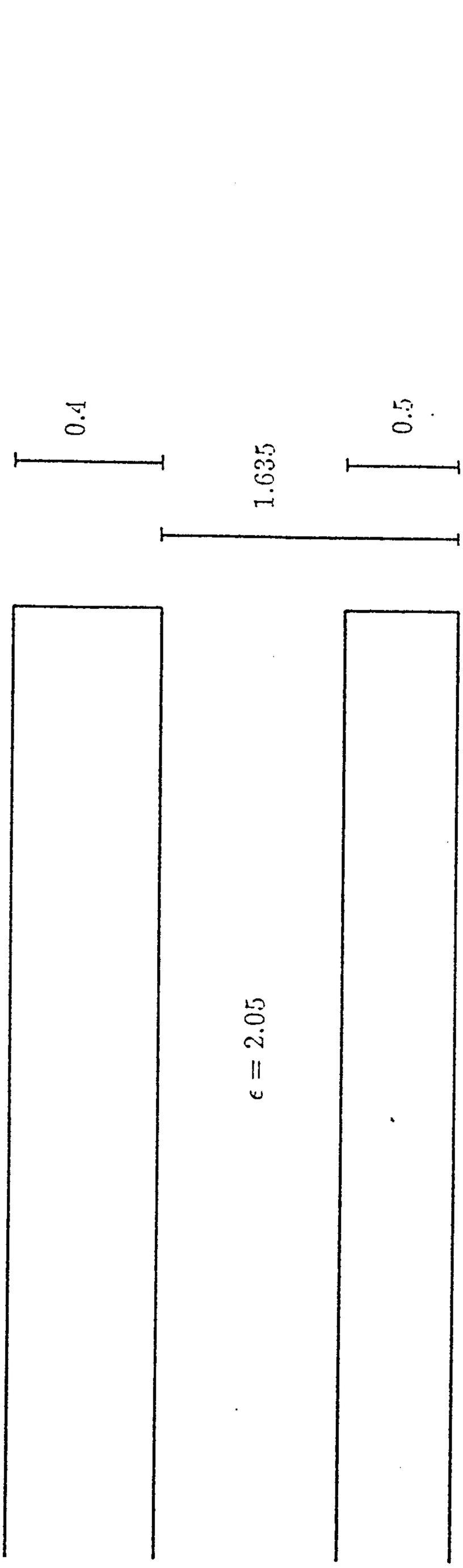

Fig 3.18 A 0.5mm inner radius teflon filled probe.

If the calculated values are taken as the limits of the capacitance the value obtained experimentally, 0.017 pf, is low. This may be explained in two ways. Firstly the simulation is run under absolutely perfect conditions. That is, the dimensions of the probe constructed may drift due to the errors introduced in the manufacture by both man and machine. Secondly the probe measured is vulnerable to experimental wear and tear which cannot be accounted for in a two dimensional model. This error can be influenced by scratches on the face of the probe or the teflon. However without taking these details into account the magnitude of the capacitance calculated deviates form the experimental less than 10%.

3.4.2 The Analysis of a Conical Probe

Although the results of the preliminary analysis suggest that the number of subsections can be set at a value of around 100 the structure of the conical probe, Fig 3.19, was thought to be too complex in nature for an accurate model to be formed. As a result the maximum number of subsections allowable by the system, 170, was used to obtain the results from the MOM and 1500 nodes with the polynomial set at N=2 was used in the FEM.

The probe, constructed and designed in the laboratory, consists of a fixed length of standard 7mm airline with a teflon filled conical section attached to it. The permittivity of the conical section was taken to be 2.05 (Gabriel 1988).

The results for the capacitances C_o and C_f are presented in Table 3.12. The model was run under the varying sample permittivity conditions. In each case, as well as the TEM capacitance, the capacitances associated with the interface at the air-teflon discontinuity have to be subtracted.

	FEM		MOM	
ϵ_m	C_o	C_f	C_o	C_f
5	26.745	1.6771	24.998	4.4413
10	26.560	2.8622	23.945	5.4941
30	25.990	3.4322	23.434	6.0051
50	25.669	3.7531	22.981	6.4587
70	25.428	3.9745	22.777	6.6622
90	24.952	4.4722	22.654	6.7853
100	24.601	4.8229	22.576	6.8654

Table 3.12 : Variation of the fringe field capacitances, C_o and C_f, with increasing permittivity for a conical probe. All capacitance values are in $10^{-14}F$.

All dimensions are in millimeters

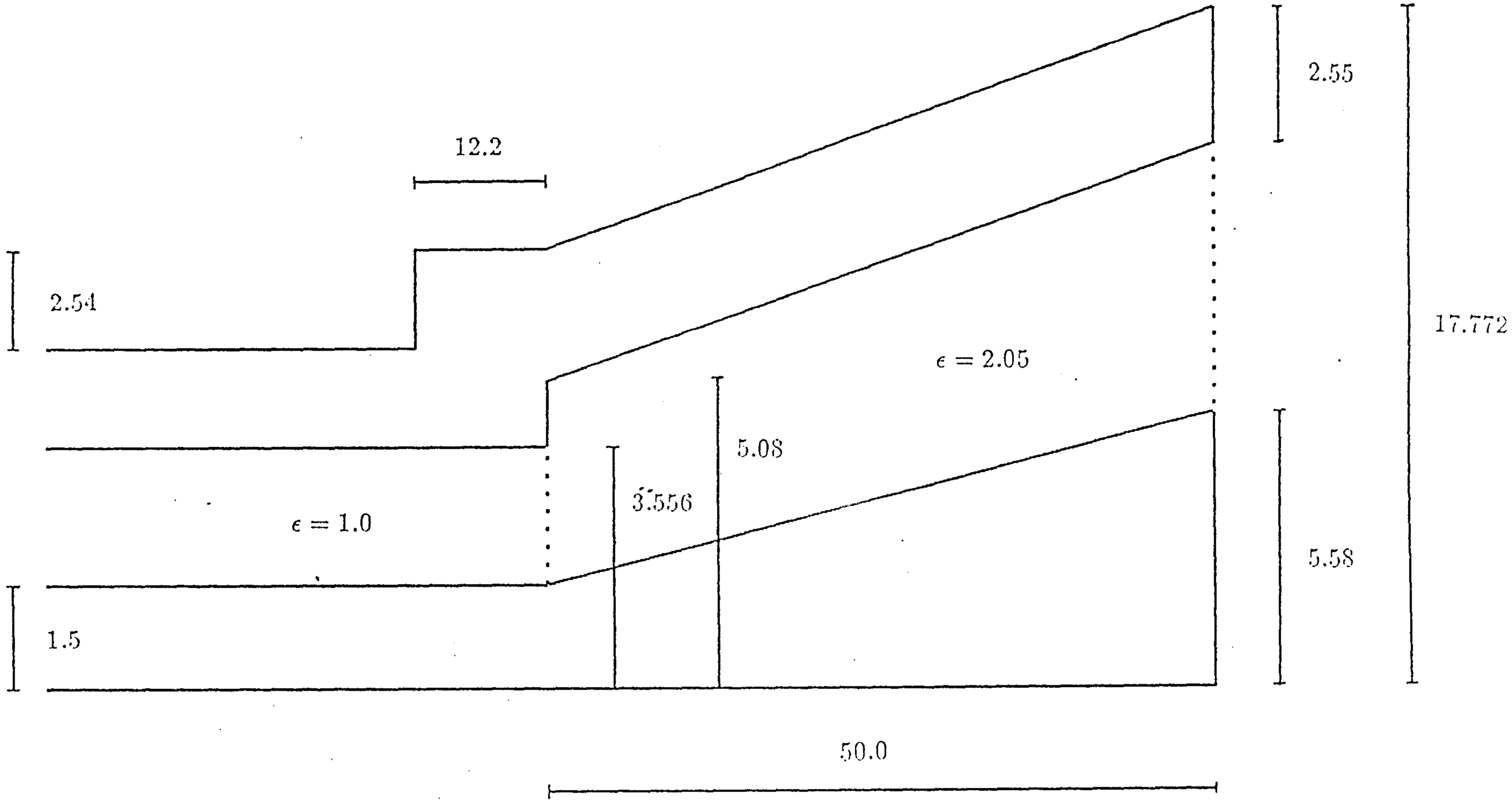

Fig 3.19 The dimension of a conical probe.

From the values obtained for the two techniques the capacitance can be seen to be a linear function of the sample permittivity. C_o varies from an average value of 0.2270 pf to 0.2550 pf as compared to the experimental value of 0.204 pf.

The results obtained are within 20% of the experimental values. This discrepancy can be attributed to the internal fringing capacitances at the air-teflon interface as these can only be approximated in any model and in the case of the FEM to the number of nodes. A more accurate method of finding these internal fringing capacitances will result in a better model for the probe. However the analysis verifies that the probe has a high C_o value and a corresponding low ratio for C_f/C_o. As C_o is high this particular probe may be used in the low frequency range.

3.4.3 The Analysis of a Probe with an Internal Discontinuity

The probe in Fig 3.20 was constructed. The probe consists of an inner conductor of fixed radius while the outer conductor inner radius encounters a change in size 4mm from the aperture opening.

The model was run with 100 subsections in the MOM and 1500 nodes with $N = 2$ for the FEM. The results of the simulation for C_o and C_f are shown in Table 3.13. Again there is a discrepancy between the experimental value, 0.056 pf, and the average values of 0.065 pf for the FEM and 0.061 pf for the MOM. The difference is around 10% in the case of the MOM while the FEM is slightly higher.

	FEM		MOM	
ϵ_m	C_o	C_f	C_o	C_f
5	7.2436	0.2115	6.2575	1.1726
10	6.8917	0.5633	6.1810	1.2498
30	6.6127	0.8426	6.1666	1.2635
50	6.5561	0.8989	6.1589	1.2712
70	6.5324	0.9226	6.1472	1.2823
90	6.5069	0.9451	6.1406	1.2892
100	6.4839	0.9711	6.1352	1.2954

Table 3.13 : Variation of the fringe field capacitances with increasing permittivity for a probe containing an internal discontiniuty. All capacitance values are in $10^{-14}F$.

The discrepancy in the FEM results can again be accounted for by the size of the model. Also the same situation exists that was discovered in the analysis of the conical probe, that is there must be a small fringing effect at the internal discontinuity.

All dimensions are in millimeters

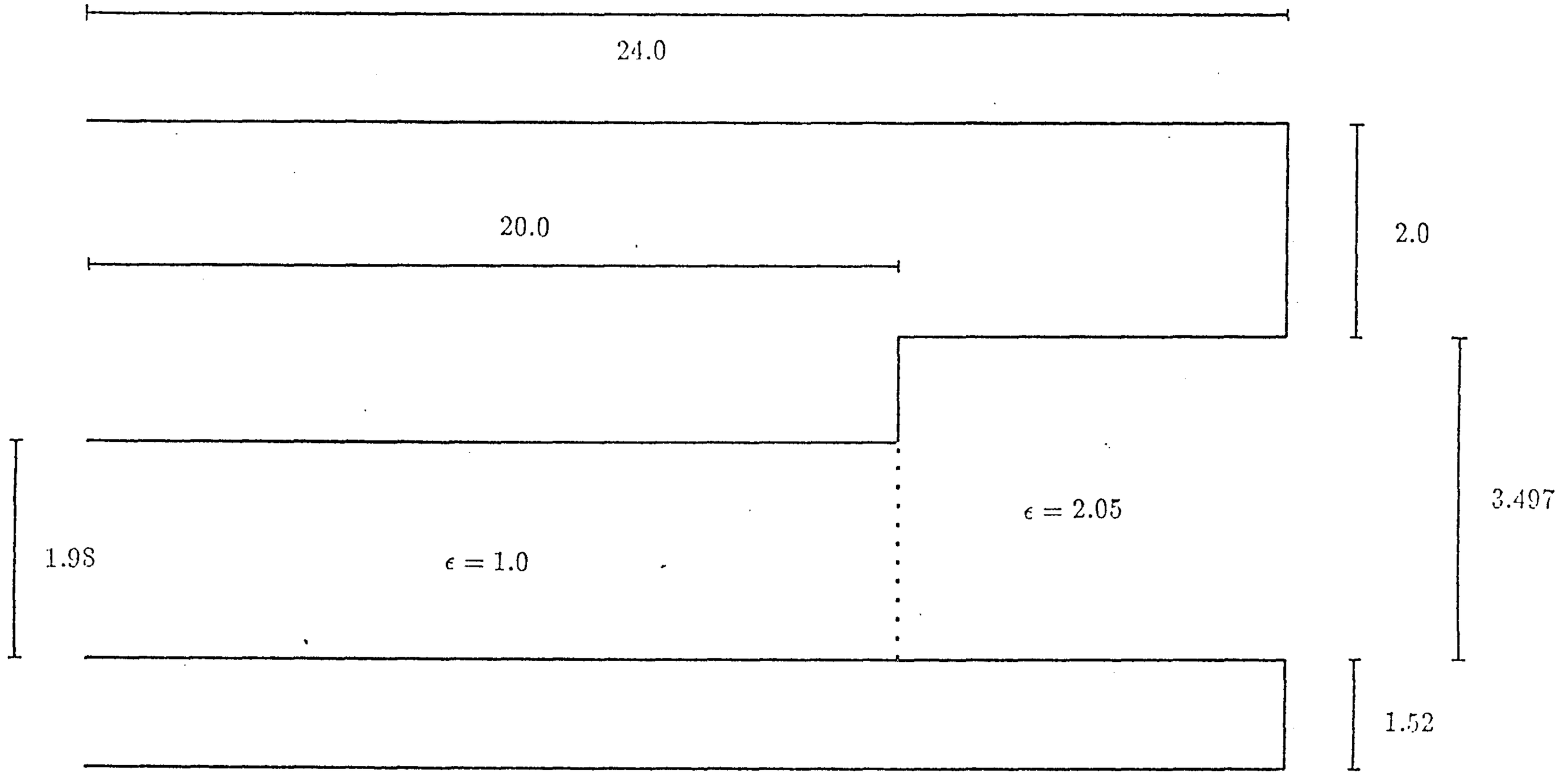

Fig 3.20 Structure of the probe with an internal discontinuity.

3.5 Summary of Chapter 3

Two techniques have been successfully applied to solve Laplace's equation for rotationally symmetric systems. The MOM solution can be thought of as the true lower bound for the capacitance values as any increase in the model dimensions has no effect on the values obtained. The FEM however needs improvement if the results are to be taken as the upper bound. This can be seen from the fact that the total capacitance is still converging towards an unknown value, the true upper limit on the capacitance, as the number of nodes in the problem is increased.

It has also been shown that there is an improvement in the results as the order of the approximating polynomial is stepped from one to two, but there is nothing more to be gained by stepping it any higher. Both programs are written in a manner that will allow the region of solution to be easily set up and consequently the only gain is in the relative run times of each simulations. With the greater accuracy in the MOM there is a trade off with the time required to obtain the solution, this being in excess of 9 times the FEM.

Both the FEM and the MOM yield results for the new designs that are higher than those found experimentally by Gabriel (1987). These differences can be attributed to three reasons. As mentioned there will be a small fringing capacitance network set up at the internal dielectric interface. As present it is difficult to distinguish this from the main dielectric interface at the aperture. Secondly the probes modelled were idealised and no variations in the actual dimensions were taken into account. Finally there will be experimental errors on the results obtained by Gabriel (1987).

As a general conclusion the two techniques used provide a very flexible design tool. New probe designs may be simulated to find the value of C_o and C_f before the construction stage resulting in a saving of both time and money. However before the probes are used in an experimental set up the values of the fringing capacitances should be found experimentally.

Chapter 4

Design and Implementation of a Time Domain Spectrometer System

4.1 Introduction

Traditionally impedance bridges and frequency domain systems have been employed in the measurement of dielectric parameters but over the past decade great interest has been aroused by time domain spectroscopy. This technique enables a much wider frequency range to be covered with a single impulse measurement.

In this chapter the design and implementation of a new time domain spectrometer is presented. The theory of time domain spectroscopy is introduced together with the principal experimental techniques adopted for the new design. The hardware and the software systems associated with the spectrometer are then described.

4.2 The Theory of Time Domain Spectroscopy

4.2.1 Definitions of $\hat{\epsilon}$ and Z_0

By examining only linear isotropic media, where the charge density is zero, it can be shown (Stratton 1941, Seshadri 1971) that the electromagnetic field equations postulated by Maxwell can be written as

$$\nabla \times E = -\mu \frac{\delta H}{\delta t} \qquad (4.1(a))$$

$$\nabla \times H = \epsilon \frac{\delta E}{\delta t} + \sigma E \qquad (4.1(b))$$

where σ is referred to as the conductivity, ϵ is the permittivity and μ is the permeability of the medium. ϵ and μ are specified in terms of a relative permittivity ϵ_r and permeability μ_r such that

$$\epsilon = \epsilon_r \epsilon_0 \qquad (4.2(a))$$

$$\mu = \mu_r \mu_0 \qquad (4.2(b))$$

where ϵ_0 and μ_0 are the free space permittivity and permeability respectively. If the E and H fields are sinusoidal in nature the derivative with respect to t may be expanded and equations 4.1(a) and 4.1(b) can be written as

$$\nabla \times E = -j\omega\mu H \qquad (4.3(a))$$

$$\nabla \times H = j\omega\hat{\epsilon}E \qquad (4.3(b))$$

where the quantity $\hat{\epsilon}$ is regarded as the effective permittivity of the medium and is a complex quantity. $\hat{\epsilon}$ may be written as

$$\begin{aligned}\hat{\epsilon} &= \epsilon_0[\epsilon_r - \frac{j\sigma}{\omega\epsilon_0}] \\ &= \epsilon_0[\epsilon' - j\epsilon'']\end{aligned} \qquad (4.4)$$

where the component ϵ' is a measure of the polarisation of the medium and ϵ'' is a measure of the energy dissipated in the medium per cycle of applied field.

By noting that the principal mode of propagation in a coaxial transmission line is an axially symmetric transverse electromagnetic wave, it can be shown that solving equations 4.3(a) and 4.3(b) for a cylindrical coordinate system, r, z and θ, will give the characteristic impedance of the line as (Seshadri 1971)

$$Z_0 = \frac{\sqrt{\mu}}{2\pi\sqrt{\hat{\epsilon}}} ln(a/b) \qquad (4.5)$$

where a and b represent the inner and outer conductor radii respectively.

4.2.2 Reflections and Transmissions from a Coaxial Line Discontinuity

If a TEM wave propagating along a coaxial line encounters a change in the characteristic impedance of the line due to some discontinuity, part of the wave will be reflected and part will be transmitted. By applying basic circuit theory it can be shown that (Seshadri 1971)

$$V^+ = \frac{2Z_2}{Z_2 + Z_1} V \qquad (4.6(a))$$

$$V^- = \frac{Z_2 - Z_1}{Z_2 + Z_1} V \qquad (4.6(b))$$

where V^+ is the amplitude of the transmitted wave, V^- is the amplitude of reflected wave, Z_1 is the characteristic impedance before the discontinuity and Z_2 is the characteristic impedance after the discontinuity, Fig 4.1. The reflection coefficient ρ_{12} and the transmission coefficient τ_{12} can then be defined as

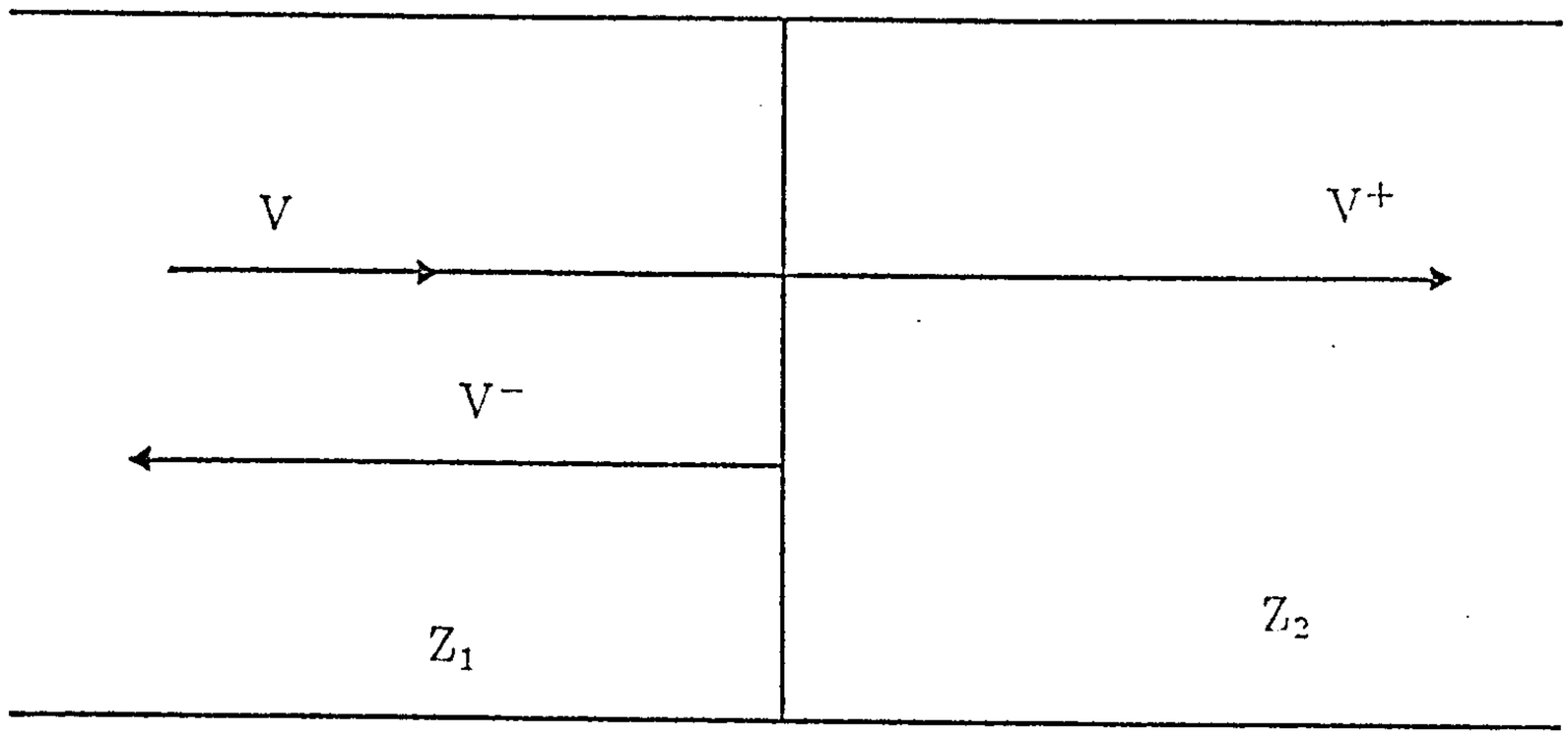

Fig 4.1 Reflection and transmission from a discontinuity.

$$\rho_{12} = \frac{V^-}{V} = \frac{Z_2 - Z_1}{Z_2 + Z_1} \tag{4.7}$$

and

$$\tau_{12} = \frac{V^+}{V} = \frac{2Z_2}{Z_2 + Z_1} \tag{4.8}$$

where the suffices of ρ and τ denote the direction of travel of the wave.

From equations 4.7 and 4.8 it is easily shown

$$\tau_{12} = 1 + \rho_{12} \tag{4.9}$$

By a similar analysis the reflection and transmission coefficients for a wave travelling in the opposite direction, ρ_{21} and τ_{21}, can be found and may be expressed in terms of ρ_{12} and τ_{12} by

$$\rho_{21} = -\rho_{12} \tag{4.10(a)}$$

$$\tau_{21}\tau_{12} = 1 - \rho_{12}^2 \tag{4.10(b)}$$

If the case is considered where the characteristic impedance of a coaxial line, Z_0, is changed by inserting a sample of impedance Z_s, the incident wave will undergo multiple reflections and transmissions, Fig 4.2. By equating the resulting system to a two port network it can be shown that

$$V^- = S_{11}V \tag{4.11(a)}$$

$$V^+ = S_{21}V \tag{4.11(b)}$$

where S_{11} and S_{21} are referred to as the scattering coefficients of the system and are given by the sum of all reflections and transmissions undergone by the incident wave.

With reference to Fig 4.3 it can be shown that in the general case, when a sample of length l and propagation constant γ_s is inserted into a coaxial line of propagation constant γ_0,

$$V_2 = (1 - \rho_{12})V - \rho_{12}V_3 e^{-\gamma_s l} \tag{4.12(a)}$$

$$V_3 = \rho_{23}V_2 e^{-\gamma_s l} \tag{4.12(b)}$$

$$V^- = \rho_{12}V + (1 + \rho_{12})V_3 e^{-\gamma_s l} \tag{4.12(c)}$$

Upon substitution of equations 4.12(a) and 4.12(b) into equation 4.12(c)

$$S_{11} = \frac{\rho_{12}(1 - e^{-2\gamma_s l})}{1 - \rho_{12}^2 e^{-2\gamma_s l}} \tag{4.13}$$

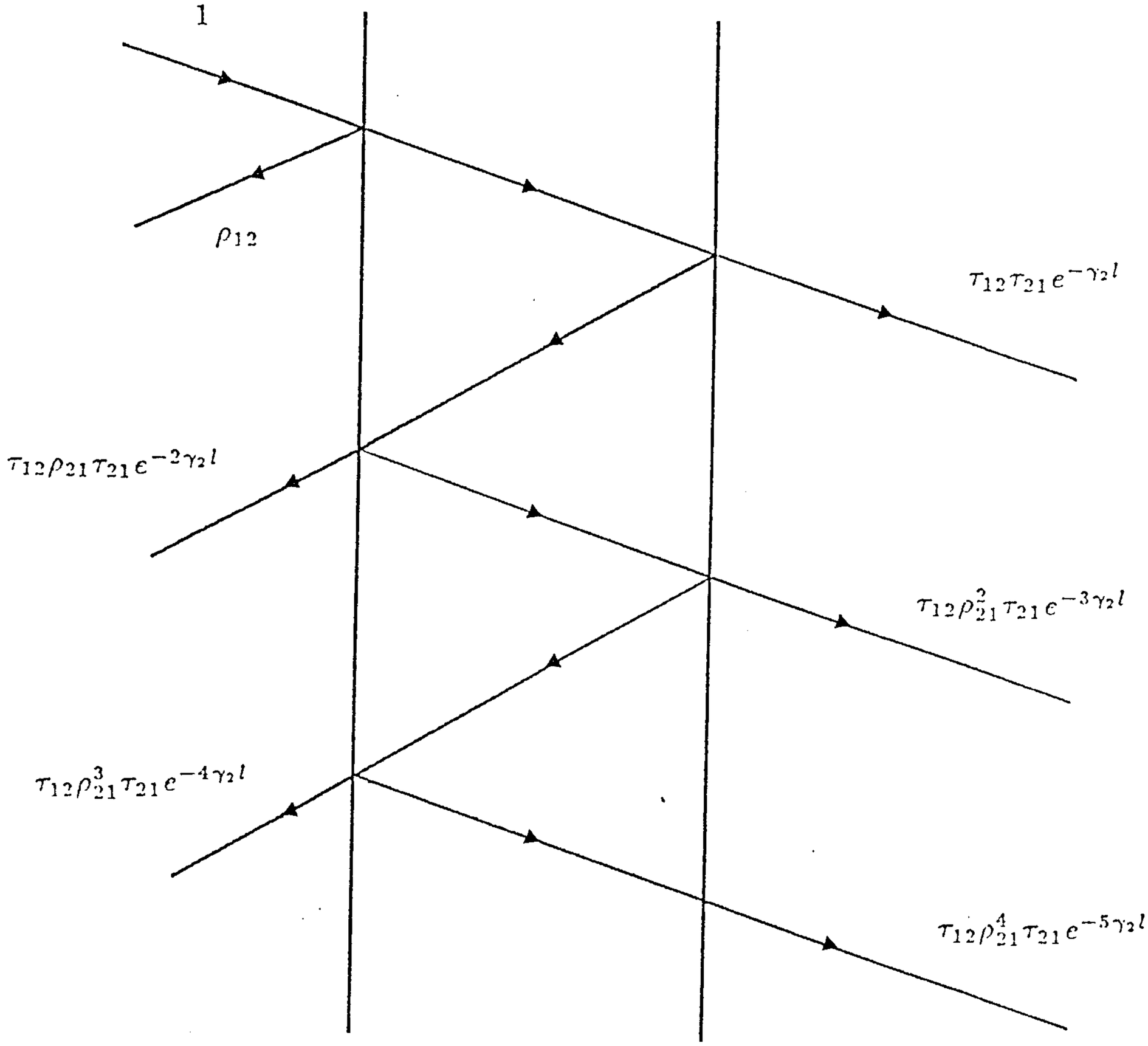

Fig 4.2 Reflections and transmissions at a dielectric interface due to insertion of sample with propagation constant γ_s.

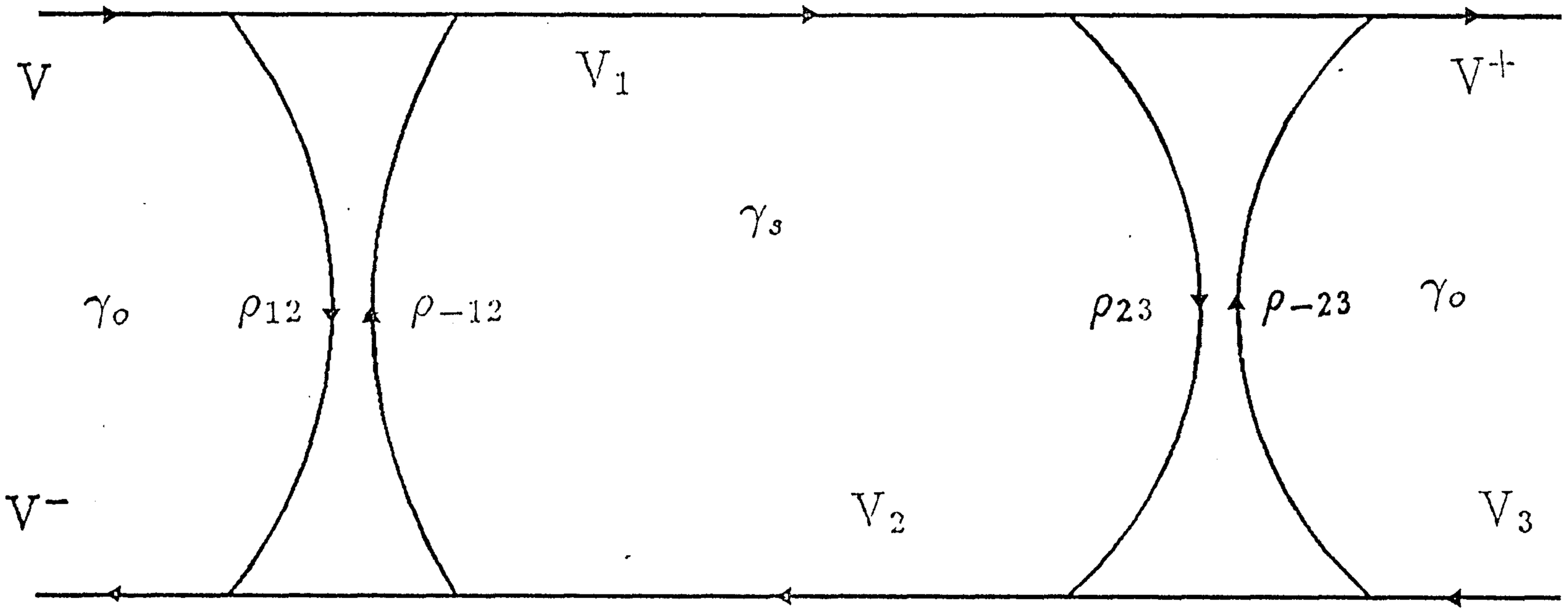

Fig 4.3 General reflection and transmission model.

By treating V^+ and V_4 in a similar manner it can be shown

$$S_{21} = \frac{(1-\rho_{12}^2)e^{-\gamma_s l}}{1-\rho_{12}^2 e^{-2\gamma_s l}} \tag{4.14}$$

where (Seshadri 1971)

$$\gamma_s = j\frac{\omega}{c}\sqrt{\hat{\epsilon}}(\omega) \tag{4.15}$$

c is the velocity of light in free space. Upon substitution of equation 4.5 into equation 4.7, assuming the relative permeability is one,

$$\rho_{12} = \frac{\sqrt{\hat{\epsilon}_1} - \sqrt{\hat{\epsilon}_2}}{\sqrt{\hat{\epsilon}_1} + \sqrt{\hat{\epsilon}_2}} \tag{4.16}$$

The complex permittivity may then be found from the S parameters of the system.

4.2.3 Transfer Function of Linear Systems

Let $v(t)$ and $r(t)$ be the input and output signals from a simple system. If the system is said to be linear and time invariant the output signal is related to the input by the convolution equation (Schwartz 1976)

$$\begin{aligned} r(t) &= \int_{-\infty}^{t} v(t-t_1)h(t_1)dt_1 \\ &= v(t) * h(t) \end{aligned} \tag{4.17}$$

where h(t) is the impulse response function of the system. The convolution theorem states that the convolution of two functions in the time domain is equivalent to taking the product of their Fourier transforms such that

$$v(t) * h(t) = V(\omega)H(\omega) \tag{4.18}$$

where $V(\omega)$ and $H(\omega)$ are the Fourier transorms of $v(t)$ and $h(t)$ respectively and $V(\omega)$ is given by

$$V(\omega) = \int_{-\infty}^{\infty} v(t)e^{-j\omega t}dt \tag{4.19}$$

This allows equation 4.17 to be written as

$$R(\omega) = V(\omega)H(\omega) \tag{4.20}$$

or the system transfer function to be

$$H(\omega) = \frac{\int_{-\infty}^{\infty} r(t)e^{-j\omega t}dt}{\int_{-\infty}^{\infty} v(t)e^{-j\omega t}dt} \tag{4.21}$$

If the observed output is the totally reflected wave, the transfer function is then the scattering coefficient S_{11}.

4.2.4 Application to Time Domain Measurements

In time domain measurements the input to the medium under investigation is an aperoidic function of time, usually a step or pulse function. This input function has a fast rise time to enable the frequency range covered to be of a wide bandwidth. The response to the applied input, either a reflection or transmission, is measured until it reaches a constant value and the medium may then be characterised by firstly Fourier transforming $v(t)$ and $r(t)$ and secondly forming the transfer function of the system, $H(\omega)$, at each frequency of interest.

4.2.5 Practical Elements Involved in a Time Domain System

The basic elements involved in the construction of a time domain system are an input signal source, a transmission medium, a sample cell or coaxial line applicator, a detector, a data acquisition system and a means of processing the data (Fig 4.4).

The input signal used in time domain measurements is usually supplied by a tunnel diode generator. The fast rise-time of the pulse is achieved by biasing the diode at the correct point on its characteristic curve, point A in Fig 4.5(a). A current impulse, defined as the triggering signal, momentarily raises the operating point to point B. After this change in level it switches rapidly to point C producing a very fast change in voltage across the diode. This corresponds to the leading edge of the pulse. The current through the diode is allowed to decay to a finite value, point D, after which it will switch rapidly back to point E. The signal produced is shown in Fig 4.5(b).

The data acquisition component is usually a sampling oscilloscope which is capable of sampling the signal over a wide frequency range. The signal is built up in time as a series of sampled points, each corresponding to a single sample taken

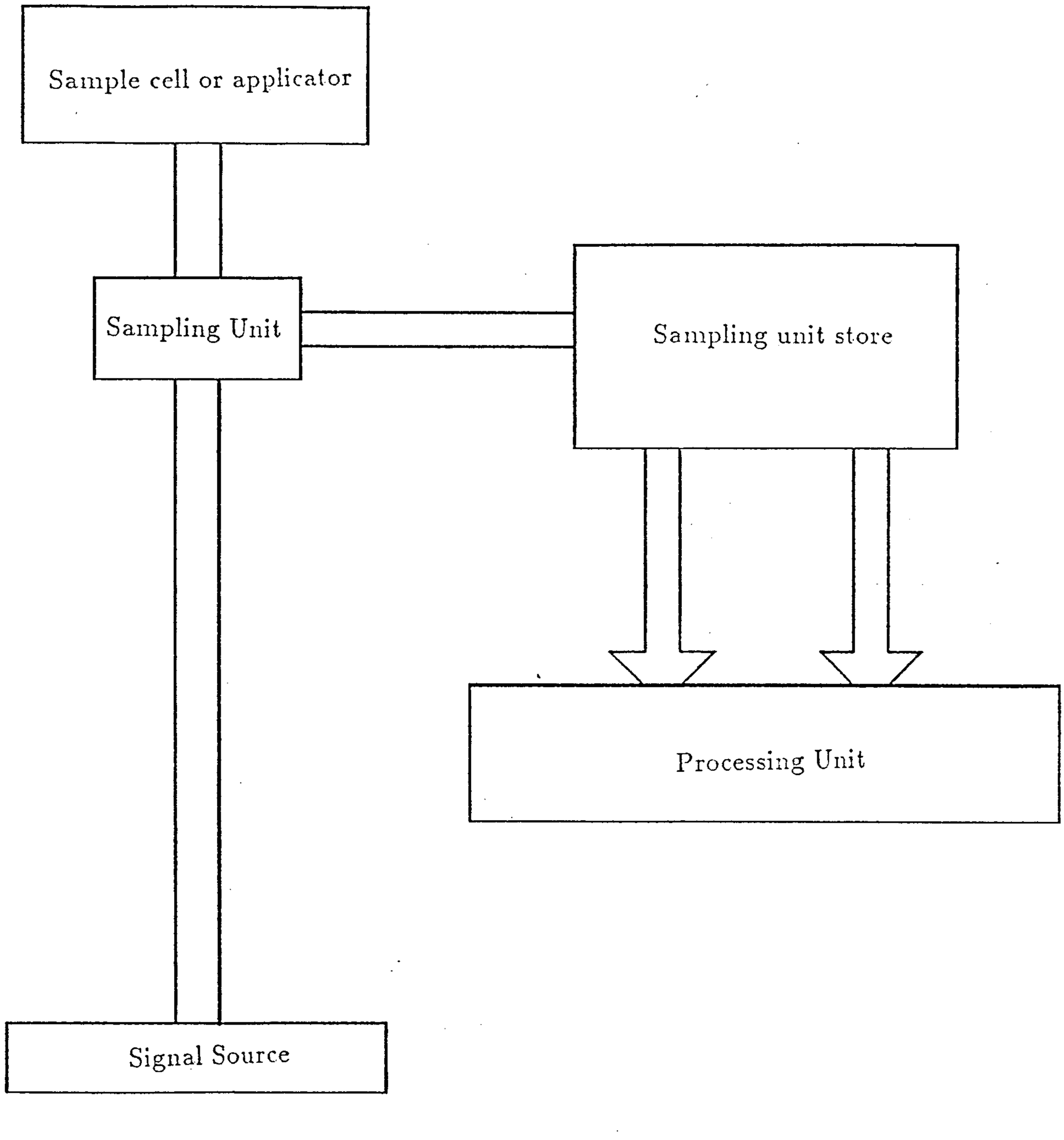

Fig 4.4 The basic structure of a Time Domain Spectrometer.

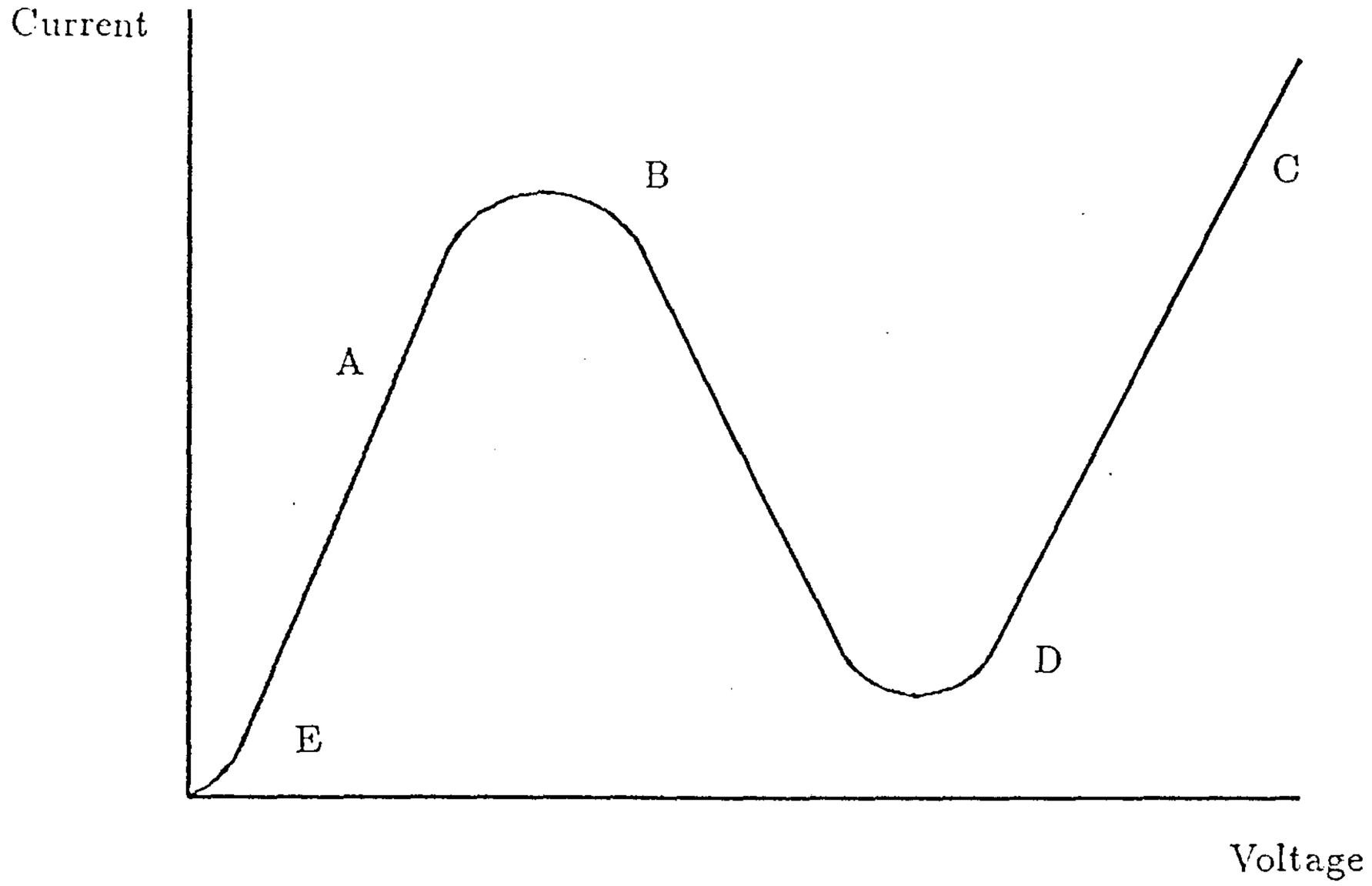

Fig 4.5(a) Characteristic curve for a tunnel diode.

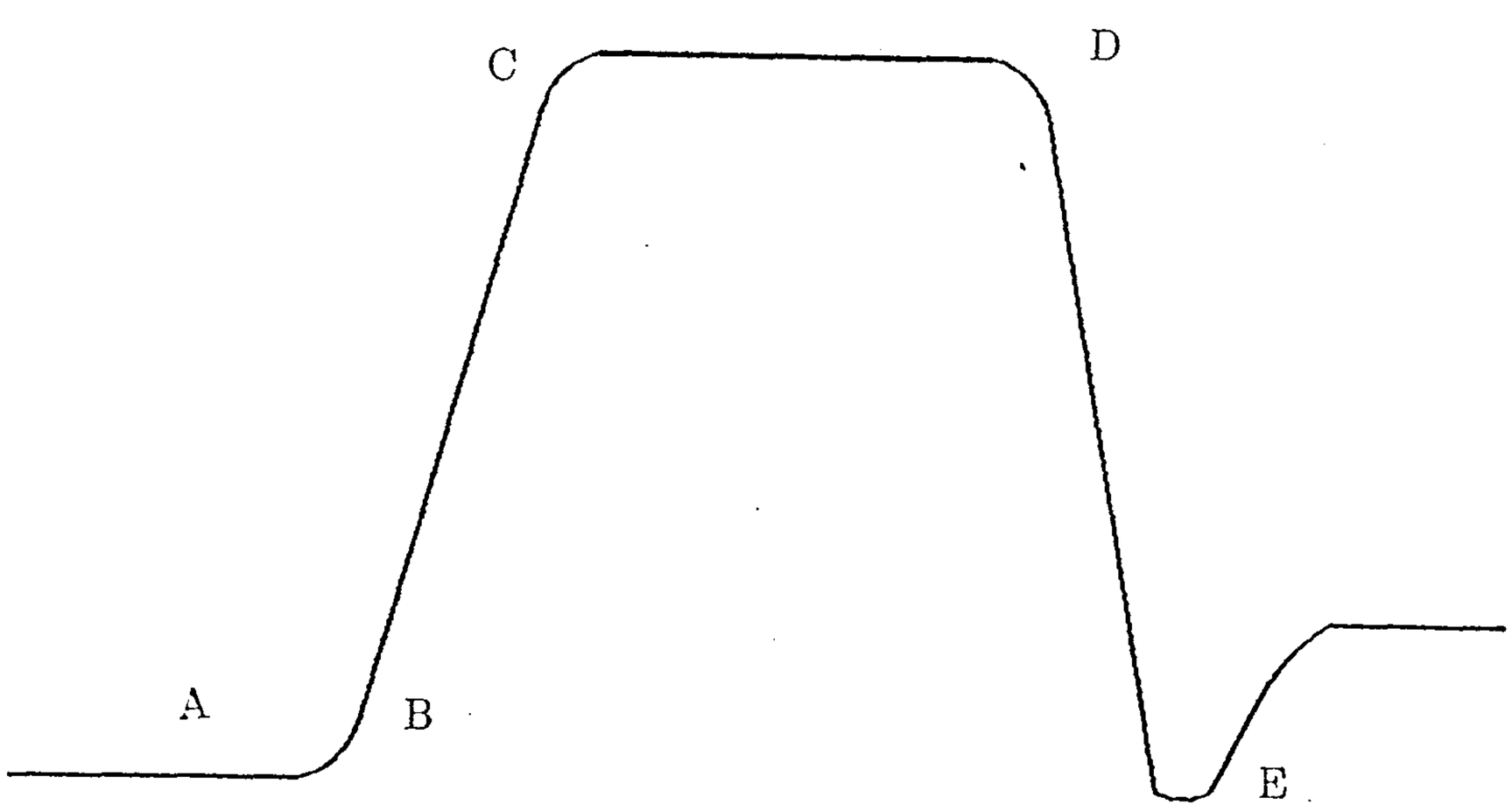

Fig 4.5(b) Typical output of a tunnel diode.

from the signal. However each of the samples is taken on separate repetitions of the signal, as shown in Fig 4.6, and the waveform is gradually constructed by stepping the sampling window along the pulse. The apparent sampling interval $\triangle t$ is determined by the sweep setting on the time base of the oscilloscope.

With the advent of relatively cheap computer hardware the processing unit is typically a small dedicated microcomputer, enabling the calculations to be carried out in real time.

4.3 Experimental Procedures Incorporated in the New TDS

There have been several time domain spectrometers developed in recent years, each adopting similar design techniques (Loeb *et al* 1971, Cole *et al* 1980, Dawkins *et al* 1979, Gestblom *et al* 1980). Several of the experimental techniques in use have been adopted in the new design and are explained in the following sections.

4.3.1 Digitization of the Waveforms

As mentioned in section 4.2.5 the data set is gradually built up over a series of waveforms. However the data must be transferred back into the processing unit and the oscilloscope must have some indication as to when the transfer is complete, enabling the next sample to be taken. This may be achieved in two ways.

The oscilloscope can be self triggering and the time taken between samples must be large enough to enable the data transfer to be completed. Although this is a simplistic approach the consequences in using it may prove costly if the time intervals between alternate samples drift slightly. This could lead to new samples being available from the oscilloscope before the transfer mechanism has successfully completed the last task, and as a result, important data points being lost in the system.

The second way involves a crude handshaking mechanism (Dawkins *et al* 1979, Gestblom *et al* 1980) where the triggering of the oscilloscope is controlled externally by the dedicated microcomputer. After capturing the sample the oscilloscope waits for a pulse from the transfer hardware before it samples the waveform, the scanning rate voltage, the X voltage, of the sampling oscilloscope being controlled by the transfer mechanism. The actual cycle may be characterised by Fig 4.7. The transfer hardware sends trigger pulses until the flyback is detected, region A. After detection 1200 samples are captured, the oscilloscope being stepped after each successful data transfer (region B). The data set representing the waveform is then transferred into main memory and manipulated, region C and the cycle is then repeated by looking for the flyback.

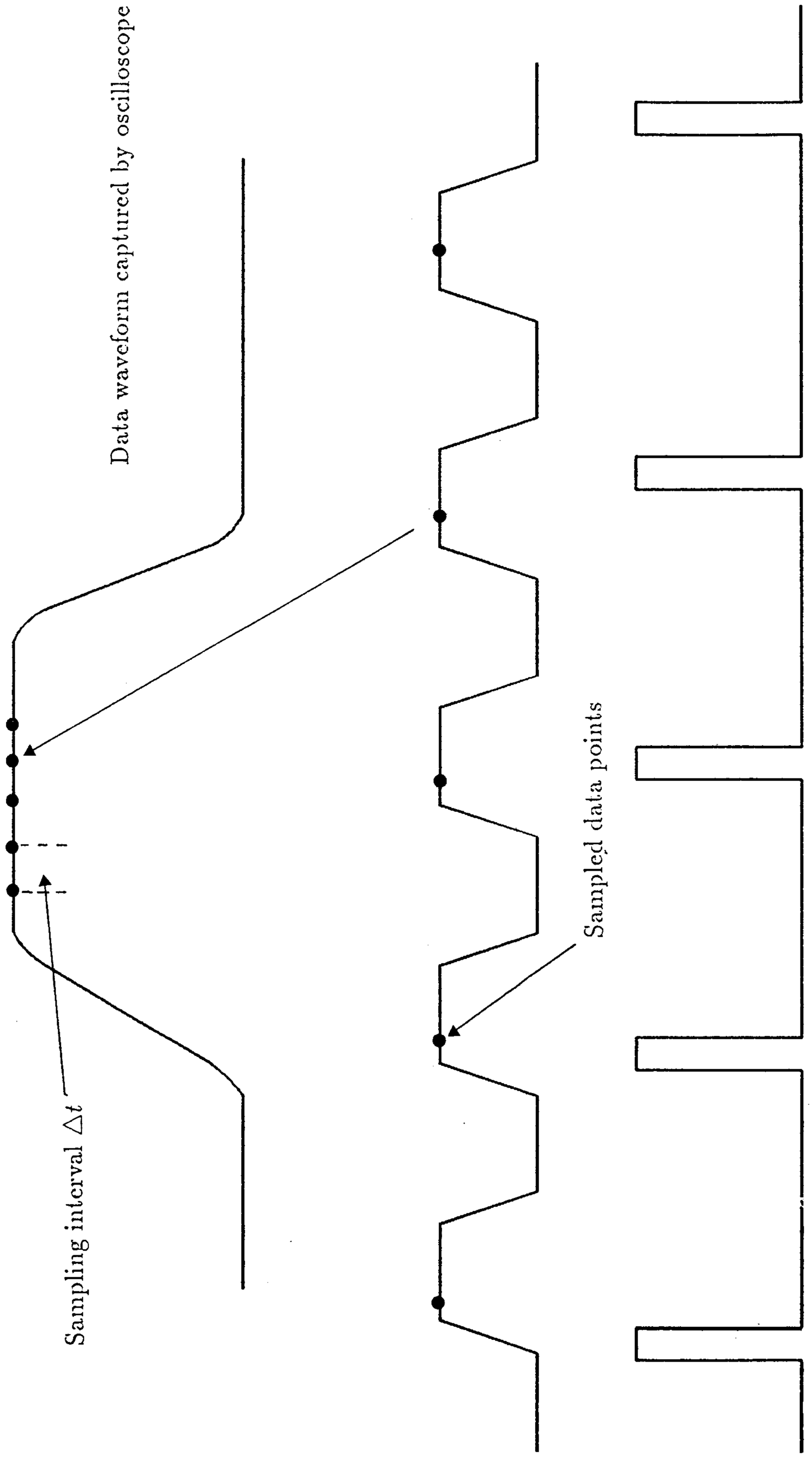

Fig 4.6 Capture of the data waveform by repeatedly sampling the main signal.

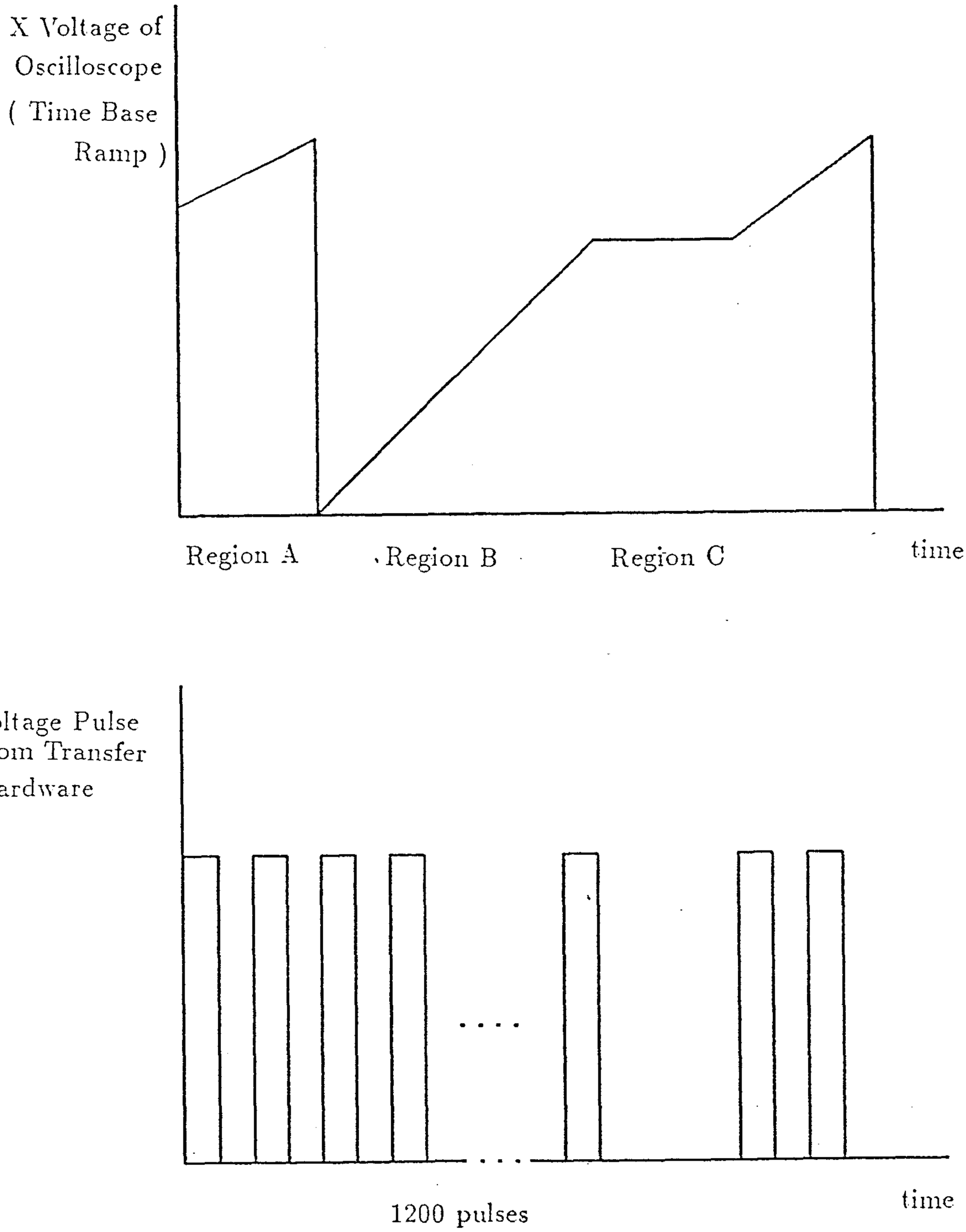

Fig 4.7 The data acquisition cycle showing the X voltage output from the oscilloscope together with the digital pulses from the transfer hardware.

4.3.2 Averaging of the Waveforms

As the signal is passed through the data acquisition circuits noise will be injected. This could give distorted results and consequently, an attempt must be made to remove the noise. Any noise which is Gaussian in nature and uncorrelated to the signal, may be adequately removed by averaging the signal over several cycles (Schwartz 1976, Dunlop 1983).

Each data set is averaged by summing together separate scans of the waveform. However before they can be summed the waveforms will have to be aligned to compensate for any drift in the oscilloscope sampler, achieved by means of a predefined procedure (Dawkins *et al* 1979).

Basically, the first waveform is captured and a reference point, p_{ref}, is found on the leading edge, defined in terms of a point, p_{base}, on the flat baseline portion of the data and the half height, $h/2$, of the waveform (Fig 4.8(a)). Thereafter the waveforms are aligned to the first by taking a moving average over 16 points, to remove the effect of timing jitter noise on the leading edge, until a point similar in amplitude to that at point p_{ref} is reached, point p_2, Fig 4.8(b). The waveforms are then shifted relative to each other by an amount $p_{ref} - p_2$, effectively a measure of the drift, and added together. Upon completion of the process the maximum number of points drifted must be discarded from each end of the averaged data set.

4.3.3 Calibration of the Sampling Interval

The sampling interval, $\triangle t$, is determined by the sweep speed of the oscilloscope time base. In order to accurately calculate the Fourier transform of the waveform captured $\triangle t$ must be known. Since the sweep speed settings are accurate to only 3%, a similar error in reading $\triangle t$ will result.

In order to calculate $\triangle t$ accurately a calibration procedure of connecting a suitable length of air line to the sampler and terminating with a short circuit may be used, Fig 4.9 (Dawkins *et al* 1979). The waveform is examined until the half height $h/2$ is found on the rising and falling edges. If p, the pulse width, is denoted as the number of sampling intervals between the two half height points, the sampling interval $\triangle t$ can be found from

$$\triangle t = \frac{2(l_c + l_{sh} + l_{sam})}{pc} \tag{4.22}$$

where l_c is the length of the air line, l_{sh} is the length of the short circuit, l_{sam} is the length of the line between the sampler head and the top of the sampler and c is the velocity of light in free space.

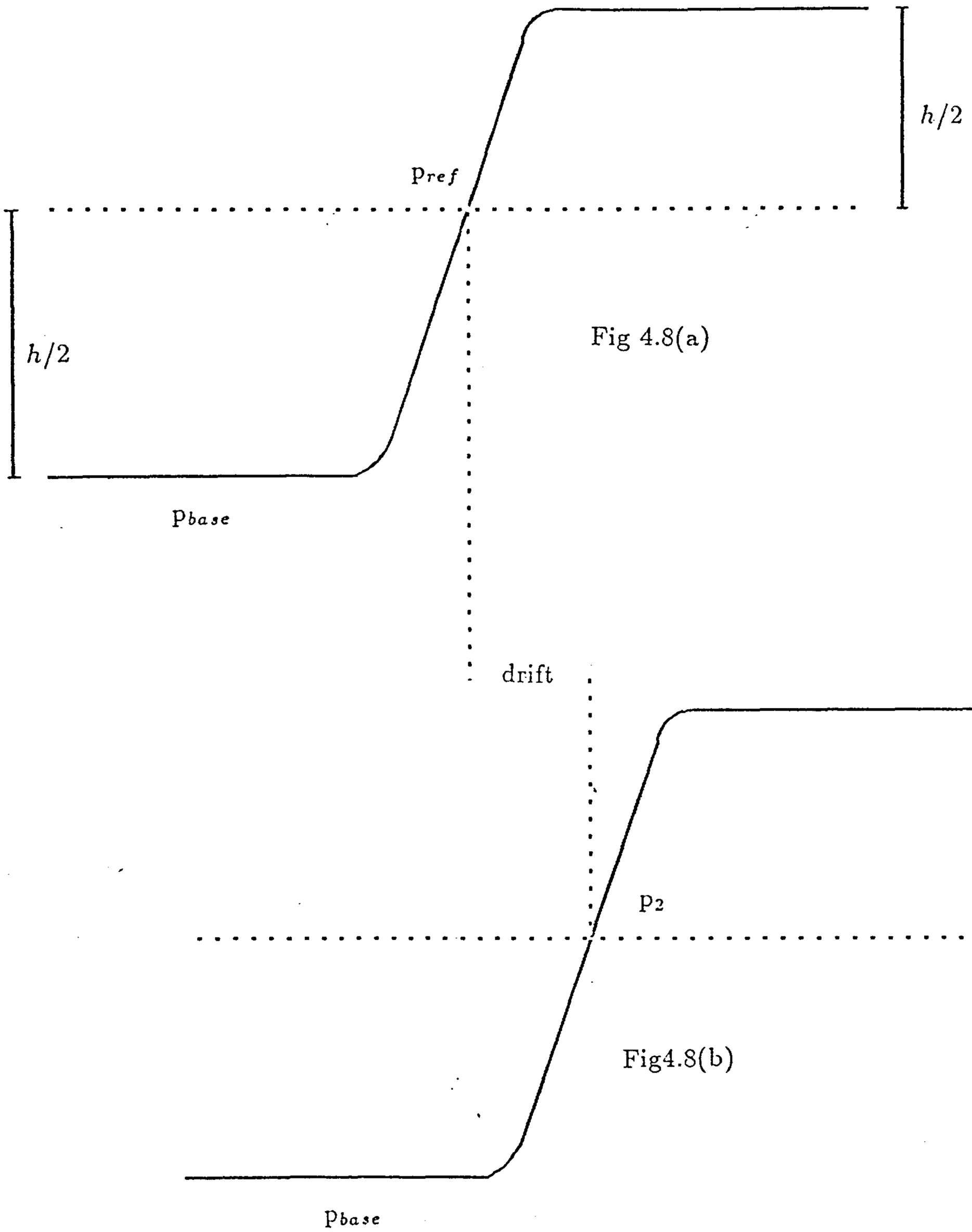

Fig 4.8(a)

Fig4.8(b)

Fig 4.8 **The definition of the points p_{base}, p_{ref}, p_2 in the averaging procedure.**

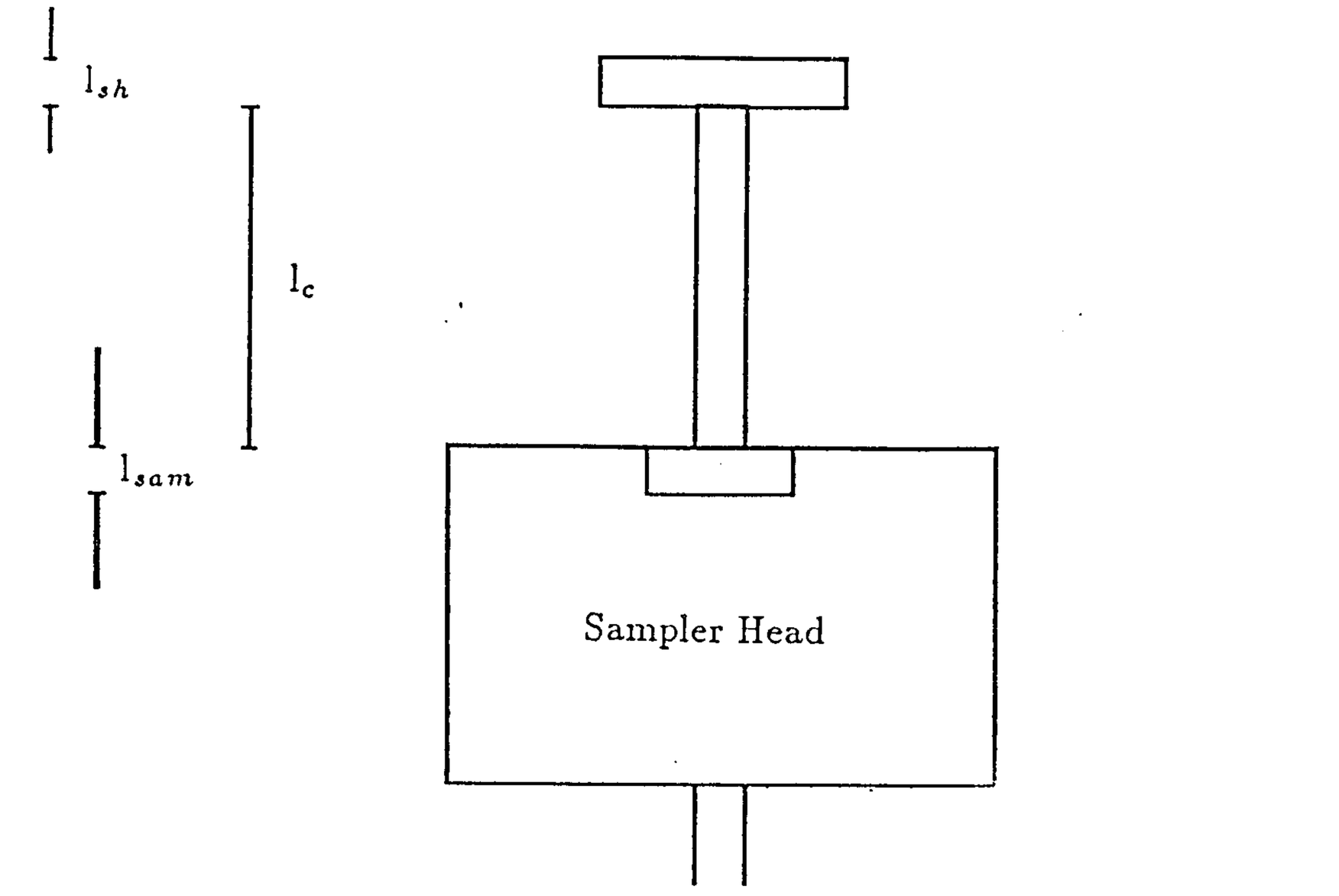

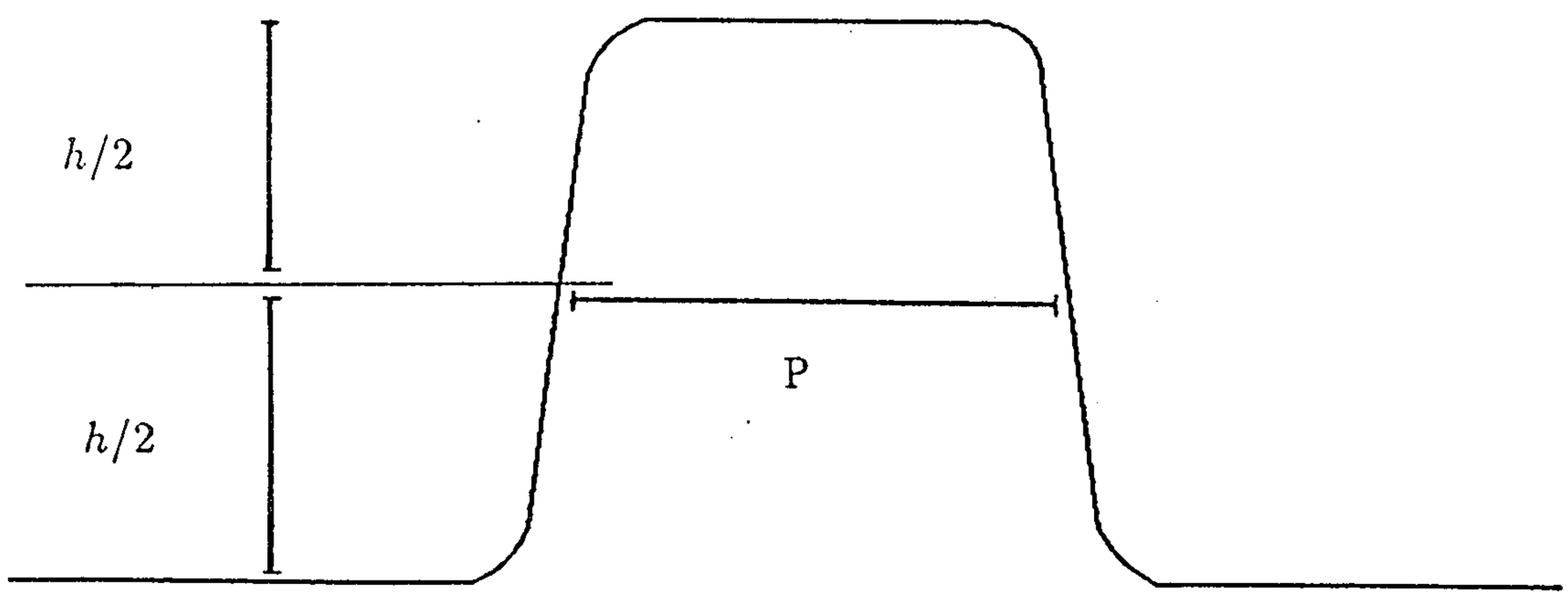

Fig 4.9 Step waveform produced for the sampling time interval calibration.

The main source of error in this procedure is the determination of p. However provided the pulse width is greater than 5cm the accuracy of $\triangle t$ is at least 0.5% (Dawkins *et al* 1979).

4.3.4 Discrete Fourier Transform

The Fourier transform $F(\omega)$ of a waveform $f(t)$ is given by equation 4.19 as

$$F(\omega) = \int_{-\infty}^{\infty} f(t)e^{-j\omega t}dt$$

In practice a numerical approximation to the continuous integral is used, based on the sampling theorem (Shannon 1949) . If $F(\omega)$ has no frequency components at or above $\omega = \omega_c$, $f(t)$ can be accurately defined if one sample is taken every π/ω_c seconds. Thus if

$$F(\omega) = 0 \qquad |\ \omega\ | > \omega_c \tag{4.23}$$

the Fourier transform may be written as (Blackman *et al* 1958, Dunlop 1983)

$$F(\omega) = \triangle t \sum_{n=-\infty}^{\infty} f(n \triangle t)e^{-j\omega n \triangle t} \tag{4.24}$$

Only a finite number of terms in the summation are needed if $f(t)$ decays to zero in a finite time. However in time domain spectroscopy the signals analysed will assume a constant finite value and the summation in equation 4.24 will not converge. In this case a modified version of equation 4.24 (Samulon 1951)

$$F(\omega) = \frac{\triangle t}{2j sin(\omega \triangle t)} \sum_{n=1}^{N} [f(n \triangle t) - f((n-1) \triangle t)]e^{-j\omega n \triangle t} \tag{4.25}$$

may be used, which is exact if

$$F(\omega) = 0 \quad \omega_c < \omega \tag{4.26}$$

This condition is reached if the signal to be transformed reaches a constant value. However in practice this is never the case as the time window cannot be large enough. This restriction may be avoided if the initial and final sample values are set to zero.

To ensure that the data are well behaved at time $t = T$, where T is the total sampling time window, the difference terms in equation 4.25 are multiplied by a smoothing function $w(t)$, defined by

$$\begin{aligned} w(t) &= 1 && n < 0.75N \\ &= cos[\frac{\pi(4n - 3N)}{2N}] && 0.75N \leq n < N \end{aligned} \tag{4.27}$$

4.3.5 Calculation of a Common Time Origin

To correctly evaluate the Fourier transform a common time origin must be established for each waveform. Any small differences in the origin, δt, will result in an error of $\omega\delta t$ in the phase of the Fourier transform at a frequency of ω (Dawkins *et al* 1979). This change in phase, $\delta\theta$, may be expressed as

$$\delta\theta = 0.36^{o} GHz^{-1} ps^{-1} \tag{4.28}$$

and it becomes apparent that a timing error of 1ps will produce a phase error of 3.6° at 10GHz.

Two techniques may be used to find the common time origin

(a) Extrapolation Technique (Loeb *et al* 1971)

The common time origin t_{ref} is found by extrapolating the steepest linear portion of the waveform, AB, to the initial baseline, CD, Fig 4.10. To determine the steepest linear portion a line is fitted over a series of points on the leading edge and the line used is that with the maximum gradient.

(b) Marker Pulse Technique

A small portion of the signal is directed through one sampling channel terminated in a matched load. Before the waveform is digitised the two output signals of the sampling oscilloscope are added together and a small marker pulse will appear at exactly the same position in time independent of the medium under investigation, Fig 4.11(a). The rising edge of the marker can be approximated by a straight line while the decay is exponential in nature. The common time origin may then be found from the intersection of the line, AB, and the exponential fuction Ce^{-D}, Fig 4.11(b).

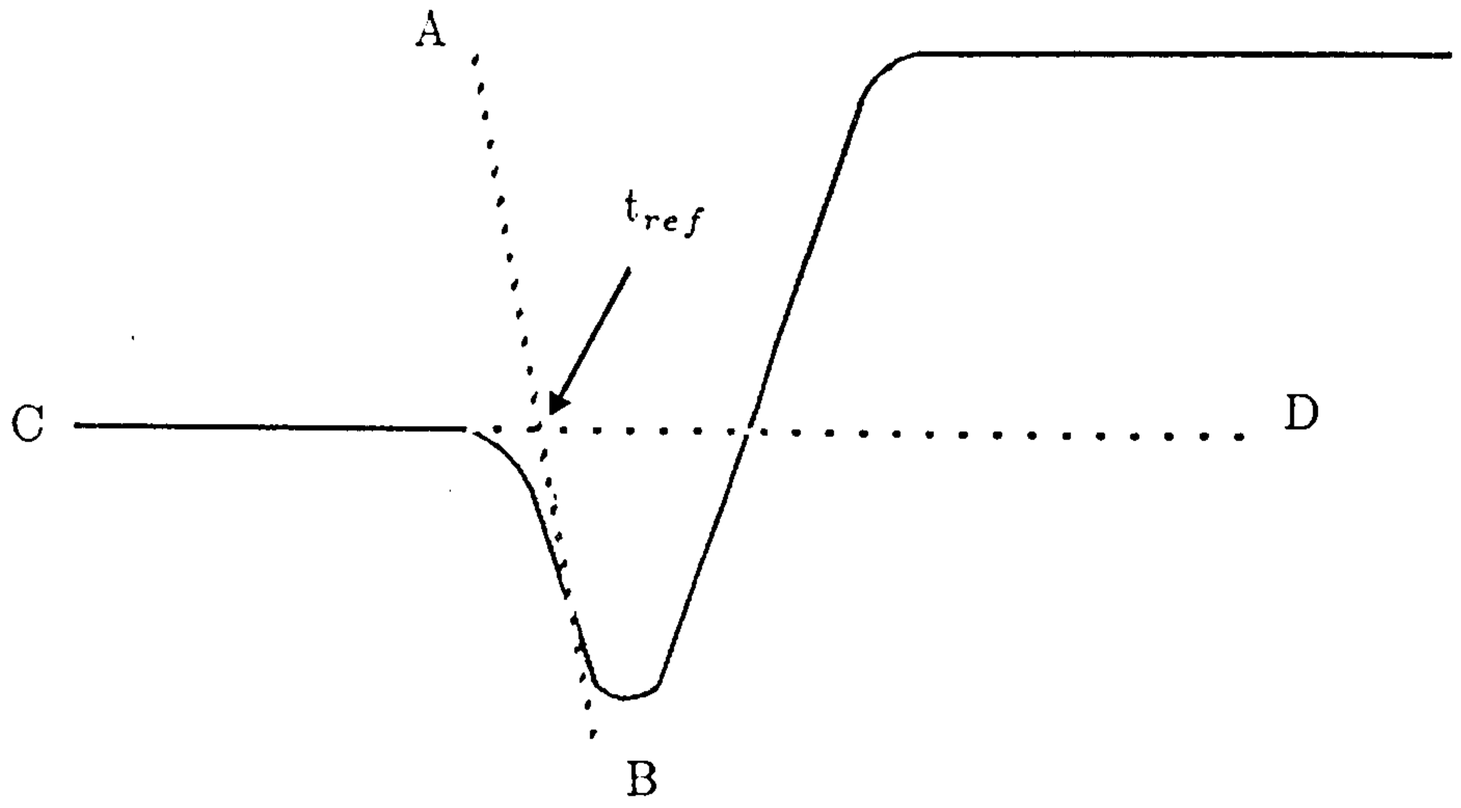

Fig 4.10 Definition of terms in the extrapolation technique.

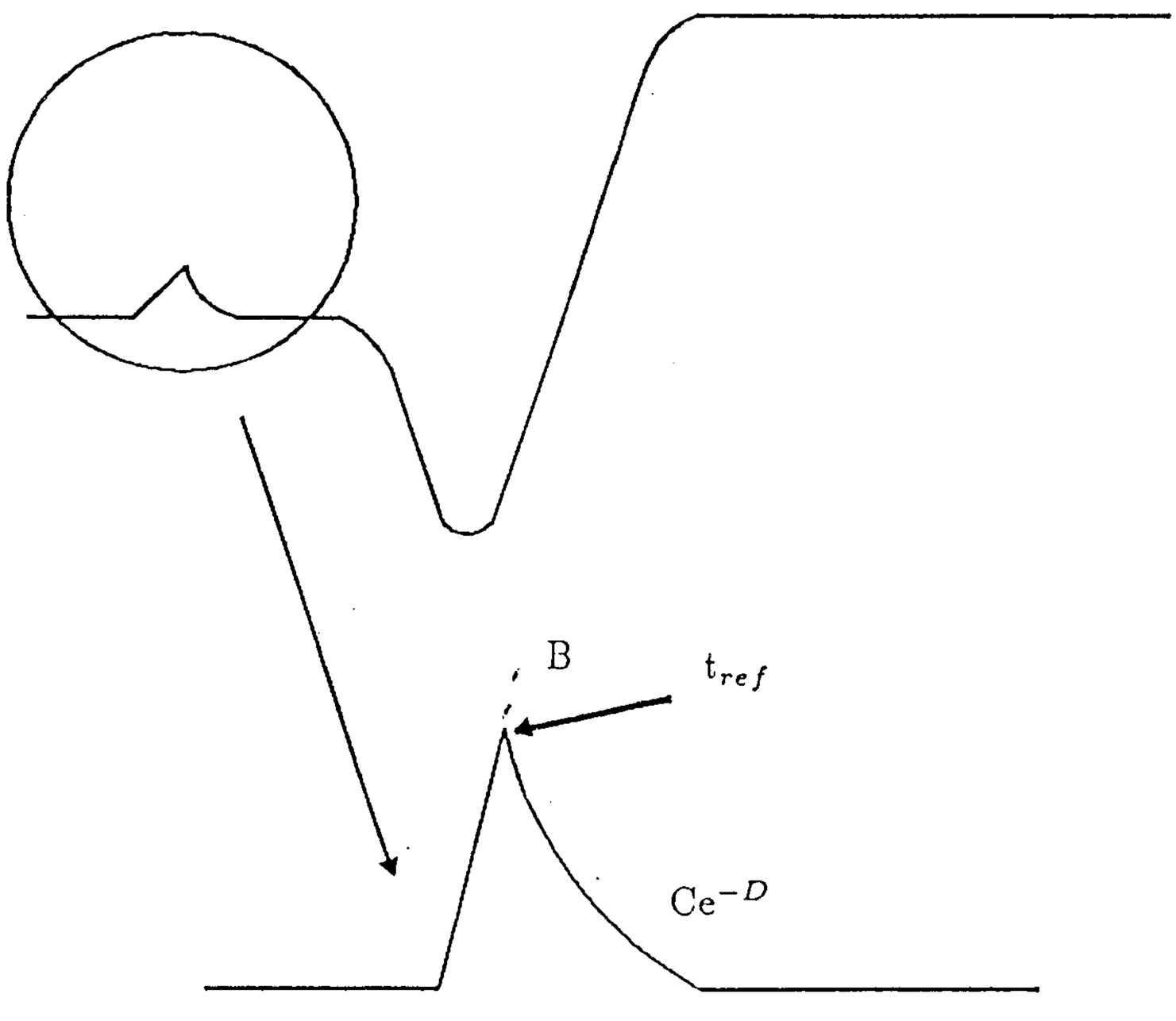

Fig 4.11 Definition of terms used in the two pulse technique.

4.3.6 Unwanted Reflections in the System

In an ideal system only the input signal and its reflection or transmission, would be measured. However in practice there will be reflections from the sampling head and from any connections between the sample and the input signal source. These will give rise to erroneous reflections.

This effect may be reduced by using a sample of known dielectric properties, known as the reference, to correct for the errors, such that

$$H(\omega) = \frac{R(\omega)}{REF_m(\omega)} * REF_t(\omega) \tag{4.29}$$

$$H(\omega) = \frac{R(\omega) - REF_m(\omega)}{INPUT(\omega)} + REF_t(\omega) \tag{4.30}$$

where $R(\omega)$ is the measured sample response, $INPUT(\omega)$ s the input waveform, $REF_m(\omega)$ is the measured reference response and $REF_t(\omega)$ is the theoretical reference response.

4.3.7 Calculation of Permittivity

With the advent of open-ended coaxial line probes dielectric measurements have been greatly simplified compared with techniques using in line sample cells. By studying the perturbation of the fringe fields of the probe by an unknown dielectric the properties of the dielectric may be characterised. The transfer function, $H(\omega)$, is the reflection coefficient, $\mid \Gamma \mid e^{j\phi}$, of the sample at the open end of the probe. Using the equivalent circuit outlined in chapter 1, reproduced in Fig 4.12, the permittivity, $\hat{\epsilon}$, may be found directly from the transfer function, $H(\omega)$, by (Gabriel *et al* 1986)

$$\hat{\epsilon} = \frac{1 - \mid \Gamma \mid e^{j\phi}}{j\omega C_o Z_o (1 + \mid \Gamma \mid e^{j\phi})} - \frac{C_f}{C_o} \tag{4.31}$$

where C_0 is the capacitance associated with the external fringe fields, C_f is the capacitance associated with the internal fringe fields and Z_0 is the characteristic impedance of the probe and air line.

As the sample mainly effects the external fringe fields and the dimensions of the line are small compared with the propagating wavelength the conductance, G, accounting for the radiation losses, may be ignored. In the general case the effects of the conductance term may be accounted for by the use of the reference sample in the experimental procedure to minimise unwanted reflections. The measured reflection coefficient Γ may then be expressed as (Gabriel *et al* 1986)

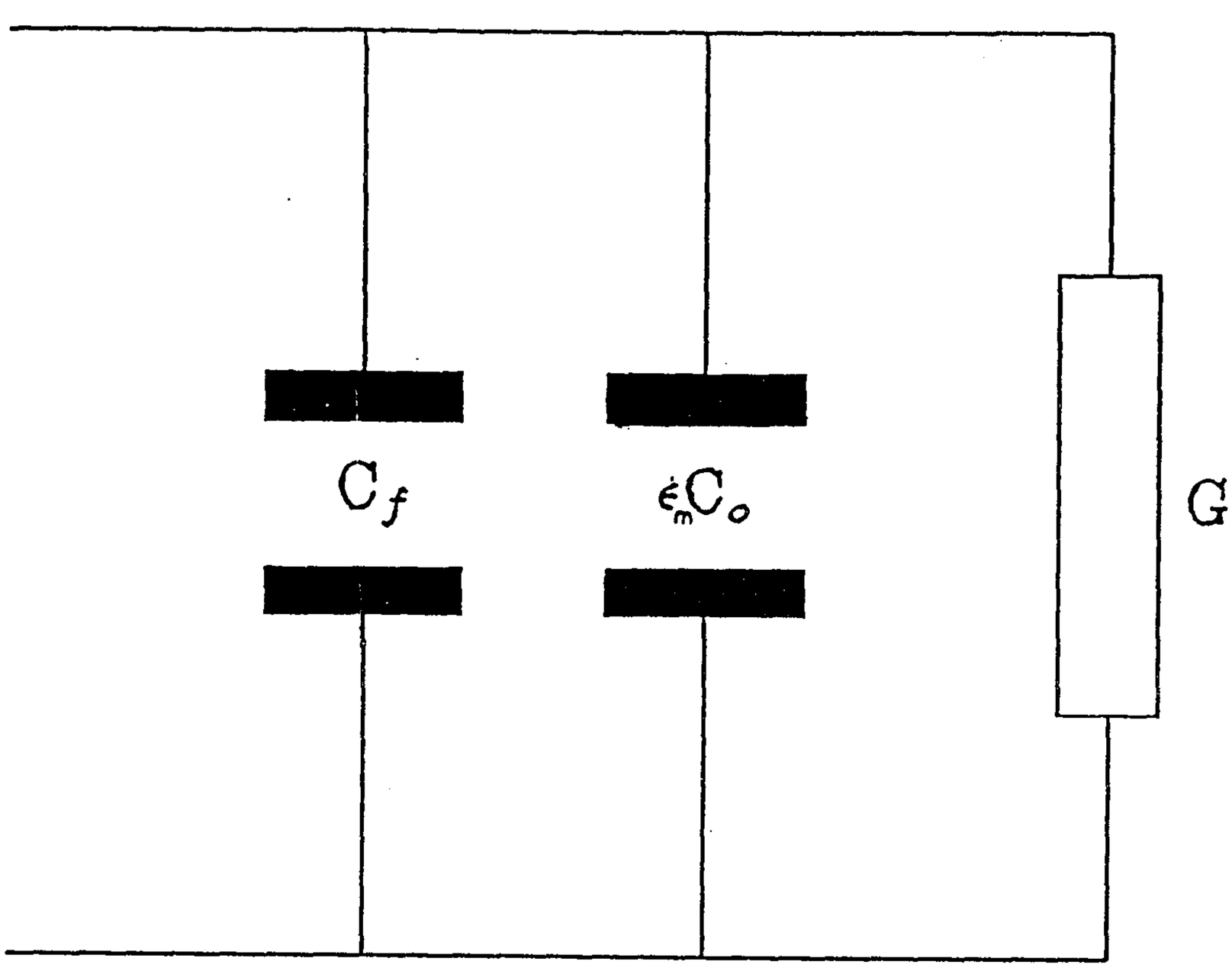

Fig 4.12 Equivalent circuit of open-end coaxial line.

$$\Gamma_m = \Gamma(\hat{\epsilon}, C_o) + F(\hat{\epsilon}, G) \tag{4.32}$$

By a choice of reference that is well matched to the sample at high frequencies the term $F(\hat{\epsilon}, G)$may be cancelled out.

From the results of the previous chapter the dependence of C_o on $\hat{\epsilon}$ is negligible and its dependence on the frequency may be accounted for by a correction factor (Gabriel *et al* 1986)

$$C_o^{corr} = C_o + Af^2$$

where A is an empirical constant dependent on the probe dimensions.

4.4 Construction of a Time Domain Spectrometer

4.4.1 The TDS System Hardware

The hardware involved in the construction of the TDS consists of a fast rise-time pulse generator, a detector, a sampling oscilloscope, precision coaxial air lines, an analogue to digital interface and a Hewlett Packard HP9216 microcomputer (Fig 4.13).

The input pulse is produced from a HP1106B tunnel diode which generates a step voltage of 200mV with a rise-time of approximately 40 picoseconds. The DC bias and triggering for the diode is provided by a HP1105A pulse generator, which is controlled by means of a synchronising pulse transmitted from the sampling oscilloscope. The input pulse is transmitted to the sample via high precision, low loss, gold plated coaxial air lines of 7mm interior diameter. The inner conductor is centred by means of APC-7 connectors. When the marker pulse technique is used (section 4.3.4) the output of the diode is applied to a directional coupler, the HP11691D, which splits the signal for transmission through the two sampling channels. The coupler operates in the frequency range 2 to 18 GHz and has a coupling output of -22 dB.

The sampling oscilloscope consists of one HP180D, a general purpose plug-in oscilloscope, used in conjuction with a HP1811A dual channel sampling time base and vertical amplifier and a HP1430C dual sampling head. The oscilloscope is triggered externally by a pulse from the acquisition circuit upon completion of each successful data transfer. On reception the oscilloscope outputs the synchronising pulse to the diode circuits.

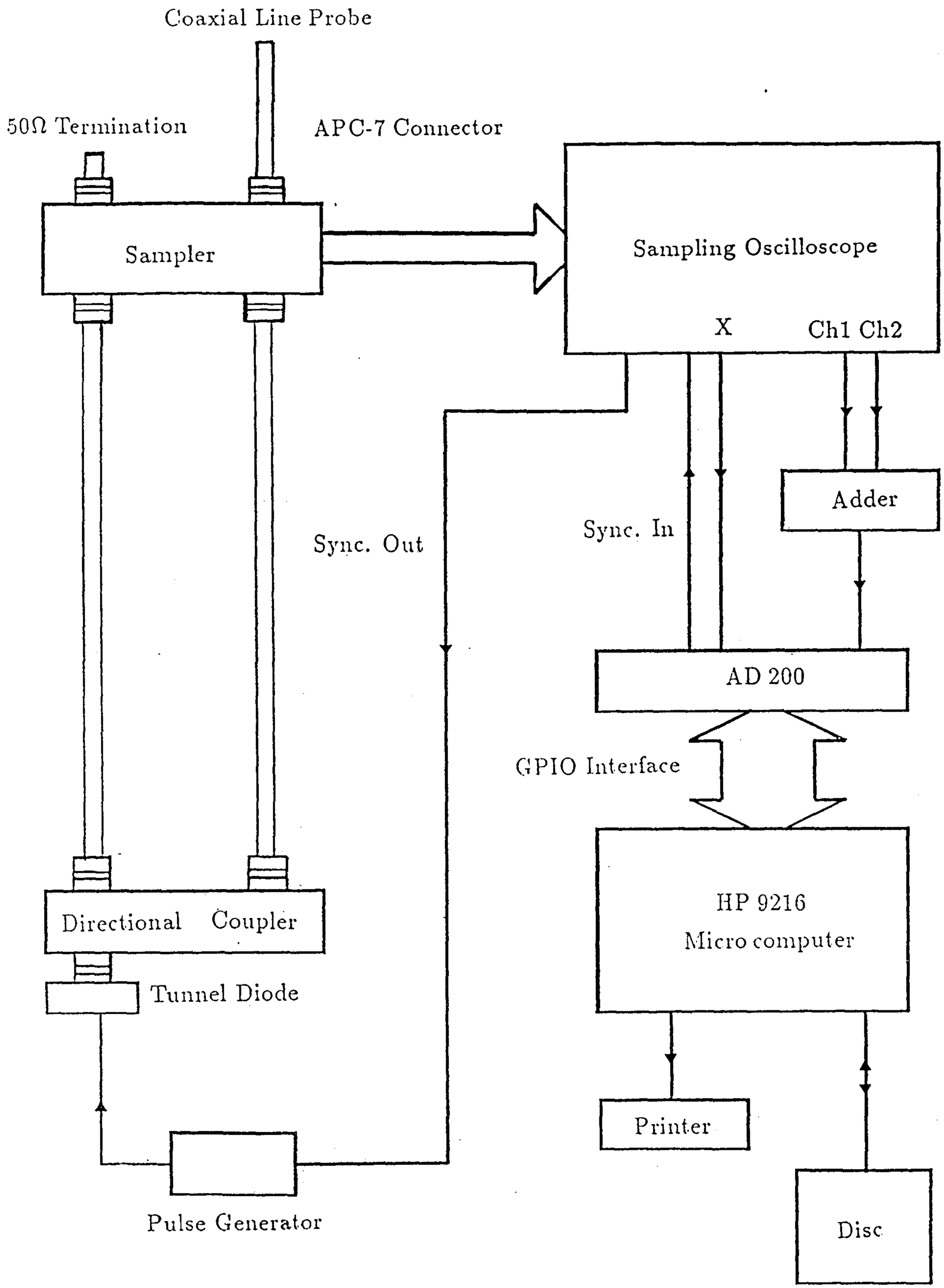

Fig 4.13 Experimental configuration of the Time Domain Spectrometer.

Once the data sets have been captured by the oscilloscope they are transferred to the microcomputer via two stages. Firstly the analogue voltage representing the sample is passed through a wide bandwidth analogue adder, used to add the outputs of the two sampling channels together. Secondly the signal is digitised by an analogue to digital converter, the INFOTEK AD200, and transferred over the microcomputer bus to the microcomputer memory. The AD200 is a 12 bit, 8 differential input analogue to digital converter which is fully programmable by the host processor and consists of three conceptual components. These are the bus interface, the controller and the converter (Fig 4.14). The interface is the HP General Purpose Input Output interface which can be accessed from the host computer via high level PASCAL instructions.

The control and processing in the experiment are achieved using a HP9216 microcomputer. This processor is a 16 bit single user system currently configured with 1.25 Mbyte of main memory, two 3.5in disc drives, storing up to 500 Kbytes, and capable of running the BASIC, FORTRAN 77 and PASCAL high level languages as well as the 68000 assembler language.

4.4.2 The TDS System Software

The software needed to control the experiment and process the data has been written in five modules each linked to a main body of code, Fig 4.15. The experimental procedures explained in section 4.3 have been incorporated in the design and are coded in the module software. The modules may be characterised as

(a) Data Acquisition Module

Controls the data flow from the AD200 to the microcomputer. The code was written in 68000 to achieve greater transfer rates than was possible with the standard operating transfer instructions. The effective sampling rate using 68000 is 40 kHz while implementation in PASCAL results in a rate of 23.5 kHz. The averaging process is also carried out within this module, each data set being averaged 100 times.

(b) Fortran Data Processing Module

As the permittivity and the transfer function are complex quantities any data manipulation code has to be written in FORTRAN 77. The code calculates the Fourier transform of the waveforms captured and forms the transfer function. The solution for the permittivity can then be found directly from equation 4.30.

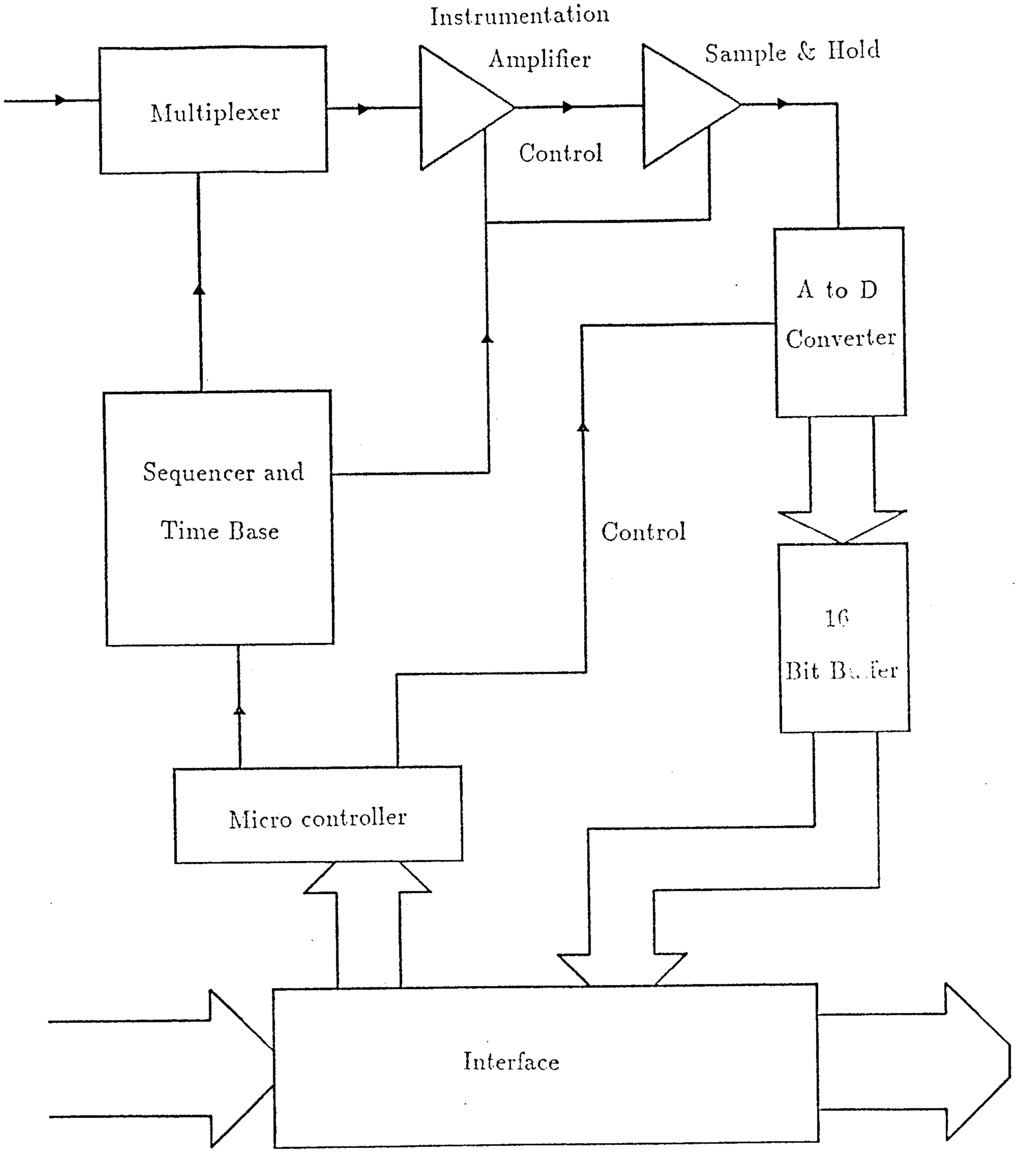

Fig 4.14 AD200 circuit block diagram.

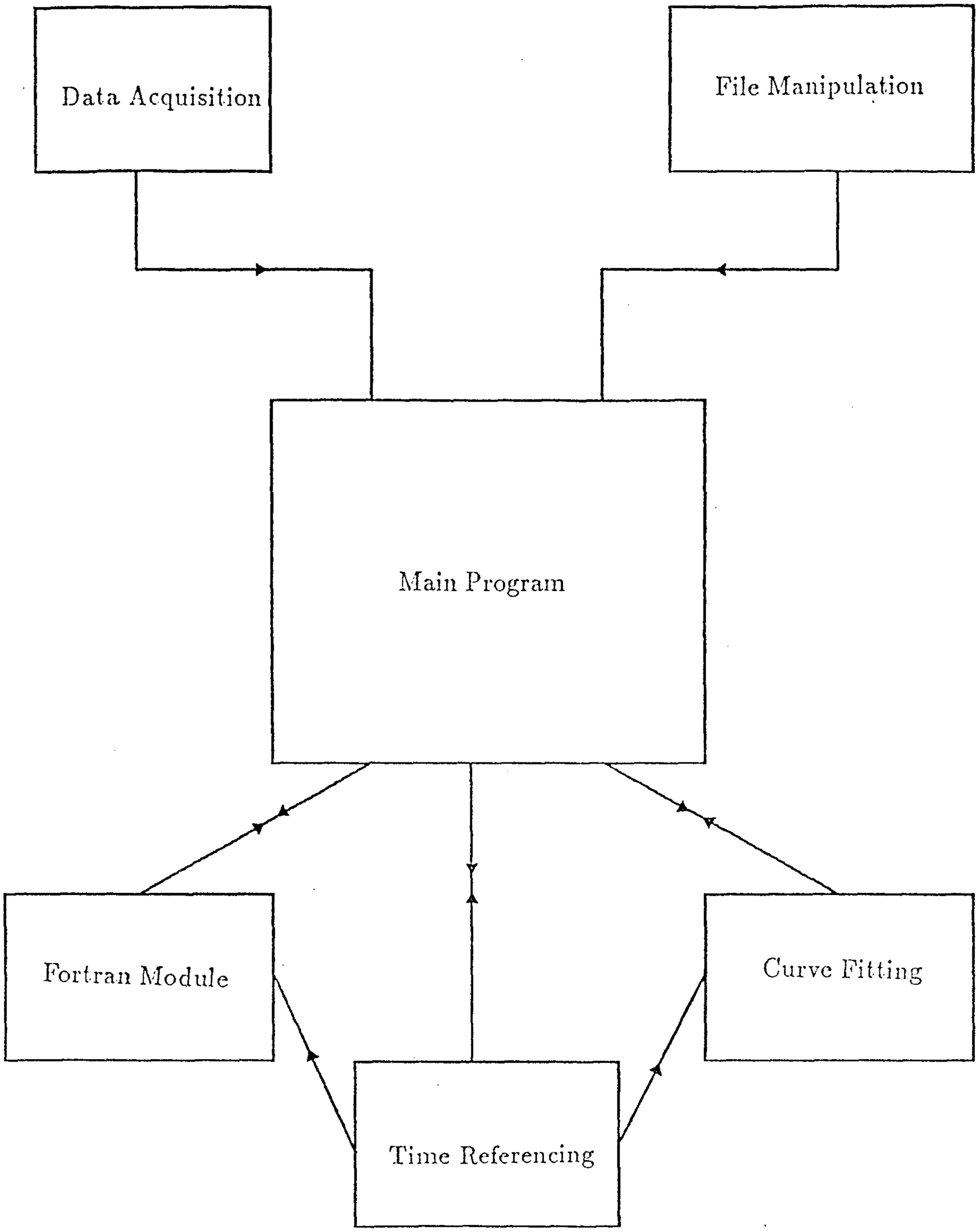

Fig 4.15 The software configuration and links between modules.

(c) Time Referencing and Calibration Module

Perfoms the calibration of the sampling interval $\triangle t$ and finds a common time origin for the Fourier transform using the techniques outlined in section 4.3.5. Both of the time referencing techniques are impelemented.

(d) Curve Fitting Module

Calculates the exponential decay of the curve to enable the common time origin to be found using the least squares minimisation technique (Sheppard 1973).

(e) File Management Module

Controls the movement of data between main memory and the discs. It has the facilities to compare the differences in two data files or take the average of a set of data files.

Chapter 5

Evaluation of a New Time Domain Spectrometer and Human In-Vivo Measurements.

5.1 Introduction

The Time Domain Spectrometer of the previous chapter was tested with two known standards, formamide and ethanediol. The results obtained are used to make a decision on the best time referencing technique from the two incorporated in the system. The difference and ratio techniques of removing the unwanted reflections are also examined. After presentation of the test results new *in-vivo* measurements are made on several parts of the human body.

5.2 Errors Inherent to TDS Experiments

5.2.1 Introduction

The purpose of the testing stage is to examine the results and from these decide on an experimental procedure that will yield the best data. Subsequently the errors inherent to all Time Domain Spectrometers should be examined and explained. These errors, termed systematic, are functions of the apparatus used and to a certain extent are controllable. Provided there is no change in the equipment or the transmission medium between experiments these errors can be regarded as constant (statistically they are not but the fluctuations should be minimal).

5.2.2 Errors Introduced by the Transmission Medium

Any transmission network suffers from impedence mismatches and unwanted reflections. The main way to minimise this effect is to insert sufficient airline between the generator and the sample head ($\approx 60cm$), thus ensuring that the primary unwanted reflections are not in the time window being analysed (Suggett *et al* 1970, Dawkins 1979).

5.2.3 Random Errors in the Electronic Circuits

If a signal is transmitted through an electronic circuit noise will be superimposed which will be totally uncorrelated to the signal. As the noise is random in nature the Fourier transformation should be constant and will therefore contribute to the complete spectrum. As is the case with any random phenomena the effect can be greatly reduced by averaging the waveform over several cycles.

Another form of error is drift in the timing circuitry of the sampling oscilloscope. This will effect the fast rising slope of the pulse and subsequently the sharpness of the transform. Like the random electronic noise this can be reduced by the averaging process.

5.2.4 Errors in the Digital Fourier Transform (DFT)

The two majors errors arising in the DFT of the response signal are related to each other. The first, termed aliasing, arises when the effective sampling interval $\triangle t$ does not satisfy the Nyquist criterion. That is

$$\triangle t^{-1} \geq f_c \tag{5.1}$$

where f_c is the Nyquist frequency of the sampled signal. One way of overcoming this problem is to chose $\triangle t$ to be less than $0.1 f_c^{-1}$.

The second error is termed leakage and results when the waveform being analysed is truncated abruptly in time. In the present application of Samulon's algorithm this stipulates that the waveforms must reach a constant value in the observation time window. In order to ensure a good truncation the time window, $N \triangle t$, where N is the number of sampled points, must be relatively large. Since N is constant this leads to a greater $\triangle t$ and in turn to a greater aliasing problem.

5.2.5 Errors due to Mechanical Damage

The transmission of the input signal to the sample and the subsequent reflection from the sample must be error free. This implies that the connectors and the transmission medium used must be highly precision made and maintained to their original specifications.

During any experiment there may be a requirement for connecting and disconnecting various parts of the system. This will result in wear and damage to the parts which will in turn be seen in the experimental results.

5.3 Experimental Results for Formamide and Ethanediol

5.3.1 Experimental Procedure

In order to test the relative merits of each time referencing technique two liquid standards were used. Formamide and ethanediol have both been studied previously (Jordan *et al* 1978) and their dielectric behaviour is well documented. As a result good agreement between the experimental results and those found by Jordan *et al* (1978) are necessary before the system can be considered accurate. Due to the extensive literature on the subject of the dielectric properties of formamide and ethanediol no attempt is made to analyse the dispersion curves.

In each case the experiment should follow a systematic procedure that will enhance the reproducibility of the results. This may be outlined as :

(1) The time base was calibrated after the instruments had an initial warm up period of approximately one hour. This was repeated until the deviation in $\triangle t$ was less than 0.2%.

(2) The sample was loaded into a temperature controlled cell (fig 5.1) and allowed to settle to the desired temperature. The probe used in the measurements had a thermocouple attached to allow accurate determination of the temperature.

(3) The reference measurements were repeated using the same procedures that were used in the sample case.

(4) Several runs for each sample and reference were taken to allow the deviation of results to be examined.

5.3.2 Results for Formamide

Formamide was measured over the temperature range of 20 to 40°C using both the ratio and difference techniques outlined in section 4.3.6. Both the two pulse and the extrapolation time referencing techniques were used in separate experiments.

Using the criteria developed in chapter 3 the sample placed in the holder was larger than a sphere of radius $3.0b$, where b is the inner radius of the outer conductor. This is the volume predicted in the theoretical calculations of the probe needed to simulate a semi-infinite sample. The small probe of section 3.6.1 was used in order to cover the frequency range 10 MHz to 10 GHz.

The reference used for the experiment was water which is both a good match with formamide and is accurately known in the frequency range of interest for a wide

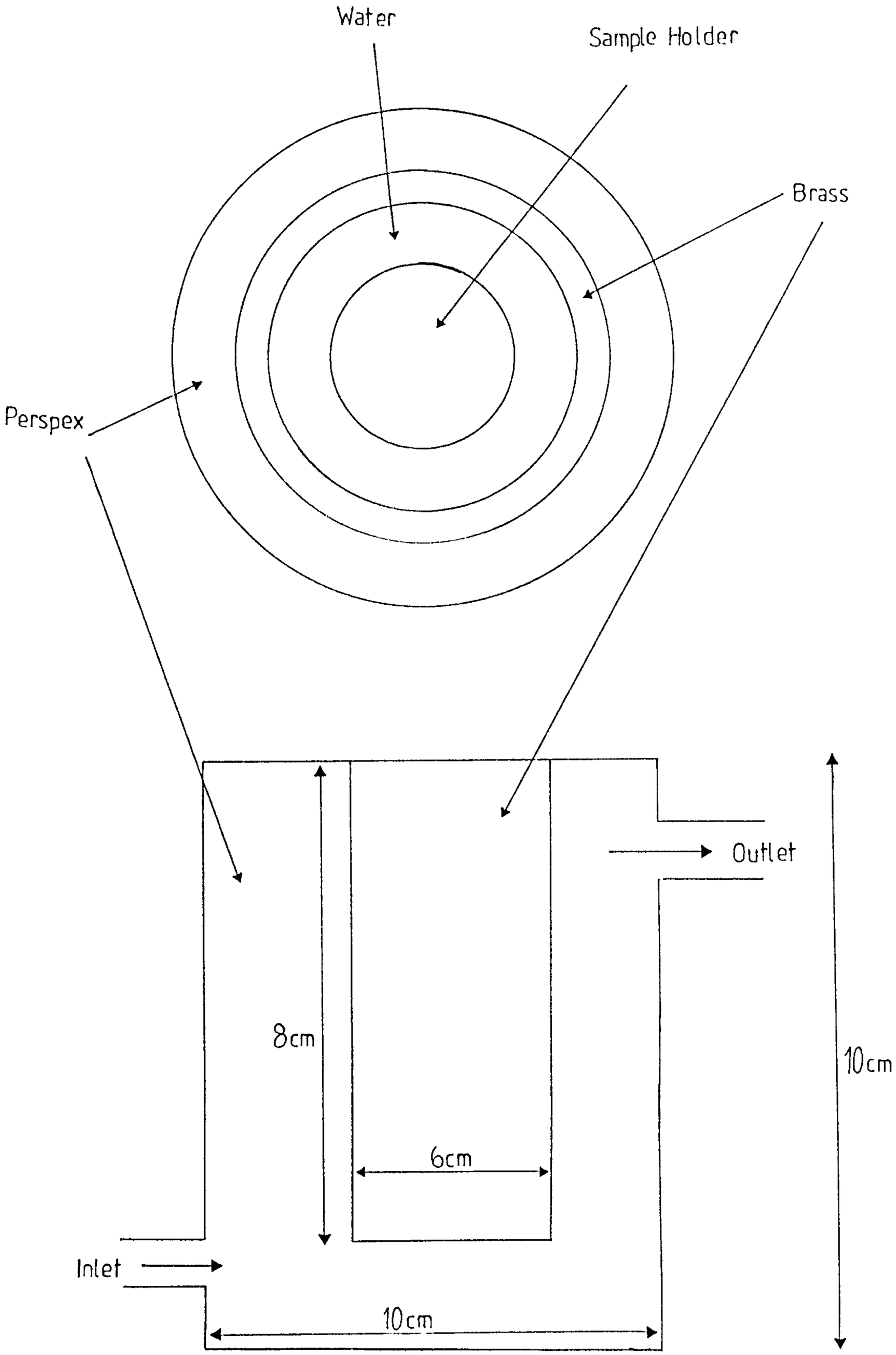

Fig 5.1 Temperature controlled cell used in test experiments.

temperature variation. Each of the experiments was repeated 10 times in order to examine the fluctuations in the results.

Results are shown in Figs 5.2 to 5.7. The theoretical results are generated from the studies on formamide and ethanediol by Jordan *et al* (1978). The parameters used in the generation of the results are shown in table 5.1 and the data were generated using a single Debye function.

5.3.3 Results for Ethanediol

The experiments outlined for formamide were repeated for ethanediol. However the reference used was air. Again the temperature and the frequency range covered were 20 to 40°C and 10 MHz to 10 GHz respectively. Results are shown in Figs 5.8 to 5.13. The generated data was obtained by using the parameters in table 5.1 and a double Debye function.

5.4 Discussion of the Results for Formamide and Ethanediol

Each of the experiments will suffer from the systematic errors outlined in section 5.2. However as these errors are of a consistent nature the different techniques adopted in the experiments may be examined without any loss of generality. The two main sources of experimental error will be the time referencing procedure used and the effect of the approximations in the equivalent circuit when used with either the difference or ratio techniques.

5.4.1 The Two Time Referencing Techniques

From the previous studies regarding the relative merits of the two time referencing techniques it was thought that the differences would be clearly visible in the results obtained (Gestblom 1981). However this is not the case. Although the results for the two pulse technique are slightly better at the higher frequencies, the differences are not as large as predicted by Gestblom (1981). During the comparison by Gestblom (1981) the input and reflection were simulated by a $\sin^5$ function which , upon examination of the experimental results, may not have been sufficiently accurate. The study of Arcone *et al* (1986) where the pulse was described by a more accurate function verifies the results of the experimental work where the differences predicted was not large.

The slight difference between the generated and experimental results when the extrapolation technique is used as the frequency approaches 10 GHz is due

Dielectric parameters for formamide.

Temperature	ϵ_s	ϵ_∞	τ (ps)
20	111.8	6.9	42
30	107.8	6.4	33
40	103.0	6.7	27

Dielectric parameters for ethanediol.

Temperature	ϵ_s	ϵ_H	ϵ_∞	τ_1 (ps)	τ_2 (ps)
20	42.8	7.3	3.8	145	10
30	40.5	7.8	4.1	100	12
40	38.2	7.3	3.8	70	7

Symbols are defined in Jordan *et al* (1978)

Table 5.1 Parameters used in the generation of the formamide and ethanediol data.

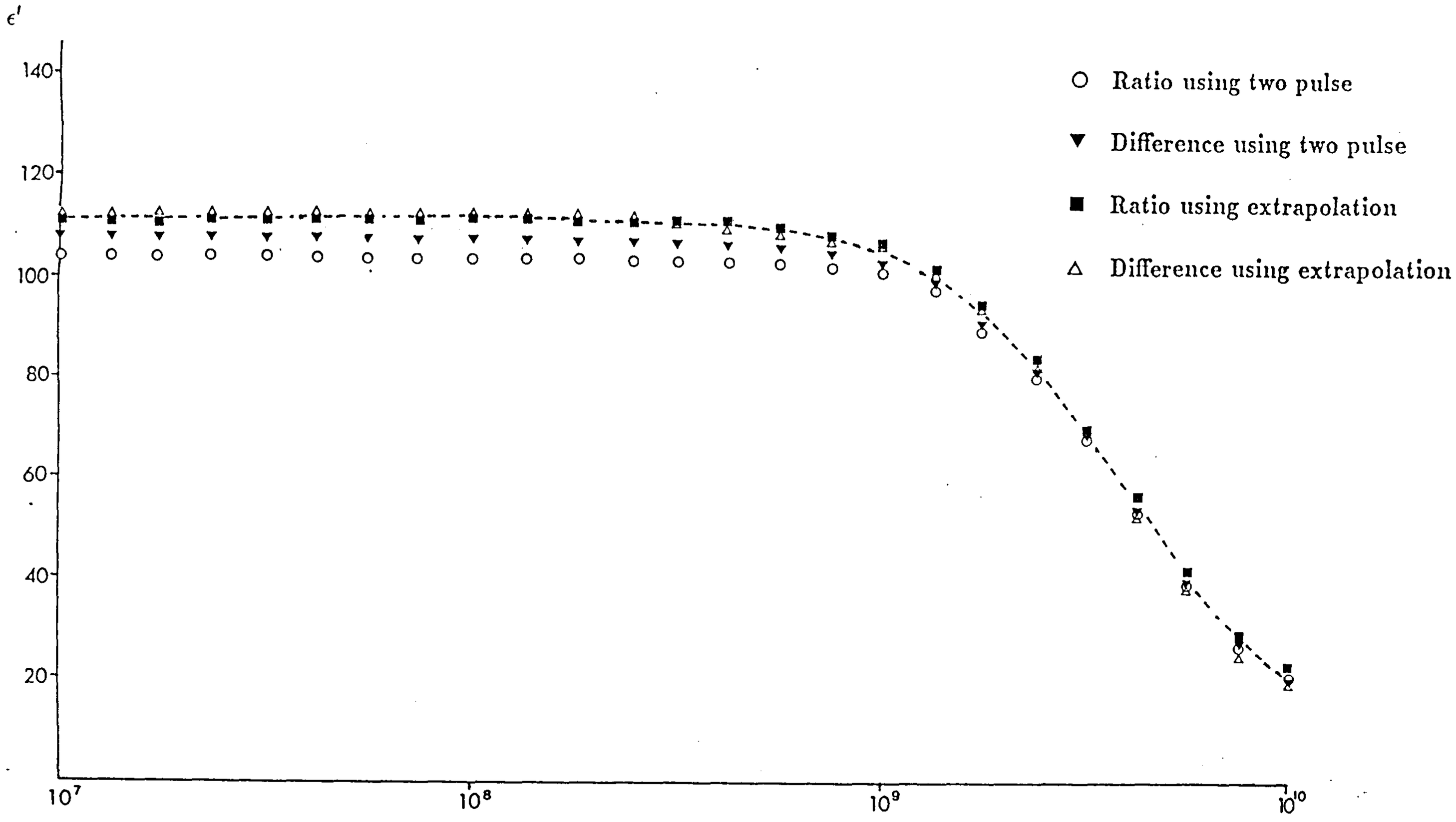

Fig 5.2 ϵ' **versus frequency for formamide at 20°C.**

Random errors in experimental data :
0.2% up to and including 1 GHz, 3.5% up to 10 GHz.

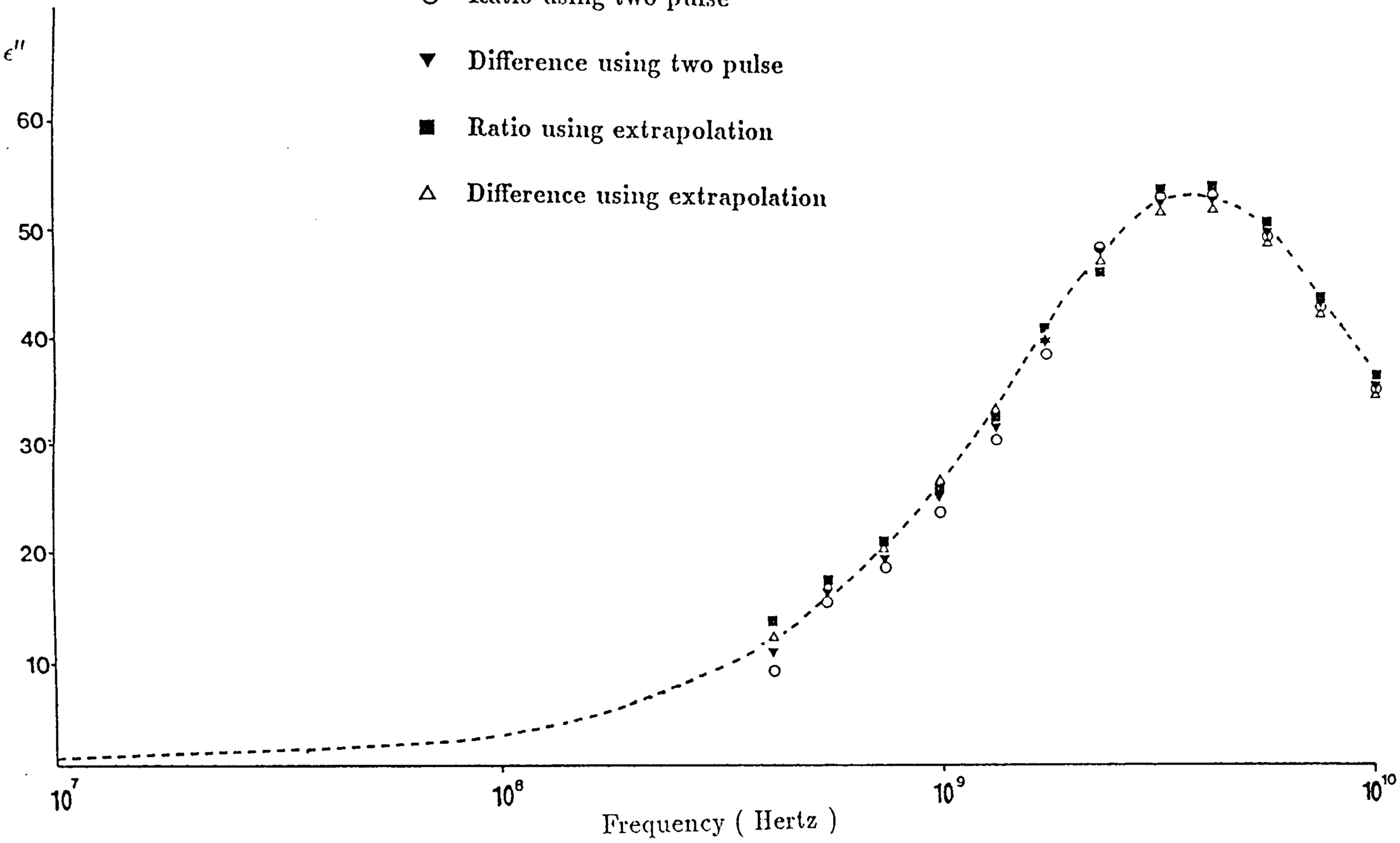

Fig 5.3 ϵ'' versus frequency for formamide at 20°C.

Random errors in experimental data :
0.3% up to and including 1 GHz, 2.8% up to 10 GHz.

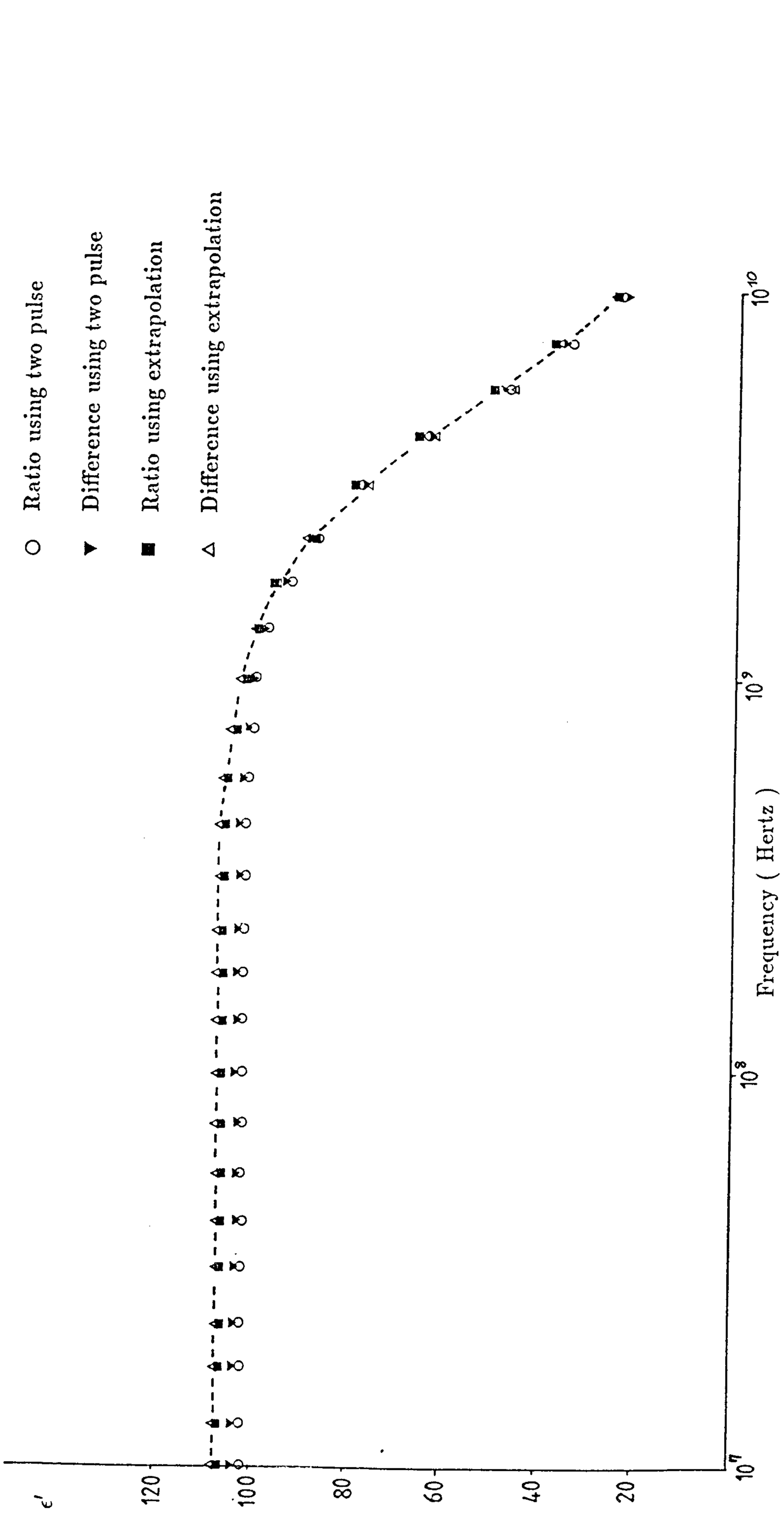

Fig 5.4 ϵ' versus frequency for formamide at 30°C.

Random errors in experimental data :
0.13% up to and including 1 GHz, 3.2% up to 10 GHz.

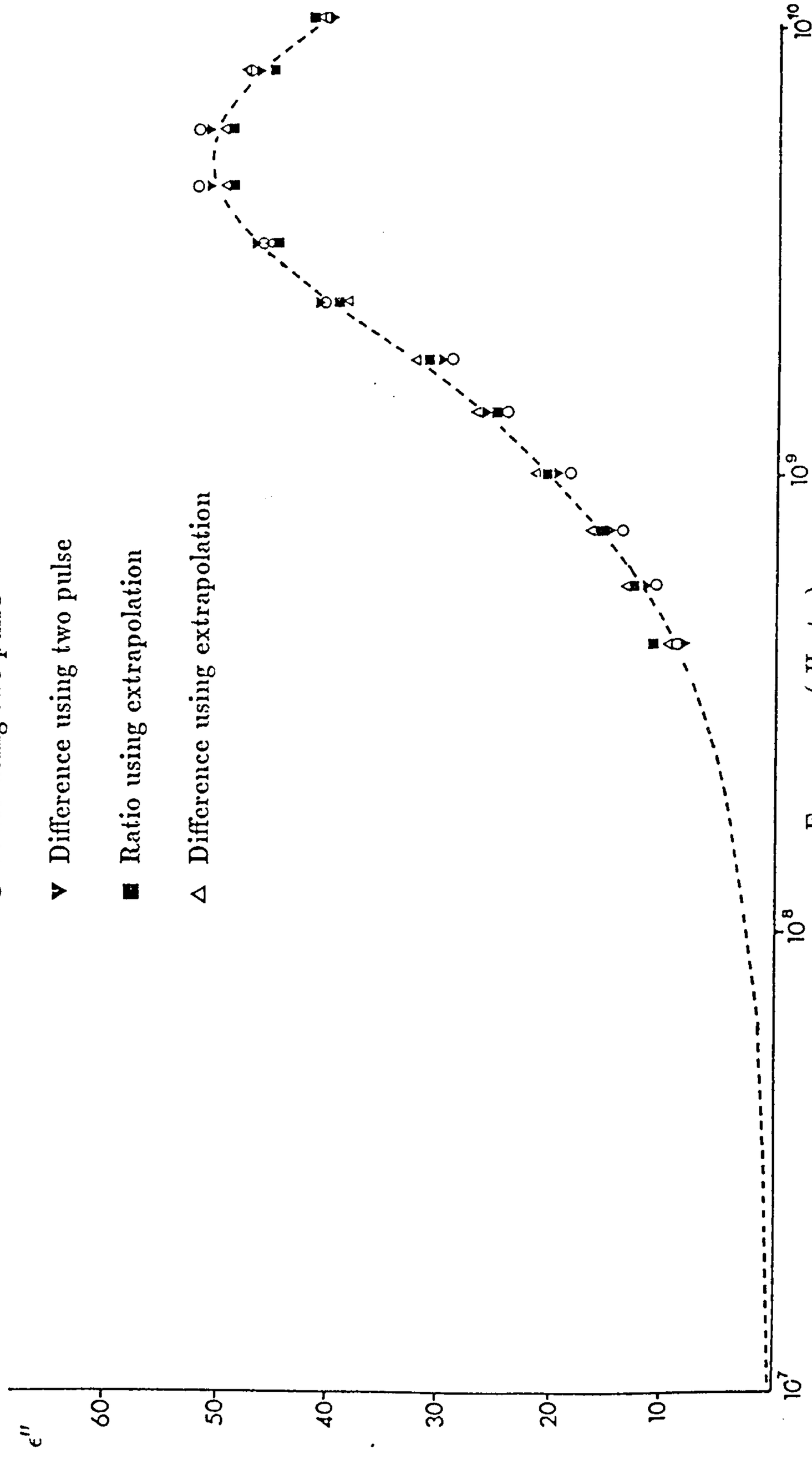

Fig 5.5 ϵ'' versus frequency for formamide at 30°C.

Random errors in experimental data :
0.3% up to and including 1 GHz, 2.6% up to 10 GHz.

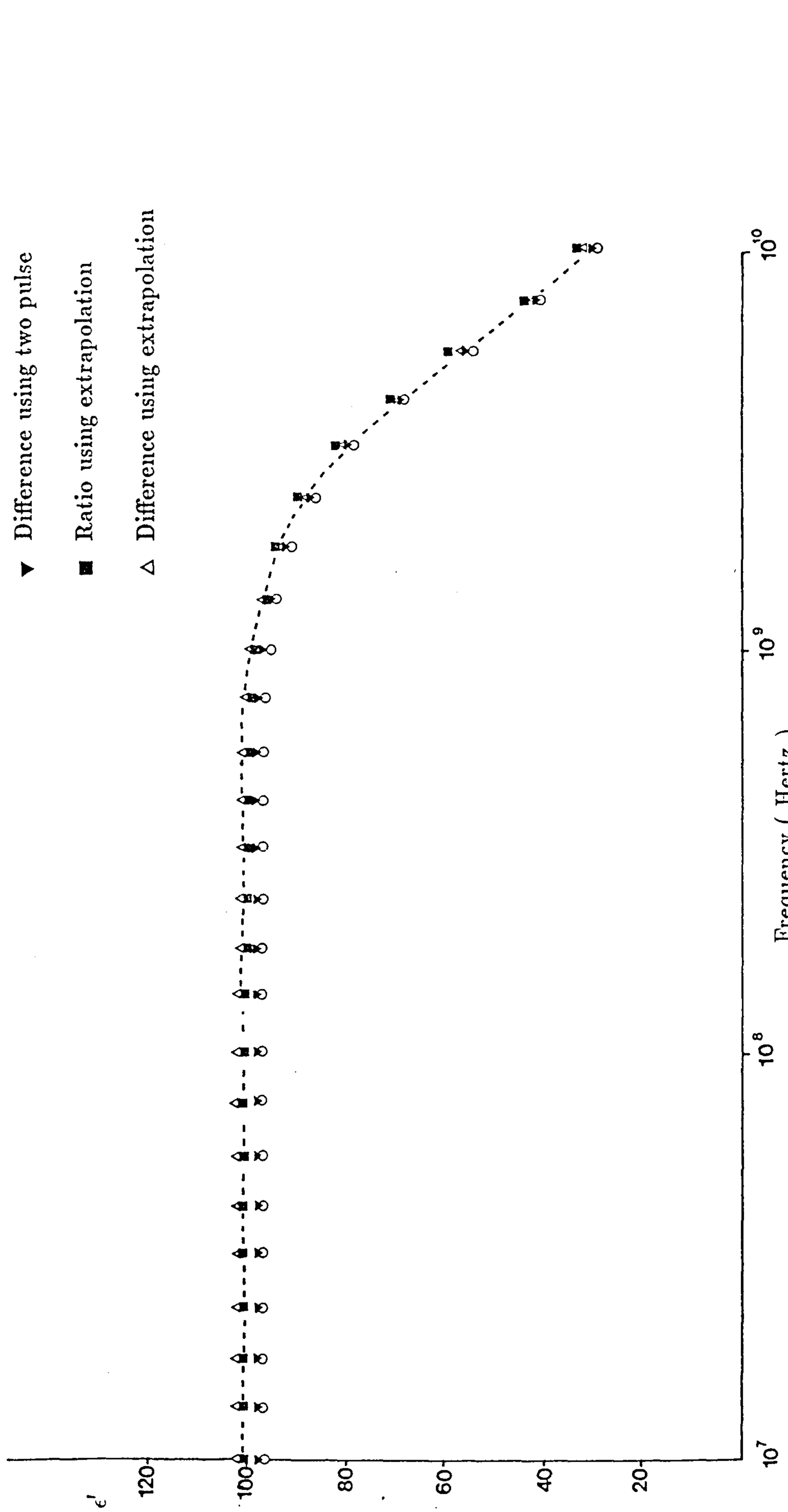

Fig 5.6 ϵ' versus frequency for formamide at 40°C.

Random errors in experimental data :
0.18% up to and including 1 GHz, 2.2% up to 10 GHz.

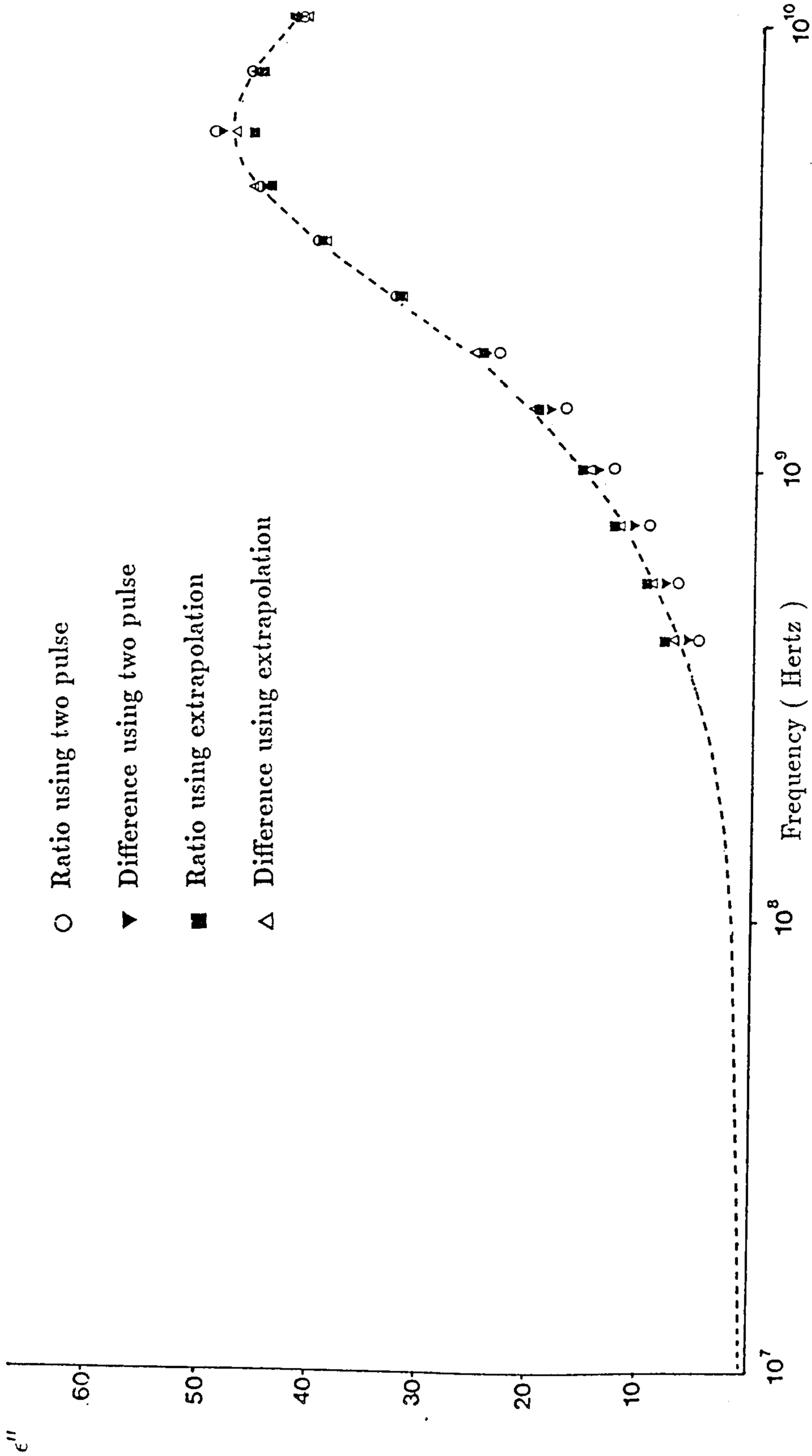

Fig 5.7 ϵ'' versus frequency for formamide at 40°C.

Random errors in experimental data :
0.22% up to and including 1 GHz, 3.0% up to 10 GHz.

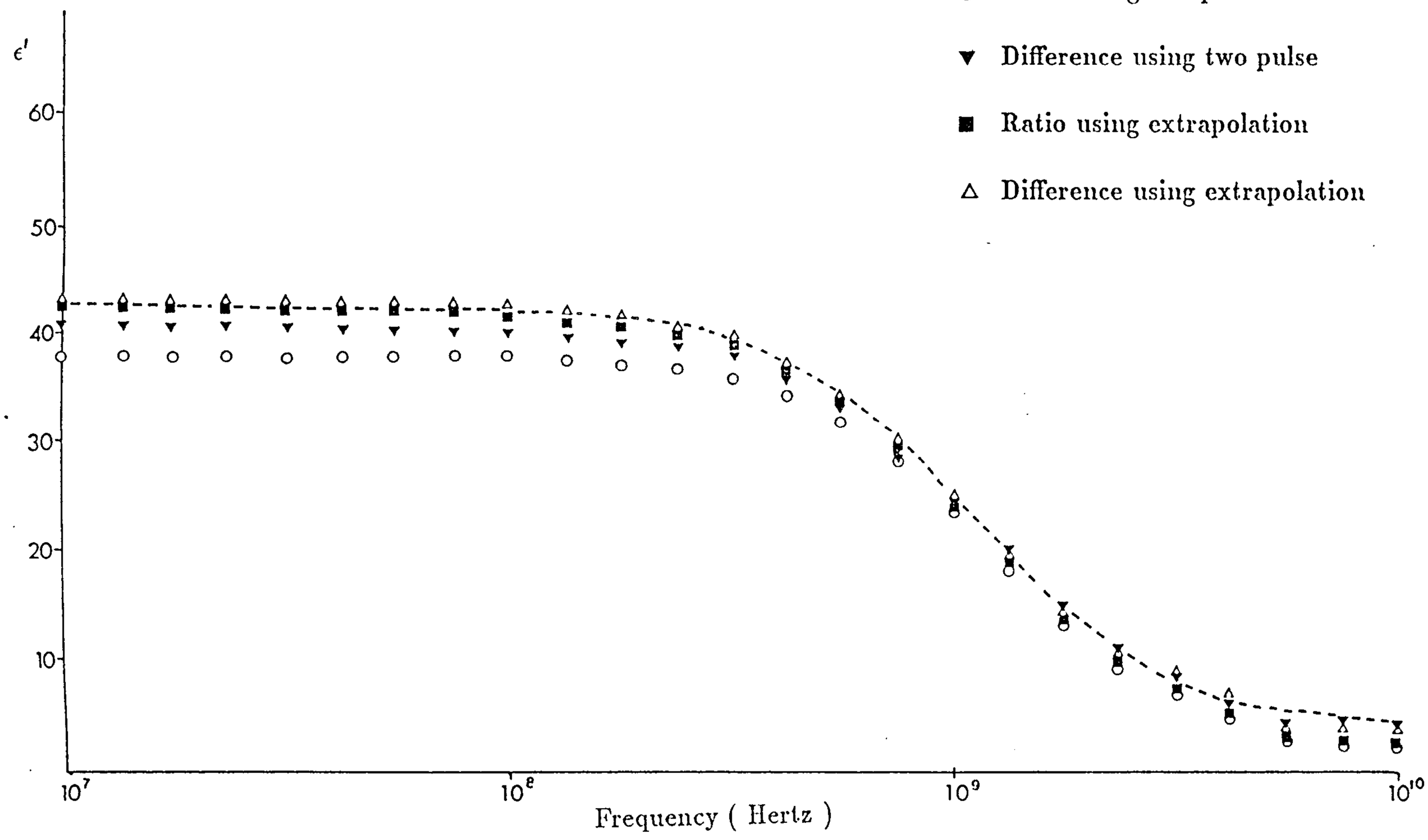

Fig 5.8 ϵ' versus frequency for ethanediol at 20°C.

Random errors in experimental data :
0.3% up to and including 1 GHz, 5.5% up to 10 GHz.

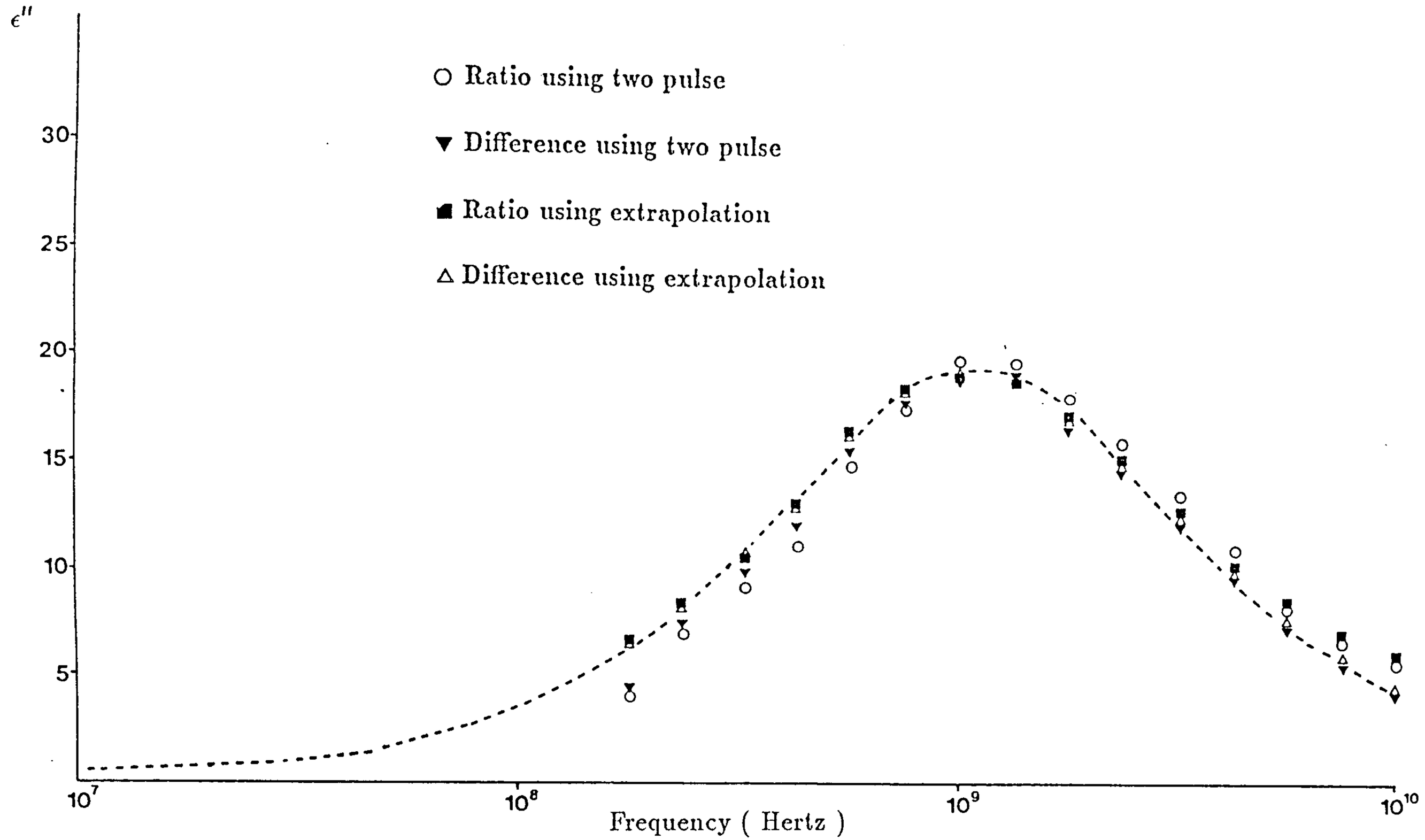

Fig 5.9 ϵ'' versus frequency for ethanediol at 20°C.

Random errors in experimental data :
0.5% up to and including 1 GHz, 3.8% up to 10 GHz.

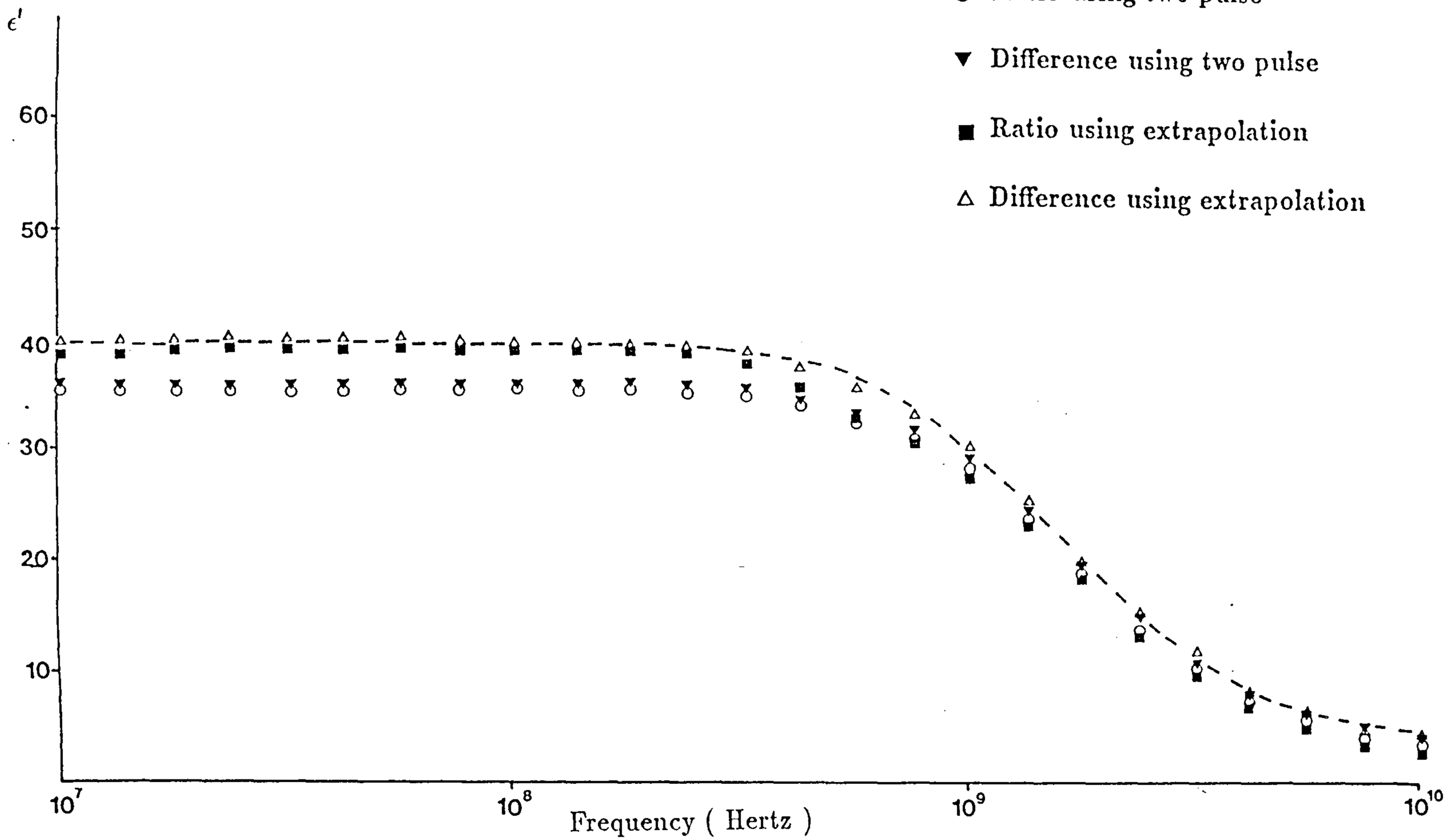

Fig 5.10 ϵ' versus frequency for ethanediol at 30°C.

Random errors in experimental data :
0.3% up to and including 1 GHz, 5.5% up to 10 GHz.

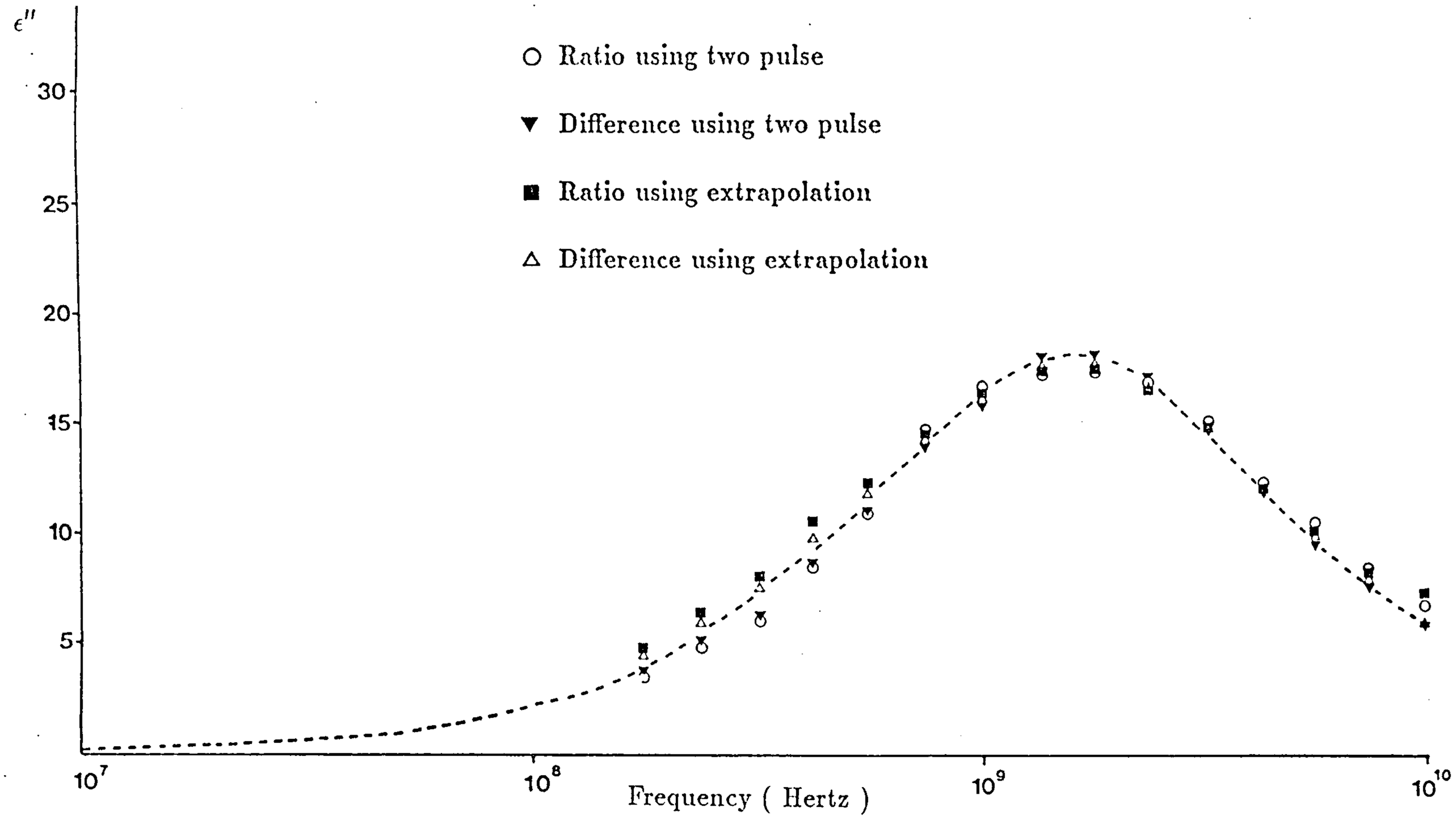

Fig 5.11 ϵ'' versus frequency for ethanediol at 30°C.

Random errors in experimental data :
0.46% up to and including 1 GHz, 4.5% up to 10 GHz.

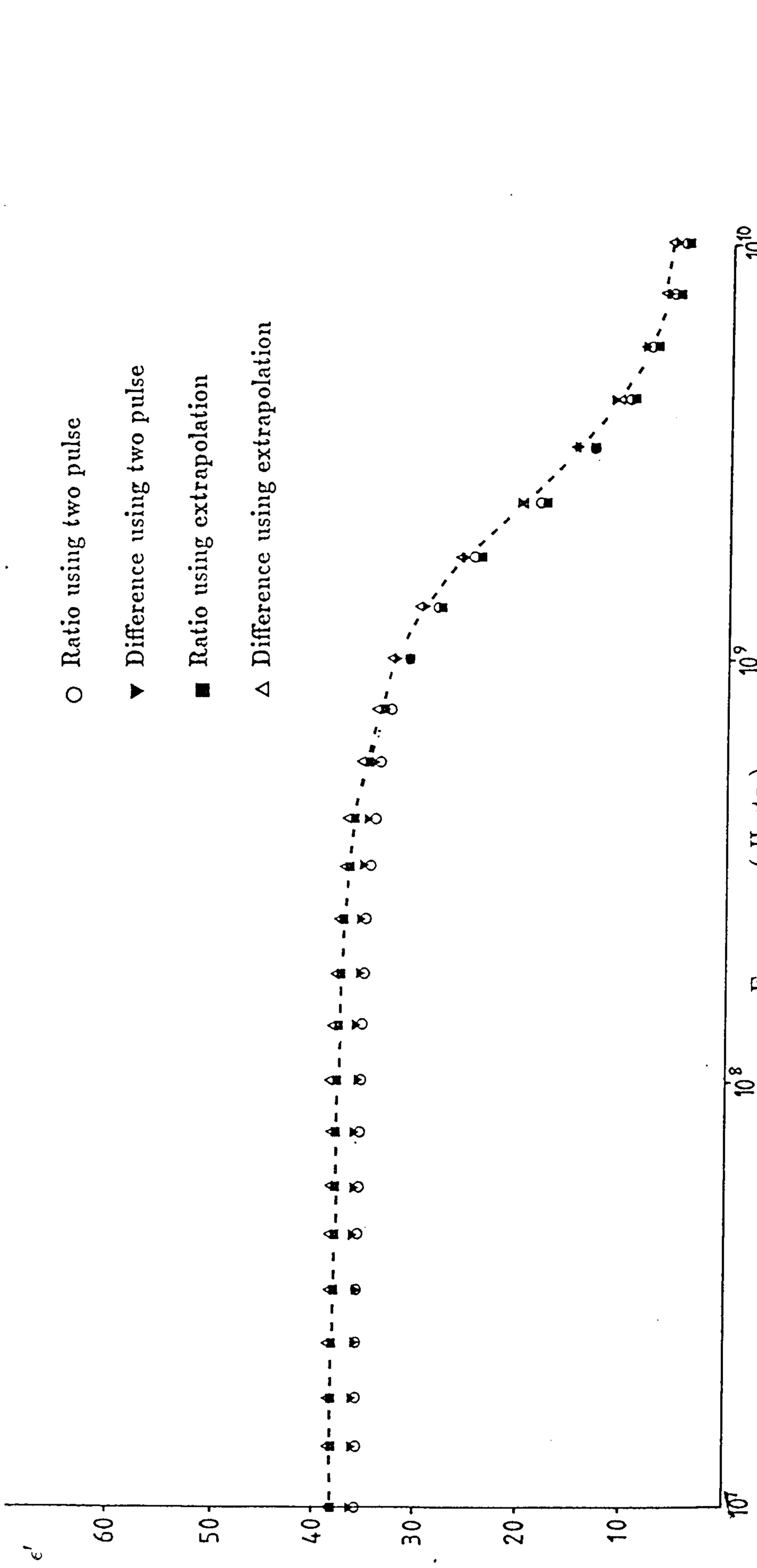

Fig 5.12 ϵ' versus frequency for ethanediol at 40°C.

Random errors in experimental data :
0.5% up to and including 1 GHz, 4.5% up to 10 GHz.

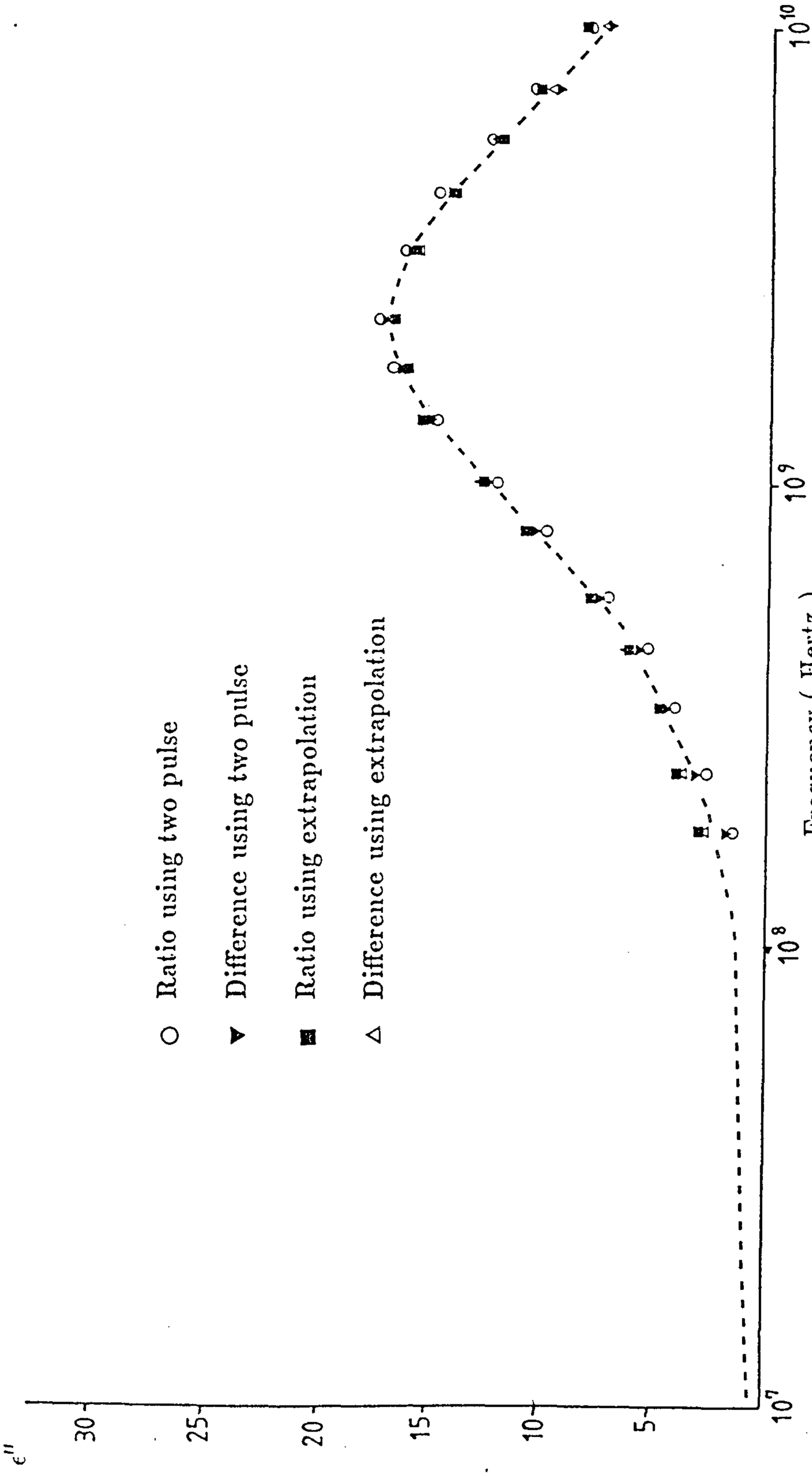

Fig 5.13 ϵ'' versus frequency for ethanediol at 40°C.

Random errors in experimental data :
0.44% up to and including 1 GHz, 3.6% up to 10 GHz.

to the misalignment in the time origin between the sample and the reference. At these high frequencies the error introduced by the term $\omega \triangle t$ becomes significant. This appears in the extrapolation as a function of the leading edge. If the sample and the reference are exactly the same there will be no error, due to the fact the leading edge would not change. However when two different liquids are used there will be a slight difference in the response. This will then become apparent in the calculation of the time origin and introduce an error in the permittivity calculated. The two pulse does not suffer such a drawback as the marker is independent of the sample used and therefore does not change shape. Thus the method of fitting to the marker pulse should find the same time origin each time the experiment is run.

It is also apparent that the two pulse time referencing technique does not give accurate results in the low frequency end of the spectrum. With reference to Fig 5.15, this can be attributed to the loss of some of the steady state information due to the need for the marker pulse to be in the time window. When this happens the pulse is shifted and the low frequency information content is reduced. One answer to this point is that the time base setting on the oscilloscope may be increased resulting in a much wider time window. However, this only results in increasing the steady state component at the expense of a well defined marker pulse (Fig 5.16). The marker pulse is derived from the leading edge of the input pulse and subsequently longer sweep speeds only reduce the width of the marker. At settings greater than 20 ns cm^{-1} the marker appears as a glitch and will only contribute to the noise spectrum.

The results for the ethanediol merely confirm the fact that the two techniques are of similar accuracy. However it is seen that the difference between the experimental and the generated values at the high frequency components of the spectrum are relatively large, particularly when the ratio technique is used. These errors are not functions of the time referencing technique chosen but are due to the complex errors introduced by the use of the equivalent circuit in conjuction with either the ratio and difference techniques. These errors can be more fully explained by examining the reflection coefficient.

5.4.2 Errors Introduced by the Ratio and Difference Techniques.

From Gabriel (1987) the reflection coefficient measured is of the form

$$\Gamma_{act} = A\Gamma_{meas} + B \tag{5.1}$$

where A and B are functions of the probe used. In using the difference and ratio techniques certain assumptions have to be made as to the magnitude of these constants. In the ratio technique the value of B is assumed to equal 0, whereas in the difference technique the value is assumed to be the same in each case which is valid provided there is a good match between the sample and the reference.

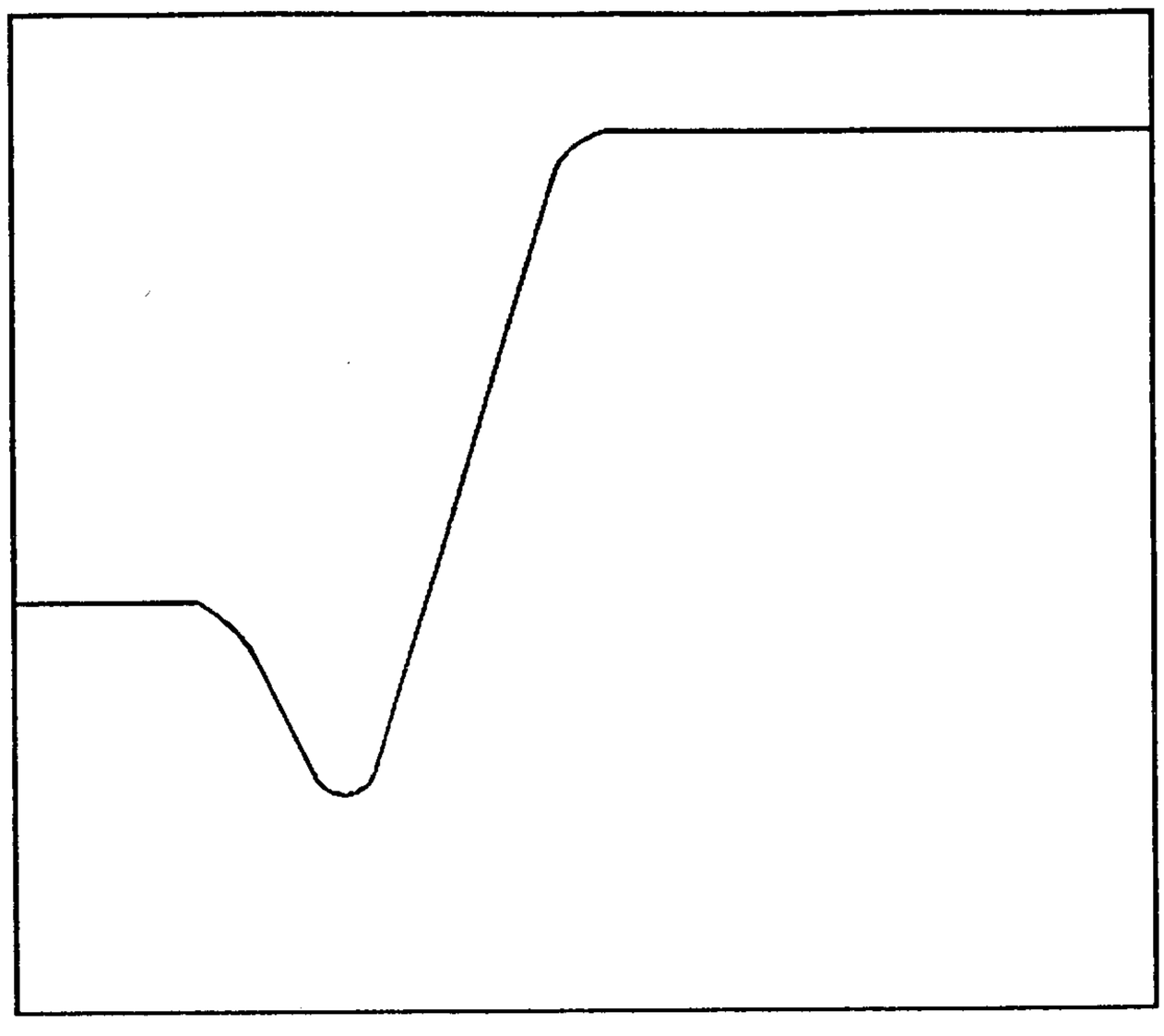

Fig 5.14(a) Time window for the extrapolation time referencing technique.

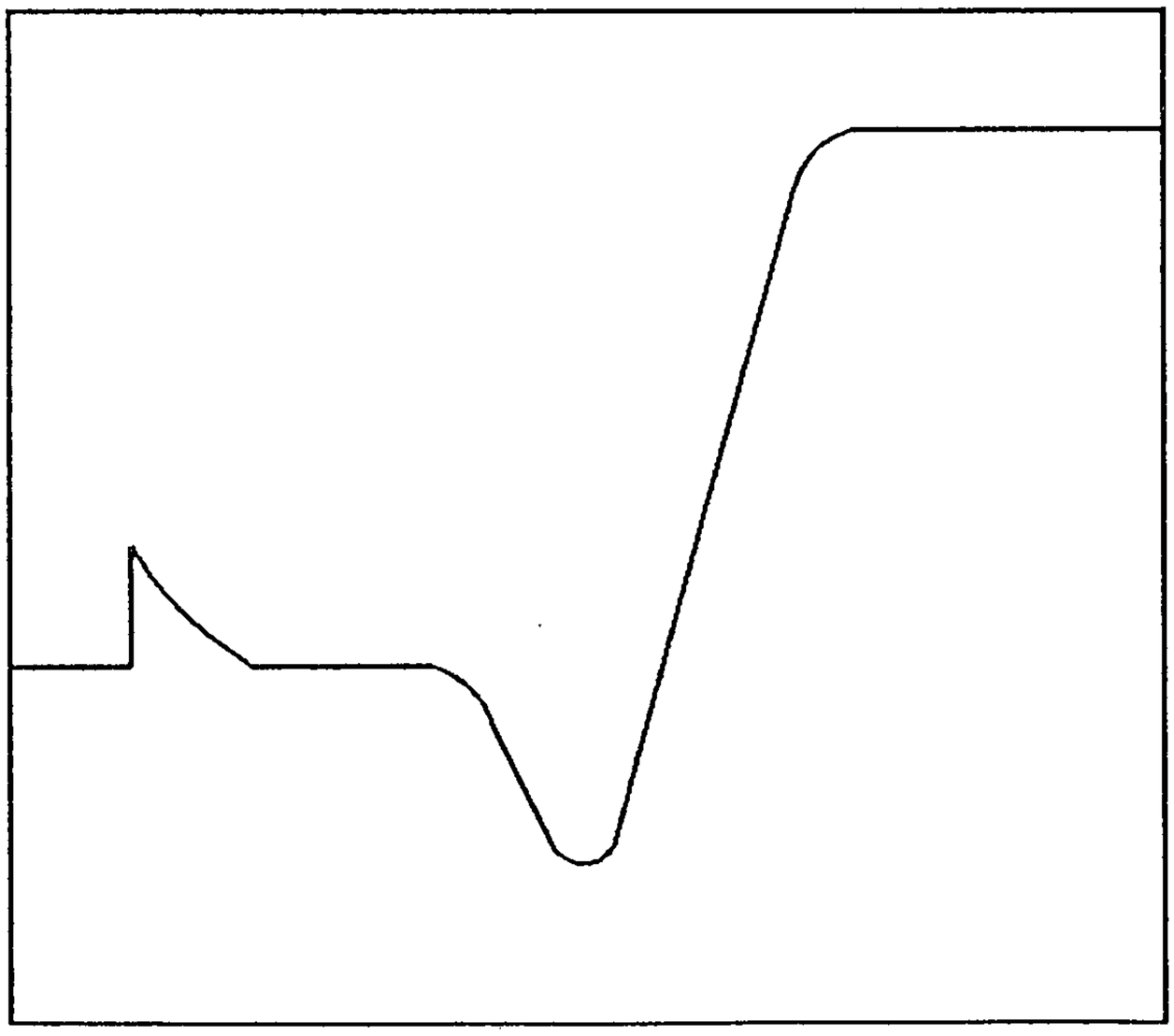

Fig 5.14(b) Time window for the two pulse time referencing technique.

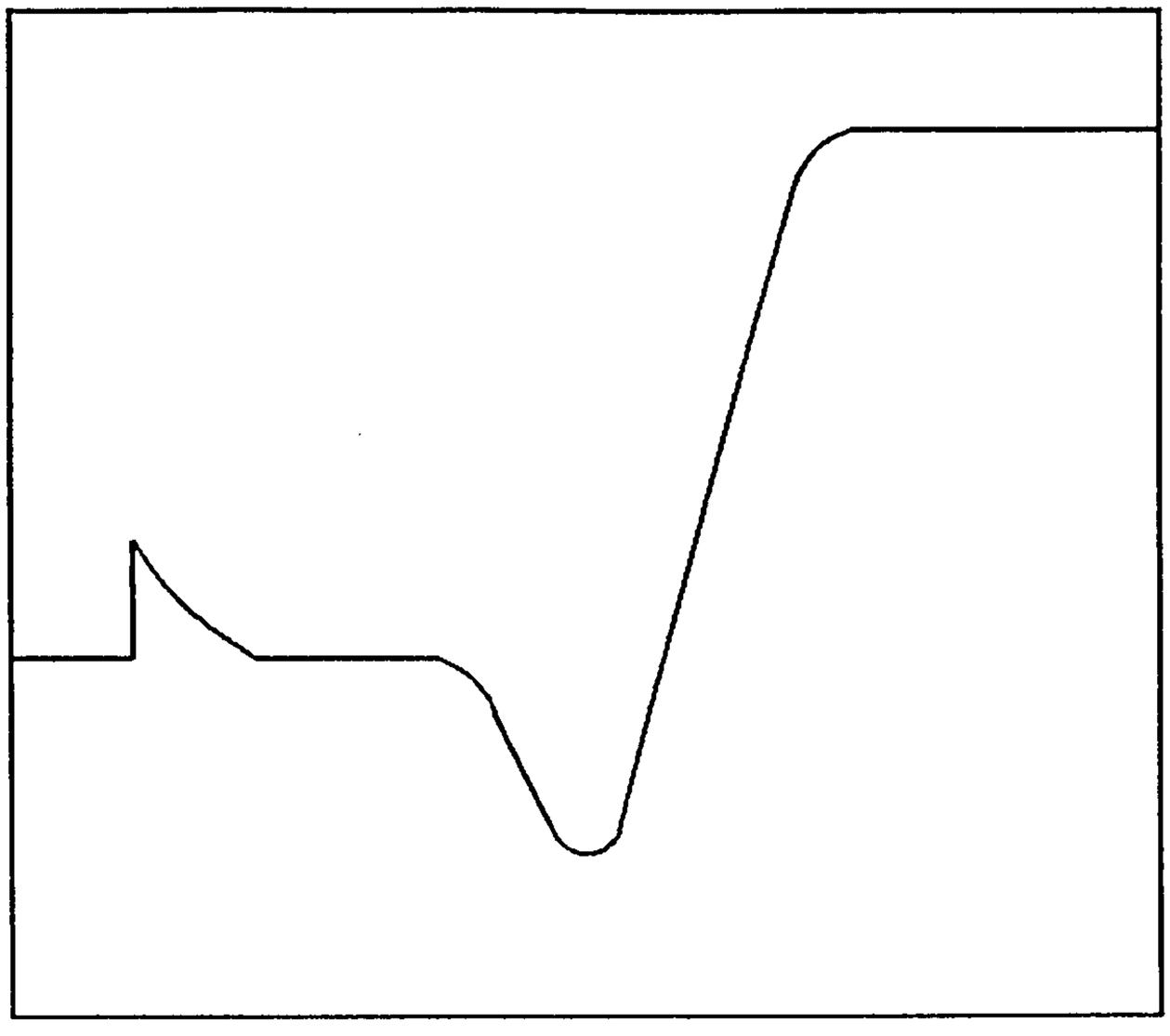

Fig 5.15(a) Waveform captured using a sampling interval of 5 ps.

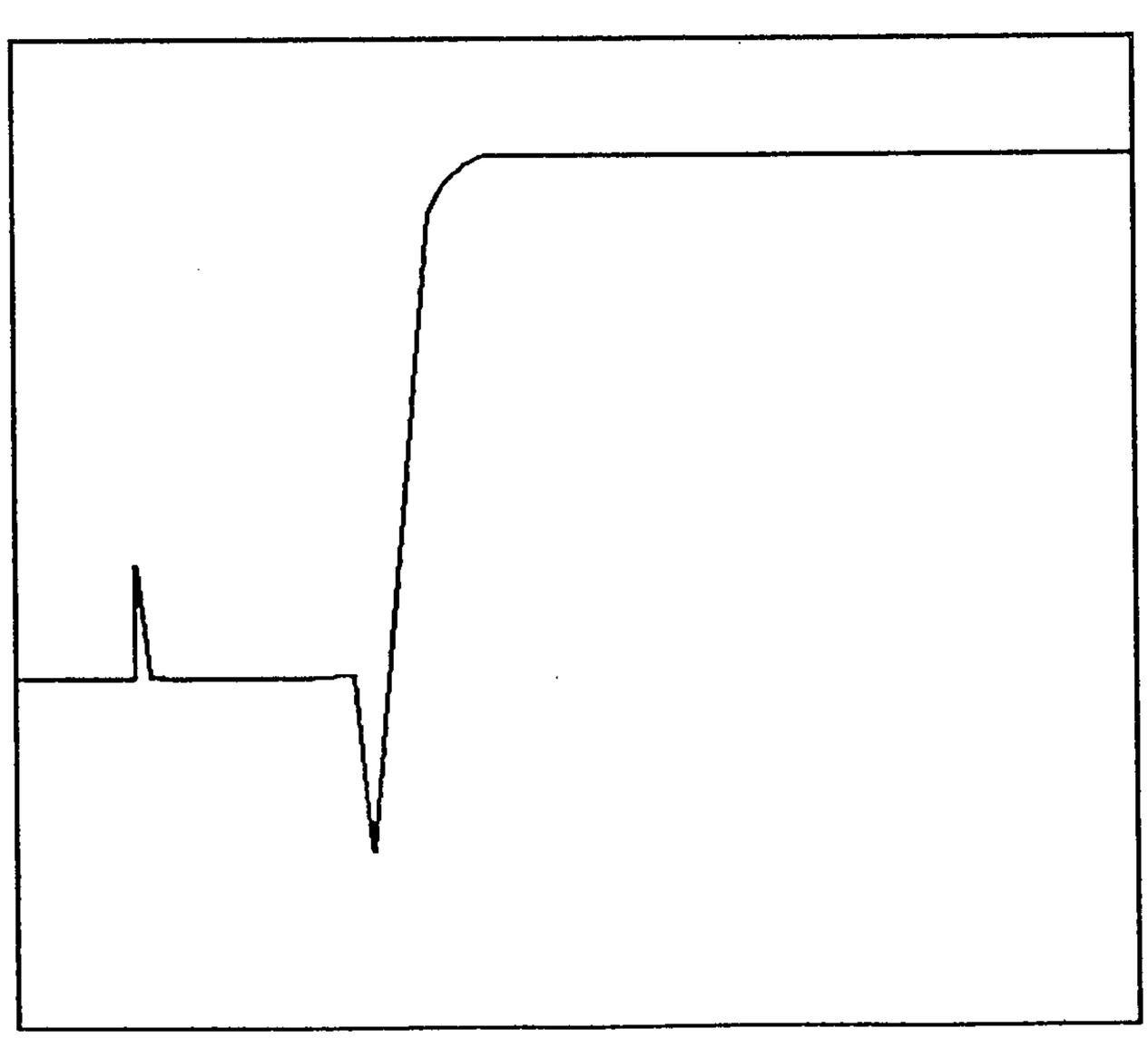

Fig 5.15(b) Waveform captured using a sampling interval of 10 ps.

If Γ_s and Γ_r are the reflection coefficients of the sample and the reference respectively, the difference technique yields

$$A\Gamma_s + B - (A'\Gamma_r + B') + \Gamma_r \tag{5.2}$$

If the same probe is used for both measurements and the sample and reference are well matched then $A = A'$ and $B = B'$ and equation (5.2) can be written as

$$A(\Gamma_s - \Gamma_r) + \Gamma_r \tag{5.3}$$

If $A \approx 1$ then the corrected reflection coefficient will be Γ_s. Any relatively small differences in the values of B and B' will only contribute a small error in Γ_s due to the nature of the difference. However in the ratio technique the significance of B and B' increases. By using equation 5.1 and 4.27 the ratio equation becomes

$$\frac{A\Gamma_s + B}{A'\Gamma_r + B'} \times \Gamma_r \tag{5.4}$$

Provided $B = B' = 0$ and $A = A'$ the reflection coefficient Γ_s can be easily found. However if there is a mismatch the contribution of B and B' will result in errors in the permittivity calculated particularly in the higher frequency components. This is more evident in the case of the ethanediol than that of the formamide. As the sample and reference are matched in each the differences are probably due to the low sensitivity of the probe for permittivities below a value of 10.

5.4.3 Summary of Results for Ethanediol and Formamide.

The choice of the best time referencing technique is dependent on the frequency range and the time base setting on the oscilloscope. If components greater than 1 GHz are required then the two pulse technique gives slightly better results. However the difference between these and those obtained by the extrapolation technique are within experimental error limits.

The use of the difference technique over the ratio technique is strongly recommended when dealing with low permittivity substances. The significance in the variation of the probe parameters is clearly evident from the results of the ethanediol experiment with the ratio technique in use. These errors are less prominent in the difference technique but contribute to the errors in the calculation of the permittivity from the reflection coefficient.

5.5 Human in-vivo Measurements.

Measurements are made *in-vivo* on different parts of the human body. The outer jaw, inner jaw, ear lobule and the tongue of one volunteer are measured, while the palm of the hand and the fore-arm of two humans are also examined. Results for each experiment are presented.

5.5.1 Experimental Procedure for in-vivo Measurements

It was hoped that the three probes analysed in chapter 3 would be used in the measurements on human tissue. This was not possible due to the low sensitivity of the small radius probe. Another problem encountered was due to the size of the conical probe. When measuring the inner jaw, outer jaw, tongue and ear lobule the surface area of the probe was too large for adequate contact to be made with the tissue. Therefore all measurements on these parts of the body were taken using the 7 mm probe.

In each case the surface was cleaned and dried. Some AGAR * conductive gel was then placed on the area of interest to increase the electrical coupling and was spread evenly. Sufficient pressure was then applied between the probe and the sample area to ensure a good contact. After each sample run the reference response was taken. This procedure was repeated for each experimental run.

The most important point is that of ensuring the same amount of pressure and sample area is used in each run. This can be difficult when the tongue, ear, and inner jaw are being analysed. As a result larger experimental fluctuations are expected for these samples than for the palm, forearm and outer jaw.

5.5.2 Histological Overview

In order to fully understand the difference in the results for each of the tissues measured a brief description of the tissue structure will be given. The inner and outer jaw measurements were taken on the cheek part of the mouth and the structure of the cheek as well as the tongue are explained in detail. The other parts of the body studied are relatively similar to each other being a tissue structure covered with a skin of varying thickness. Consequently the histological analysis concentrates on the skin. A full glossary of the medical terms used is given in the Appendix to chapter 5.

---

* AGAR is the trade name of the hypoallergenic aqueous electromedical coupling agent designed for use with electrical nerve stimulators and other contact electrodes.

The composition of the cheeks consists of a muscular stratum, and a large quantity of fat, together with areolar tissue, vessels, nerves and buccal gland, covered with skin externally and with mucous membrane internally (McArthur 1988). The principal muscle is the buccanitor. The buccal glands are small mucous glands placed between the mucous membrane and the buccanitor.

The tongue is a muscular organ covered by a mucous membrane which is firmly bound to the underlying muscle by a dense, collagenous, lamina propria which is continuous with the epimysium of the muscle (McArthur 1988). The surface of the tongue is crowded with four papillae : filiform, fungiform, circumvallate and foliate papillae (Fig 5.16). The filiform are the most numerous and consist of a dense connective tissue core and heavily keratinised surface. Fungiform have a thin non-keratinised epithelium and a richly vascularised connective tissue. The circumvallate are the largest and least common paillae and are set into the tongue surface and circled by a deep cleft. The foliate papillae are very rarely evident in humans.

The skin forms the continuous covering of the body and varies in thickness, reflecting the various functional purposes. However the basic structure remains the same (Fig 5.17). The external surface, the epidermis, is supported and nourished by a thick layer of dense, fibro-elastic connective tissue called the dermis. The junction between the epidermis and the dermis is characterised by downward folds, the epidermal ridges, which interdigitate with upward projections from the dermis, termed the dermal papillae. The dermis, in turn, is attached by the hypodermis to the underlying tissue.

The epidermis itself consists of the stratum granulosm, the stratum corneum, the stratum spinosum and the stratum basale (in order of appearence from the outer surface of the epidermis to the dermis transition). In some specimens of thick skin there is another layer between the stratum granulosm and the corneum termed the stratum lucidium.

5.5.3 Measurements on the Outer and Inner Jaw, Ear lobe and Tongue

Measurements on the tissues were taken in the frequency range 100 MHz to 10 GHz. As a sampling interval of 5 ps was used certain points in the frequency spectrum have to be ignored. Consequently the experimental results cover the frequency range 200 MHz to 10 GHz.

The reference used for the experiment was water. The room temperature and the reference sample were held at 21°C. Each experiment was repeated eight times.

The results for each of the series of measurements are tabulated in tables 5.2 to 5.5 for the inner cheek, outer cheek, tongue and ear lobule, respectively, and in Figs 5.18 and 5.19.

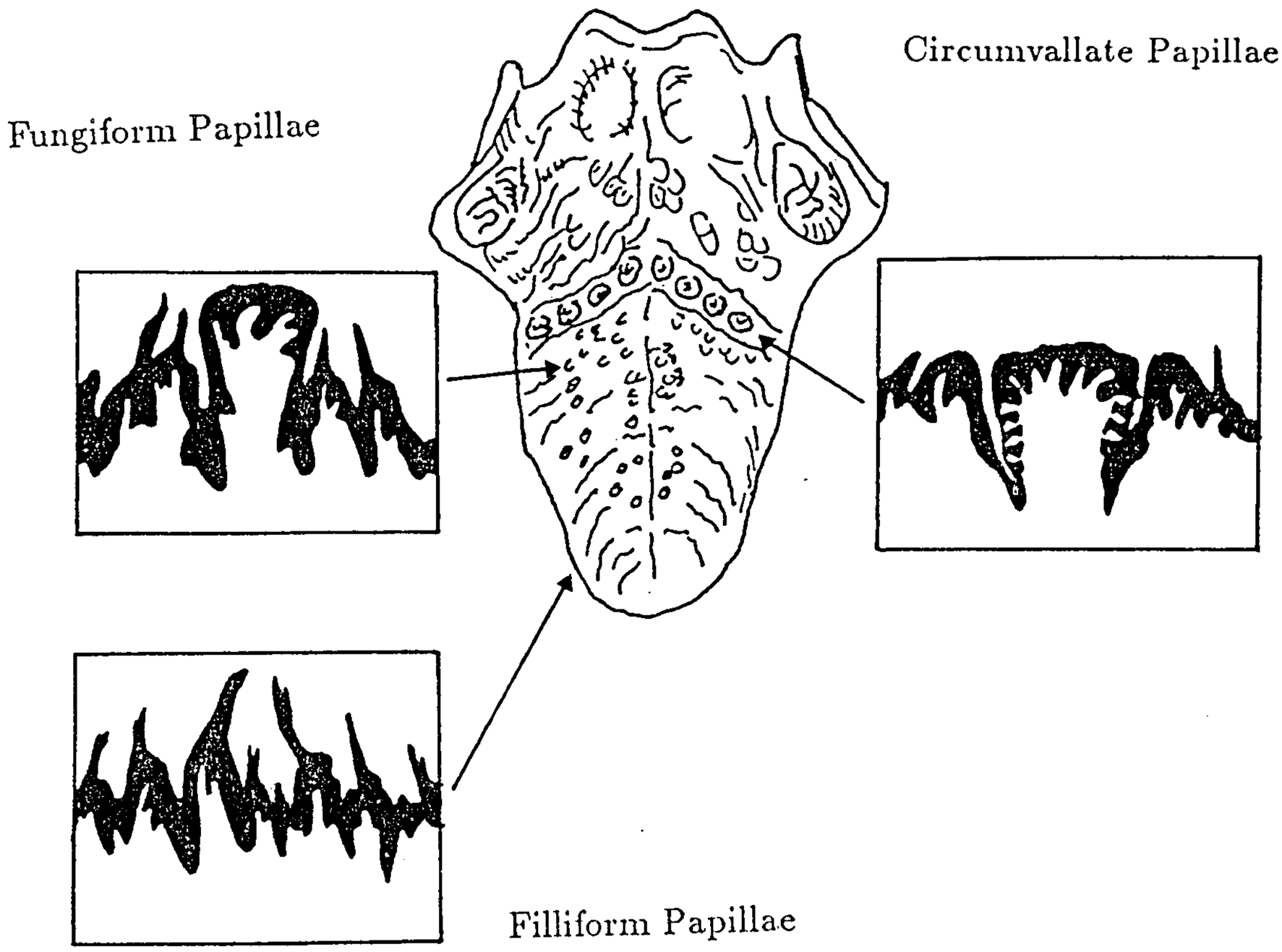

Fig 5.16 Histological description of the tongue.

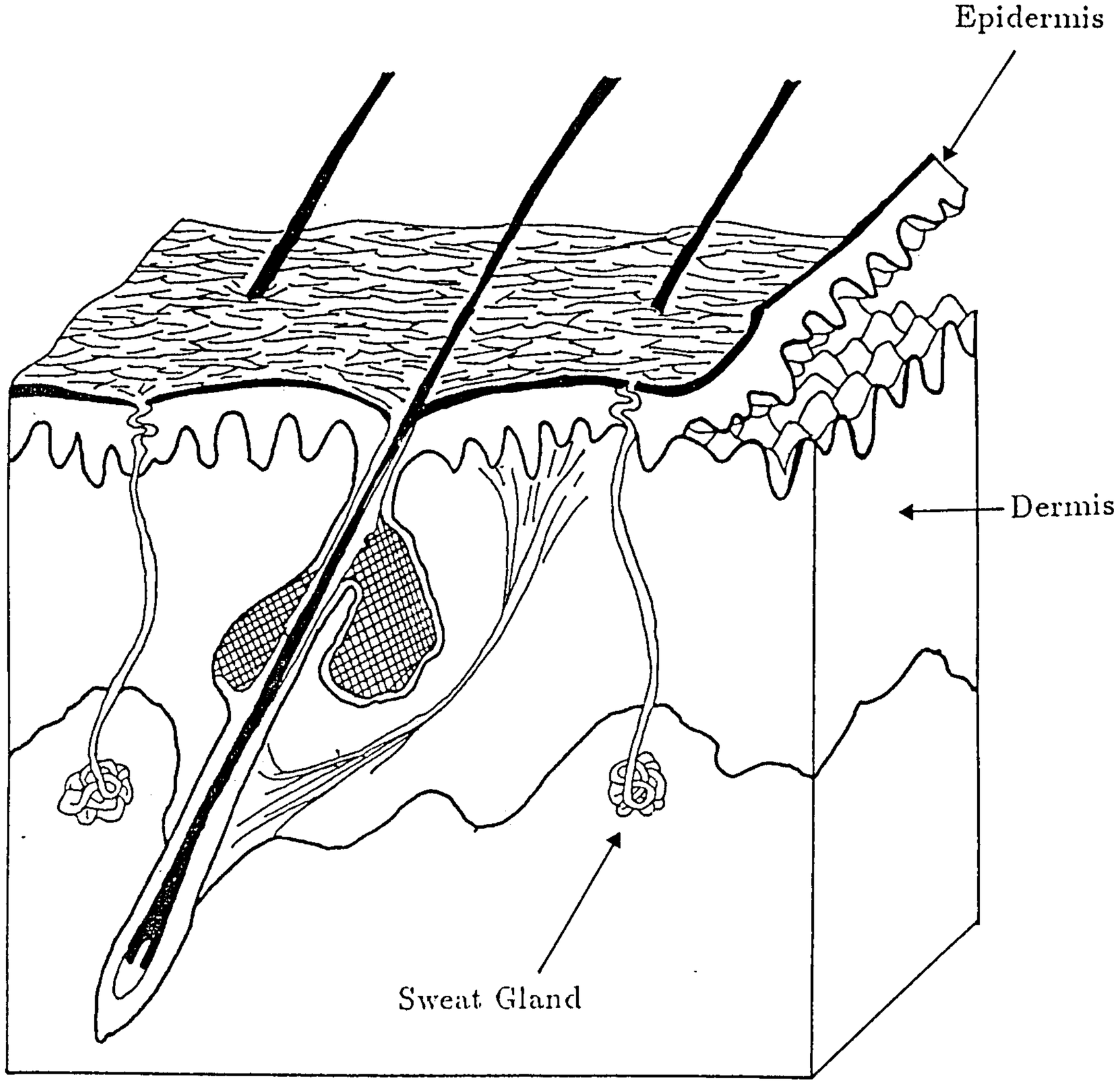

Fig 5.17 Diagram of the human skin structure.

freq (GHz)	ϵ'	$\triangle\epsilon'$	ϵ''	$\triangle\epsilon''$
0.215	73.2	0.8	45.1	2.0
0.216	72.1	0.8	39.5	1.7
0.316	70.8	0.8	35.2	1.4
0.383	69.2	0.8	31.7	1.3
0.464	67.5	0.7	29.0	1.1
0.562	65.7	0.7	26.9	1.1
0.681	63.7	0.8	25.1	1.1
0.825	61.6	0.7	23.2	1.0
1.000	59.1	0.7	21.2	1.0
1.211	57.2	0.7	18.1	0.7
1.467	56.0	0.7	15.8	0.7
1.778	55.5	0.7	14.5	0.6
2.154	55.2	0.7	14.0	0.7
2.610	55.5	0.7	14.7	0.7
3.162	55.0	0.6	15.7	0.7
3.831	55.5	0.7	16.5	0.6
4.641	55.1	0.5	20.2	0.7
5.623	55.6	0.7	29.9	1.0
6.812	55.7	1.3	36.5	2.0
8.254	53.2	1.0	41.9	5.0
10.000	48.5	3.4	55.9	8.2

Table 5.2 ϵ' and ϵ'' for the inside of the human cheek.

freq (GHz)	ϵ'	$\triangle\epsilon'$	ϵ''	$\triangle\epsilon''$
0.215	61.0	0.3	41.0	1.9
0.216	59.4	0.3	37.2	1.5
0.316	57.4	0.3	34.2	1.2
0.383	55.1	0.3	31.7	1.0
0.464	52.5	0.3	29.6	0.8
0.562	49.7	0.3	27.7	0.6
0.681	46.9	0.3	26.1	0.5
0.825	44.1	0.3	24.2	0.5
1.000	41.4	0.2	21.9	0.4
1.211	39.5	0.2	18.2	0.4
1.467	39.2	0.3	16.5	0.4
1.778	37.7	0.3	16.4	0.3
2.154	38.0	0.3	15.0	0.3
2.610	37.7	0.2	13.4	0.4
3.162	38.5	0.2	12.5	0.3
3.831	38.1	0.3	12.8	0.3
4.641	38.0	0.4	13.5	0.4
5.623	36.7	0.6	16.1	1.6
6.812	35.5	0.7	22.8	1.3
8.254	36.0	1.8	32.9	3.4
10.000	34.0	3.7	52.2	3.6

Table 5.3 ϵ' and ϵ'' for the outside of the human cheek.

freq (GHz)	ϵ'	$\triangle\epsilon'$	ϵ''	$\triangle\epsilon''$
0.215	69.4	0.3	40.1	0.8
0.216	68.0	0.3	35.7	0.7
0.316	66.4	0.2	31.3	0.6
0.383	64.7	0.3	27.4	0.5
0.464	63.3	0.3	24.1	0.4
0.562	62.1	0.4	21.4	0.4
0.681	60.9	0.6	19.5	0.3
0.825	59.5	0.7	17.7	0.3
1.000	58.0	0.7	16.0	0.2
1.211	57.3	0.7	14.8	0.2
1.467	55.8	0.7	14.3	0.2
1.778	55.0	0.8	13.0	0.2
2.154	54.1	0.8	12.3	0.1
2.610	53.6	1.1	13.5	0.3
3.162	54.0	1.0	14.2	0.5
3.831	54.3	0.8	15.2	1.0
4.641	52.3	1.2	19.3	1.0
5.623	51.6	1.2	21.0	0.7
6.812	51.3	1.1	21.2	0.6
8.254	49.5	1.8	28.4	2.0
10.000	39.9	1.6	45.7	6.2

Table 5.4 ϵ' and ϵ'' for the human tongue.

freq (GHz)	ϵ'	$\triangle\epsilon'$	ϵ''	$\triangle\epsilon''$
0.215	58.3	0.8	38.7	2.1
0.216	56.4	0.8	33.8	1.8
0.316	54.2	0.8	29.5	1.5
0.383	52.3	0.8	25.3	1.4
0.464	50.8	0.8	21.8	1.2
0.562	49.7	0.8	19.2	0.9
0.681	48.0	0.8	17.3	0.9
0.825	46.1	1.0	15.3	0.8
1.000	44.3	1.1	13.8	0.7
1.211	43.0	1.0	12.1	0.6
1.467	42.6	1.2	11.2	0.6
1.778	41.0	1.0	10.3	0.6
2.154	39.4	1.2	9.8	0.6
2.610	39.0	1.2	10.0	0.6
3.162	39.5	1.2	9.6	0.6
3.831	38.6	1.2	9.4	0.6
4.641	38.1	1.2	10.7	0.7
5.623	37.6	1.1	13.6	0.8
6.812	36.5	1.5	14.8	0.8
8.254	35.9	1.4	19.7	1.2
10.000	29.5	1.8	31.8	4.3

Table 5.5 ϵ' and ϵ'' for the human ear lobule.

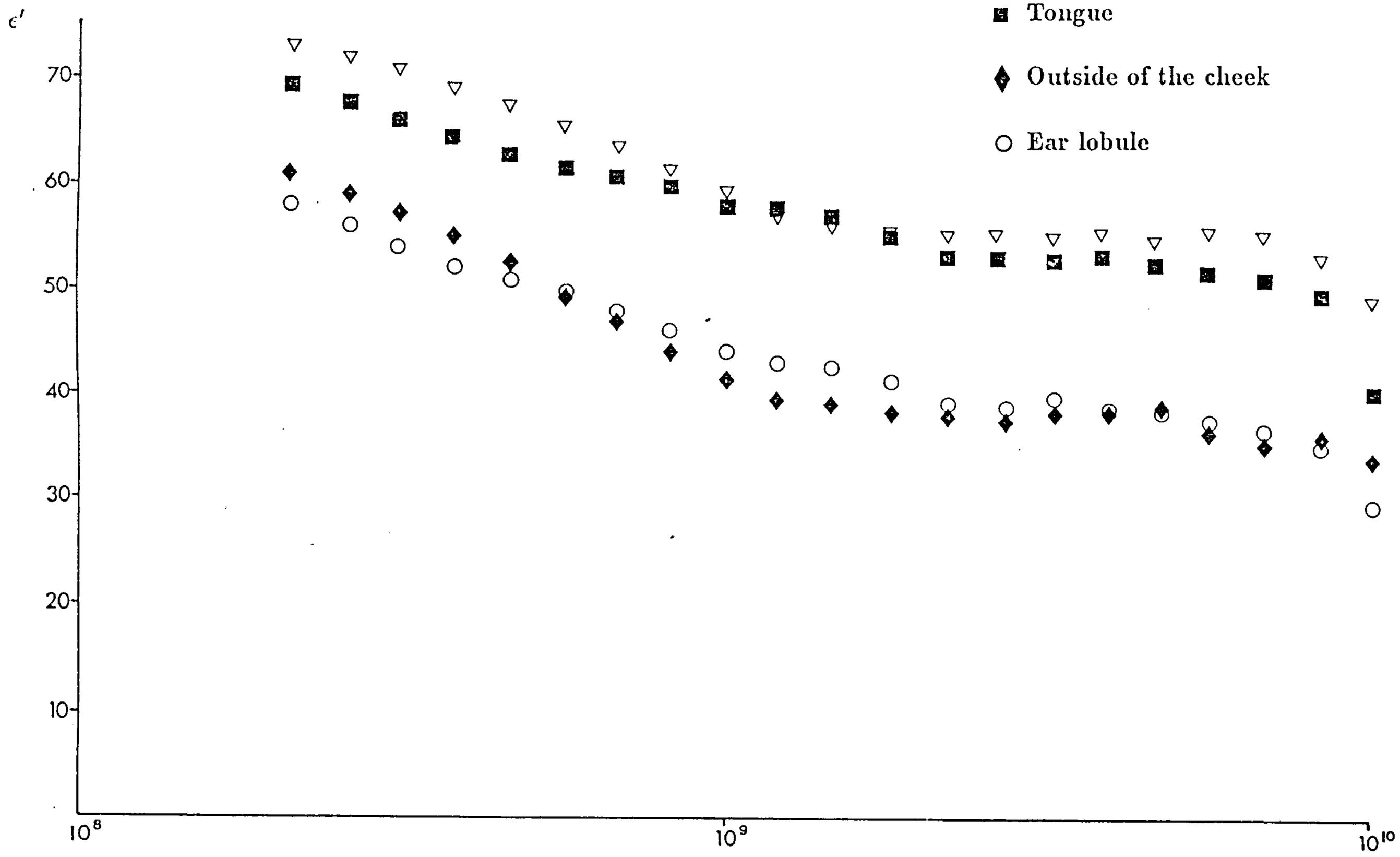

Fig 5.18 ϵ' versus frequency for the inner and outer cheek, the tongue and the ear lobule at 21°C.

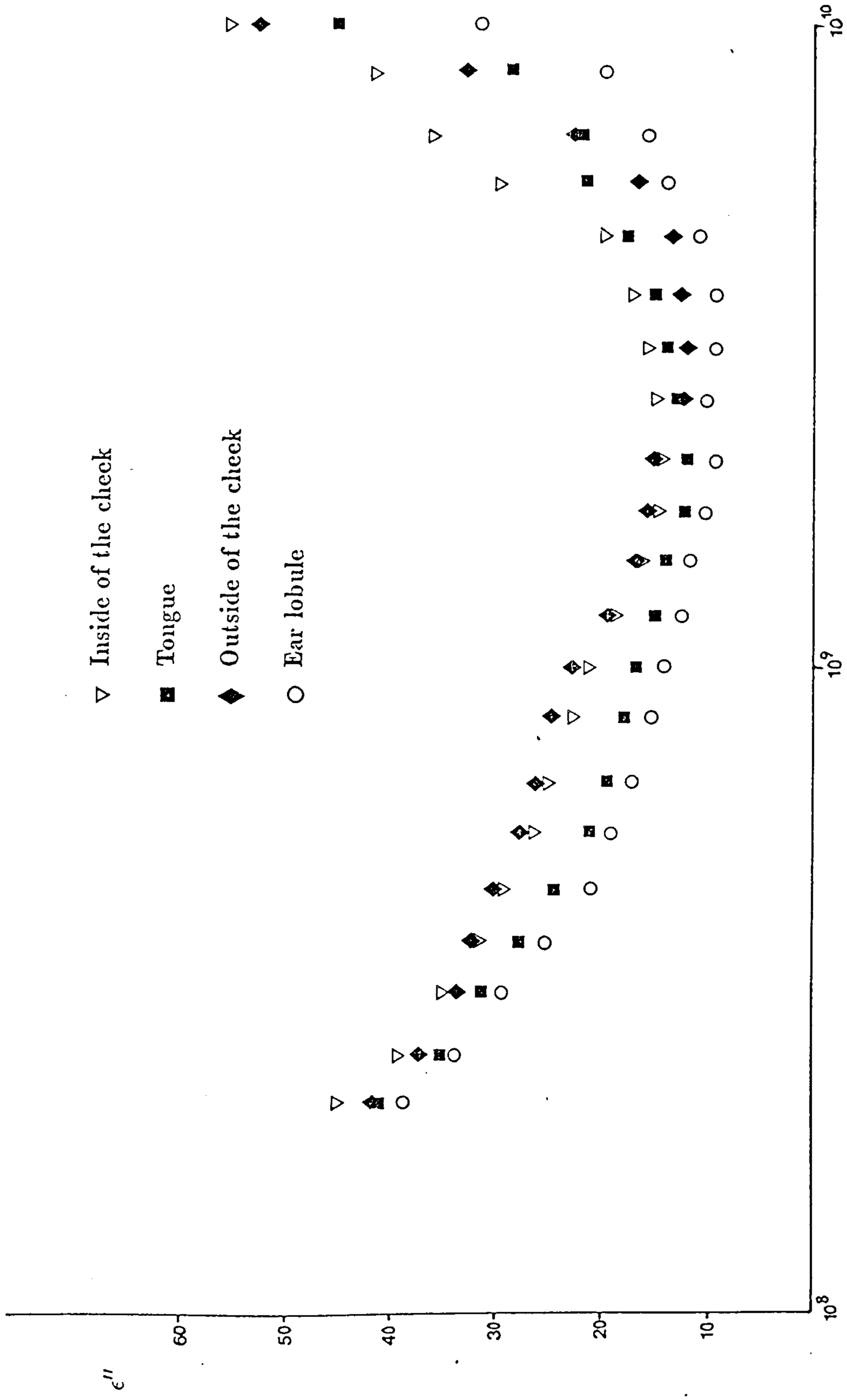

Fig 5.19 ϵ'' versus frequency for the inner and outer cheek, the tongue and the ear lobule at 21°C.

The differences in the random errors for the different tissue samples can be explained simply. When repeated measurements are made on the inner cheek and the tongue it is difficult to analyse the same section of the tissue for each experimental run. Therefore different sections can be, and are, examined. The probe can be positioned exactly on the same section of the ear lobule for each measurement. However this suffers from the fact that the surface area of this part of the body is small and adequate contact may not be made.

Using the histological description of the tissues the dielectric results can be interpreted. The higher values for the inner cheek and tongue are easily explained. The lining of the cheek is mucous membrane which will have a much higher water content than the outer skin layer. Subsequently one would expect the ϵ' to be higher. The fact that it is also higher than the tongue is due to the presence of the papillae on the tongue's surface which effectively shield the mucous membrane and muscle layers. The ear lobule and the outer cheek exhibit similar dispersion curves. However the slight increase in the results for the outer cheek leads to an interesting point. The main difference between the ear lobule and the outer cheek is the presence of a fatty layer below the dermis of the skin. This would result in a much lower water content and subsequently lower ϵ' values for the ear (Cook 1951). This is clearly evident form the results shown in Fig 5.18 and as a result it can be concluded that the probe does have some penetration into the fat layer.

The main dielectric dispersion in the frequency range covered in this particular experiment is known as the β, γ and δ dispersion (Grant *et al* 1978). The sharp fall in the ϵ' values in the 8 to 10 GHz region can be attributed to the classical γ dispersion. This is due to the dielectric relaxation of the bulk water in the tissue and behaves in a similar manner to pure water (Schwan *et al* 1980, Gabriel *et al* 1985). The δ dispersion resulting from the relaxation of the bound water cannot be distinguished from the main β dispersion. As only the high frequency end of this dispersion is apparent in the data no attempt has been made to fit any dielectric dispersion function.

5.5.4 Measurements on the Palm and the Forearm.

The 7mm probe was used in conjunction with a sampling interval of 5 ps for measurements on the palm and the forearm. This allowed the frequency range covered to extend from 100 MHz to 10 GHz. As in the previous section the actual lower working limit was restricted to 200 MHz. Again the reference used was water and the operating temperature held at 21°C. Each experiment was repeated for both volunteers for eight experimental runs.

The results are tabulated in tables 5.5 to 5.8 and shown graphically in figs 5.20 and 5.21.

freq (GHz)	ϵ'	$\triangle\epsilon'$	ϵ''	$\triangle\epsilon''$
0.215	53.0	0.5	32.1	2.5
0.216	51.2	0.6	28.5	2.1
0.316	48.9	0.6	25.3	1.8
0.383	46.7	0.6	22.2	1.6
0.464	44.8	0.8	19.5	1.3
0.562	43.1	0.8	17.3	1.1
0.681	41.3	0.8	15.7	1.0
0.825	39.1	1.0	14.1	0.9
1.000	36.9	1.1	12.5	0.8
1.211	34.1	1.0	11.2	0.8
1.467	33.6	1.0	10.2	0.7
1.778	32.5	1.0	10.5	0.7
2.154	30.4	1.0	10.0	0.6
2.610	29.9	1.0	9.8	0.6
3.162	27.3	1.0	9.6	0.6
3.831	26.5	1.0	9.0	0.6
4.641	25.8	1.0	8.7	0.6
5.623	24.7	1.2	10.0	0.6
6.812	24.3	1.3	10.4	0.6
8.254	21.9	1.4	10.7	0.8
10.000	21.5	1.3	11.3	1.0

Table 5.6 ϵ' and ϵ'' for the palm of the first subject.

freq (GHz)	ϵ'	$\triangle\epsilon'$	ϵ''	$\triangle\epsilon''$
0.215	51.6	1.0	30.9	3.0
0.216	49.8	1.0	27.5	2.7
0.316	47.6	1.1	24.5	2.4
0.383	45.4	1.1	21.6	2.1
0.464	43.4	1.1	19.0	1.8
0.562	41.7	1.1	17.0	1.6
0.681	39.8	1.1	15.5	1.4
0.825	37.6	1.1	14.0	1.1
1.000	35.2	1.2	12.6	1.0
1.211	32.3	1.2	11.2	0.8
1.467	32.0	1.1	10.1	0.8
1.778	30.7	1.2	10.9	0.6
2.154	28.3	1.1	9.3	0.7
2.610	27.9	1.1	9.2	0.7
3.162	25.1	1.0	9.5	0.7
3.831	24.4	1.0	9.0	0.5
4.641	23.6	1.0	9.2	0.6
5.623	22.4	1.4	10.0	0.9
6.812	21.4	1.5	11.0	1.3
8.254	18.6	1.6	12.1	1.8
10.000	18.0	2.0	12.6	2.1

Table 5.7 ϵ' and ϵ'' for the palm of the second subject.

freq (GHz)	ϵ'	$\triangle\epsilon'$	ϵ''	$\triangle\epsilon''$
0.215	53.0	0.3	33.5	1.2
0.216	51.6	0.3	29.8	1.2
0.316	49.9	0.3	27.5	1.3
0.383	48.1	0.4	25.0	1.4
0.464	46.5	0.4	23.7	1.3
0.562	44.6	0.3	22.0	1.1
0.681	42.1	0.3	20.1	1.0
0.825	39.8	0.4	18.5	1.1
1.000	37.7	0.4	17.5	1.0
1.211	35.0	0.4	14.5	0.9
1.467	35.1	0.5	13.3	0.9
1.778	34.2	0.6	13.1	0.8
2.154	33.4	0.6	13.0	0.8
2.610	33.2	0.6	11.6	0.9
3.162	34.3	0.6	11.5	1.0
3.831	32.8	0.8	12.6	1.0
4.641	32.8	1.4	13.3	1.3
5.623	32.3	1.9	14.3	1.5
6.812	32.4	2.7	16.1	1.6
8.254	33.0	3.9	17.3	2.4
10.000	32.5	4.8	20.0	2.5

Table 5.8 ϵ' and ϵ'' for the arm of the first subject.

freq (GHz)	ϵ'	$\triangle\epsilon'$	ϵ''	$\triangle\epsilon''$
0.215	63.5	1.0	46.7	1.1
0.216	61.8	1.0	41.8	0.9
0.316	59.7	1.0	38.0	0.7
0.383	57.4	1.0	35.1	0.6
0.464	54.9	1.0	32.9	0.5
0.562	52.1	0.9	31.2	0.5
0.681	49.2	0.9	29.3	0.5
0.825	46.8	1.1	26.9	0.4
1.000	44.0	1.0	25.0	0.4
1.211	40.6	1.1	22.1	0.4
1.467	39.8	1.1	19.0	0.2
1.778	38.5	1.1	18.6	0.6
2.154	38.0	1.1	18.0	0.3
2.610	37.5	1.1	17.5	0.4
3.162	37.6	1.3	17.7	0.4
3.831	38.0	1.3	18.7	0.4
4.641	37.2	1.5	18.8	0.4
5.623	37.1	1.5	21.5	0.5
6.812	37.3	1.7	27.4	0.8
8.254	37.6	1.8	30.3	1.8
10.000	31.0	2.5	37.5	3.4

Table 5.9 ϵ' and ϵ'' for the arm of the second subject.

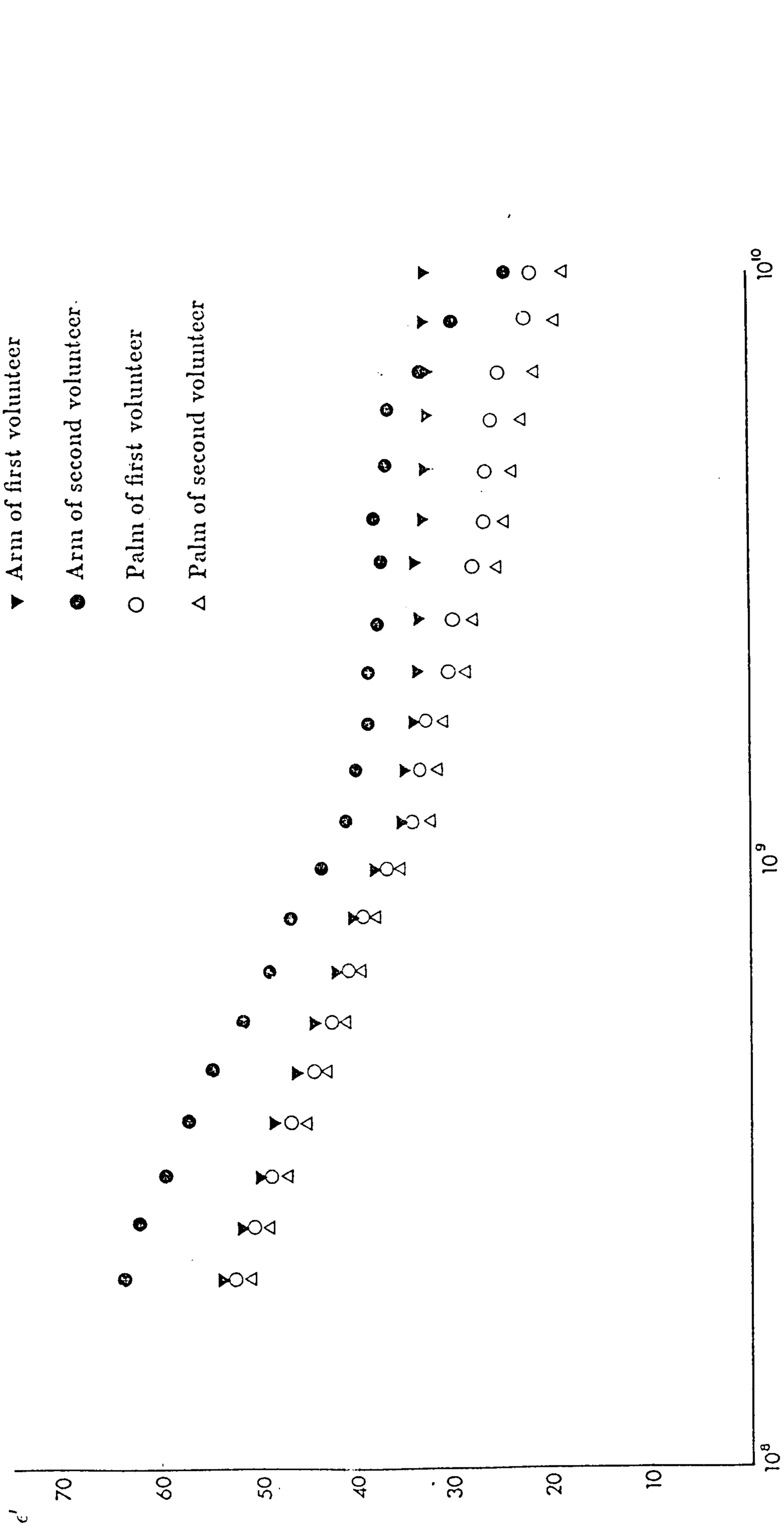

Fig 5.20 ϵ' versus frequency for the palm of the hand and the forearm for two different volunteers.

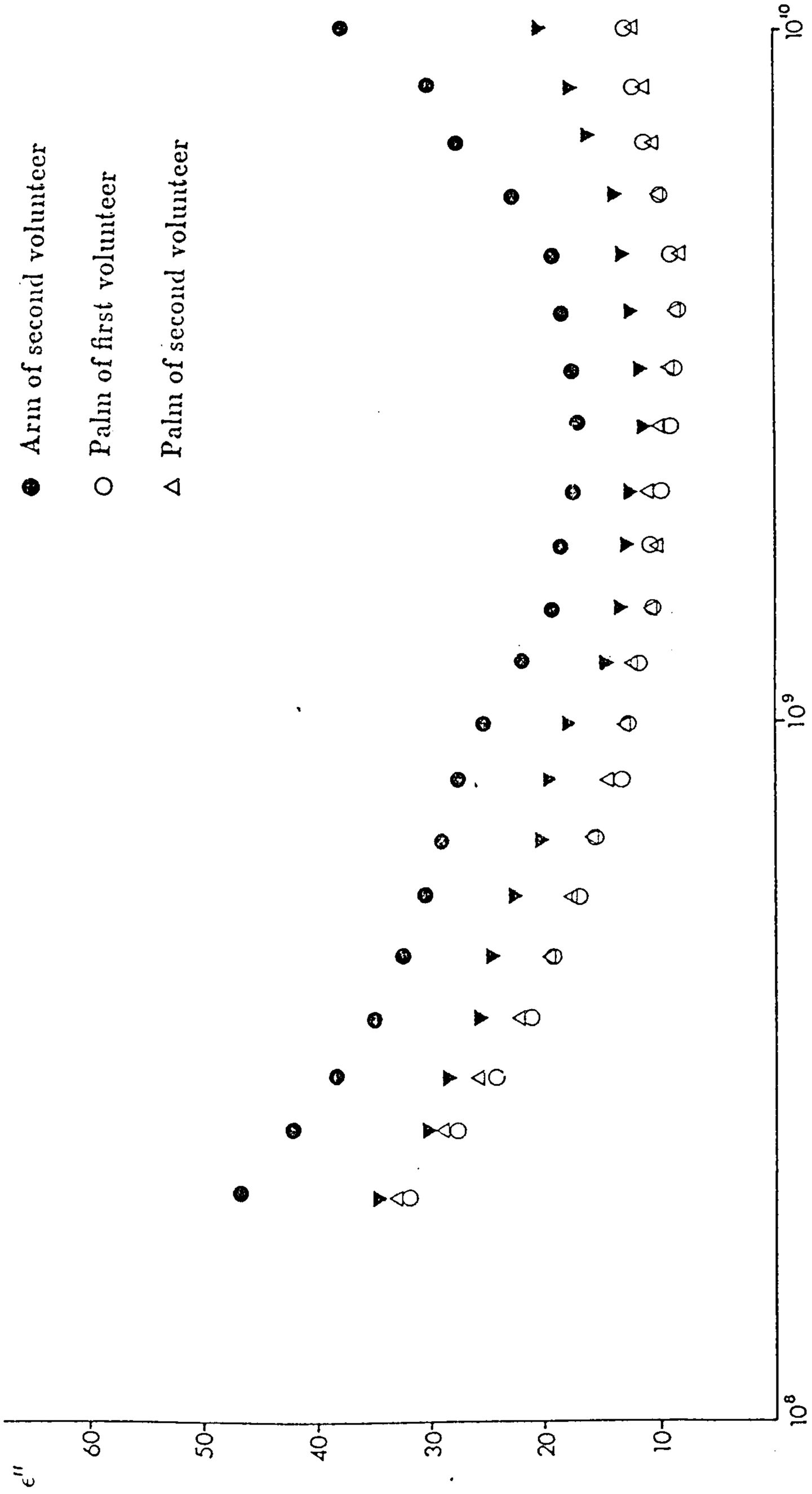

Fig 5.21 ϵ'' versus frequency for the palm of the hand and the forearm for two different volunteers.

The dispersion curves obtained from the 7mm probe are extremely interesting. The first point that can be seen is the difference in the skin thickness between the palm and the forearm resulting in the much higher value of ϵ' for the arm. As the water content of the epidermis is less than that of the dermis, the palm, having a much thicker epidermis layer, will have a lower value. The other point of interest is the difference in the same parts of the body for the two subjects. It may therefore be inferred that differences in skin thickness for different individuals may be predicted by this technique although, of course, a true validation would rely on a vast population being examined.

The main γ dispersion is seen from the data with the exception of one of the forearm experiments, where the subject did not maintain a constant pressure between the probe and the skin during the time taken for the complete experiment. The tail of the β dispersion is also clearly seen although there are not sufficient data points to allow accurate dielectric parameters fit to be attempted.

5.6 General Conclusions.

The object of the present work was two fold. In the first part coaxial line probes, to be used in a new Time Domain Spectrometer, were simulated using two numerical analysis techniques. Both of these techniques, namely the Method of Moments and the Finite Element Method, were used to to study the equivalent circuitof probes with known capacitance circuits. From these results several conclusions were reached, as follows

Previous studies concerning the relative accuracy of the Finite Element and the Method of Moments are not strictly valid (Gajda 1982). The size of the model in each of the simulations is not of the same relative order of magnitude for a conclusion to be drawn. However with a much more powerful computer facility large enough models may be run to have a strict critical evaluation of each technique.

The static equivalent circuit is valid for relative permittivites in excess of 10. Below this value of ϵ_m, the sample medium's real permittivity, the capacitance values in the equivalent circuit are varying by about 10% above the steady state value.

The two techniques provide a powerful design tool that can be used quickly to evaluate different probe designs before they are constructed.

The two techniques are ONLY design tools and once a probe is constructed the capacitances must be measured experimentally to obtain the correct values. This is due to the model running an ideal situation and subsequently not including machine tolerence errors in the manufacture.

The second part of the study concerned putting the results of the simulation work into a real experiment. A new Time Domain Spectrometer was designed that included two time referencing techniques. Both of these techniques were evaluated using standard liquids and the results of the experiments were critically analysed. The

main conclusion to arise from these results was that there is no significant difference in the performance of the two techniques.

During the testing stage it became apparent that the TDS, in conjunction with coaxial line probes, provides good, accurate data over a broad frequency band. The results show that the TDS is of comparable accuracy to frequency domain techniques up to a frequency of 10 GHz.

Several parts of the human body were then measured to show the versatility of the TDS when used in conjunction with the coaxial line probes. Each of the *in-vivo* measurements can be related to the histological features of the particular part of the body examined.

Several interesting points have been uncovered by the work. Although the results of the *in-vivo* experiments can be accounted for in simple terms, it would be interesting to try to interpret the results comprehensively in terms of the different skin and tissue layers. This would involve extensive numerical work on the fields around the probe's aperture in conjuction with using a model that would include conductivity terms in the simulation. If this problem can be solved a new diagnostic tool for diagnostic medicine could be developed.

A further development that would take place in conjunction with the detailed analysis of the results is the refining of the equivalent ciruit. This would involve studying the propagation effects at the aperture for the high frequencies.

Appendix to Chapter 5 Glossary of Histology Terms.

areolar tissue	Fibrous connective tissue having the fibres loosely arranged in a net or meshwork.
buccal	Relating to the cheek.
buccal gland	Small mucous glands in the cheek lining.
collagenous	An insoluable fibrous protein that occurs in vertebrates as the chief constituent of the fibrils of connective tissue.
epimysium	The external connective tissue sheath of a muscle.
epithelium	A membrane cellular tissue that protects other parts of the body.
keratin	Any of the various sulphur containing fibrous proteins that form the chemical basis of horny epidermal tissue.
lamina propia	A highly vascular layer of connective tissue under the basement lining of the membrane.
membrane	A thin soft pliable sheet or layer of cells.
mucous membrane	A membrane rich in mucous glands.
papillae	A small projecting body.
stratum	A layer of tissue.

Acknowledgements

To the following people I give my sincere thanks

Professor E. H. Grant for providing a place within his research group, for altering the direction of the project to meet my talents and for his active interest and support in the work.

Dr. I. R. Young, of GEC Research, who gave me the opportunity of working with the best NMR team in the world and encouraging me to start an external Ph.D.

Dr. C. Gabriel, a fountain of TDS knowledge and inspiration.

Dr R.W.M Lau for his friendship, encouragement and interest in the electrostatic simulation work.

Mr A.G. Collins, of GEC Research, who taught me more in the first six months at Hirst than the previous four years at university.

Mr G. Evans, my room mate.

Mr D.A. Sarup, Mr M.G.M. Richards and Mr J.M. Alison for their interest and friendship.

and finally my wife Catherine without whose constant support and encouragement this thesis would not exist.

References

Abrahamowitz A., "Tables of Mathematical Functions", National Bureau of Standards, Washington, 1964.

Amsel G., Bosshard R., "Sampling and Averaging Techniques in the Analysis of Fast Random Signals", Review of Sci. Instrum., vol 41, April 1970.

Anderson L., M.A.Sc. Thesis, University of Ottawa 1984.

Anderson L., Gajda G.B., Stuchly S.S., "Analysis of an Open-ended Coaxial Line Sensor in Layered Dielectrics", IEEE Trans. Instrum. Meas., vol IM-35, March 1986.

Anderson L., Stuchly S.S., Gajda G.B., "Parallel-plate Coaxial Sensor for Dielectric Measurements - Further Analysis", IEEE Trans. Instrum. Meas., vol IM-35, March 1986.

Arcone S.A., Wills R., "A Numerical Study of Dielectric Measurements Using Single Reflection Time Domain Reflectrometry", J. Phys. E. : Sci. Instrum. vol 19, 1986.

Athey T.W., Stuchly M.A., Stuchly S.S., "Measurement of Radio Frequency Permittivity of Biological Tissues with an Open-ended Coaxial Line : Part 1", IEEE Trans. Microwave Theory Tech., vol MTT-30, January 1982.

Barbenza G.H., "Measurement of Complex Permittivity of Liquids at Microwave Frequencies", J. Phys. E. : Sci. Instrum., vol 2., 1969.

Beezley R.S., Krueger R.J., "An Electromagnetic Inverse Problem for Dispersive Media", J. Math. Phys., vol 26, February 1985.

Bellamy W.L., Nelson S.O., Leffler R.G., "Developement of a Time Domain Reflectometry System for Dielectric Properties Measurement", American Society of Agricultural Engs., Paper No. 84-3548.

Bergland G.D., "Digital Real-time Spectral Analysis", IEEE Trans. Electronic Computers, vol EC-16, April 1967.

Blackman R.B., Turey J.W., "The Measurement of power spectra from the point of view of communications engineering", Dover Publications, New York, 1958.

Boast W.B., "Vector Fields", Harper International, 1964.

Burdette E.C., Cain F.L., Seals J., "*In-vivo* Probe Measurement Technique for Determining Dielectric Properties at VHF Through Microwave Frequencies" IEEE Trans. Microwave Theory Tech., vol IM-28, April 1980.

Chan P.C., "An Implicit Method for Solving Maxwell's Equations", IEEE Trans Nuclear Sc., NS-33, December 1986.

Chahine R., Bose T.K, "Measurements of Dielectric Properties by Time Domain Spectroscopy", J. Phys. Chem., vol 65, September 1976.

Chahine R., Bose T.K, "Comparative Studies of Various Methods in Time Domain Spectroscopy", J. Phs. Chem., vol 72, January 1980.

Chahine R., Bose T.K, "Measurement of Small Dielectric Loss by Time Domain Spectroscopy : Application to Water/Oil Emulsions", IEEE Trans. Instrum. Meas., vol IM-32, June 1983.

Clark A.H., Quickenden P.A., Suggett A., "Multiple Reflection Time Domain Spectroscopy", J. Chem. Soc. : Faraday II, vol 70, 1974.

Cole R.H., "Evaluation of Dielectric Behaviour by Time Domain Spectroscopy. I. Dielectric Response by Real Time Analysis", J. Phys. Chem., vol 79, 1975.

Cole R.H., "Evaluation of Dielectric Behaviour by Time Domain Spectroscopy. II. Complex Permittivity", J. Phys. Chem., vol 79, 1975.

Cole R.H., "Time Domain Spectroscopy of Dielectric Materials", IEEE Trans. Instr. Meas., vol IM-25, December 1976.

Cole R.H., Mashimo S., Winsor, P. IV., "Evaluation of Dielectric Behaviour by Time Domain Spectroscopy. III. Precision Difference Methods", J. Phys. Chem., vol 84, 1980.

Collin R.E., "Field Theory of Guided Waves", McGraw-Hill, 1960.

Cook H.F., British Jour. Appl. Phys., vol 2, 1951.

Costache G.I., "Finite Element Method Applied to Skin-effect Problems in Strip Transmission Lines", IEEE Trans. Microwave Theory Tech., vol MTT-35, November 1975.

Cronson H.M., Nicolson A.M., Mitchell P.G., "Extensions of Time Domain Metrology Above 10 GHz to Materials Measurements", IEEE Trans. Instrum. Meas., vol IM-23, December 1974.

Daffe J., Olsen R.G, "An Integral Equation Technique for Solving Rotationally Symmeteric Electrostatic Problems in Conducting and Dielectric Material", IEEE Trans. Power Apparatus Systems, vol PAS-98, January 1979.

Dawkins A.W.J., Ph.D Thesis, University of London, 1979.

Dawkins A.W.J., Sheppard R.J., Grant E.H., "An Online Computer Based System for Performing Time Domain Spectroscopy 1. Main Features of the Basic System", J. Phys. E : Sci. Instrum., vol 12, 1979.

Dawkins A.W.J., Sheppard R.J., Grant E.H., "An Online Computer Based System for Performing Time Domain Spectroscopy 2. Analysis of Errors in Total Reflection TDS", J. Phys. E : Sci. Instrum., vol 14, 1981.

Dawkins A.W.J., Sheppard R.J., Grant E.H., "An Online Computer Based System for Performing Time Domain Spectroscopy 3. Presentation of Results for Total Reflection TDS", J. Phys. E : Sci. Instrum., vol 14, 1981.

Deming X., Liping L., Zhiyan J., "Measurements of the Dielectric Properties of Biological Substances Using an Improved Open-ended Coaxial Line Resonator Method", IEEE Trans. Microwave Theory Tech., vol MTT-32, December 1987.

Dunlop J., "Lecture Course on Signal Processing", University of Strathclyde Lectures at G.C.H.Q., 1983.

El-Samahy A., Gestblom B., Sjoblom J., "The Dielectric Spectra of Some Linear 1,2-Diols", Finn. Chm. Lett., February 1984.

Epstein B.R., Gealt M.A., Foster K.R., "The Use of Coaxial Probes for Precise Dielectric Measurements : A Reevaluation", IEEE Trans. Microwave Theory Tech. Symposium, MTT-S 1987.

Fellner-Feldegg H., "The Measurement of Dielectrics in the Time Domain", Journal Phys. Chem., vol 73, 1969.

Fellner-Feldegg H., "A Thin Sample Method for the Measurement of Permeability, Permittivity and Conductivity in the Frequency and Time Domain", Journal Phys. Chem., vol 76, 1972

Fernadez P.H., Private Communication, University of London, 1987.

Fusco V.F., "Microwave Circuits Analysis and Computer-aided Design", Prentice-Hall International, Cambridge, 1987.

Gabriel C., Ph.D Thesis, University of London, 1983.

Gabriel C., Dawkins A.W.J., Sheppard R.J., Grant E.H., "Comparison of the Single Reflection and Total Reflection TDS Techniques", J. Phys. E: Sci. Instrum., vol 17, 1984.

Gabriel C., Bentall R.H., Grant E.H., "Comparison of the Dielectric Properties of Normal and Wounded Human Skin Material", Bioelectromagnetics, vol 8, 1985.

Gabriel C., Grant E.H., Young I.R., "Use of Time Domain Spectroscopy for Measuring Dielectric Properties With a Coaxial Line Probe", J. Phys. E: Sci. Instrum., vol 19, 1986.

Gabriel C., Private Communication, 1987.

Gabriel C., Patent Pending, 1988.

Gabriel C., Grant E.H., Tata R., Brown P.R., Gestblom B., Noreland E., "Dielectric Behaviour of Aqueous Solutions of Plasmid DNA at Microwave Frequencies", Biophys. J. *in press*, 1989.

Gajda G.B, "A Method for the Measurement of Permittivity at Radio and Microwave Frequencies", IEEE Int. Electrical, Electronics Conf. and Exposition, Conference Digest, Toronto, Canada, October 1979.

Gajda G.B., M.A.Sc. Thesis, University of Ottawa 1982.

Gajda G.B, Stuchly S.S., "An Equivalent Circuit of an Open-ended Coaxial Line", IEEE Trans. Instrum. Meas., vol IM-32, December 1983.

Gajda G.B, Stuchly S.S., "Numerical Analysis of Open-ended Coaxial Lines", IEEE Trans. Microwave Theory Tech., vol MTT-31, May 1983.

Galejs J., "Antennas in Inhomogeneous Media", Pergammon Press, Oxford, 1969.

Gestblom B., Noreland E., "On the Fourier Transformation of Dielectric Time Domain Spectroscopy Data", J. Phys. Chem., vol 80, 1976.

Gestblom B., Noreland E., "Transmission Methods in the Dielectric Time Domain Spectroscopy", J. Microwave Power, vol 12, 1977.

Gestblom B., Noreland E., "Transmission Methods in the Dielectric Time Domain Spectroscopy", J. Phys. Chem., vol 81, 1977.

Gestblom B., Noreland E., "A New Transmission Method in Dielectric Time Domain Spectroscopy", Chem. Phys. Lett., vol 47, April 1977.

Gestblom B., Noreland E., "On the Method of Reflection and Short in Dielectric Time Domain Spectroscopy", Chem. Phys. Lett., vol 74, September 1980.

Gestblom B., Jonsson B., "A Computer Controlled Dielectric Time Domain Spectrometer", J. Phys. E : Sci. Instrum., vol 13, 1980.

Gestblom B., "On the Time Referencing Problem in Time Domain Spectroscopy", J. Phys. E : Sci. Instrum., vol 14, 1981.

Gestblom B., "The Sampling Oscilloscope in Dielectric Frequency Domain Spectroscopy", J. Phys. E : Sci. Instrum., vol 15, 1982.

Gestblom B., Noreland E., "The Single Reflection in Dielectric Time Domain Spectroscopy", J. Phys. Chem., vol 88, 1984.

Gestblom B., Private Communication, University of Uppsala, 1987.

van Germet J.C., de Loor G.P., Bordewijk P., Quickenden P.A., Suggett A., "Dielectric Relaxation of some Normal Alcohols in Non-Polar Solvents", Adv. Mole. Relax. Proc., vol 5., 1973.

Gradshteyn I.S., "Tables of Integrals, Series and Product", New York : Academic 1965.

Grant E.H., Sheppard R.J, South G.P, "Dielectric Behaviour of Biological Molecules in Solution", Clarendon Press, Oxford, 1978.

Harrington R.F., "Field Computation by Moment Methods", Macmillan, New York, 1968.

Infotek Systems, "AD 200 Analogue/Digital Converter", Infotek Systems, Anaheim, California, 1986.

Jones D.S., "Methods in Electromagnetic Wave Propagation", Oxford University Press, 1979.

Jordan B.P., Sheppard R.J., Szwarnowski S., "The Dielectric Properties of Formamide, Ethanediol and Methanol", J. Phys. D. : Appl. Phys., vol 11, 1978.

Kaatze U. Giese K. "Dielectric Relaxation Spectroscopy of Liquids : Frequency Domain and Time Domain Experimental Methods ", J. Phys. E : Sci. Instrum., vol 13, 1980.

King R.W.P., "Transmission Line Theory", McGraw-Hill, 1955.

Konrad A., "High-Order Triangular Finite Elements for Electromagnetic Waves in Anisotropic Media", IEEE Trans. Microwave Theory Tech., vol MTT-25, May 1977.

Kraszwski A., Stuchly S.S., "Capacitance of Open-ended Dielectric Filled Coaxial Lines - Experimental Results", IEEE Trans. Instrum. Meas., vol IM-32, December 1983.

Kraszwski A., Stuchly S.S., Stuchly M.A., Symons S.A., "On the Measurement Accuracy of the Tissue Permittivity *in-vivo*", IEEE Trans. Instrum. Meas., vol IM-32, March 1983.

Lau R.W.L., Sheppard R.J., "The Modelling of Biological Systems in Three Dimensions using the Time Domain Finite Difference Method : I. The Implementation of the model", Phys. Med. Biol., vol 31, November 1986.

Ligthart L.P., "A Fast Computational Technique for Accurate Permittivity Determination Using Transmission Line Methods", IEEE Trans. Microwave Theory Tech., vol MTT-31, March 1983.

Lin Y., Shafai L., "Moment Method Solution of the Near-field Distribution and Far-field Patterns of Microstrip Antennas", IEE Proceedings, vol 132, October 1985.

Loeb H.W., Young G.M, Quickenden P.A., Suggett A., "New Methods for the Measurement of Complex Permittivity up to 13 Ghz and their Application to the Studies of Dielectric Relaxation of Polar Liquids including Aqueous Solutions", Ber. Bunsenges. Phys. Chem., vol 75, 1971.

de Loor G.P., van Germet M.J.C., Gravesteyn H., "Measurement of Dielectric Permittivity with Time Domain Reflectometry. Extension of the Method to Lower Relaxation Frequencies", Chem. Phys. Lett., vol 18, 1973.

Marcuvitz N., "Waveguide Handbook", Dover Publications, Boston Mass., 1951.

McArthur C.M., Private Communication, 1988.

McDonald B.H., Wexler A., "Finite Element Solution of Unbounded Field Problems", IEEE Trans. Microwave Theory Tech., vol MTT-20, 1972.

McDonald B.H., Friedman M., Wexler A., "Variational Solution of Integral Equations", IEEE Trans. Microwave Theory Tech., vol MTT-22, March 1974.

Misra D.K, "A Study of Coaxial Line Excited Monopole Probes for *in Situ* Permittivity Measurements", IEEE Trans Instrum. Meas., vol IM-36, December 1987.

Molinari G.H., University of Genoa, Private Communication, 1987.

Mosig J.R., Besson J.E., Gex-Fabry M., Gardiol F.E., "Reflection of an Open-ended Coaxial Line and Apllication to Nondestructive Measurement of Materials", IEEE Trans. Instrum. Meas., vol IM-30, March 1981.

Ney M.M., "Method of Moments as Applied to Electromagnetic Problems", IEEE Trans. Microwave Theory Tech., vol MTT-33, October 1985.

Nicolson A.M., "Broad-Band Microwave Transmission Characteristics from a Single Measurement of the Transient Response", IEEE Trans. Instrum. Meas., vol IM-17, December 1968.

Norrie D.H, de Vries G., "An Introduction to Finite Element Analysis", Academic Press, 1978.

Pethig R., "Dielectric Properties of Biological Materials : Biophysical and Medical Applications", IEEE Trans. Electical Insulation, vol EI-19, October 1984.

Pethig R., "Dielectric Properties of Body Tissues", Clin. Phys. Physiol. Meas., vol 8, August 1987.

Richter K., Private Communication, 1987.

Richards D.J., Wexler A., "Finite Element Solutions Within Curved Boundaries", IEEE Trans. Microwave Theory Tech., vol MTT-20, December 1972.

Samulon H.A., "Spectrum Analysis of Transient Response Curves", Proc. IRE, vol 39, 1951.

Schwan H.P., Foster K.R., "RF-Field Interactions with Biological Systems : Electrical Properties and Biophysical Mechanisms", Proc. IEEE, vol 68, January 1980.

Schwartz M., "Signal Processing : Discrete Signal Analysis, Detection and Estimation", McGraw-Hill 1976.

Seshadri S.R., "Fundamentals of Transmission Lines and Electromagnetic Fields", Addison-Wesley, 1971.

Shannon C.E., "Communication in the Presence of Noise", Proc. I.R.E., 1949.

Sheppard R.J., Jordan B.P., Grant E.H., "Least Squares Analysis of Complex Data with Applications to Permittivity Measurements", J. Phys. D : Appl. Phys., vol 3, 1970.

Sheppard R.J., "Least Squares Analysis of Complex Weighted Data with Dielectric Applications", J. Phys. D : Appl. Phys., vol 6, 1973.

Silvester P., "High Order Ploynomial Triangular Finite Elements for Potential Problems", Int. J. Enging. Sci., vol 7, 1969

Silvester P., "Construction of Triangular Finite Element Universal Matrices", Int. J. Numerical Meth. Engin., vol 12, June 1978.

Silvester P., Ferrari R.L., "Finite Elements for Electrical Engineers", Cambridge University Press, 1986.

Silvester P., Private Communication, McGill University, 1987.

Simkin J., Trowbridge C.W., "Lecture Notes on Computation of Electromagnetic Fields", Vector Fields, 1986.

Stone G.O., "High Order Finite Elements for Inhomogeneous Acoustic Guiding Structures", IEEE Trans. Microwave Theory Tech., vol MTT-21, August 1973.

Stratton J.A., "Electromagnetic Theory", McGraw-Hill, 1941.

Stuchly M.A., Stuchly S.S, "Coaxial Line Reflection Methods for Measuring Dielectric Properties of Biological Substances at Radio and Microwave Frequencies - A Review", IEEE Trans. Instrum. Meas., vol IM-29, September 1980.

Stuchly M.A., Brady M.M, Stuchly S.S, Gajda G.B., "Equivalent Circuit of an Open-ended Coaxial Line in a Lossy Dielectric", IEEE Trans. Instrum. Meas., vol IM-31, June 1982.

Stuchly S.S., Rzepecka M.A., Iskander M.F., "Permittivity Measurement at Microwave Frequencies Using Lumped Elements", IEEE Trans. Instrum. Meas., vol IM-23, March 1974.

Stuchly S.S., Internal Report, University of Ottawa, 1979.

Stuchly S.S., Gajda G.B., Anderson L., Kraszewski A., "A New Sensor for Dielectric Measurements", IEEE Trans. Instrum. Meas., vol IM-35, June 1986.

Suggett A., Mackness P.A., Tait M.J., Loeb H.W., Young G.M., "Dielectric Relaxation Studies by Time Domain Spectroscopy", Nature, vol 228, 1970.

Trowbridge C.W., Private Communication, London, 1987.

Voss G., Happ H., "Time Domain Spectroscopy of Dielectric Properties up to 15 GHz with Voltage Pulses. Application to Solids and Liquids", J. Phys. E : Sci. Instrum., vol 17, 1984.

Wexler A., "Computation of Electromagnetic Fields", IEEE Trans. Microwave Theory Tech., vol MTT-17, August 1969.

Whiteman J.R., "The Mathematics of Finite Elements and Applications", Academic Press, 1973.

Whittingham T.A., J. Phys. Chem., vol 74, 1970.

Zienkiewicz O.C. "The Finite Element Method", McGraw-Hill, 1977.